

Technische Universität München
TUM School of Engineering and Design

On the Primary Zone Flame Dynamics of Air-Staged Combustion Chambers in Aero Engines

Martin March

Vollständiger Abdruck der von der TUM School of Engineering and Design
der Technischen Universität München zur Erlangung eines

DOKTORS DER INGENIEURWISSENSCHAFTEN (DR.-ING.)

genehmigten Dissertation.

Vorsitz:

Prof. Dr.-Ing. Volker Gümmer

Prüfende der Dissertation:

Prof. Dr.-Ing. Thomas Sattelmayer

Prof. Wolfgang Polifke, Ph.D.

Die Dissertation wurde am 14.08.2024 bei der Technischen Universität München eingereicht
und durch die TUM School of Engineering and Design am 19.12.2024 angenommen.

In liebevoller Erinnerung an meinen Vater.

Vorwort

Die vorliegende Arbeit entstand im Rahmen meiner Tätigkeit als wissenschaftlicher Mitarbeiter am Lehrstuhl für Thermodynamik der Technischen Universität München im Rahmen des Luftfahrtforschungsprogrammes des Bundes (LuFo V-3) innerhalb der Programmlinie "ökoeffizientes Fliegen". Das Thema des Forschungsprojektes waren die "Grundlagenuntersuchungen zur Modellierung von Verbrennungsinstabilitäten in Flugtriebwerksbrennkammern mit Luftstufung" (Akronym: "ViFlumiLu", Förderkennzeichen: 20E1715). Das Forschungsprojekt wurde durch die finanzielle Unterstützung des Bundesministeriums für Wirtschaft und Klimaschutz ermöglicht, wofür ich meinen Dank aussprechen möchte.

Meinem Doktorvater Herrn Professor Dr.-Ing. Thomas Sattelmayer möchte ich herzlich für das entgegengebrachte Vertrauen, sowie die fachliche Unterstützung bei der Durchführung des Forschungsprojektes danken. Herrn Dr.-Ing. Christoph Hirsch gilt ebenso mein herzlicher Dank, insbesondere für die Hilfestellung während der Auslegungs- und Konstruktionsphase des neu aufgebauten Prüfstandes.

Herrn Professor Wolfgang Polifke, Ph.D., danke ich herzlich für die freundliche Übernahme des Koreferats und die Begutachtung meiner Arbeit. Weiterhin danke ich Herrn Professor Dr.-Ing. Volker Gümmer für den Vorsitz bei der mündlichen Prüfung.

Bei allen ehemaligen Kollegen möchte ich mich für die freundliche Atmosphäre am Lehrstuhl bedanken. Vielen Dank meinem Projektkollegen Julian Renner für die produktive Zusammenarbeit während der Aufbauphase des neuen, thermoakustischen Prüfstandes. Zudem möchte ich allen Studenten, welche tatkräftig zum Erfolg des Forschungsprojektes beigetragen haben

meinen Dank aussprechen.

Besonderer Dank gilt der mechanischen und elektrischen Werkstätte, vor allem Jens Hümmer, Gerhard Giel, Helmut Koller und Thomas Schleussner für die unzähligen Fertigungs- und Installationsaufgaben im Rahmen des Prüfstandaufbaus. Das Sekretariat mit Helga Basset, Brigitte Hirsch, sowie Frau Schulz-Reichwald danke ich ebenso für die Hilfestellung bei den zahlreichen administrativen Aufgaben am Lehrstuhl.

Mein größter Dank gilt abschließend meinen Eltern für die großzügige Unterstützung in allen Lebenslagen.

München, im Januar 2025

Martin March

Abstract

The aim of the present work is the investigation of the flame dynamics of the primary zone in air-staged aero engine combustion chambers (RQL). Furthermore, the transfer of the flame dynamics of the isolated primary zone to the compact RQL arrangement is examined. A new experimental approach realized in a specifically designed thermoacoustic test rig allows the identification of the isolated thermoacoustic behavior of the primary and secondary zone respectively. In addition, both combustion zones can be arranged in one compact RQL combustion chamber to investigate the combined flame dynamics.

The quantification of the flame dynamics in terms of flame transfer functions (FTF) is performed by using the purely acoustic multimicrophone method (MMM) and the Rankine-Hugoniot jump conditions, as well as the optical method based on the flame's chemiluminescence (OH^* , CH^* , C_2^* and CO_2^*). The quality of the acoustic wavefield reconstruction is improved by implementing a thermocouple correction method for the hot gas environment, as well as a criterion for the selection of three out of four dynamic pressure transducers in each impedance measurement duct for the application of the multimicrophone method.

The purely acoustically measured FTF amplitudes of the fuel-rich operated primary zone demonstrate a reduction of the amplitude with increasing equivalence ratio. A root cause study is conducted to clarify the origin of the observed behavior of the FTF amplitudes primary flame under fuel-rich combustion conditions. The study reveals that the influence of atomization and evaporation, as well as thermal effects are found not to be the root cause for the observed behavior. Lastly, the dynamic of the synthesis gas formation during fuel-rich combustion and the contact of the flame with the cold combustion chamber wall are assumed to alter the flame dynamics.

An alternative approach for the determination of the FTF from the FTM22-element is provided, which considers the chemical conversion and the temperature dependencies of the specific heat capacities across the flame, as well as the unsteady flame movement. The resulting FTFs reveal a substantial deviation in FTF amplitude compared to the classic Rankine-Hugoniot relations.

The optical determination of FTFs in the isolated primary zone using the chemiluminescence of the flame shows good agreement with the acoustic method for all of the investigated radicals (OH^* , CH^* , C_2^* and CO_2^*).

In practical aero engine combustion chambers the overall flame dynamics of both combustion zones are of interest. Therefore, an estimation based on the superposition of the flame dynamics of both isolated combustion chambers demonstrates the contribution of the individual zones to the overall thermoacoustic behavior of compact RQL combustion chambers. The assumption of the dominating primary zone is experimentally verified by evaluating thermoacoustic measurements for the compact RQL arrangement using a one-dimensional acoustic network model and the 2-port multimicrophone method.

Kurzfassung

Das Ziel der vorliegenden Arbeit ist die Untersuchung der Flammendynamik der Primärzone in luftgestuften Flugtriebwerksbrennkammern (RQL). Darüber hinaus soll der Transfer der Flammendynamik der isolierten Primärzone auf die kompakte RQL-Anordnung untersucht werden. Zu diesem Zweck wird ein experimenteller, wissenschaftliche Ansatz in einem speziellen thermoakustischen Prüfstand realisiert. Dieser Ansatz erlaubt die Identifizierung des isolierten thermoakustischen Verhaltens der Primär- und Sekundärzone. Zusätzlich ist deren Kombination in einer kompakten RQL-Brennkammer zur Vermessung der kombinierten Flammendynamik möglich.

Die Quantifizierung der Flammendynamik in Form von Flammentransferfunktionen (FTF) erfolgt mit Hilfe der rein akustischen Multimikrofonmethode (MMM) und den Rankine-Hugoniot Beziehungen, sowie mit der optischen Methode, welche auf der Chemilumineszenz der Flamme basiert (OH^* , CH^* , C_2^* und CO_2^*). Die Rekonstruktionsqualität des akustischen Wellenfeldes wird durch die Implementierung einer Thermoelement-Korrekturmethode innerhalb der Heißgasumgebung und einem Kriterium für die Wahl von 3 aus 4 dynamischen Druckaufnehmer zur Anwendung der Multimikrofonmethode optimiert.

Die rein akustisch gemessenen FTF-Amplituden der fett betriebenen Primärzone zeigen einen zunehmenden Abfall der Amplitude mit steigendem Äquivalenzverhältnis. Eine Studie zur Ursache für das Verhalten der FTF-Amplituden bei fetter Verbrennung wird durchgeführt. Aus dieser Studie geht hervor, dass der Einfluss von Zerstäubung und Verdampfung, sowie thermische Effekte nicht die Ursache für das beobachtete Verhalten sind. Schließlich bleibt die Vermutung, dass die Dynamik der Synthesegasproduktion und der Kontakt der Flamme mit der kalten Brennkammerwand für das beobachtete Verhalten der FTF-Amplituden bei fetter Verbrennung in der Primärzone

mögliche Ursachen sind.

Ein alternativer Ansatz zur Bestimmung der FTF aus dem FTM22-Element wird hergeleitet, welcher die chemische Umwandlung und die Temperaturabhängigkeit der Gaseigenschaften stromauf und stromab der Flamme, sowie die instationäre Flammenbewegung berücksichtigt. Im Vergleich zu den klassischen Rankine-Hugoniot-Beziehungen, zeigen die resultierenden alternativen FTFs eine erhebliche Abweichung bezüglich der FTF-Amplitude.

Die optische Untersuchung der FTFs in der isolierten Primärzone unter Verwendung der Flammenstrahlung aller gemessenen Radikale (OH^* , CH^* , C_2^* and CO_2^*) zeigt gute Übereinstimmung mit der rein akustischen Methode.

In praktischen Brennkammern von Flugzeugtriebwerken ist die globale Flammendynamik beider Verbrennungszonen von Interesse. Aus diesem Grund wird eine Abschätzung des Beitrags der einzelnen Verbrennungszonen zur gesamten Flammendynamik von RQL Brennkammer unter Verwendung des Superpositionsprinzips gezeigt. Die Annahme einer dominierenden Primärzone hinsichtlich der Flammendynamik von RQL Brennkammern wird durch Auswertung experimenteller Daten der kompakten Anordnung mit Hilfe eines eindimensionalen, akustischen Netzwerkmodells und der 2-Port Multimikrofonmethode verifiziert.

Contents

List of Figures	xv
List of Tables	xxiii
Nomenclature	xxv
1 Introduction	1
1.1 Technological Background	1
1.2 RQL Technology	2
1.3 Combustion Instabilities	3
1.3.1 Thermoacoustic Driving Mechanisms in RQL Combustors	4
1.3.2 Literature Review on RQL Flame Dynamics	7
1.4 Research Objectives and Thesis Structure	9
2 Fundamentals	11
2.1 Linear Acoustics	11
2.1.1 Wave Equation and Solution	12
2.1.2 Convective Wave Equation and Solution	14
2.1.3 Acoustic Boundaries	15
2.1.4 Network Modeling	16
2.2 Flame Dynamics	18
2.2.1 Flame Transfer Functions	18
2.2.2 Rankine-Hugoniot Relations	20
2.3 Chemiluminescence	23
3 Test Rig and Experimental Setup	25
3.1 Test Rig	25
3.1.1 Concept for the Primary Zone Investigations	26

3.1.2	Primary Zone Combustion Chamber	28
3.1.3	Compact RQL Combustion Chamber	33
3.1.4	Thermodynamic Design	35
3.1.5	Acoustic Design	40
3.2	Experimental Setup for the Primary Zone Measurements	45
3.3	Experimental Setup for the Compact RQL Measurements	47
4	Measurement Methods	49
4.1	Data Acquisition System	50
4.2	Chemiluminescence Measurements	51
4.2.1	Global Chemiluminescence	51
4.2.2	Planar Line-of-Sight Chemiluminescence	53
4.3	Thermoacoustic Measurements	56
4.3.1	Operating Points	56
4.3.2	Acoustic Method	58
4.3.3	Optical Method	64
4.3.4	Optimization of Acoustic Wavefield Reconstruction	65
5	Steady Flame Behavior Primary Zone	71
5.1	Commissioning Tests and Operation Range	71
5.2	Global Chemiluminescence	75
5.3	Chemiluminescence Images	79
6	Primary Zone Flame Dynamics	85
6.1	Acoustic Flame Transfer Functions	85
6.2	Root Cause Study	90
6.2.1	Atomization and Evaporation	90
6.2.2	Thermal Effects	92
6.2.3	Synthesis Gas Formation	94
6.3	Alternative Determination of Flame Transfer Functions	95
6.4	Optical Flame Transfer Functions	109
7	Compact RQL Combustor Flame Dynamics	113
7.1	Transfer of the Isolated Flame Dynamics	113
7.2	Measured Flame Dynamics	117
7.2.1	Operating Points and Flame Images	117

7.2.2 Compact RQL Model and Evaluation Method	119
7.2.3 Case without Combustion	125
7.2.4 Case with Combustion	129
8 Summary and Conclusions	139
Previous Publications	145
Supervised Student Theses	147
References	149

List of Figures

1.1	Working principle of a rich-quench-lean (RQL) combustion chamber.	2
1.2	RQL NO _x reduction strategy.	3
1.3	Driving mechanisms in RQL combustion chambers.	5
2.1	Sketch of acoustic two-ports in terms of transfer matrices.	17
2.2	Rankine-Hugoniot jump conditions across the flame.	20
2.3	Typical chemiluminescence spectrum of a lean, premixed kerosene flame under atmospheric conditions.	23
2.4	Energy levels of diatomic molecules.	24
3.1	Basic concept of the test rig setup for the primary zone investigations.	26
3.2	CAD model of the test rig configuration for measurements in the primary zone.	28
3.3	CAD model of the injector segment (left), Injector (middle) and primary zone combustion chamber (right).	29
3.4	Design intent of the non-premixed natural gas nozzle for the primary zone. The red solid line shows the geometric injection angle for the natural gas nozzle $\alpha_{\text{geo,NG}}$, the black solid line for the kerosene nozzle $\alpha_{\text{geo,kero}}$. The red dashed line shows the calculated jet-in-cross-flow trajectory for the natural gas $\dot{m}_{\text{NG,PZ}}$ injected into the primary air $\dot{m}_{\text{a,PZ}}$	30
3.5	Sketch of the design and working principle of the natural gas ignition burner in the primary zone.	32
3.6	CAD model of the injector segment (left), Injector-1 (middle) and compact RQL combustion chamber (right).	34

3.7	Adiabatic flame temperature and combustion products over the equivalence ratio for a kerosene surrogate and thermodynamic equilibrium conditions.	35
3.8	Temperatures and heat fluxes for one control volume along the primary zone and transition duct.	36
3.9	Temperatures and heat fluxes along the primary combustion chamber using a 1D calculation.	37
3.10	Temperatures and heat fluxes along the transition duct using a 1D calculation.	38
3.11	Estimation of the auto-ignition time delay in the secondary zone using a homogeneous constant pressure reactor in <i>Cantera</i>	39
3.12	CAD model of the transition duct including PCBs and thermocouples.	42
3.13	Frequency response in terms of relative velocity fluctuation u'/\bar{u} at the burner outlet calculated with 1D-NWM approach for different loudspeaker models.	43
3.14	CAD model of the loudspeaker housings and connecting ducts to the test rig with ceramic honeycomb.	44
3.15	Test rig setup for the measurements in the primary zone combustion chamber (side view).	45
3.16	Setup for the measurements in the compact RQL combustion chamber (top view).	48
4.1	DAQ system for optical and thermoacoustic measurements for the primary zone setup (cf. Fig. 3.15).	50
4.2	Photo of the PMT array setup for the primary zone measurements.	53
4.3	Photo of the high-speed imaging setup for the primary zone measurements.	54
4.4	Evaluation process of the high-speed imaging data for steady and unsteady measurements.	55
4.5	Adiabatic flame temperature for a kerosene surrogate (black line) and equivalence ratios for the operating points in the primary zone (red and blue squares).	57
4.6	Working principle of the multimicrophone method (MMM) for the determination of acoustic transfer matrices.	58

4.7	Comparison of the calculated adiabatic flame temperatures $T_{ad,PZ}$ and measured corrected hot gas temperatures $T_{TC,corr,1}$ at the first thermocouple position downstream the primary zone. .	63
4.8	Measured T_{TC} and corrected $T_{TC,corr}$ temperatures along the transition duct.	66
4.9	FTF amplitudes (top) and phases (bottom) for an operating point with an equivalence ratio of $\phi = 1.18$ and different approaches for the selection of the PCB combination for the acoustic wavefield reconstruction.	69
5.1	Normalized pressure spectra for a thermal power of $\dot{Q}_{th} = 56$ kW and a preheating temperature of $T_{a,PZ} = 473$ K for a stable (top) and unstable (bottom) operating point with an equivalence ratio of $\phi_{PZ} = 1.33$ and $\phi_{PZ} = 1.11$, respectively.	73
5.2	Stability map of the primary zone for an air preheating temperature of $T_{a,PZ} = 473$ K.	74
5.3	Flame shapes in the primary zone for an air preheating temperature of $T_{a,PZ} = 473$ K and a thermal power of $\dot{Q}_{th} = 53.2$ kW. Conical flame (left), constricted flame (middle) and lifted flame (right).	75
5.4	Normalized mean PMT chemiluminescence intensity for four different radicals against the equivalence ratio in the primary zone.	75
5.5	Normalized mean PMT chemiluminescence intensity for four different radicals against the equivalence ratio and a variation in thermal power of +/-20%.	77
5.6	Normalized chemiluminescence intensity ratio of CH^*/C_2^* against the equivalence ratio and a variation in thermal power of +/-20%.	79
5.7	Time-averaged line-of-sight (upper plots) and inverse Abel-transformed (lower plots) OH^* -images for operating points with an equivalence ratio of $\phi_{PZ} = 0.8, 0.9, 1.11, 1.25$ (from left to right). The white dashed line indicates the axial location of the center-of-gravity $x_{CoG,fl}$ (Eq. 4.1) and the cross the pixel with the maximum intensity. The chemiluminescence intensity is normalized to the corresponding maximum of each image.	80

5.8	Time-averaged line-of-sight (upper plots) and inverse Abel-transformed (lower plots) CH^* -images for operating points with an equivalence ratio of $\phi_{\text{PZ}} = 0.8, 0.9, 1.11, 1.25$ (from left to right). The white dashed line indicates the axial location of the center-of-gravity $x_{\text{CoG,fl}}$ (Eq. 4.1) and the white cross the pixel with the maximum intensity. The chemiluminescence intensity is normalized with the corresponding maximum of each image.	81
5.9	Normalized axial distance of the center-of-gravity $x_{\text{CoG,fl}}$ from the burner outlet (Eq. 4.1) of the Abel-transformed OH^* - (purple) and CH^* -images (blue).	82
6.1	FTF amplitudes (top) and phases (bottom) for rich (left) and lean (right) equivalence ratios, an air preheating temperature of $T_{\text{a,PZ}} = 423\text{K}$ and a pressure loss of $\Delta p_{\text{a,PZ}}/p_{\text{a,PZ}} \approx 4\%$ obtained with the purely acoustic MMM and the Rankine-Hugoniot relations.	86
6.2	Normalized mean velocity from an isothermal CFD simulation in the mid plane of the primary zone combustion chamber. The streamlines are starting at the burner outlet and are color coded according to the normalized velocity. Additionally, an LoS OH^* -image is superimposed as an example.	88
6.3	Comparison of the phase delay for all rich (left) and lean (right) operating points measured with the purely acoustic MMM (bottom) and calculated with the phase delay model (top).	89
6.4	Time averaged LoS OH^* -images for kerosene (top) and natural gas combustion (bottom) in the primary zone for an equivalence ratio of $\phi_{\text{PZ}} = 0.91$ (left) and $\phi_{\text{PZ}} = 1.11$ (right). The white dashed line indicates the axial location of the center of gravity $x_{\text{CoG,fl}}$ (Eq. 4.1) and the white cross the pixel with the maximum intensity.	91
6.5	Comparison of the purely acoustically measured FTF_{RH} for kerosene and natural gas combustion for an equivalence ratio of $\phi_{\text{PZ}} = 1.11$ (left) and $\phi_{\text{PZ}} = 0.91$ (right).	92
6.6	Control volume for an acoustically compact flame with the cold state upstream (c) and the hot state downstream (h) of the flame.	96

6.7	Contribution of the m' -term compared to the h' -term to the overall heat release fluctuation in Eq. 6.21 for an air preheating temperature of $T_a = 423$ K for varying equivalence ratios and FTM22-amplitudes.	103
6.8	FTF amplitudes (top) and phases (bottom) for rich (left) and lean (right) equivalence ratios, an air preheating temperature of $T_{a,PZ} = 423$ K and a pressure loss of $\Delta p_{a,PZ}/p_{a,PZ} \approx 4\%$ obtained with the purely acoustic MMM and the alternative approach using Eq. 6.22 for the determination of the FTF from the FTM22-element (cf. Fig. 6.1).	105
6.9	Ratio of the FTF_{AN} - and FTF_{RH} -amplitudes on top and phase difference on bottom for all rich (left) and lean (right) operating points of the isolated primary zone.	106
6.10	Ratio of the $FTF_{AN, FaR}$ - and FTF_{RH} -amplitudes on top and phase difference on bottom for all rich (left) and lean (right) operating points of the isolated primary zone.	107
6.11	Ratio of the $FTF_{AN, RO}$ - and FTF_{RH} -amplitudes on top and phase difference on bottom for all rich (left) and lean (right) operating points of the isolated primary zone.	108
6.12	Comparison of the purely acoustically measured FTF_{RH} with the optically measured FTF_{hyb} using OH^* , CH^* , C_2^* , and CO_2^* for one rich $\phi_{PZ} = 1.25$ (left) and one lean $\phi_{PZ} = 0.91$ (right) operating point with the same adiabatic flame temperature.	110
6.13	Amplitude calibration factor C_{amp} for the optically measured FTF_{hyb} related to the purely acoustically measured FTF_{RH}	111
7.1	Simplified cross section of the compact RQL combustor with mass flows, as well as relevant reference positions.	118
7.2	Flame images of the compact RQL flame (top) and isolated primary zone flame (bottom) for an equivalence ratio in the primary zone of $\phi_{PZ} = \phi_{PZ,RQL} = 1.43$ (left) and $\phi_{PZ} = \phi_{PZ,RQL} = 1.00$ (right).	119

7.3	Acoustic network model of the RQL combustor (BFTM _{RQL}) as linear combination of the burner and flame transfer matrix of the primary zone (BTM _{PZ,RQL} and FTM _{PZ,RQL}), as well as the burner and flame transfer matrix of the secondary zone (BTM _{SZ,RQL} and FTM _{SZ,RQL}).	120
7.4	Acoustic network model of the secondary zone burner BTM _{SZ,RQL} with the dilution holes represented as an acoustic area jump and the acoustic three-port inside the RQL combustion chamber.	121
7.5	Burner transfer matrices of the isolated primary zone BTM _{PZ} (blue dots), the primary zone in the compact RQL combustor without consideration of the dilution hole acoustics BTM _{PZ,RQL} ($u'_{DH} = 0$) (red squares), with consideration of the dilution holes acoustics using the Bernoulli approach BTM _{PZ,RQL} (Bernoulli) (green diamonds) and with consideration of the dilution holes acoustics using the continuity approach BTM _{PZ,RQL} (Cont.) (purple triangles).	126
7.6	Comparison of the calculated pressure fluctuation at the exit of the dilution holes using the continuity approach p'_{DH} with the pressure fluctuation downstream at the location of the dilution holes p'_{DS}	129
7.7	FTM_{22} amplitudes (top) and phases (bottom) of the fuel-rich and stoichiometric primary zone in the compact RQL (green symbols on the left) and the isolated primary zone arrangement (blue symbols on the right) for varying equivalence ratios in the primary zone ϕ_{PZ}	132
7.8	FTM_{22} -amplitudes (top) and -phases (bottom) of the primary zone in the compact RQL arrangement for varying equivalence ratios in the primary zone $\phi_{PZ,RQL}$ (green symbols on the left) and the stoichiometric and lean operated, isolated primary zone (blue symbols on the right). The FTM_{22} -amplitudes of the compact RQL combustor were calculated by considering the additional secondary air being entrained into the primary zone. . . .	136

-
- 7.9 FTF_{RH} -amplitudes (top) and -phases (bottom) of the primary zone in the compact RQL arrangement for varying equivalence ratios in the primary zone $\phi_{PZ,RQL}$ (green symbols on the left) and the stoichiometric and lean operated, isolated primary zone (blue symbols on the right). The FTF amplitudes of the compact RQL combustor were calculated by considering the additional secondary air being entrained into the primary zone. 137

List of Tables

2.1	Acoustic reflection coefficient R and impedance Z for different boundary conditions.	16
3.1	Tested design versions of the non-premixed natural gas nozzle. .	31
4.1	Radicals and corresponding bandpass filter specifications. . . .	52
4.2	Selection possibilities for the acoustic wavefield reconstruction using four PCBs per impedance measurement duct.	67
5.1	Parameter range for the commissioning tests of the isolated primary zone combustion chamber.	72
5.2	Coefficients of the linear regression between the chemiluminescence intensities of the baseline operating points and operating points with varying thermal power of +/-20%.	78
7.1	Equivalence ratios for the investigations of the compact RQL combustion chamber.	117

Nomenklatur

Latin Letters

<i>a</i>	Side Length [m]
<i>A</i>	Area [m ²]
<i>A</i>	Linear Regression Coefficient [-]
<i>c</i>	Speed of Sound [m/s]
<i>C</i>	Amplitude Calibration Factor [-]
<i>c_p</i>	Specific Heat at Constant Pressure [J/(kg · K)]
<i>d</i>	Diameter [m]
<i>e</i>	Exponential Function [-]
<i>e</i>	Specific Energy [J/kg]
<i>f</i>	Frequency [Hz]
<i>f</i>	Riemann Invariant [m/s]
<i>FAR</i>	Fuel-to-Air Ratio [-]
<i>g</i>	Riemann Invariant [m/s]
<i>h</i>	Enthalpy [J/kg]
H	Coefficient Matrix [-]
<i>\dot{H}</i>	Enthalpy Flux [W]
<i>i</i>	Imaginary Part [-]
<i>I</i>	Intensity [J/m ²]
<i>I</i>	Identity Matrix [-]
<i>k</i>	Acoustic Wave Number [rad/m]
<i>l</i>	Length [m]
<i>m</i>	Mass [kg]
<i>\dot{m}</i>	Mass Flow [kg/s]
<i>N</i>	Amount [-]
<i>n</i>	Sample Frequency [Hz]
<i>p</i>	Pressure [Pa]

\dot{q}	Volumetric Heat Release [J/(m ³ · s)]
\dot{Q}	Heat Release Rate [J/s]
r	Radius [m]
R	Coefficient of Determination [-]
R	Reflection Coefficient [-]
R	Specific Gas Constant [J/(kg · K)]
s	Entropy [J/(kg · K)]
s	Flame Speed [m/s]
SM	Scattering Matrix [-]
t	Time [s]
T	Temperature [K]
T	Transmission Coefficient [-]
Th	Threshold [-]
TM	Transfer Matrix [-]
u	Velocity in x-direction [m/s]
V	Volume [m ³]
x, y, z	Spatial Coordinate [m]
X	Mole Fraction [-]
Y	Mass Fraction [-]
Z	Acoustic Impedance [kg/(m ² · s)]

Greek Letters

α	Heat Transfer Coefficient [J/(m ² · K)]
γ	Ratio of Specific Heats [-]
Δ	Difference [m]/[Pa]/[W]
ϵ	Error Measure [-]
λ	Thermal Conductivity [W/(m · K)]
ν	Kinematic Viscosity [m ² /s]
ρ	Density [kg/m ³]
σ	Standard Deviation [-]
τ	Time Delay [s]
$\boldsymbol{\tau}$	Viscous Stress Tensor [Pa]
ϕ	Equivalence Ratio [-]
φ	Phase Angle [rad]

ψ	Arbitrary Transport Variable [-]
ω	Angular Velocity [rad/s]

Superscripts

	Absolute Value or Amplitude
~	Complex Valued Quantity
A	Excitation Location Upstream
B	Excitation Location Downstream
·	Flux
pu	Matrix in <i>pu</i> -notation
fg	Matrix in <i>fg</i> -notation
∠	Phase
†	Pseudo-Inverse
*	Radical
/	Temporal Coherent Perturbation
-	Time Averaged Quantity
T	Transpose
0	Fluid Properties at Standard State

Indices

∞	Infinity
a	Air
A	Per Area
acst	Acoustic
ad	Adiabatic
AI	Auto-Ignition
AN	Alternative
amp	Amplitude
BO	Burner Outlet
c	Cold
ch	Chemical
CC	Combustion Chamber

CO	Carbon Monoxide
CoG	Center of Gravity
cond	Conduction
conv	Convection
cool	Cooling
corr	Corrected
d	Droplet
dil	Dilution
DS	Downstream
elec	Electrical
exc	Excitation
ext	External
FaR	Flame at Rest
f	Fuel
f – a – mix	Fuel-to-Air Mixture
fl	Flame
g	Gas
geo	Geometric
h	Hot
H ₂	Hydrogen
hyb	Hybrid
i	Individual Component
i	Inner
IB	Ignition Burner
ign	Ignition
IMD	Impedance Measurement Duct
in	Inlet
inj	Injector
int	Internal
kero	Kerosene Jet-A1
l	Laminar
len	Length
LoS	Line of Sight
LS	Loudspeaker
max	Maximum

min	Minimum
N ₂	Nitrogen
NG	Natural Gas
o	Outer
out	Outlet
PCB	Dynamic Pressure Transducer
PP	Perforated Plate
pr	Products
pur	Purging
PZ	Primary Zone
R	Chemical Reaction
rad	Radiative
reac	Reactor
ref	Reference
res	Resonance
RH	Rankine-Hugoniot
RO	Reactants Only
RQL	Rich-Quench-Lean
s	Sample
SD	Supply Duct
stoich	Stoichiometric
syn	Synthesis Gas
SI	Side
SZ	Secondary Zone
TC	Thermocouple
TD	Transition Duct
TDM	Time Delay Model
th	Thermal
US	Upstream
w	Wall

Dimensionless Numbers

<i>He</i>	Helmholtz number
<i>Ma</i>	Mach number

<i>Nu</i>	Nusselt number
<i>Re</i>	Reynolds number
<i>Sr</i>	Strouhal number
<i>St</i>	Stokes number

Abbreviations

1D – NWM	One-Dimensional Network Modeling
ACARE	Advisory Council for Aviation Research and Innovation in Europe
AirPre	Air Preheater
BFTM	Burner and Flame Transfer Matrix
BNC	Binary Network Connector
BTM	Burner Transfer Matrix
CAD	Computer Aided Design
CAEP	Committee on Aviation Environmental Protection
CC	Combustion Chamber
CFD	Computational Fluid Dynamics
Comb	Combination
DAQ	Data Acquisition
FAR	Fuel-to-Air Ratio
FDF	Flame Describing Function
FFT	Fast Fourier Transform
fps	Frames per Second
FTF	Flame Transfer Function
FTM	Flame Transfer Matrix
HS	High-Speed
JIC	Jet-in-Cross-Flow
kero	Kerosene/Jet-A1
LBO	Lean Blow-Out
LFC	Lean Flame Constriction
LoS	Line of Sight
LPP	Lean Premixed Prevaporized
LS	Loudspeaker
MMM	Multimicrophone Method

NG	Natural Gas
OP	Operating Point
PCB	Piezodynamic Pressure Transducer
PMT	Photomultiplier Tube
PZ	Primary Zone
RBO	Rich Blow-Out
REC	Record
RFC	Rich Flame Constriction
RH	Rankine Hugoniot
RQL	Rich Quench Lean
SM	Scattering Matrix
SZ	Secondary Zone
TM	Transfer Matrix
TTL	Transistor Transistor Logic
UV	Ultraviolet

1 Introduction

The following chapter first describes the most important emissions regulations for a more climate-friendly aviation. The rich-quench-lean (RQL) combustion technology is highlighted as it is one of the prevalent combustion concepts in today's aero engines. Subsequently, the thermoacoustic instabilities and the main driving mechanisms in an RQL combustor with differentiation between the primary and secondary zone are explained. In addition, a brief literature review on previous work concerning the flame dynamics of RQL combustors is shown. Finally, the research objectives reveal the framework and knowledge gaps that will be addressed in the present work.

1.1 Technological Background

Global air traffic has increased again since the COVID-19 pandemic and passenger numbers in 2023 are almost back to the prepandemic level in 2019 [1]. According to forecasts of air traffic in the European Union, the number of flights will increase by approximately 35% until 2050 compared to 2023, leading to a rise of aircraft emissions and noise [2]. Although the contribution of the aviation sector in 2023 to global anthropogenic pollution is only 4%, efforts are being made to limit the impact of aviation on global warming by regulating aircraft emissions, for example, CAEP emission standards [3]. In addition to carbon dioxide emissions (CO_2), the aviation sector emits nitrogen oxides (NO_x), water vapor and soot at high altitudes. NO_x can potentially form ozone (O_3) in the atmosphere, while water vapor and soot can form contrails. Both, ozone and contrails contribute to the greenhouse effect and consequently to global warming [4].

The Advisory Council for Aviation Research and Innovation in Europe (ACARE) launched the Flightpath 2050 program to reduce aviation emissions and improve aircraft technology in Europe [5]. The targets of Flightpath 2050 are a reduction of 75% in carbon dioxide (CO_2), 90% of nitrogen oxide (NO_x) and 65% of noise until 2050 compared to 2000. The further development of

aircraft engine combustion technology that leads to lower emissions is a key step toward achieving these ambitious goals.

1.2 RQL Technology

The rich-quench-lean combustion technology (RQL) is currently the most prevalent combustion process for reducing aero engine emissions, especially NO_x [6–9]. In RQL combustion chambers the combustion process is staged into a rich primary, a quenching, and a lean secondary or burn-out zone. Figure 1.1 illustrates the working principle of an RQL combustor. The burner directs the fuel \dot{m}_f and the swirled primary air $\dot{m}_{a,PZ}$ into the primary zone. There, the fuel is burned under lack of oxygen under fuel-rich conditions ($\phi_{PZ} > 1$), especially during take-off of an aircraft. Outer and inner recirculation zones are formed, which aerodynamically stabilize the rich burning flame. The still reactive hot gases (mainly CO and H_2) leaving the primary zone are quickly mixed with secondary air $\dot{m}_{a,SZ}$ and burned out in the secondary zone with an excess of air ($\phi_{SZ} < 1$). Compared to lean-premixed-prevaporized combustion technology (LPP), the RQL process offers the advantage of being significantly more reliable in terms of combustion stability and safety, which is crucial for aero engines [8, 10]. Furthermore, the thermal formation of NO_x can be reduced using the RQL principle by up to 60% compared to traditional combustors.

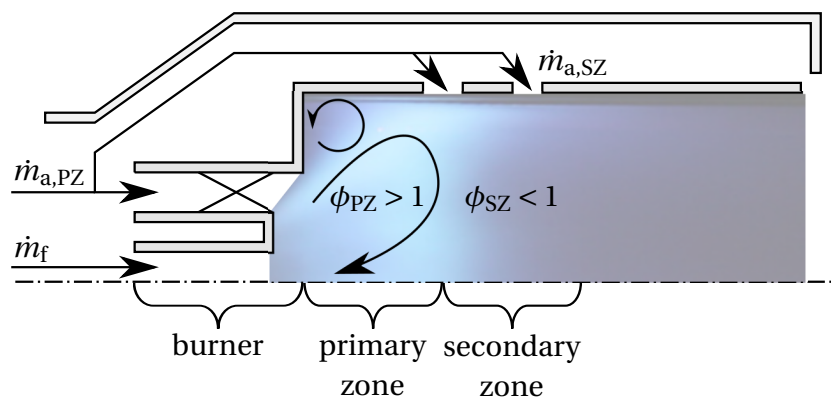


Figure 1.1: Working principle of a rich-quench-lean (RQL) combustion chamber.

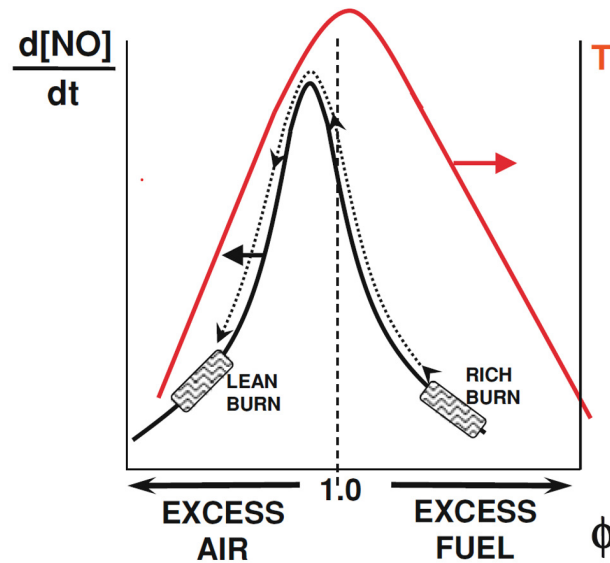


Figure 1.2: RQL NO_x reduction strategy.

Figure 1.2 depicts the adiabatic flame temperature and the formation of thermal NO_x versus the equivalence ratio, adapted from Samuelsen [8]. The suppression of thermal NO_x in RQL combustors is achieved by a lack of oxygen in the primary zone and by avoiding regions with high flame temperatures in the secondary zone [11]. Therefore, a quick and efficient mixing process of the hot primary gases with the secondary air is essential, which is commonly performed using the jet-in-cross-flow principle [12, 13].

The reduction of weight and size of aero engines is a key element in increasing the overall efficiency of the aircraft. For this reason, the power density of aero engines is constantly being ramped up. However, an increase in power density carries an increased risk for the occurrence of thermoacoustic instabilities, which can deteriorate engine operability and durability [14–16].

1.3 Combustion Instabilities

Thermoacoustic instabilities are caused by a feedback loop of the heat release \dot{Q} with the acoustics of the environment, e.g., of the combustion chamber [14, 15, 17]. The flame inside the combustor can be interpreted as an acous-

tic actuator, whereas the surrounding hardware acts as a damped acoustic resonator. If the coupling between the flame and the acoustic properties of the surroundings fulfills certain requirements, self-sustained large amplitude oscillations of acoustic pressure and velocity arise inside the combustion chamber. Lord Rayleigh proposed a necessary requirement for the occurrence of thermoacoustic instabilities in 1878 [18]. The statement of Lord Rayleigh is known as Rayleigh's criterion and can be formulated according to Eq. 1.1:

$$\int_0^\tau \dot{Q}'(t) \cdot p'(t) dt > 0. \quad (1.1)$$

In Eq. 1.1 \dot{Q}' and p' are the heat release and acoustic pressure fluctuations, respectively, while τ corresponds to the time period of an oscillation. According to Rayleigh's criterion, constructive interference between the heat release and acoustic pressure fluctuation is a necessary requirement for a combustion instability to form (Eq. 1.1). Assuming a harmonically oscillating heat release fluctuation $\dot{Q}'(\omega t - \varphi)$ which lags a harmonic oscillating pressure fluctuation $p'(\omega t)$ in time, the corresponding phase difference φ has to be smaller in magnitude than $\pi/2$ to satisfy Rayleigh's criterion for a combustion instability to arise. However, Rayleigh's criterion is a necessary but not a sufficient requirement for the occurrence of thermoacoustic instabilities. In addition, the acoustic energy added to the system by the oscillating flame has to exceed the dissipating mechanisms of the acoustic energy for the instability to grow. Vice versa, the oscillating amplitude will diminish, and the system will tend to stabilize as the dissipating mechanisms dominate the overall thermoacoustic system. The maximum amplitude of a thermoacoustic instability is reached whenever the acoustic energy added by the flame is in balance with the dissipating energy of the acoustic surroundings. This amplitude is also known as the limit cycle amplitude and is always caused by acoustic, non-linear effects.

1.3.1 Thermoacoustic Driving Mechanisms in RQL Combustors

Figure 1.3 illustrates a simplified acoustic model of an RQL combustor with differentiation between the primary and secondary flame dynamics and the corresponding driving mechanisms. The figure was inspired by [19] and adapted for the typical RQL configuration. On the left, the burner or injector is

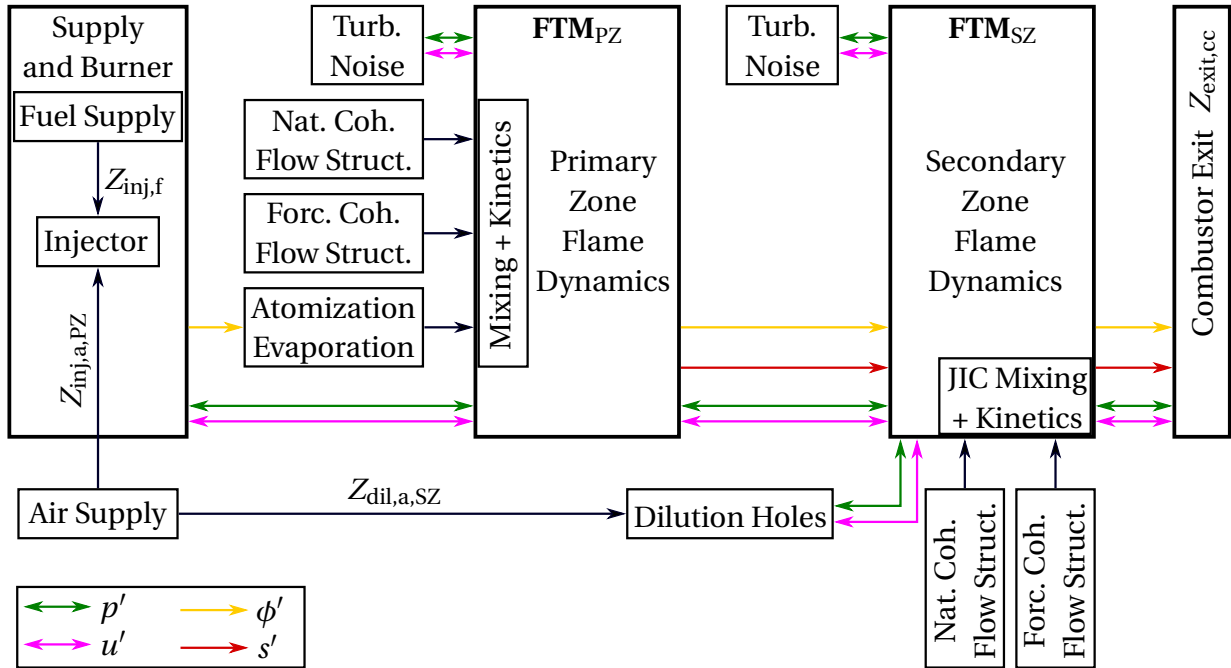


Figure 1.3: Driving mechanisms in RQL combustion chambers.

represented, including the air and fuel supply. The acoustic transfer behavior of the primary air and fuel supply to the injector can be characterized by the two impedances $Z_{inj,a,PZ}$ and $Z_{inj,f}$, respectively. Analogously, the acoustic behavior of the secondary air to the dilution holes is represented by the acoustic impedance $Z_{dil,a,SZ}$. Both, the primary and secondary air supply are coupled in real aero engines due to the common air supply from the compressor to the combustion chamber. The acoustic transfer behavior of the primary and secondary zone's flame can be expressed in terms of two flame transfer matrices FTM_{PZ} and FTM_{SZ} , relating the acoustic variables p' and u' up- and downstream of the flame. The combustor exit at the right end of Fig. 1.3 can be acoustically represented by the impedance $Z_{exit,cc}$, which would be the first turbine stage in real aero engines.

Several driving mechanisms that influence FTM_{PZ} and FTM_{SZ} can be identified from Fig. 1.3 and will be described in the following:

- **Turbulent Noise:** The turbulent air injection into the primary and secondary flame generates broadband acoustic background noise. Consequently, the combustion process and therefore the flame is turbulent.

The emitted turbulent noise couples with the combustor acoustics and is amplified accordingly to the eigenfrequencies of the acoustic system. This acoustic coupling may lead to a modulation of the heat release rate in both, primary and secondary zone. Turbulent noise is an autonomous source of sound and potentially triggers other driving mechanisms, e.g. forced coherent flow structures or droplet dynamics [20–22].

- **Natural and Forced Coherent Flow Structures:** Each type of periodic flow instability can be referred to as a coherent flow structure, e.g. vortex shedding. Coherent flow structures are able to alter the heat release of the flame by modifying the local turbulent mixing timescales and/or the flame surface. In gas turbine combustors most typically vortex shedding, swirl fluctuations and precessing vortex cores can form [23–25]. Natural coherent flow structures are independent of the combustor acoustics and consequently not affected by the thermoacoustic feedback loop. Often natural coherent flow structures are linked to the cold flow by characteristic Strouhal numbers. In contrast, forced coherent flow structures are triggered by the combustor acoustics being dependent on the eigenfrequencies of the system and on the thermoacoustic feedback loop. Both types of coherent flow structure are transported convectively into the flame zone. Most coherent flow structures evolve at the burner outlet and reach the flame after a convective time delay τ_{conv} [26–28].
- **Equivalence Ratio Waves:** The acoustic coupling of the air and fuel supply with the acoustics of the combustor can potentially lead to equivalence ratio fluctuations ϕ' . In non-premixed and technically premixed flames the air and fuel mass flow can be altered due to an acoustic velocity perturbation u' upstream of the flame resulting in fluctuating equivalence ratio waves [19, 29–31]. Similar to coherent flow structures, equivalence ratio fluctuations are convectively transported to the flame front modifying the flame temperature. Consequently, the energy content of the flow and chemical reaction rates in the flame vary and lead to heat release fluctuations. In liquid-fueled combustors, the fuel supply can generally be considered to be acoustically stiff due to the high acoustic impedance of the liquid fuel injector $Z_{\text{inj},f}$. However, atomization and evaporation after fuel injection are prone to acoustic velocity fluctua-

tions [32–34]. Depending on the droplet size and distribution, number density waves can evolve, if the Stokes number of the droplets is small enough. The Stokes number relates the characteristic timescale of the droplet τ_d to the acoustic time scale τ_{acst} .

- **Entropy Waves:** Entropy waves s' can be interpreted as harmonically fluctuating temperature patterns that may result from coherent flow structures or equivalence ratio fluctuations in the flame. Temperature fluctuations are convectively transported to the combustor outlet and accelerated in the first turbine guide vane to velocities close to Mach number one ($Ma \approx 1$). The acceleration process generates a conversion of the entropy waves to acoustic pressure and velocity waves. The acoustic waves can travel in the upstream direction to the flame and burner altering the flame dynamics [35–39].

Natural coherent flow structures and turbulent noise are largely independent of the combustor acoustics and consequently the thermoacoustic feedback loop. In contrast, forced coherent flow structures, equivalence ratio waves, and entropy waves are part of the thermoacoustic feedback loop, which depend on the eigenfrequencies of the system.

Apart from the thermoacoustic driving mechanisms, the acoustic damping effects decide whether the combustor tends to be stable or unstable. Acoustic damping mechanisms are, for example, radiative and viscous damping, acoustic-vorticity interaction or non-linear self-detuning of the combustor [16, 40, 41].

1.3.2 Literature Review on RQL Flame Dynamics

A few experimental studies on the flame dynamics of RQL combustion chambers have been reported in the past.

Eckstein [42] conducted one of the first studies that examined the dynamics of RQL combustors. His research was focusing on the low-frequency phenomenon known as "rumble" or "growl" that occurs when aero engines are in idle or sub-idle conditions. The researcher studied the coupling between entropy waves and the combustor exit nozzle of a non-premixed kerosene flame by implementing primary air forcing. The author concluded that the process

of atomization and evaporation is essential for the evolvment of thermoacoustic instabilities. Furthermore, Eckstein formulated a simplified model to explain the flame dynamics that were observed in experiments. Due to limitations in his experimental setup, he was unable to directly measure FTFs. Therefore, he developed an analytical FTF.

Cai et al. [43] conducted a study on the dynamics of an atmospheric RQL combustor segment powered by natural gas. The observed combustion instabilities were associated with the mixing of the hot gases from the primary zone and the secondary air jets. The experimental work was conducted using chemiluminescence imaging data and dynamic pressure measurements. However, the flame dynamics were not measured in terms of FTFs.

Abdelnabi et al. [44] conducted an analysis of the identical combustor, employing propane and methane as fuel. Both fuels showed similar unstable frequencies. The presence of these instabilities was ascribed to hydrodynamic phenomena occurring in the combustion chamber. The quantification using FTFs was not carried out.

Weber et al. [45] conducted a study that focused on the thermoacoustic analysis of combustion instabilities using fuel-rich kerosene flames. The dynamics of the spray flame in a model gas turbine combustor was analyzed through the measurement of the dynamic pressure and the chemiluminescence of different species. The researchers discovered that, for flames with soot, the emission of the OH^* -band was the only suitable indicator to measure fluctuations in heat release, while the emissions from CH^* - and C_2^* -bands were not effective.

Venkatesan et al. [46] carried out a recent study in which they used the multimicrophone method (MMM) to measure and quantify flame transfer functions in a liquid-fueled rich combustor. The results indicated a significant dependence between the FTF and the operating pressure, while the relationship with the inlet air temperature was found to be only moderate.

Renner examined the flame dynamics of the isolated secondary zone on the same test rig used in the current study [47]. The author derived a 1D acoustic model to assess the secondary zone's flame dynamics with respect to fluctuations of the hot primary zone gases as well as the dilution air. The author's model was applied to the experimental data obtained by using the multimicrophone method and acoustic forcing of the secondary zone. The resulting

FTFs showed rapidly diminishing amplitudes over frequency with values close to zero at a frequency of $f \approx 200$ Hz for upstream forcing and $f \approx 300$ Hz for forcing of the dilution air.

Still missing is the quantification of the flame dynamics of the non-premixed kerosene spray flame in the isolated primary zone in terms of FTFs. Additionally, a knowledge gap exists on the contribution of the primary zone's flame dynamics to the overall thermoacoustic behavior in a compact RQL arrangement with both combustion zones located in one combustion chamber.

1.4 Research Objectives and Thesis Structure

The main objective of this study is to improve the physical understanding of the flame dynamics in the primary zone of RQL combustors. The experimental scientific approach is the individual investigation of the primary and secondary zone in an atmospheric RQL combustion test rig. In a compact aero engine both combustion zones (primary and secondary zone) are positioned in close proximity. As a result, it is difficult to experimentally differentiate the dynamics of both zones, especially in the low frequency range ($f < 1000$ Hz). The present study assumes that both zones exhibit individual flame behaviors. Based on this assumption, a new thermoacoustic test rig was designed and commissioned to separate the primary from the secondary zone. The primary zone's burner is composed of a prototype double-radial aero engine swirler as well as a generic pressure-swirl atomizer nozzle. To analyze the primary and secondary zone independently of each other, they are spatially separated and the isolated primary zone is characterized in terms of flame transfer functions (FTF) using the classical Rankine-Hugoniot relations and a newly derived alternative approach. Furthermore, the suitability of different radicals as potential measures for representing heat release and fluctuations during non-premixed kerosene combustion will be discussed in this work. Finally, the contribution of the individual flame dynamics on the overall flame dynamics of the RQL combustor is examined and reveals which combustion zone dominates the overall thermoacoustic behavior of RQL combustors.

The structure of the thesis is given in the following. Chapter 2 provides the essential fundamentals used in this study. The governing equations used in the field of linear acoustics are explained. In addition, the theory of FTFs and the

Rankine-Hugoniot jump conditions are described. At the end of the chapter a brief summary on the most important chemiluminescence physics is given. In Chapter 3 the design of the new thermoacoustic test rig is introduced and the most important aspects of the design process are highlighted. The experimental setup for the measurements in the isolated primary zone as well as the compact RQL configuration conclude this chapter. In the following, Chapter 4 contains the detailed measurement setup and the major measurement methods used in the current work. The application of the purely acoustic multimicrophone method (MMM), as well as the measurement of the flame's chemiluminescence using photomultiplier tubes (PMT) is given. Furthermore, the determination of the rich and lean operating points for the thermoacoustic investigations is explained. Chapter 5 starts by describing the commissioning and operating range of the new test rig, focusing on the primary zone. Subsequently, the results for the steady chemiluminescence behavior of the primary zone using PMT and high-speed camera provide further insight into the behavior of OH^* , CH^* , C_2^* and CO_2^* for rich and lean combustion conditions. The detailed flame dynamics in terms of FTFs is discussed in Chapter 6. The purely acoustically measured FTFs over a wide operating range by using the Rankine-Hugoniot relations are given and the time delay model is used to reproduce the phases with isothermal CFD and OH^* -imaging. Subsequently, a root cause study investigates the influence of atomization and evaporation, as well as thermal effects on the flame dynamics of the primary zone. In addition, an alternative approach for the determination of the FTF from the FTM22-element by considering chemical conversion and temperature dependent fluid properties is presented. At the end of this chapter, the suitability of OH^* , CH^* , C_2^* and CO_2^* for measuring FTFs is examined for fuel-rich and lean combustion conditions. In Chapter 7, the transfer of the flame dynamics of the isolated primary and secondary zone to the compact RQL combustor is estimated first by assuming superposition of the individual flame dynamics. Second, the flame dynamics of the compact RQL configuration is experimentally evaluated by using a one-dimensional acoustic network model and the 2-port technique to compare the results of the isolated primary zone to the primary zone in the compact RQL combustor. Finally, Chapter 8 summarizes the present study and points out the main conclusions that are potentially useful for future work.

2 Fundamentals

This chapter describes the theoretical background and assumptions used in the present work. The theory of one-dimensional linear acoustic behavior and its application in network modeling is explained first. Subsequently, the most important aspects of flame dynamics and flame transfer functions (FTF) are given. The Rankine-Hugoniot relations will be described in detail, since they are a fundamental principle in the field of FTF measurements. Lastly, a short summary of the underlying chemiluminescence physics is presented.

2.1 Linear Acoustics

The starting point for the description of the acoustic wave propagation is the conservation equations for mass Eq. 2.1 and momentum 2.2, as well as the ideal gas law Eq. 2.3 [48]:

$$\frac{\partial \rho}{\partial t} + \frac{\partial (\rho u_i)}{\partial x_i} = 0, \quad (2.1)$$

$$\frac{\partial (\rho u_i)}{\partial t} + \frac{\partial (\rho u_i u_j)}{\partial x_j} + \frac{\partial p}{\partial x_i} = 0, \quad (2.2)$$

$$p = p(\rho, s). \quad (2.3)$$

In Eq. 2.1-2.3 ρ is the density, p the pressure, and $u_{i/j}$ the velocity field component according to Cartesian coordinates $x_{i/j}$. The conservation of momentum in Eq. 2.2 is valid for inviscid flows ($\tau_{ij} = 0$) and without the presence of external body forces ($f_i=0$).

The assumption will be made that each flow variable of Eq. 2.1-2.3 can be expressed as a superposition of a mean and a fluctuating quantity according to Eq. 2.4-2.6

$$p(x, t) = \bar{p}(x, t) + p'(x, t), \quad (2.4)$$

$$\rho(x, t) = \bar{\rho}(x, t) + \rho'(x, t), \quad (2.5)$$

$$u(x, t) = \bar{u}(x, t) + u'(x, t). \quad (2.6)$$

Furthermore, it will be supposed that the mean flow quantities are in steady state (e.g. $\partial \bar{p} / \partial t = 0$) and homogeneously distributed (e.g. $\partial \bar{p} / \partial x_i = 0$). If the acoustic pressure p' and density ρ' are much smaller than the corresponding mean quantities (e.g. $p' / \bar{p} \ll 1$), products of fluctuating quantities can be neglected.

In the low-frequency acoustic regime, as studied in the present work, one-dimensional wave propagation can be assumed due to the small radial extension compared to the axial one [49]. Applying the assumptions made to Eq. 2.1 and 2.2 results in Eq. 2.7 and 2.8:

$$\frac{\partial \rho'}{\partial t} + \bar{\rho} \frac{\partial u'}{\partial x} = 0, \quad (2.7)$$

$$\bar{\rho} \frac{\partial u'}{\partial t} + \frac{\partial p'}{\partial x} = 0. \quad (2.8)$$

An equation is needed that correlates the density fluctuation ρ' with the pressure fluctuation p' . For an isentropic flow ($ds = 0$) the formulation for the speed of sound can be obtained according to Eq. 2.9:

$$c^2 = \left(\frac{\partial p}{\partial \rho} \right)_s. \quad (2.9)$$

Applying Eq. 2.4 and 2.5 to Eq. 2.9, as well as neglecting products of fluctuating quantities leads to a linear correlation between p' and ρ' in Eq. 2.10:

$$c^2 = \frac{p'}{\rho'}. \quad (2.10)$$

2.1.1 Wave Equation and Solution

Differentiating Eq. 2.7 with respect to t and Eq. 2.8 with respect to x , as well as subtracting them gives the one-dimensional wave equation according to Eq. 2.11 [50]:

$$\frac{\partial^2 \rho'}{\partial t^2} - \frac{\partial^2 p'}{\partial x^2} = 0. \quad (2.11)$$

Additionally, using the relation for ρ' and p' in Eq. 2.10 results in the classical, one-dimensional wave equation for a quiescent flow ($\bar{u} = 0$) given in Eq. 2.12:

$$\frac{\partial^2 p'}{\partial t^2} - c^2 \frac{\partial^2 p'}{\partial x^2} = 0. \quad (2.12)$$

The general solution for the one-dimensional wave equation in Eq. 2.12 can be obtained by using D'Alemberts method which results in Eq. 2.13 for the acoustic pressure fluctuation p' :

$$\frac{p'}{\bar{\rho}c}(x, t) = f(x - ct) + g(x + ct). \quad (2.13)$$

In Eq. 2.13 f and g are the Riemann invariants, which can be interpreted as two waves traveling up- and downstream, respectively [51]. Using Eq. 2.10 the solution for the acoustic density fluctuation can be obtained according to Eq. 2.14:

$$\frac{c\rho'}{\bar{\rho}}(x, t) = f(x - ct) + g(x + ct). \quad (2.14)$$

The acoustic velocity fluctuation can be obtained using equation 2.7 resulting in Eq. 2.15:

$$u'(x, t) = f(x - ct) - g(x + ct). \quad (2.15)$$

Assuming that the Riemann invariants are harmonic functions in time and space and using the Fourier transform, a harmonic solution can be obtained given in Eqs. 2.16-2.18 [39]:

$$p'(x, t) = \bar{\rho}c(\tilde{f} e^{(i\omega t - ikx)} + \tilde{g} e^{(i\omega t + ikx)}), \quad (2.16)$$

$$\rho'(x, t) = \frac{\bar{\rho}}{c}(\tilde{f} e^{(i\omega t - ikx)} + \tilde{g} e^{(i\omega t + ikx)}), \quad (2.17)$$

$$u'(x, t) = \tilde{f} e^{(i\omega t - ikx)} - \tilde{g} e^{(i\omega t + ikx)}. \quad (2.18)$$

In Eq. 2.16-2.18 \tilde{f} and \tilde{g} are the complex-valued Riemann invariants, ω is the angular velocity and k the wave number calculated with equation. 2.19 and

2.20:

$$\omega = 2\pi f, \quad (2.19)$$

$$k = \frac{\omega}{c}. \quad (2.20)$$

2.1.2 Convective Wave Equation and Solution

In flows with mean velocity ($\bar{u} \neq 0$) the convective, one-dimensional wave equation can be derived analogously to the previous section resulting in Eq. 2.21:

$$\left(\frac{\partial}{\partial t} + \bar{u} \frac{\partial}{\partial x} \right)^2 p' - c^2 \frac{\partial^2 p'}{\partial x^2} = 0. \quad (2.21)$$

The solution for the convective wave equation is as follows:

$$\frac{p'}{\bar{\rho}c}(x, t) = f(x - (c + \bar{u})t) + g(x + (c - \bar{u})t), \quad (2.22)$$

$$\frac{c\rho'}{\bar{\rho}}(x, t) = f(x - (c + \bar{u})t) + g(x + (c - \bar{u})t), \quad (2.23)$$

$$u'(x, t) = f(x - (c + \bar{u})t) - g(x + (c - \bar{u})t). \quad (2.24)$$

Equations 2.22-2.24 consider that the Riemann invariant f is traveling in mean flow direction with the velocity $c + \bar{u}$, whereas g travels opposite to the mean velocity $c - \bar{u}$.

Again, the solution of the wave equation can be written in harmonic form resulting in Eqs. 2.25-2.26 [39]:

$$p'(x, t) = \bar{\rho}c \left(\tilde{f} e^{(i\omega t - ik^+ x)} + \tilde{g} e^{(i\omega t + ik^- x)} \right), \quad (2.25)$$

$$\rho'(x, t) = \frac{\bar{\rho}}{c} \left(\tilde{f} e^{(i\omega t - ik^+ x)} + \tilde{g} e^{(i\omega t + ik^- x)} \right), \quad (2.26)$$

$$u'(x, t) = \tilde{f} e^{(i\omega t - ik^+ x)} - \tilde{g} e^{(i\omega t + ik^- x)}. \quad (2.27)$$

The convective wave number $k^{+/-}$ is defined according to Eq. 2.28:

$$k^{+/-} = \frac{\omega}{c \pm \bar{u}}. \quad (2.28)$$

With the assumptions made in this section, the acoustic field can be fully described by two acoustic variables, e.g. p' and u' . Due to this, only p' and u' are considered hereafter and the density fluctuation ρ' is omitted.

2.1.3 Acoustic Boundaries

The acoustic behavior at the boundaries of a domain considered can be formulated in terms of the acoustic reflection coefficient R or the impedance Z . The former is relating the reflected wave to the incident wave given in Eq. 2.29:

$$R_{\text{in}} = \frac{f}{g}, \quad R_{\text{out}} = \frac{g}{f}. \quad (2.29)$$

R_{in} refers to a reflection coefficient for an acoustic boundary at the inlet and R_{out} at the outlet of the domain. There are three limit cases for the acoustic reflection coefficient. First, on a rigid wall, the acoustic velocity fluctuations vanish ($u' = 0$) and the reflection coefficient consequently results in $R = 1$ as $f = g$ due to Eq. 2.27. Second, at an open end the pressure fluctuation is zero ($p' = 0$) resulting in $R = -1$ because of $f = -g$ according to Eq. 2.25. Third, an anechoic end represents a boundary condition without reflection of acoustic waves and consequently the reflection coefficient becomes zero $R = 0$.

The acoustic impedance Z is the ratio of the acoustic pressure fluctuation p' and the acoustic velocity fluctuation u' for the representation of an acoustic boundary resulting in Eq. 2.30:

$$Z = \frac{1}{\bar{\rho}c} \frac{p'}{u'}. \quad (2.30)$$

The acoustic impedance Z and the reflection coefficient R are complex quantities depending on the location x and the frequency ω , but independent of time t . The additional factor $\bar{\rho}c$, already been used to normalize the Riemann invariants in Eq. 2.13 and 2.22, is often referred to as the characteristic impedance of the medium. For liquids (e.g. kerosene fuel), the density and speed of sound are substantially higher than those of gases (e.g. air), leading to a negligible velocity fluctuation for a given pressure perturbation of the liquid. Due to this, the liquid fuel supply in combustors is generally assumed to be acoustically stiff ($Z_f \rightarrow \infty$).

Both, the reflection coefficient R and the impedance Z are related to each other by Eq. 2.31:

$$Z = \frac{f + g}{f - g} = \frac{1 + R}{1 - R}. \quad (2.31)$$

Table 2.1 summarizes the values for R and Z for the three cases of a rigid wall,

open and anechoic end.

Table 2.1: Acoustic reflection coefficient R and impedance Z for different boundary conditions.

Boundary condition	Reflection Coefficient R	Impedance Z
Rigid Wall	1	∞
Open End	-1	0
Anechoic end	0	1

2.1.4 Network Modeling

In analogy to electrical engineering, an acoustic element can be described by relating independent acoustic variables at the inlet to the acoustic variables at the outlet [52, 53]. The acoustic variables must fully describe the state of the acoustic field and can be summarized in acoustic state vectors at the in- and outlet. With this approach, the detailed physics inside the acoustic element does not have to be taken into account, meaning the acoustic element is considered as a 'black box' [54].

In the framework of linear one-dimensional acoustics, knowledge of two independent acoustic variables at the in- and outlet is required to fully describe the acoustic state, e.g. p' and u' or f and g . For acoustic measurements, p' and u' are most meaningful, as they can be experimentally measured.

The simplest acoustic element is illustrated in Fig. 2.1, namely the acoustic two-port.

The behavior of an acoustic two-port can be described by a 2x2 transfer matrix \mathbf{TM} , relating the acoustic variables upstream (inlet) to downstream (outlet), according to Eq. 2.32 and 2.33:

$$\begin{pmatrix} \frac{p'}{\rho c} \\ u' \end{pmatrix}_{\text{DS}} = \underbrace{\begin{pmatrix} TM_{11} & TM_{12} \\ TM_{21} & TM_{22} \end{pmatrix}}_{\mathbf{TM}^{\text{pu}}} \cdot \begin{pmatrix} \frac{p'}{\rho c} \\ u' \end{pmatrix}_{\text{US}}, \quad (2.32)$$

$$\begin{pmatrix} f \\ g \end{pmatrix}_{\text{DS}} = \underbrace{\begin{pmatrix} TM_{11} & TM_{12} \\ TM_{21} & TM_{22} \end{pmatrix}}_{\mathbf{TM}^{\text{fg}}} \cdot \begin{pmatrix} f \\ g \end{pmatrix}_{\text{US}}. \quad (2.33)$$

The conversion of the two transfer matrices \mathbf{TM}^{fg} and \mathbf{TM}^{pu} into each other can be obtained by using Eq. 2.34 and 2.35 [54, 55], respectively:

$$\mathbf{TM}^{\text{fg}} = \mathbf{\Omega} \cdot \mathbf{TM}^{\text{pu}} \cdot \mathbf{\Omega}^{-1}, \quad (2.34)$$

$$\mathbf{TM}^{\text{pu}} = \mathbf{\Omega}^{-1} \cdot \mathbf{TM}^{\text{fg}} \cdot \mathbf{\Omega}. \quad (2.35)$$

The conversion matrix $\mathbf{\Omega}$ is defined in Eq. 2.36:

$$\mathbf{\Omega} = \begin{pmatrix} 1 & 1 \\ 1 & -1 \end{pmatrix}. \quad (2.36)$$

An additional possibility to describe the acoustic behavior of acoustic elements is represented by the scattering matrix \mathbf{SM} , relating the waves traveling towards the acoustic element (f_{US} and g_{DS}) to the waves traveling away from it (f_{DS} and g_{US}) [56]:

$$\begin{pmatrix} f_{\text{DS}} \\ g_{\text{US}} \end{pmatrix} = \underbrace{\begin{pmatrix} T^+ & R^- \\ R^+ & T^- \end{pmatrix}}_{\mathbf{SM}^{\text{fg}}} \cdot \begin{pmatrix} f_{\text{US}} \\ g_{\text{DS}} \end{pmatrix}. \quad (2.37)$$

The scattering process of the Riemann invariants f and g is described by the transmission $T^{+/-}$ and reflection coefficients $R^{+/-}$ in Eq. 2.37. A conversion of

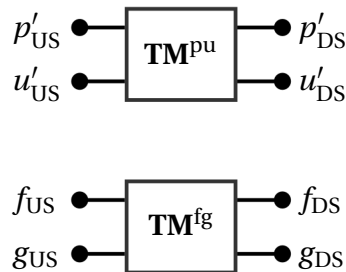


Figure 2.1: Sketch of acoustic two-ports in terms of transfer matrices.

the transfer matrix \mathbf{TM}^{fg} into the scattering matrix \mathbf{SM}^{fg} can be performed by using the transformation given in Eq. 2.38:

$$\mathbf{SM}^{\text{fg}} = \frac{1}{TM_{22}^{\text{fg}}} \begin{pmatrix} TM_{11}^{\text{fg}} TM_{22}^{\text{fg}} - TM_{12}^{\text{fg}} TM_{21}^{\text{fg}} & TM_{12}^{\text{fg}} \\ -TM_{21}^{\text{fg}} & 1 \end{pmatrix}. \quad (2.38)$$

2.2 Flame Dynamics

The combustion process in flames generates a volumetric expansion of the combustion gas due to the heat release of the chemical process. Especially for turbulent flames, the momentary volumetric heat release rate can fluctuate and thus couples with the acoustics: the flame acts as a broadband source of sound (cf. Section 1.3).

2.2.1 Flame Transfer Functions

In the field of thermoacoustics, the linear coupling of the flame with the acoustics is most commonly described by flame transfer functions (FTF). The FTF correlates the normalized fluctuating heat release rate \dot{Q}'/\bar{Q} with the normalized fluctuation of the acoustic velocity $u'_{\text{ref}}/\bar{u}_{\text{ref}}$ at a given reference plane x_{ref} and for a given frequency ω according to Eq. 2.39:

$$FTF(\omega) = \frac{\dot{Q}'/\bar{Q}}{u'_{\text{ref}}/\bar{u}_{\text{ref}}}. \quad (2.39)$$

Both, the heat release rate and acoustic velocity fluctuation are normalized, resulting in a dimensionless FTF. With this approach, the FTFs of different flames and burners can easily be compared. Additionally, if the acoustics surrounding of the burner and flame is changed, the FTF is still valid. From Eq. 2.39 it can be seen that the heat release fluctuation is only related to the acoustic velocity fluctuation. In Fig. 1.3 additional effects were identified, which can alter the heat release rate, e.g. equivalence ratio fluctuations. However, due to the feedback loop of the heat release with the acoustics, the formulation of the FTF in Eq. 2.39 also captures those additional effects [57, 58].

Assuming that the heat release rate and acoustic velocity are a linear, time-invariant quantities and thus harmonically fluctuating, both can be expressed

in complex form by applying the Fourier transform resulting in Eq. 2.40 and 2.41:

$$\tilde{Q}'(\omega) = |\tilde{Q}'|(\omega)e^{i\omega t + \varphi_{Q'}}, \quad (2.40)$$

$$\tilde{u}'_{\text{ref}}(\omega) = |\tilde{u}'_{\text{ref}}|(\omega)e^{i\omega t + \varphi_{u'_{\text{ref}}}}. \quad (2.41)$$

Usually the complex-valued FTF is represented in terms of amplitude $|FTF|(\omega)$ and phase $\angle FTF(\omega)$, as written in Eq. 2.42 and 2.43:

$$|FTF|(\omega) = \frac{|\tilde{Q}'|/|\bar{Q}|}{|\tilde{u}'_{\text{ref}}|/\bar{u}_{\text{ref}}}, \quad (2.42)$$

$$\angle FTF(\omega) = \varphi_{\tilde{Q}'} - \varphi_{u'_{\text{ref}}}. \quad (2.43)$$

The amplitude $|FTF|$ provides the frequency-dependent sensitivity of the flame due to acoustic perturbations, independent of the acoustic environment of the burner and the flame. The FTF indicates the frequency-depending sensitivity of the heat release due to acoustic velocity fluctuations, but it does not reveal the root cause of the flame dynamics. The phase $\angle FTF(\omega)$ quantifies the time delay between the acoustic velocity fluctuation and the heat release rate reacting to it. Due to this, the phase of the FTF is often represented as a global time lag τ_{conv} in Eq. 2.44 [58]:

$$\angle FTF(\omega) \approx -\omega\tau_{\text{conv}}. \quad (2.44)$$

The global time delay τ_{conv} is commonly estimated by assuming that a disturbance (e.g. equivalence ratio fluctuation, vortex shedding) is convectively transported from the reference plane to the main heat release zone, resulting in a fluctuating heat release and acoustic velocity due to the thermoacoustic feedback loop (cf. Section 1.3). For this reason, the global time delay can be calculated by knowing the mean flow field velocity $\bar{u}(x)$ and distance from the acoustic reference plane to the heat release zone Δx as given in Eq. 2.45:

$$\tau = \frac{\Delta x}{\bar{u}(x)}. \quad (2.45)$$

The formulation of the FTF in Eq. 2.39 is only valid for a linear coupling of the heat release fluctuation \dot{Q}' to the acoustic velocity fluctuation u' . This lin-

ear behavior is a prerequisite for the present work. On the contrary, for sufficiently high perturbations in the combustion chamber, the heat release rate may respond in a non-linear manner being usually characterized by a flame-describing function (FDF) and resulting in a limit cycle amplitude [59–62]. For high frequencies, the spatial distribution of the heat release may cause the flame response to be dispersed. Due to this, the global flame response and thus the FTF amplitude is decreasing with increasing frequency.

2.2.2 Rankine-Hugoniot Relations

The equations of sound propagation, derived in Section 2.1, are only valid for isentropic flow and do not hold across flames, since they are highly non-isentropic. For this reason, a coupling between the fluctuating heat release rate and the acoustic field is required.

The Rankine-Hugoniot relations assume the flame as a discontinuity with a temperature jump and the domain up- and downstream of the flame to be isentropic, as illustrated in Fig. 2.2 [63]. The index c refers to cold conditions and h to hot conditions, which means after the addition of heat due to the presence of the flame. The representation of the flame as a discontinuous temperature jump is only valid if the axial length of the flame l_{fl} is small compared

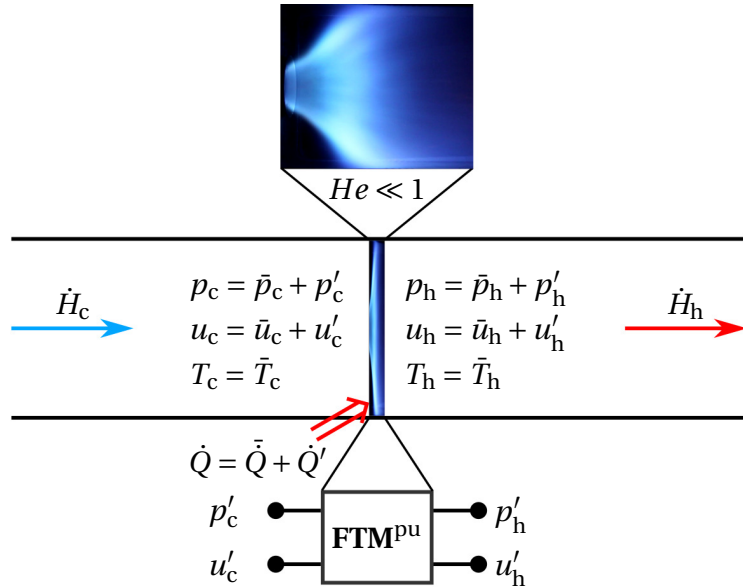


Figure 2.2: Rankine-Hugoniot jump conditions across the flame.

to the acoustic wavelength λ :

$$He = \frac{\omega l_{fl}}{c} = kl \ll 1. \quad (2.46)$$

The Helmholtz number in Eq. 2.46 relates a characteristic length, e.g. flame length l_{fl} , to the acoustic wave length λ . If the requirement in Eq. 2.46 is satisfied, the flame can be treated as acoustically compact and the Rankine-Hugoniot relations can be applied.

The derivation of the Rankine-Hugoniot jump conditions is based on the integrated equations for mass, momentum, and energy in Eqs. 2.47-2.49 [63]:

$$[\rho u]_c^h = 0 \quad (2.47)$$

$$[p + \rho u^2]_c^h = 0 \quad (2.48)$$

$$\rho u \left[h + \frac{1}{2} u^2 \right]_c^h = \dot{Q}_A. \quad (2.49)$$

The variable \dot{Q}_A denotes the heat release rate per unit area of the flame and the specific enthalpy h . For a perfect gas, the enthalpy h can also be written according to Eq. 2.50:

$$h = c_p T = \frac{\gamma}{\gamma - 1} \frac{p}{\rho}. \quad (2.50)$$

Additionally, using Eq. 2.10 five equations for the five unknowns c , u , T , p and ρ are present to determine the coupling over the flame. Furthermore, the assumption of constant caloric properties over the flame (γ and R) finally results in the Rankine-Hugoniot relations as written in Eqs. 2.51-2.53 [36, 37, 63]:

$$\frac{\rho_c}{\rho_h} = \frac{u_h}{u_c} = 1 + \frac{(\gamma - 1)\dot{Q}_A}{\gamma p_c u_c} + O(Ma^2), \quad (2.51)$$

$$\frac{p_h}{p_c} = 1 - \frac{(\gamma - 1)\dot{Q}_A}{p_c u_c} Ma_c^2 + O(Ma^4), \quad (2.52)$$

$$\frac{T_h}{T_c} = \left(\frac{c_h}{c_c} \right)^2 = 1 + \frac{(\gamma - 1)\dot{Q}_A}{\gamma p_c u_c} + O(Ma^2). \quad (2.53)$$

The higher order Mach number terms in Eq. 2.51-2.53 can be neglected for typical combustion chambers Mach numbers smaller than 0.1. The determination of the Rankine-Hugoniot relations for the acoustic fluctuations can be performed by using the decomposition of each quantity into a mean $\bar{\psi}$ and

fluctuating value ψ' (e.g. Eq. 2.4-2.6).

Finally, the Rankine-Hugoniot relations for the coupling of the acoustic field up- and downstream of the acoustically compact flame can be obtained, resulting in Eqs. 2.54 and 2.55:

$$\left(\frac{p'}{\rho c}\right)_h = \beta \left(\frac{p'}{\rho c}\right)_c - \beta \left(\frac{T_h}{T_c} - 1\right) Ma_c u'_c \left(1 + \frac{\dot{Q}'/\bar{Q}}{u'_c/\bar{u}_c}\right), \quad (2.54)$$

$$u'_h = -\left(\frac{T_h}{T_c} - 1\right) \gamma Ma_c \left(\frac{p'}{\bar{\rho} c}\right)_c + \left(1 + \left(\frac{T_h}{T_c} - 1\right) \frac{\dot{Q}'/\bar{Q}}{u'_c/\bar{u}_c}\right) u'_c. \quad (2.55)$$

In Eq. 2.54 and 2.55 β is defined as written in Eq. 2.56:

$$\beta = \frac{\bar{\rho}_c c_c}{\bar{\rho}_h c_h}. \quad (2.56)$$

Inserting the formulation for the FTF (Eq. 2.39) allows to reformulate the acoustic Rankine-Hugoniot relations of Eq. 2.54 and 2.55 by means of the so-called flame transfer matrix (FTM) in pu notation, given in Eq. 2.57:

$$\begin{pmatrix} \frac{p'}{\bar{\rho} c} \\ u' \end{pmatrix}_h = \underbrace{\begin{pmatrix} \beta & -\beta \left(\frac{T_h}{T_c} - 1\right) Ma_c (1 + FTF) \\ -\left(\frac{T_h}{T_c} - 1\right) \kappa Ma_c & 1 + \left(\frac{T_h}{T_c} - 1\right) FTF \end{pmatrix}}_{FTM^{pu}} \cdot \begin{pmatrix} \frac{p'}{\bar{\rho} c} \\ u' \end{pmatrix}_c. \quad (2.57)$$

The FTM can be further simplified to Eq. 2.58 when assuming a low Mach number upstream of the flame front ($Ma_c < 0.1$) and consequently neglecting the FTM_{12} - and FTM_{21} -elements:

$$\begin{pmatrix} \frac{p'}{\bar{\rho} c} \\ u' \end{pmatrix}_h = \underbrace{\begin{pmatrix} \beta & 0 \\ 0 & 1 + \left(\frac{T_h}{T_c} - 1\right) FTF \end{pmatrix}}_{FTM^{pu}} \cdot \begin{pmatrix} \frac{p'}{\bar{\rho} c} \\ u' \end{pmatrix}_c. \quad (2.58)$$

In this limit, the FTM_{11} -element with respect to Eq. 2.56 reveals that the acoustic pressure over the flame is assumed to be constant when using the Rankine-Hugoniot relations ($p'_c = p'_h$).

Knowing the FTM elements one can easily extract the FTF according to Eq. 2.59:

$$FTF = \frac{FTM_{22} - 1}{\frac{T_h}{T_c} - 1}. \quad (2.59)$$

2.3 Chemiluminescence

Chemiluminescence is the emission of light from atoms, molecules or radicals due to excitation during a chemical reaction, e.g. a combustion process [64]. The molecules can be excited by the chemical reaction itself or collision with other atoms, which may raise the molecule from its ground state to a higher energetic state. As the higher energetic state is unstable, the molecules tend to fall back to their ground state. During the fall back to the molecule's ground state, energy in form of light can be emitted, which is commonly used in combustion research as a measurement quantity. However, the loss of energy cannot only occur through the emission of light, but occurs mostly due to a collisional quenching reaction or collision with other molecules [65].

The most prominent chemiluminescence species when burning hydrocarbon fuels are OH^* , CH^* , C_2^* and CO_2^* [66, 67]. Figure 2.3 shows a typical chemiluminescence spectrum of a lean, premixed kerosene flame under atmospheric conditions, adapted from Vogel [68].

The emission spectrum of CO_2^* is broadband due to the triatomic structure of the molecule. In contrast, OH^* , CH^* , C_2^* are diatomic and consequently show distinct emission wavelengths.

Figure 2.4 illustrates the possible atomic states of diatomic molecules, adapted from Woisetschläger [69]. Diatomic molecules can only have distinct energy states: an electronically excited state, as well as a vibrational and rota-

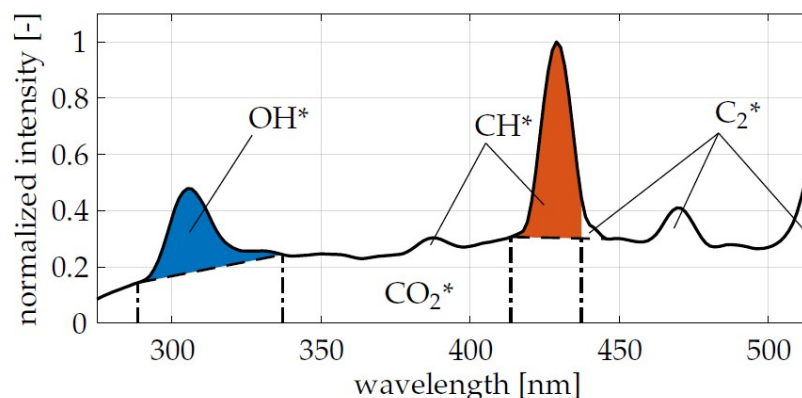


Figure 2.3: Typical chemiluminescence spectrum of a lean, premixed kerosene flame under atmospheric conditions.

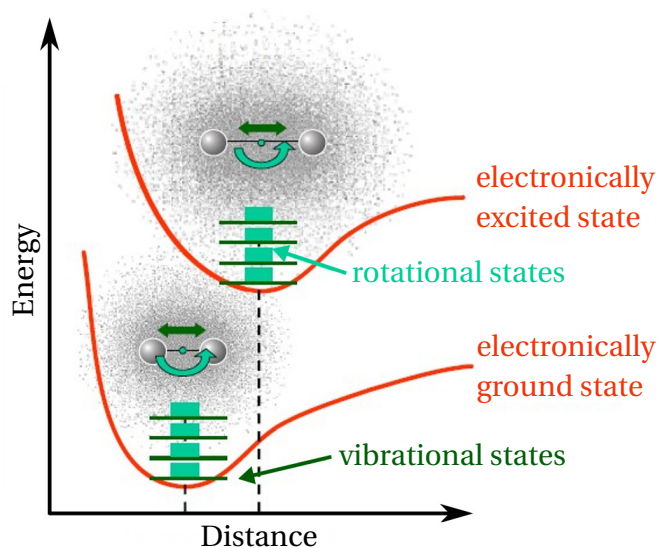


Figure 2.4: Energy levels of diatomic molecules.

tional excitation state. The first excitation mode contains most of the energy (main peaks in Fig. 2.3), whereas the latter two have minor contribution to the overall light emission (small side peaks in Fig. 2.3). For this reason, the main emission peaks of the electronically excited state of each diatomic radical are most useful.

The chemiluminescence measurement of flames is a commonly employed technique in combustion experiments to assess the amount of heat release and fluctuations. Thermal power, temperature, and strain have a significant impact on chemiluminescence physics. Hence, the quantification of heat release in turbulent flames, such as swirl flames in gas turbine combustors, is prone to errors [65]. In several studies, the flame's chemiluminescence has already been proven to be a reliable indicator of both heat release and equivalence ratio fluctuations for perfectly premixed kerosene and natural gas flames [68, 70, 71].

3 Test Rig and Experimental Setup

This chapter presents the design of a novel thermoacoustic combustion test rig used to assess the flame dynamics of the individual combustion zones, namely the primary and secondary zone. The basic working principle of the test rig is demonstrated by explaining the air and fuel paths, as well as the combustion chamber configurations and possible arrangements. Furthermore, the thermodynamic design approach for ensuring auto-ignition in the secondary zone is briefly described, as well as the most important aspects of the acoustic design. Finally, the experimental setup for the primary zone investigations and the compact RQL setup is shown, including the positioning of the relevant measurement devices.

3.1 Test Rig

The aim of the present work is the determination of the thermoacoustic behavior of RQL combustion chambers with focus on the primary zone (cf. Chapter 1). In real aero engine combustion chambers the primary and secondary combustion zone are arranged very close to each other, referred to as compact RQL arrangement. The new scientific approach aims at the isolated measurement of the primary and secondary zone's flame dynamics. This approach was realized in a new test rig, which allows the individual measurement of the flame dynamics of the primary and secondary zone by spatially separating the combustion regions. Additionally, the compact RQL arrangement with both zones located in the first combustion chamber is possible due to a high modularity of the test rig.

The most important aspects considered during the design phase were:

- Strict modularity to allow the multiple use of different test rig parts and measurement modules depending on the test rig configuration.
- Thermal design to guarantee the integrity of the test rig parts and to ensure stable auto-ignition in the secondary combustion chamber.

- Design of the secondary air jets to obtain similar aerodynamics and mixing as in real aero engine combustors.
- Acoustic excitation with loudspeakers giving very high repeatability, as well as flexible amplitude and phase control.
- Impedance measurement ducts to assure high quality acoustic wavefield reconstruction down to low frequencies.
- Kerosene supply system including tank, pump, coriolis mass flow meter, and valves to provide appropriate fuel mass flows to the burner in the primary zone.

3.1.1 Concept for the Primary Zone Investigations

Figure 3.1 illustrates the test rig concept for the investigations of the primary zone. The test rig supply provides all necessary operating media for the op-

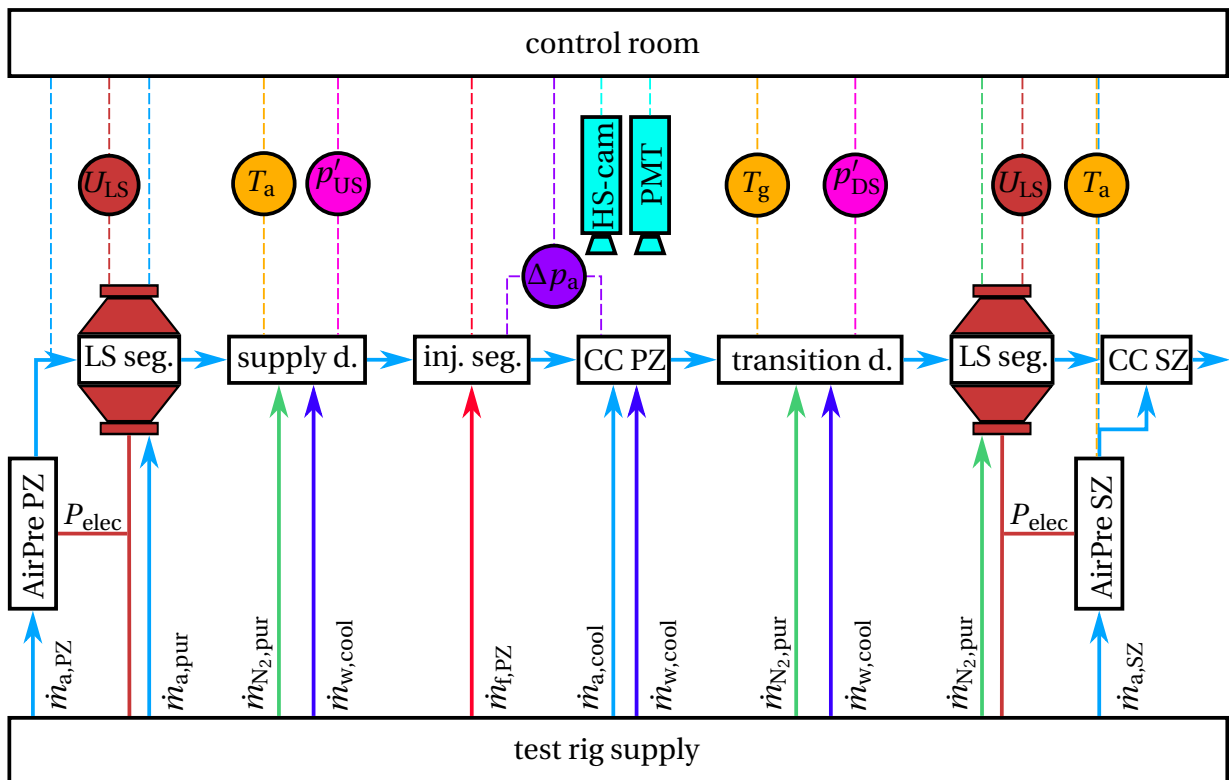


Figure 3.1: Basic concept of the test rig setup for the primary zone investigations.

eration of the facility (e.g. air), while the control room serves for monitoring and recording of the relevant measurement data. In addition to the electrical power supply of the corresponding facility components, the supply media include air (a), fuel (f), nitrogen (N_2), and water (w). These can be divided into a group necessary for combustion operation and a group necessary for the protection of test rig components and measurement technologies. The first includes combustion air for both combustion chambers, primary air $\dot{m}_{a,PZ}$ and secondary air $\dot{m}_{a,SZ}$, as well as the fuel supply $\dot{m}_{f,PZ}$, which provides natural gas or kerosene depending on the operating mode. In addition, cooling air $\dot{m}_{a,cool}$, cooling water $\dot{m}_{w,cool}$, and nitrogen $\dot{m}_{N_2,pur}$ are required to protect the components and instrumentation of the test rig. The latter is used to purge dynamic pressure transducers and loudspeakers.

Along the path of the primary air $\dot{m}_{a,PZ}$ the test rig is divided into the air preheater of the primary zone (AirPre PZ), the loudspeaker segment upstream (LS Seg.) of the supply duct (Supply D.), the injector segment with mounted burner (Inj. Seg.), the combustion chamber of the primary zone (CC PZ), the transition duct (Transition D.), the loudspeaker segment downstream (LS Seg.), and the combustion chamber of the secondary zone (CC SZ) with laterally arranged air preheaters (AirPre SZ). For the investigation of the flame dynamics acoustic drivers and impedance measurement ducts are required. The acoustic drivers in the form of loudspeakers are mounted on the loudspeaker segments up- and downstream of the corresponding impedance measurement duct (supply and transition duct).

In the control room all relevant test rig parameters and measurement values of the corresponding sensors are recorded. The most important ones are shown in Fig. 3.1 as dashed lines. The blue group monitors and controls all relevant air mass flows. Colored in orange are static temperature measurements of air T_a and exhaust gas T_g at various positions along the test rig. The measurement of the air differential pressure across the burner Δp_a is given in violet. For the investigation of thermoacoustics, dynamic pressure sensors measure the acoustic pressures upstream p'_{US} and downstream p'_{DS} of the primary zone. The magnitude and frequency of the acoustic velocity fluctuations in the test rig can be controlled by modulating the voltage signal for the loudspeakers U_{LS} . The ability to apply optical measurement techniques is guaranteed by quartz glass windows on two opposite sidewalls of the combustion chamber.

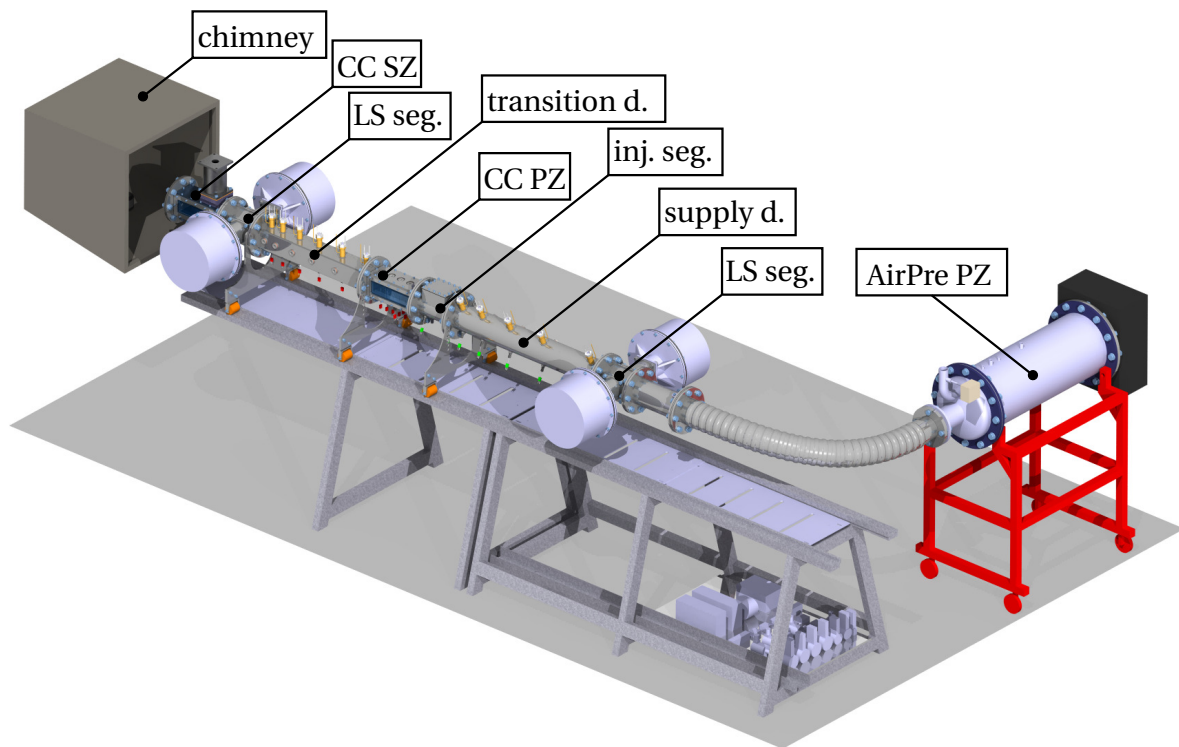


Figure 3.2: CAD model of the test rig configuration for measurements in the primary zone.

Applicable optical measurement techniques are, e.g. high-speed cameras (HS-Cam) or photomultiplier tubes (PMT).

Figure 3.2 illustrates the CAD model of the test rig configuration for the measurements of the isolated primary zone. In this setup the primary zone forms an acoustic two-port between the two impedance measurement ducts (supply and transition duct), as well as an excitation via loudspeakers from up- and downstream.

3.1.2 Primary Zone Combustion Chamber

The combustion chamber of the primary zone should approximate as closely as possible the combustion conditions prevailing in the combustion chambers of real aircraft engines, apart from pressure due to atmospheric test conditions. At the same time, it must have adequate accessibility and flexibility for the purpose of thermoacoustic and optical investigations. The entire fuel is injected via the injector into the primary zone where combustion takes

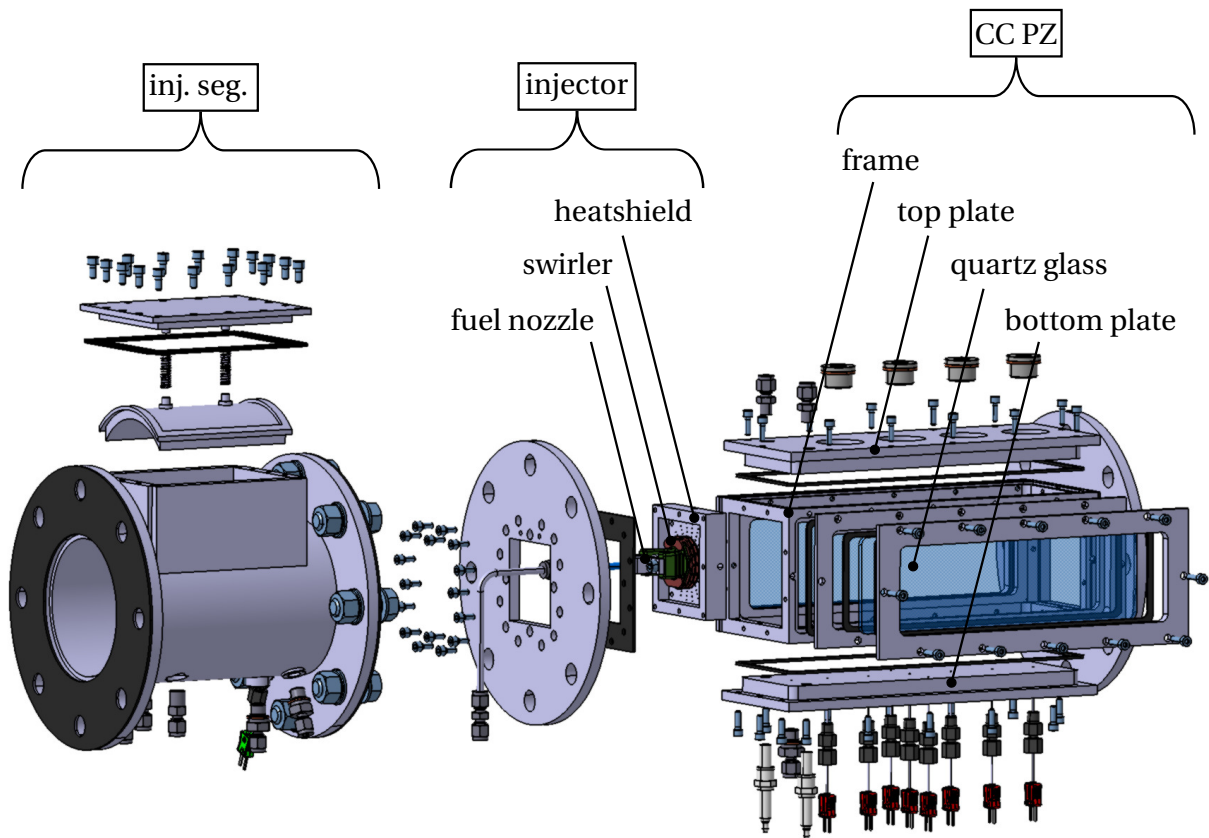


Figure 3.3: CAD model of the injector segment (left), Injector (middle) and primary zone combustion chamber (right).

place under either a lack or an excess of air. Since the operating points are in the near-stoichiometric range, there is a high thermal load on the material, which is counteracted by cooling air impingement on the outside of the combustion chamber. Additionally, the 3D printed quartz glass window frames on two opposing side walls of the chamber are internally water-cooled. The combustion chamber has a rectangular cross section of $A_{CC} = 90 \times 90 \text{ mm}^2$ and a length of $l_{CC} = 0.28 \text{ m}$.

An overview of the assembly of the primary zone, including the injector segment and the injector, is given in Fig. 3.3. The combustion chamber is equipped with a top and bottom plate, as well as two quartz glass windows on two opposing walls. The plates and windows are mounted on a high-temperature steel frame. The top and bottom plates are equipped with various fittings, as well as the spark plug and natural gas nozzle for the ignition burner.

Injector: The primary zone can accommodate two different prototype injectors, an airblast and a pressure atomizer type, provided by two different engine manufacturers [72, 73]. The injector segment (Inj.Seg.) in Fig. 3.3 upstream of the combustion chamber serves as a mounting part for the injectors. Since the injectors have very different designs, two different injector segments with associated heat shields or heat shield mounts are required. Both injector segment configurations have ports for differential pressure measurements, as well as for a thermocouple to record the inlet preheating temperature of the combustion air. In Fig. 3.3 the injector segment for the pressure atomizer type injector is illustrated.

In the present work only the pressure atomizer type injector is used (Injector in Fig. 3.3), as it exhibits less soot production, which is essential for applying optical measurement methods based on chemiluminescence. To further improve the sooting behavior, especially for fuel-rich combustion, the original kerosene atomizer nozzle was modified. The outer diameter of a *Delavan 1,00/60 B* atomizer was reduced to fit in the remaining burner hardware, maintaining the same injection position as the original nozzle. Figure 3.3 shows the

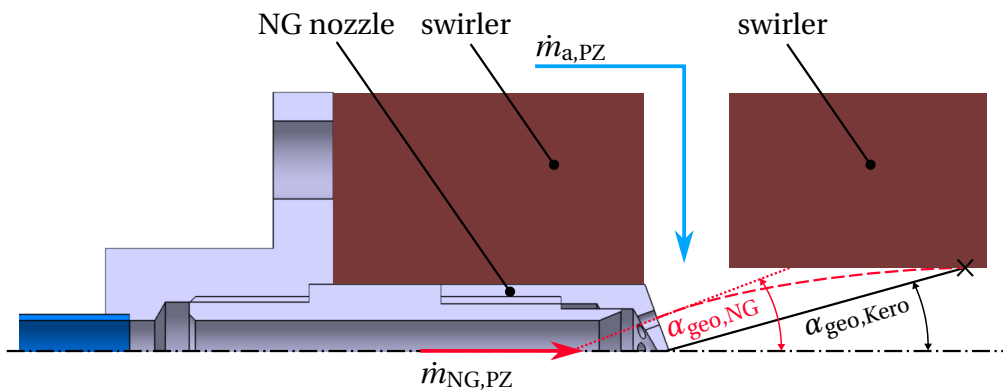


Figure 3.4: Design intent of the non-premixed natural gas nozzle for the primary zone. The red solid line shows the geometric injection angle for the natural gas nozzle $\alpha_{geo,NG}$, the black solid line for the kerosene nozzle $\alpha_{geo,kero}$. The red dashed line shows the calculated jet-in-cross-flow trajectory for the natural gas $\dot{m}_{NG,PZ}$ injected into the primary air $\dot{m}_{a,PZ}$.

Table 3.1: Tested design versions of the non-premixed natural gas nozzle.

Nr.	$N_{i,NG}$ [-]	$d_{i,NG}$ [mm]	$\alpha_{geo,NG}$ [deg]
1	8	1	45
2	8	1.3	45
3	8	1	20
4	8	1.3	20
5	8	1	15

CAD model of Injector used for the primary zone investigations, consisting of heatshield, swirler, and kerosene fuel nozzle.

The heat shield of the injector was not supplied by the manufacturer and was therefore designed by the author maintaining the same air flow splits as in the real aero engine application. The heat shield consists of 100 straight drilled holes, each with a diameter of 1 mm.

To quantify the influence of atomization and evaporation on the flame dynamics in the primary zone, a natural gas nozzle for the combustion of non-premixed gaseous fuel was designed. Figure 3.4 shows a simplified sketch of the design of the natural gas nozzle and the swirler geometry. In addition, the mass flows of natural gas $\dot{m}_{NG,PZ}$ and primary air $\dot{m}_{a,PZ}$ are indicated. The natural gas nozzle can be integrated into the swirler, sitting on the same position as the kerosene atomizer nozzle. The intent of the design is the injection of natural gas impinging on the inner swirler wall at the same position as the liquid fuel (marked as black cross in Fig. 3.4). The calculations for the geometry of the natural gas nozzle, which were made for the design optimization, are based on the jet-in-cross-flow theory and the isothermal CFD flow field within the swirler [13]. Several geometric versions of the non-premixed natural gas nozzle were obtained by varying the diameter $d_{i,NG}$ of the natural gas injection orifices, as well as the geometric injection angle $\alpha_{geo,NG}$. The number of injection orifices was kept constant at $N_{i,NG} = 8$.

The different versions of the nozzle were investigated in the test rig to evaluate whether the combustion behavior is suitable with respect to the planned investigations and operating points. The most important selection criterion during the natural gas nozzle tests was to obtain a flame shape similar to the kerosene flame, while maintaining similar operating conditions as for

kerosene combustion, e.g. burner pressure loss and equivalence ratio. However, some natural gas nozzles showed a lifted flame or a high sensitivity when changing the operating conditions leading to a blow-out of the flame. Table 3.1 lists the geometric parameters of the investigated nozzles. Nozzle Nr. 4 showed the most suitable combustion behavior, especially in the near-stoichiometric range.

Ignition Burner: The ignition of gaseous and liquid fuel in the primary zone is realized via a newly designed ignition system based on natural gas. The concept of the ignition system is the generation of an ignition flame, which surrounds the burner exit inside the combustion chamber. Figure 3.5 illustrates a cross sectional view of the primary zone from downstream visualizing the working principle of the natural gas ignition burner.

To generate the ignition flame, an orifice for natural gas injection on the top plate and a spark plug on the bottom plate are positioned opposed to each other. The combustion air for the ignition burner is provided by the main air coming from the primary zone's burner $\dot{m}_{a,PZ}$. Depending on the swirl direction of the burner two arrangements are possible (left and right configuration

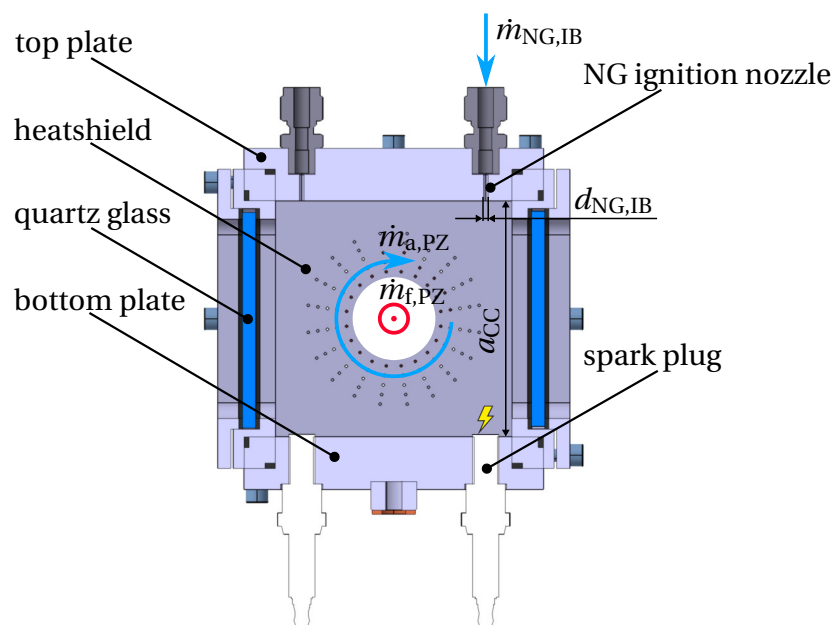


Figure 3.5: Sketch of the design and working principle of the natural gas ignition burner in the primary zone.

in Fig. 3.5). Each arrangement guarantees an injection of natural gas into the same direction as the burner's swirl motion, indicated by the circumferential component of the primary air $\dot{m}_{a,PZ}$ in Fig. 3.5. The injection method should support the mixing of natural gas and air along the combustion chamber side wall and avoid flame extinction of the ignition burner's flame. After a stable flame of the ignition burner is established, the main fuel $\dot{m}_{f,PZ}$ is injected into the primary zone via the fuel nozzle in the center and subsequently ignited with the help of the ignition flame, providing the activation energy needed to start the combustion of the main flame.

The calculation of the required nozzle diameter for the ignition gas is based on the investigations of turbulent axisymmetric free jets by Ricou and Spalding [74]. The air entrainment increases linearly with the axial distance x from the injection point. Using the equations given in [74] and substituting for the equivalence ratio and stoichiometric fuel-to-air ratio leads to Eq. 3.1:

$$1 + \frac{1}{\phi_{IB} FAR_{stoich,NG}} = 0.32 \frac{x}{d_{NG,IB}} \sqrt{\frac{\rho_a}{\rho_{NG}}}. \quad (3.1)$$

In Eq. 3.1 ϕ_{IB} is the equivalence ratio of the free jet of the ignition burner, $FAR_{stoich,NG}$ the stoichiometric fuel-to-air ratio of natural gas, $d_{NG,IB}$ the exit diameter of the free jet, and ρ_a and ρ_{NG} the densities of air and natural gas, respectively. The aim of the mixing design is to generate a near-stoichiometric fuel-to-air mixture $\phi_{IB} \approx 1$ at the spark plug. Therefore, the axial distance in Eq. 3.1 corresponds to the side length of the combustion chamber a_{CC} . Additionally, calculating the densities of air and natural gas with the ideal gas law, the diameter of the ignition burner's nozzle $d_{NG,IB} = 1.8 \text{ mm}$ was obtained.

3.1.3 Compact RQL Combustion Chamber

The compact RQL combustion chamber combines both the primary and the secondary combustion zone in one combustion chamber, similar to real aero engines. For this purpose, the combustion chamber of the primary zone (cf. Section 3.1.2) is modified so that the additional secondary zone can be integrated into the combustion chamber.

Figure 3.6 illustrates the compact RQL combustion chamber including the injector segment (left), the injector (middle), and the compact RQL combustion chamber. The integration of the secondary combustion zone is accom-

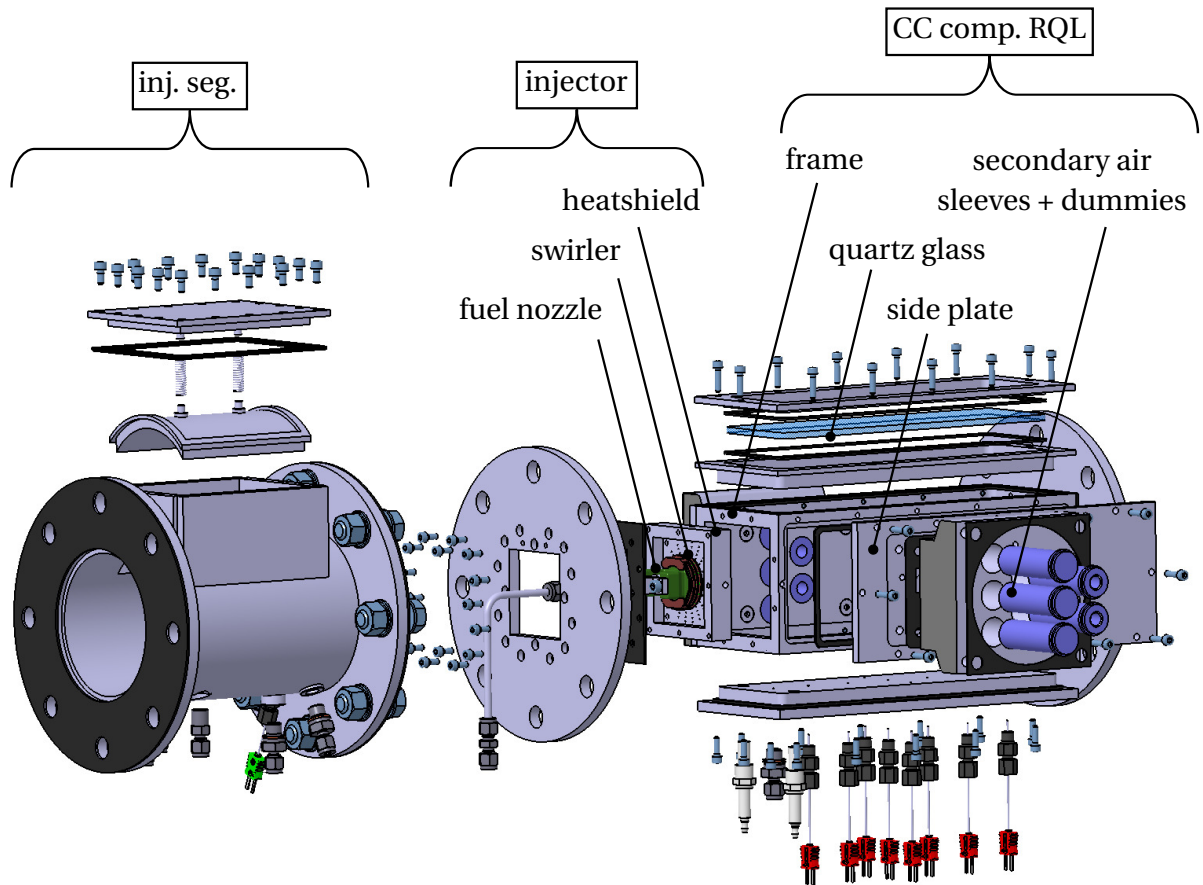


Figure 3.6: CAD model of the injector segment (left), Injector-1 (middle) and compact RQL combustion chamber (right).

plished by two opposing side plates and dilution air sleeves. The jet-in-cross-flow configuration for the dilution air is modularly designed, which allows for the implementation of various mixing-hole patterns by exchanging the secondary air sleeves. For the configuration studied in the present work, two opposing JIC rows with two dilution holes were chosen as a representative geometry. The diameter of the dilution holes was determined according to industrially relevant pressure losses ($\Delta p_{a,SZ}/p_{a,SZ} \approx 3\%$) resulting in a diameter of $d_{JIC,SZ} = 10.55\text{ mm}$ per dilution hole. Due to the integration of the mixing holes in the side plates, the quartz glass window was mounted on top of the compact RQL combustion chamber. The ignition burner is modified such that the natural gas injection orifice is located at the position of the left spark plug in Fig. 3.5. The primary zone burner and injector segment remains the same

as for the isolated primary zone investigations.

3.1.4 Thermodynamic Design

Combustion in the Primary Zone: The calculation of relevant combustion parameters in the primary zone is the starting point for the assessment of heat losses and the examination whether auto-ignition in the secondary combustion chamber is achieved. The main difference to real combustion chambers is due to the local separation of the two combustion zones and the associated effects on thermodynamics and the flow field. A design point with an equivalence ratio of $\phi_{PZ} = 1.18$, an air preheating temperature of $T_{a,PZ} = 473\text{K}$ and a thermal power of $\dot{Q}_{th,PZ} = 53.2\text{kW}$ was chosen for the design calculations. The adiabatic flame temperature $T_{ad,PZ}$ and the exhaust gas composition $X_{i,pr,PZ}$ in the primary zone are obtained with *Cantera*, using Dagaut's mechanism for a kerosene surrogate and thermodynamic equilibrium conditions [75, 76].

Figure 3.7 shows the adiabatic flame temperature and the exhaust gas composition over the equivalence ratio. For fuel-rich combustion, mainly car-

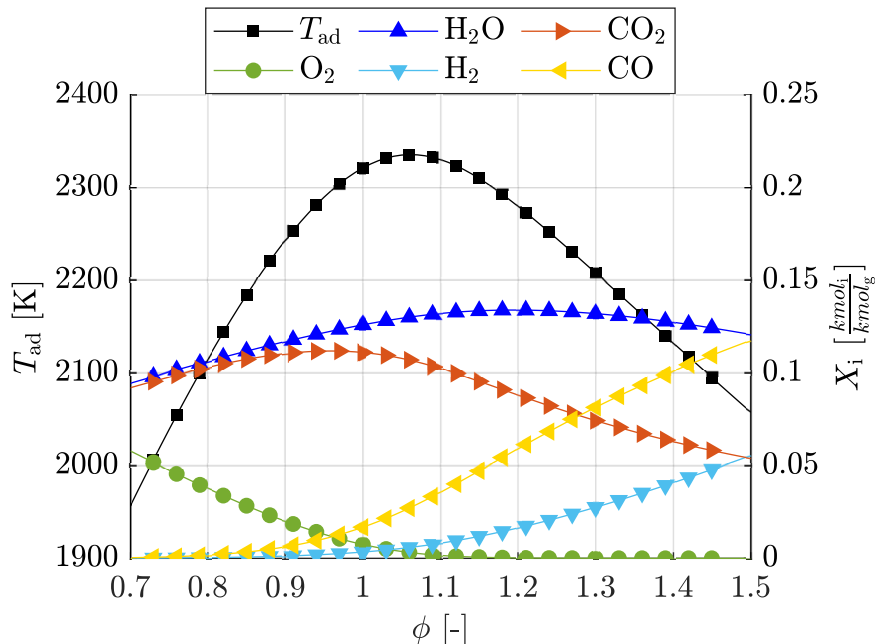


Figure 3.7: Adiabatic flame temperature and combustion products over the equivalence ratio for a kerosene surrogate and thermodynamic equilibrium conditions.

bonmonoxide CO and hydrogen H_2 are the remaining reactive species to be burned in the secondary combustion chamber. As the primary and secondary zones in the introduced test rig are approx. 1 m apart from each other, the assumption of using the thermodynamic equilibrium seems to be justified regarding the composition of the primary zone's exhaust gases $X_{i,pr,PZ}$. For the chosen design point, the adiabatic flame temperature of $T_{ad,PZ} = 2346\text{K}$ is used, together with the corresponding combustion products $X_{i,pr,PZ}$, as the inlet boundary condition for the subsequently performed thermal design.

Heat Losses: The thermal design is based on a one-dimensional enthalpy balance along the primary zone and the adjacent transition duct (cf. Fig. 3.2). The primary zone and the transition duct are discretized into finite elements in axial direction and each control volume is solved for the corresponding exit temperature, needed as input for the subsequent element. Figure 3.8 illustrates the temperatures and heat fluxes considered for each element. The amount of heat transferred from the hot gases to the combustor wall $\dot{Q}_{conv,int}$ is determined by using a Nusselt correlation for duct flows based on the local characteristics of the flow. This approach is a rough approximation for the primary zone due to the complex flow field, whereas for the transition duct it seems to represent reality better.

In the primary zone the convective heat flux of the outer wall $\dot{Q}_{conv,ext}$ is calculated by using correlations for air impingement cooling [77]. To avoid exces-

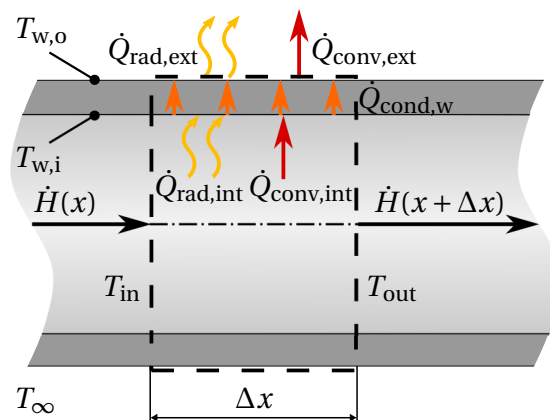


Figure 3.8: Temperatures and heat fluxes for one control volume along the primary zone and transition duct.

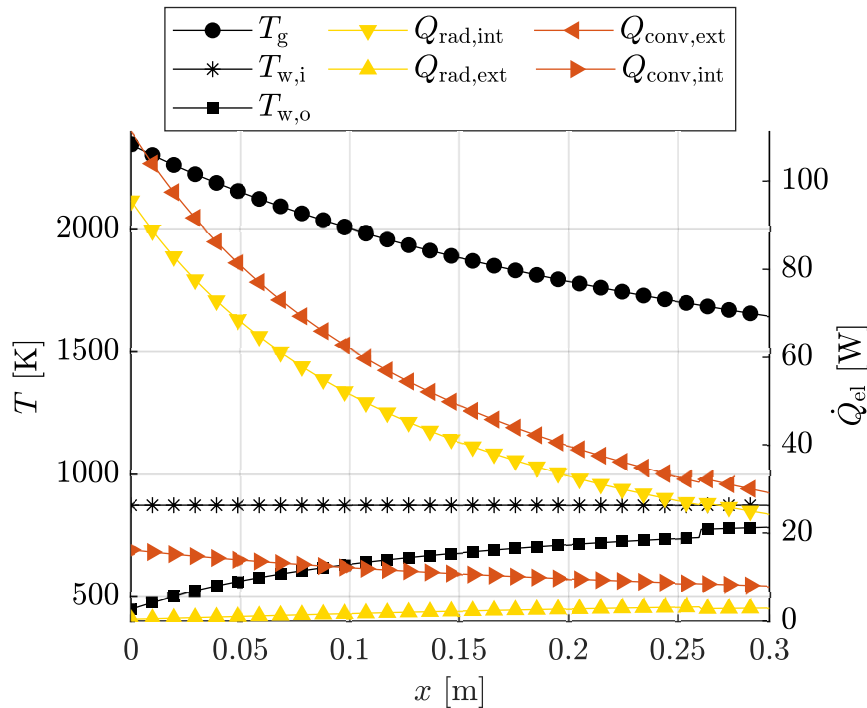


Figure 3.9: Temperatures and heat fluxes along the primary combustion chamber using a 1D calculation.

sive glowing of steel and quartz glass parts, the air cooling on the outside of the combustion chamber was adjusted, such that the inner wall temperature is limited to $T_{w,i} = 873$ K. The radiation inside the primary zone $\dot{Q}_{rad,i}$ accounts for gas and soot radiation, as well as radiation from the steel walls and quartz glass windows. The gas radiation of CO_2 and H_2O was obtained by using the corresponding temperature depending emission coefficients found in Smith's work [78]. Furthermore, the radiation of soot was taken into account according to Zalosh [79], as the fuel-rich combustion of kerosene in the primary zone is prone to soot production. The emission coefficients for the radiation of the steel walls were obtained from [77] and for the quartz glass windows according to Petrov and Reznik [80].

The results for the calculated temperatures and heat fluxes in the primary zone are plotted in Fig. 3.9 over the combustor length, starting from the burner exit plane $x = 0$ m to the combustion chamber outlet plane $x = 0.3$ m. Inside the combustion chamber the radiation $\dot{Q}_{rad,i}$ is dominating over the convection $\dot{Q}_{conv,int}$, leading to the conclusion that simplifications regarding the flow

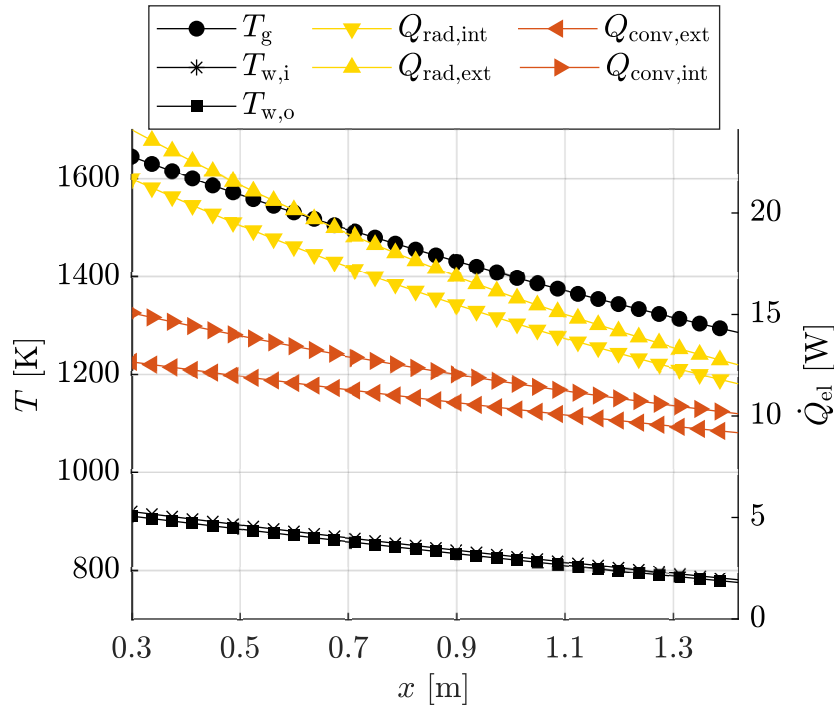


Figure 3.10: Temperatures and heat fluxes along the transition duct using a 1D calculation.

field in the combustion chamber have minor impact on the overall result. The calculated exit temperature of the primary zone of $T_{\text{exit,PZ}} = 1644 \text{ K}$ is used as the inlet condition for the transition duct together with the exhaust gas composition $X_{i,\text{pr,PZ}}$.

In contrast to the primary combustion chamber, the transition duct is only cooled with natural convection and steel radiation on the outside, minimizing further heat losses. On the inside soot radiation was neglected as no sooting flame is assumed to be inside the transition duct. In addition, the duct has no quartz glass windows, which reduces the radiation of the solid walls to steel only. The curves for the obtained temperatures and heat fluxes along the axial length of the transition duct are given in Fig. 3.10. The calculated exit temperature of the duct of $T_{\text{exit,TD}} = 1285 \text{ K}$ is further used as inlet temperature for the secondary zone.

The overall heat fluxes indicate 37% of heat losses in the primary combustor and 20% in the transition duct related to the overall thermal power of the fuel. The biggest uncertainties for the heat transfer calculations are the simplified

flow field in the primary zone and the emission coefficients of soot and the solid walls.

A more detailed assessment of the heat losses and corresponding gas temperatures was achieved by CFD calculations. For simplification, the CFD setup used methane as fuel and soot radiation was not considered. The overall results regarding the exit temperature of the primary combustion chamber $T_{\text{exit,PZ}}$ and the transition duct $T_{\text{exit,PZ}}$ showed a deviation of less than 10% between the complex CFD simulations and the simplified analytical approach shown above. More details on the CFD simulations can be found in [81].

Auto-Ignition in the Secondary Zone: The last step of the thermodynamic design approach is determining whether auto-ignition in the secondary zone takes place. For this purpose, the ignition time delay in the secondary combustion chamber must be estimated. The calculations were carried out in *Cantera*, using a constant pressure reactor including the homogeneous mixture of the exhaust gases from the primary zone $X_{\text{i,pr,PZ}}$ mixed with the air injected in the secondary zone. Considering the calculated exit temperature of the transition duct $T_{\text{exit,TD}}$, the time delay until 50% of the maximum temperature in the secondary zone is reached leads to an auto-ignition time delay of $\tau_{\text{AI,SZ}} = 0.145 \text{ ms}$.

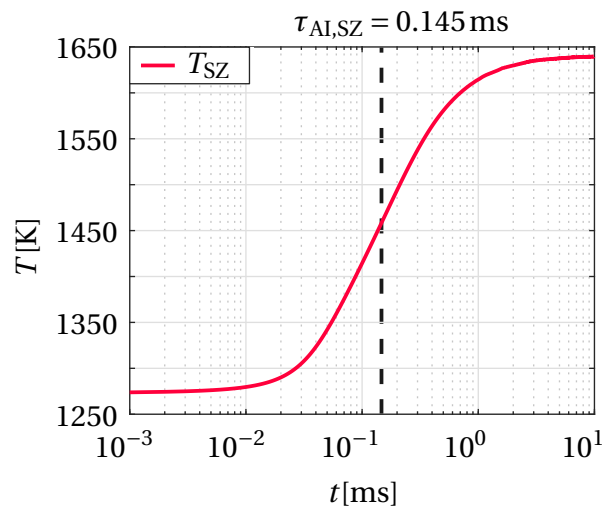


Figure 3.11: Estimation of the auto-ignition time delay in the secondary zone using a homogeneous constant pressure reactor in *Cantera*.

Figure 3.11 depicts the temperature curve over time for the auto-ignition calculations performed in *Cantera*. Taking into account the secondary air jet's exit velocity of approximately $u_{\text{jet,SZ}} = 26 \text{ m/s}$ gives a distance of 3.8 mm for the mixture to be ignited. This approach is considered conservative, as for the real conditions in the test rig the mixture would ignite along the shear layer of the jet at a most reactive mixture fraction. Due to the results for the given estimations of the chemical kinetics, auto-ignition in the secondary zone is assumed to take place.

3.1.5 Acoustic Design

Impedance Measurement Ducts: The measurement of the acoustic pressure inside the test rig is a necessary requirement for the reconstruction of the acoustic wavefield and the application of the multimicrophone method (MMM). The impedance measurement ducts provide the adapters for the piezodynamic pressure transducers (*Synotech PCB 106B*) and ensure a homogeneous air and exhaust gas flow. In addition, thermocouple mounts are installed at all dynamic pressure measurement positions along the ducts. In total two impedance measurement ducts were used, namely the supply and transition duct (cf. Fig. 3.2). Depending on the configuration to be investigated, namely primary zone, secondary zone or compact RQL arrangement, the measurement ducts can be positioned accordingly. The design of the impedance ducts considers the main parameters duct length l_{IMD} , duct cross section A_{IMD} , number N_{PCB} , and positioning x_{PCB} of the pressure transducers. To obtain the length of the measurement duct, the maximum acoustic wavelength must be estimated. The wavelength is correlated to the speed of sound of an isentropic fluid and the frequency according to Eq. 3.2:

$$\lambda = \frac{\sqrt{\gamma RT}}{f}, \quad (3.2)$$

where γ is the isentropic exponent, R the specific gas constant, and T the temperature of the fluid. The current research project is focusing on low frequency investigations, therefore the lowest frequency to be considered is $f = 100 \text{ Hz}$. Assuming a hot gas temperature downstream the primary zone of $T \approx 1500 \text{ K}$, the specific gas constant of air $R = 287 \text{ J/kgK}$ and the isentropic exponent of air $\gamma = 1.4$ leads to an acoustic wavelength of $\lambda = 7.76 \text{ m}$. The experience of

the Chair of Thermodynamics showed that a minimum of 10% of the acoustic wavelength should fit between two pressure transducers along the ducts. In addition, considering that the space inside the laboratory is limited, the maximum distance between two dynamic pressure sensors was estimated to $x_{\max, \text{PCB}, \text{SD}} = 0.83 \text{ m}$ for the supply duct and $x_{\max, \text{PCB}, \text{TD}} = 0.613 \text{ m}$ for the transition duct. In further consequence, the length of the impedance measurement ducts was obtained by considering the additional space needed for the mounting flanges on both ends.

A minimum of three acoustic pressure sensors at non-equidistant spacing are necessary for reconstructing the acoustic wavefield [54]. Six mounting ports for the piezodynamic pressure transducers are installed on each impedance measurement duct, allowing more flexibility in choosing the positioning of the PCBs. The distance between the different mounting locations was defined according to different prime numbers. This non-equidistant spacing approach guarantees that the reconstruction procedure does not fail due to the possibility of half the wavelength being enclosed between two sensors. Furthermore, the arrangement of the sensors can be adapted according to the frequency range investigated.

The square cross section of the transition duct corresponds with the cross section of the combustion chambers $A_{\text{CC}} = 90 \times 90 \text{ mm}^2$ to avoid area jumps, which influence the acoustic wavefield. The circular cross section of the supply duct upstream of the primary zone has a diameter of $d_{\text{SD}} = 117 \text{ mm}$ and is approximately 32% bigger than the combustion chamber's one. As the burner itself already represents an area jump, the difference in cross section upstream the primary zone has no influence on the transfer matrix measurements. The avoidance of the formation of transversal acoustic waves can be checked by calculating the cut-off frequency for a cylindrical tube according to Eq. 3.3:

$$f_{\text{cut-off}} = \frac{1.84c}{\pi d}. \quad (3.3)$$

Considering a worst case scenario with an air temperature of $T_a = 293 \text{ K}$, the resulting cut-off frequency for the supply duct calculates to $f_{\text{cut-off}} = 1718 \text{ Hz}$. For the rectangular transition duct the cut-off frequency can be obtained by using Eq. 3.4 [52]:

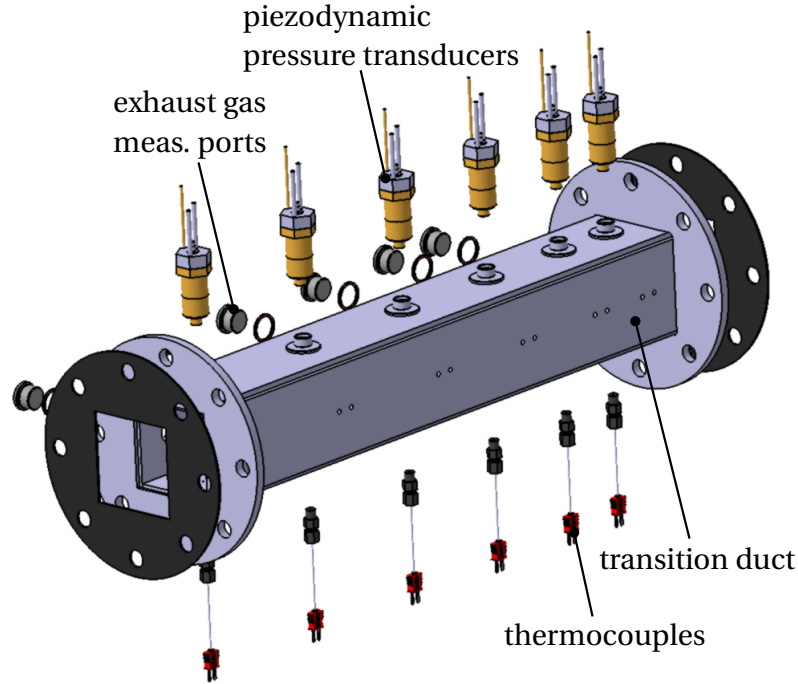


Figure 3.12: CAD model of the transition duct including PCBs and thermocouples.

$$f_{\text{cut,rec.}(1,0)} = \frac{c}{2} \sqrt{\left(\frac{m}{b}\right)^2 + \left(\frac{n}{h}\right)^2}. \quad (3.4)$$

For $m = 1$, $n = 0$, and $b = h = 0.09\text{m}$ the cut-off frequency for the rectangular transition duct results in $f_{\text{cut-off}} = 1906\text{Hz}$. The calculated frequencies are far above the maximum frequency to be investigated in the current research project. Thus, it can be concluded that transversal modes do not evolve inside the test rig during experiments. The onset of transversal modes is even more unlikely for higher gas temperatures and smaller geometry parameters as in the transition duct.

Figure 3.12 depicts the CAD model of the assembly of the transition duct. All piezodynamic pressure sensors used on the test rig are jacketed with a water-cooling (*PCB 064B06*), as well as a nitrogen-purged adapter. The former is needed due to the hot gas temperatures, whereas the latter protects the delicate membrane of the sensor from soot and liquid water deposits.

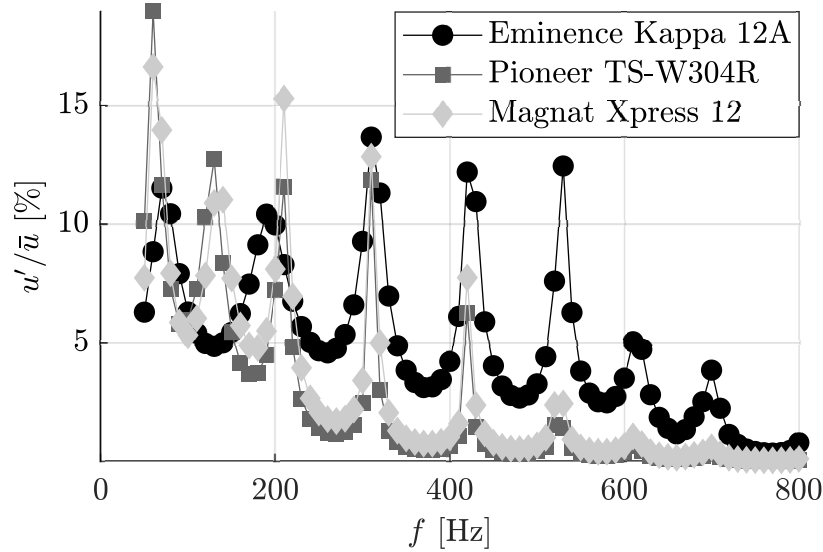


Figure 3.13: Frequency response in terms of relative velocity fluctuation u'/\bar{u} at the burner outlet calculated with 1D-NWM approach for different loudspeaker models.

Loudspeaker Design: The acoustic excitation of the primary and secondary zone's flame is performed with electromagnetic loudspeakers. The advantages resulting from this excitation method are the faster and more accurate setting of desired excitation frequencies, compared to sirens.

To evaluate the performance of the design, a dynamic loudspeaker network element was developed based on the Thiele-Small theory and tested experimentally [82–84]. This element was implemented in a one-dimensional acoustic network model (1D-NWM) of the test rig to analyze the driving capability of different types of loudspeaker. This approach takes into account the dynamics of the speaker within a housing and the characteristics of the rig, resulting in more realistic acoustical conditions. Based on the results, the selection, placement, and number of the subwoofers were defined.

Figure 3.13 depicts the calculated relative velocity fluctuation u'/\bar{u} of the 1D-NWM at the burner outlet location.

Figure 3.14 illustrates the CAD model of the acoustic excitation assembly used up- and downstream of the combustion chambers.

In contrary to sirens, common loudspeakers can not withstand high temperatures. Due to this, hot gas ingestion is prevented by purging the loudspeaker

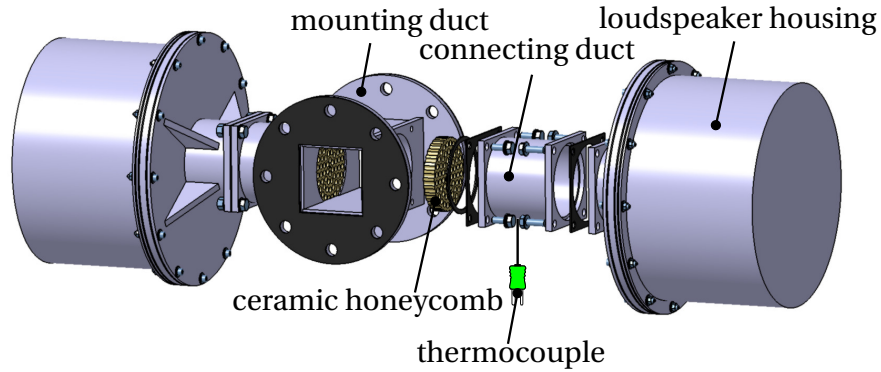


Figure 3.14: CAD model of the loudspeaker housings and connecting ducts to the test rig with ceramic honeycomb.

housing and the connecting ducts between the speaker and the rig with metered cold flow. Upstream the primary zone approximately $0.5 - 1\text{g/s}$ of air are used and taken into account for the calculation of the equivalence ratio in the combustion chamber during experiments. Downstream the primary zone $1 - 3\text{g/s}$ of nitrogen are directed into the loudspeaker housings and additional outside impingement cooling was installed. Furthermore, a 20 mm thick ceramic honeycomb structure with 60% porosity and $d = 8\text{mm}$ element size was inserted at the junction between the connecting duct of the loudspeakers and the test rig. The honeycomb prevents the formation of a detached vortex flow, which may direct hot gases into the loudspeaker housings.

Acoustic Boundaries: The optimal acoustic boundary conditions for the application of the MMM would be anechoic. However, this is difficult to implement, especially for the hot exhaust gas temperatures inside combustion test rigs. Simple perforated plates with a given porosity have shown low acoustic reflection coefficients when properly designed. For low Mach numbers, the open cross section of the perforated plate A_{pp} can be calculated according to Eq. 3.5 [55]:

$$\frac{A_{\text{pp}}}{A_{\text{duct}}} = \sqrt{Ma_{\text{duct}}}. \quad (3.5)$$

Ma_{duct} is the Mach number in the hot gas duct and A_{duct} the corresponding cross section. On the basis of this approach, perforated plates with different

area ratios were designed for the various operation points and tested during hot commissioning of the rig (cf. 5.1). The plates for which the self-excited combustion dynamics became lowest were chosen for the thermoacoustic investigations under acoustic forcing. For the primary zone setup perforated plates with a porosity of 12.4% at the entrance of the upstream and 15.7% at the exit of the downstream loudspeaker segment gave the best results.

3.2 Experimental Setup for the Primary Zone Measurements

An overview of the experimental setup for the investigations of the isolated primary zone is illustrated in Fig. 3.15. From the left, preheated primary air enters the test rig and is directed to the injector in the primary zone through the upstream excitation and the supply duct. The burner in the primary zone consists of a prototype double-radial swirler with a central fuel nozzle. Either a generic pressure atomizer nozzle for kerosene or a natural gas nozzle based

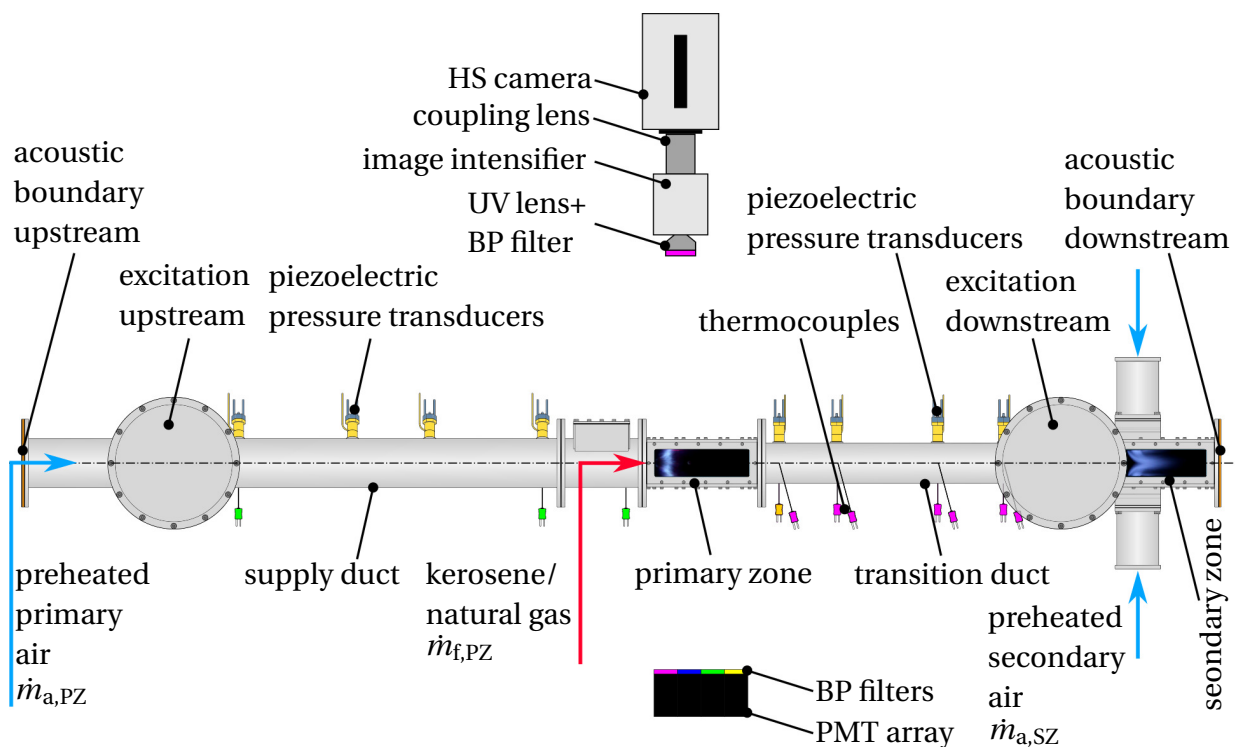


Figure 3.15: Test rig setup for the measurements in the primary zone combustion chamber (side view).

on a jet-in-cross-flow design can be used. The details of the burner hardware are given in section 3.1.2. The kerosene mass flow is measured with a coriolis mass flow meter (*BronkhorstMini coriFlowM14*), whereas for natural gas a mass flow controller (*Bronkhorst F-113AC-M50-RGD-44-V*) is used. In the primary zone the fuel is burned under rich or lean combustion conditions and subsequently directed to the secondary zone via the transition duct as well as the downstream excitation unit. The preheated secondary air guarantees the burn-out of still reactive hot gases in the secondary zone, which is located approximately 1 m downstream of the primary zone. The primary and secondary air mass flows are metered and controlled by two mass flow controllers (*Bronkhorst F-206AI-RAD-44-V*). The cross section of the primary zone, the transition duct, and the downstream acoustic boundary (perforated plate) remains constant at $A = 90 \times 90 \text{ mm}$. The hot exhaust gases leaving the secondary zone are directed into the chimney.

The impedance measurement ducts, supply duct and transition duct, are equipped with four non-equidistant spaced, water cooled, and N_2 -purged piezoelectric pressure transducers each (*Synotech PCB 106B*). The preheated air temperature in the supply duct is measured via two thermocouples of *Type K*, located at the first and fourth PCB position. The inlet temperature of the primary zone is measured with an additional thermocouple (*Type K*) inside the injector segment close to the burner entrance. Both parts, supply duct and injector segment, are insulated on the outside to prevent large temperature gradients along the locations of the PCBs upstream of the primary zone combustion chamber. For the transition duct thermocouples are situated at each PCB location, measuring the hot gas temperature on the inside, as well as the outer wall temperature. The acquisition of the hot gas temperatures is performed with a thermocouple of *Type S* at the first and three thermocouples of *Type N* at the remaining positions. The wall temperature is obtained by thermocouples of *Type N*, welded to the outer wall of the transition duct. In addition to thermocouples, some pressure sensors are mounted on the test rig at different locations. Up- and downstream of the burner a differential pressure sensor (*Burster Typ 8310*) measures the difference in air pressure across the burner. Inside the fuel line, a static pressure sensor (*Gems Sensors 3100 Series*) delivers the pressure of kerosene just before entering the test rig.

Two pairs of loudspeakers (*Eminence Kappa 12A*) are used for the acoustic ex-

citation up- and downstream of the primary zone. To monitor hot gas ingestion, which may damage the loudspeakers, the connecting ducts between the loudspeaker housings and the test rig are equipped with thermocouples of *Type K*. Purging air and nitrogen for the PCBs and loudspeakers are controlled via separate mass flow controllers. At the entrance and exit of the test rig perforated plates are mounted, providing low reflection coefficients to avoid the establishment of self-excited flame dynamics.

Regarding the optical investigations of the primary zone's flame, four photomultiplier tubes (*Hamamatsu H5784 Series*) with four different bandpass filters are oriented perpendicular to the combustion chamber. The PMT array collects the zero-dimensional, bandpass-filtered flame radiation. The optical field of view of the PMTs is restricted to avoid that glowing parts are inside the optical path. A high-speed camera (*Photron FastCam SAX*) with an image intensifier (Hamamatsu C10880-03F) and a bandpass filter is utilized to collect planar line-of-sight information of the flame, with and without acoustic excitation. Further details of the measurement techniques and their application can be found in Chapter 4.

3.3 Experimental Setup for the Compact RQL Measurements

The investigations of the close-coupled primary and secondary combustion zones are carried out using the compact RQL combustion chamber described in section 3.1.3. In addition to the supply and transition duct, impedance measurement ducts and acoustic excitation along the secondary air path are needed for thermoacoustic investigations.

Figure 3.16 depicts the top view of the compact RQL combustion chamber with the side ducts and acoustic excitation for the dilution air. The configuration shown in Fig. 3.16 is mounted between the supply and transition duct and, consequently, integrated into the test rig as shown in Fig. 3.15. The secondary combustion chamber at the end of the test rig in Fig. 3.15 is removed, while the remaining components stay the same as for the isolated primary zone setup.

In the compact RQL setup, half of the preheated secondary air $\dot{m}_{a,SZ}$ enters each of the side ducts and is guided to the opposing dilution holes for injection into the secondary zone. The entry temperature of the dilution air into

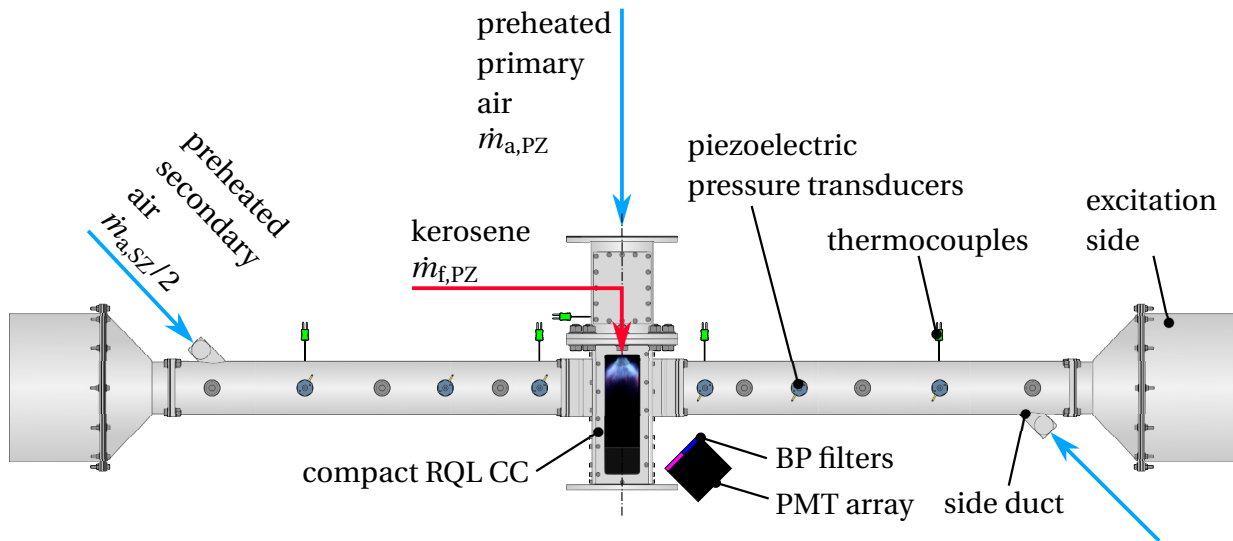


Figure 3.16: Setup for the measurements in the compact RQL combustion chamber (top view).

the compact combustor is measured via thermocouples of *Type K*. For the symmetrical acoustic excitation of the secondary air, one loudspeaker (*Eminence Kappa 12A*) per side duct is utilized. Three piezoelectric pressure transducers (*Synotech PCB 106B*) are mounted on each impedance measurement duct (supply duct, transition duct and side ducts) for the acoustic wavefield reconstruction. The differential pressure over the dilution holes $\Delta p_{a,SZ}/p_{a,SZ}$ is obtained analogously to the primary zone using a differential pressure sensor (*Burster Typ 8310*).

Regarding the optical investigations of the RQL flame, two photomultiplier tubes (*Hamamatsu H5784 Series*) with two different bandpass filters are oriented perpendicular to the combustion chamber. For the compact RQL investigations, the bandpass filters according to the wavelengths of OH^* and CH^* were chosen. Compared to the investigations of the isolated secondary zone, only two PMTs and no high-speed imaging were used for the compact RQL experiments. Furthermore, the number of PCBs per impedance measurement duct had to be reduced to three due to the total amount of available sensors.

4 Measurement Methods

The following chapter describes the experimental techniques used in the present work, as well as details about the corresponding evaluation methods. First, an overview of the data acquisition system and data routing will be given. Afterward, the chemiluminescence measurement section is divided into two parts: first, the zero-dimensional approach using photomultiplier tubes and second, the two-dimensional approach using high-speed camera and image intensifier will be discussed. For both measurement techniques, details of the experimental setup and evaluation method for the measurement of steady and unsteady chemiluminescence behavior are given. The last section of this chapter deals with the measurement of flame transfer functions (FTF). First the investigated operating points for measuring the flame dynamics are outlined. Second, the purely acoustic multimicrophone method is explained in detail. This incorporates the working principle and evaluation method for obtaining FTFs from an acoustic two-port system. Details about the data acquisition parameters and maintaining linear flame behavior are highlighted. Third, the optical approach is described by using the flame's chemiluminescence and an alternative formulation for the FTF, which is the hybrid FTF. At the end of this chapter, possibilities for improving the acoustic wavefield reconstruction are outlined. A temperature correction method based on a convective-radiative heat balance of a thermocouple in a hot gas environment is explained. In addition, a procedure for selecting different combinations of pressure transducers when having more than three PCBs is briefly described. This procedure is based on the definition of an error measure for the reconstruction of the acoustic wavefield and subsequently the selection of the most suitable combination of sensors.

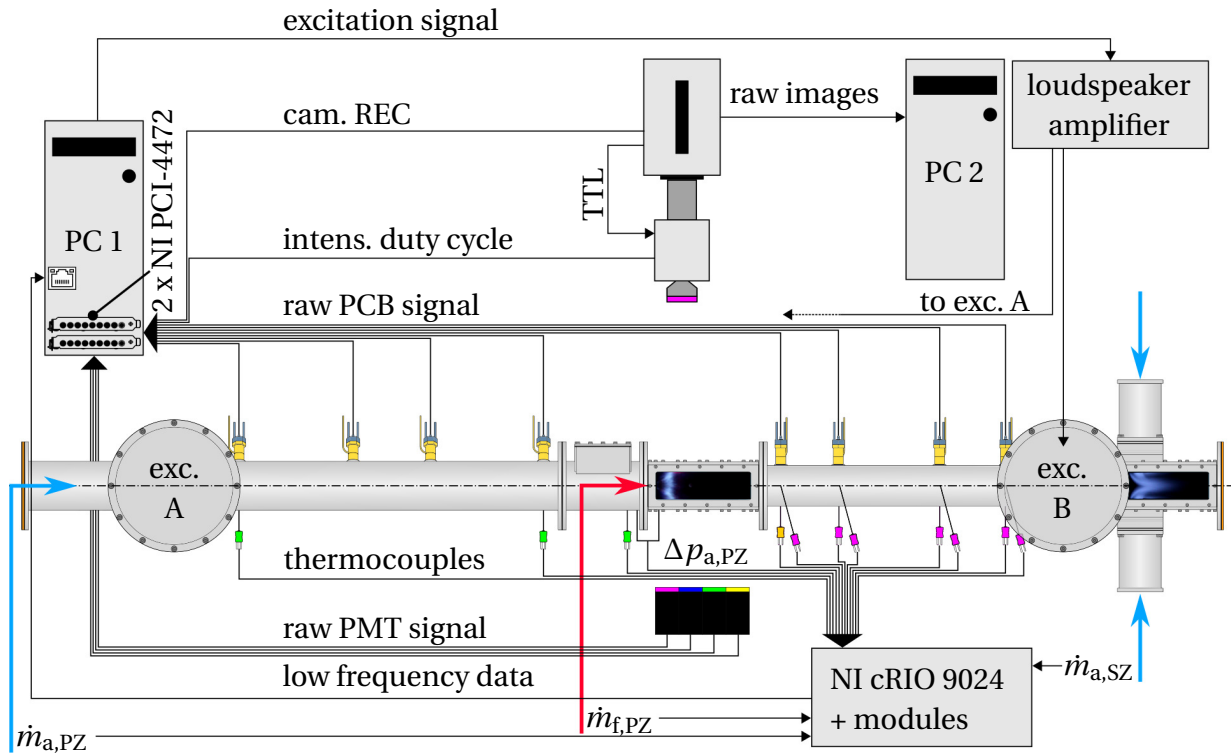


Figure 4.1: DAQ system for optical and thermoacoustic measurements for the primary zone setup (cf. Fig. 3.15).

4.1 Data Acquisition System

Figure 4.1 illustrates an overview of the data acquisition system (DAQ) and the corresponding data routing from the measurement PCs to the different measurement devices (cf. 3.15). The DAQ consists of a *NI cRIO 9024* including the corresponding measurement modules (C series) to collect low-frequency data, as well as two measurement cards *NI PCI-4472* inside PC 1 to record high-frequency signals. The low-frequency measurement device *NI cRIO 9024* collects temperatures from thermocouples, static pressures (e.g. $\Delta p_{a,PZ}$) and mass flows (e.g. $\dot{m}_{a,PZ}$, $\dot{m}_{a,SZ}$, $\dot{m}_{f,PZ}$) and sends them to PC 1 in the control room. On PC 1 the control software *NI LabView* is utilized to monitor and adjust all relevant operating parameters during experiments. The acoustic excitation via loudspeakers (Exc. A and Exc. B) is selected by specifying a harmonic excitation signal in *NI LabView*, consisting of the loudspeaker voltage and frequency. The loudspeaker amplifier provides the excitation signal

for the corresponding loudspeakers, e.g. Exc. A and Exc. B.

The raw dynamic pressure data of the PCBs, as well as the raw PMT chemiluminescence signals, are recorded with two synchronized high-frequency measurement cards *NI PCI-4472*, mounted inside PC 1. In addition, the high-speed camera record signal and the intensifier duty cycle, necessary for phase-locked imaging, are guided to the high-frequency measurement card. The high-speed camera and the intensifier are synchronized by sending a trigger signal (TTL) from the camera to the intensifier. The high-speed camera is adjusted and monitored through the software *Photron FASTCAM Viewer 4* on PC 2, where also the high-speed images are stored.

4.2 Chemiluminescence Measurements

Heat release and heat release fluctuations are often quantified by measuring the flame's chemiluminescence during combustion experiments (cf. 2.3). In the current work, two different optical measurement devices are used: photomultiplier tubes (PMT array) and a high-speed camera with image intensifier (HS-camera), both illustrated in Fig.3.15 and Fig. 4.1. The former device is only capable of measuring the zero-dimensional global chemiluminescence, whereas the latter one records two-dimensional images. Both devices can be equipped with various bandpass filters to isolate certain wavelengths of the flame's emission spectrum. The most dominant chemiluminescence emitters in hydrocarbon flames, e.g. kerosene, are OH^* , CH^* , C_2^* and CO_2^* [64, 66].

4.2.1 Global Chemiluminescence

The chemiluminescence emitted from the flame is observed through a bandpass filter, which transmits only a small part of the incident light, corresponding to the bandpass filter specifications. The photomultiplier tube collects the transmitted light on a photocathode, where the light is converted into photoelectrons. The photoelectrons are directed to an electron multiplier, which increases the amount of photoelectrons and therefore amplifies the electric signal [85]. The electric signal can then be measured and used for further data processing during data evaluation.

For the current work, a PMT array is utilized, consisting of four PMTs (*Hama-*

Table 4.1: Radicals and corresponding bandpass filter specifications.

Radical	Wavelength [nm]	FWHM [nm]
OH* + (CO ₂ *)	308	10
CH* + (CO ₂ *)	430	10
C ₂ * + (CO ₂ *)	510	10
CO ₂ *	405	10

matsu H5784 Series) equipped with four different bandpass filters.

Table 4.1 lists the wavelength and full width at half maximum (FWHM) of the bandpass filters mounted on the PMTs. The wavelength of each bandpass filter is shown in Tab. 4.1 and corresponds to the emission wavelength of a certain combustion radical (cf. 2.3). OH*, CH* and C₂* are diatomic radicals and consequently emit light only in distinct narrow bands. In contrary, CO₂* has a broadband emission spectrum and is therefore superimposed to the diatomic radicals as background radiation. In the current study the subtraction of CO₂* from OH*, CH* and C₂* is not performed, which is indicated by +(CO₂*) in Tab. 4.1.

The data acquisition for the PMT signals was performed with a sample frequency of $f_s = 65536$ 1/s.

For the steady measurements 2621440 samples (measurement time of $t_s = 40$ s) were collected with the high frequency measurement card (*NI PCI-4472*). The value for the mean intensity \bar{I} of the corresponding radical was subsequently obtained by averaging the time series of the PMT signal.

During experiments with acoustic excitation the same number of PMT samples was stored as for the PCB data, which corresponds to 524288 samples ($t_s = 8$ s) per excitation frequency and excitation location, e.g. up- or downstream. Again, the mean intensity \bar{I} is obtained by averaging the time series of the PMT signal for each excitation frequency, while the fluctuating intensity signal I' of the corresponding excitation frequency is obtained by performing a Fast-Fourier-Transform (FFT) for each PMT.

Figure 4.2 shows a photo of the PMT setup for the primary zone measurements. The PMT array including the bandpass filters is mounted on a tripod and arranged perpendicular to the combustion chamber of the primary zone. Additionally, a simple cardboard duct was attached to the PMT array, restrict-

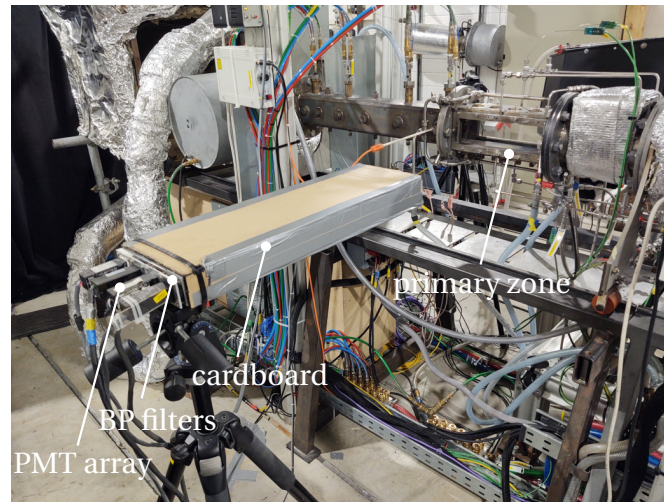


Figure 4.2: Photo of the PMT array setup for the primary zone measurements.

ing the field of view. This avoids glowing or reflecting parts of the test rig being inside the optical path and therefore distorting the measurement of the flame's chemiluminescence. To ensure that each field of view of the PMTs is restricted to the combustion chamber only, a simple candle or lighter was used. The candle was moved in front of the combustion chamber until the PMT amplifier gave an overload signal. This procedure is performed for each PMT one at a time using the maximum gain to ensure triggering of the overload signal.

4.2.2 Planar Line-of-Sight Chemiluminescence

The setup for the two-dimensional imaging consists of a high-speed camera (*Photron FastCam SAX*), an image intensifier (*Hamamatsu C10880-03F*), and a bandpass filter mounted on a camera lens (*Nikon NIKKOR 105mm*). The high-speed camera (HS-Cam) uses a highly light-sensitive CMOS camera chip to capture images with a large number of frames per second (fps). Especially for OH^* , which is in the ultraviolet, an additional image intensifier is needed, as the sensitivity of the CMOS camera chip is too small for the incident OH^* -chemiluminescence. The image intensifier collects the incoming light from the bandpass filter and converts it into an electrical signal via

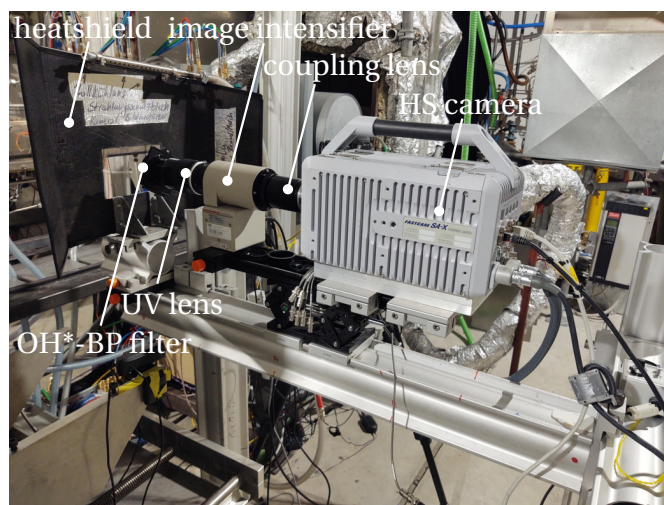


Figure 4.3: Photo of the high-speed imaging setup for the primary zone measurements.

a photocathode. Subsequently, a microchannel plate amplifies the electrical signal, which is then converted back into light on a phosphor screen and directed to the high-speed camera via a coupling lens. The high-speed camera is oriented perpendicular to the combustion chamber, thus imaging the line-of-sight (LoS) chemiluminescence of the flame. For the present work the OH^* -filter of Tab. 4.1 was used for steady and unsteady measurements, while for some steady operating points the CH^* -filter was mounted on the camera lens. Figure 4.3 shows a photo of the high-speed imaging setup in the laboratory. Between the bandpass filter and the combustion chamber, a heatshield with impingement cooling was installed, which protects the temperature-sensitive camera and intensifier from heat radiation of the test rig and the flame.

The high-speed camera and the image intensifier are synchronized via a BNC cable, sending the trigger signal (TTL) of the camera's shutter to the intensifier (cf. Fig. 4.1). To correlate the images taken during acoustic excitation to the data of the dynamic pressure sensors, additional signals from the camera and intensifier are recorded. The record signal of the camera (REC) indicates the point in time when the camera starts the overall image saving process. The intensifier duty cycle signal provides the information when the intensifier is

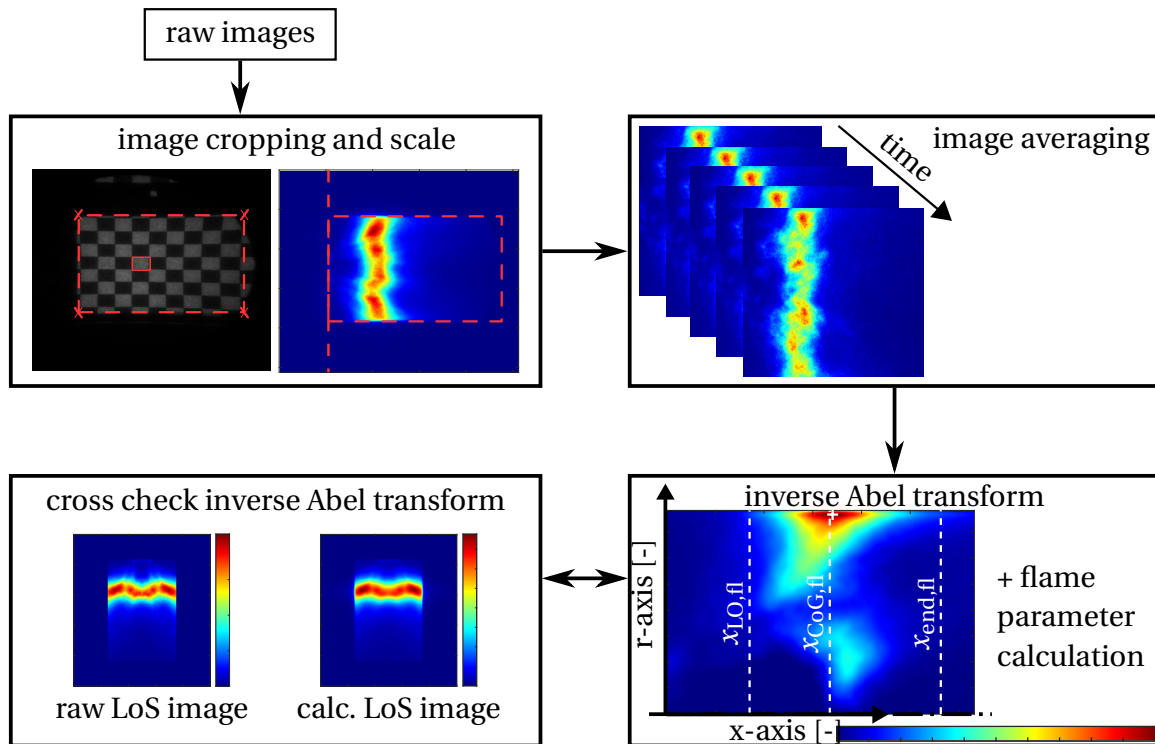


Figure 4.4: Evaluation process of the high-speed imaging data for steady and unsteady measurements.

exposing and therefore an image is stored. As all high-frequency signals are recorded synchronously with the high-frequency measurement cards *NI PCI-4472*, including the camera and intensifier signals, each image can be assigned to the corresponding dynamic pressure signal in time. A total of 8000 frames with a frame rate of 8000 frames per second (fps) were collected for a given operating point for steady and unsteady flame imaging.

Figure 4.4 illustrates the basic evaluation process for the raw high-speed camera images. For steady and unsteady measurements, the raw images are processed in *Matlab*, starting with cropping the relevant area of the image. In addition, a scale is assigned, which is obtained from a reference image with a checkerboard pattern and known scale.

The images of the steady measurements are subsequently averaged and symmetrized. Assuming that the flame is rotationally symmetric, an inverse Abel transformation can be performed to obtain a center cut of the flame's chemiluminescence. This step is performed by using the BASEX algorithm [86, 87].

In the last step the geometrical flame shape parameters can be calculated from the averaged and Abel-transformed image. In the present study, the lift-off height $x_{LO,fl}$, the flame length $x_{end,fl} - x_{LO,fl}$ and the center of gravity $x_{CoG,fl}$ of the flame are the most relevant parameters. The lift-off height and flame length are calculated with the help of a threshold value for the intensity of $Th = 0.18$. The lift-off height or flame start $x_{LO,fl}$ corresponds to the axial distance at which 5 pixels in a row along the symmetry axis are above the threshold. Analogously, the axial end of the flame $x_{end,fl}$ corresponds to the distance at which 5 pixels in a row are below the threshold Th . Subtracting the flame end $x_{fl,end}$ from the flame lift-off $x_{LO,fl}$ results in the flame length. The location of the center of gravity $x_{CoG,fl}$ along the symmetry axis is calculated according to equation 4.1:

$$x_{CoG,fl} = \frac{\sum_{i=1}^{x_{max}} \left(x_i \sum_{j=1}^{r_{max}} I_{ij} \right)}{\sum_{i=1}^{x_{max}} \sum_{j=1}^{r_{max}} I_{ij}}. \quad (4.1)$$

In Eq. 4.1 x_i is the axial distance and I_{ij} the intensity in axial (index i) and radial (index j) direction of the corresponding pixel. The center of gravity is usually a good indicator for the location of the main heat release zone. Details of the center of gravity calculation can be found in [68, 70].

4.3 Thermoacoustic Measurements

The thermoacoustic behavior of the flame is most commonly described by flame transfer functions (FTF). The quantification of the flame dynamics in terms of FTFs can be carried out using various measurement techniques. In the following, the purely acoustic multi-microphone method (MMM) and an optical method, using the global chemiluminescence of the flame, will be described. Figures 3.15 and 4.1 give an overview of the measurement devices and the data routing for FTF measurements.

4.3.1 Operating Points

The research on the isolated primary zone carried out was based on pairs of equivalence ratios with a similar adiabatic flame temperature $T_{ad,PZ}$ for both,

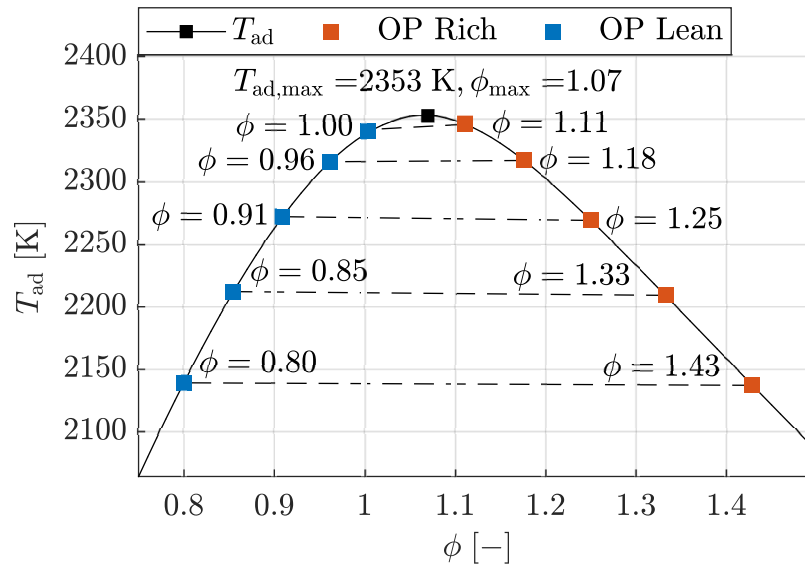


Figure 4.5: Adiabatic flame temperature for a kerosene surrogate (black line) and equivalence ratios for the operating points in the primary zone (red and blue squares).

rich and lean combustion. This should largely reduce the thermoacoustic effects caused by different flame temperatures when comparing two operating points in the rich and lean range. This effect originates from the flame temperature T_h present in Eq. 2.59.

Figure 4.5 displays the adiabatic flame temperature in relation to the equivalence ratio (black line). The horizontal dashed black lines indicate the pairs of operating points for rich (red squares) and lean (blue squares) combustion with a similar adiabatic flame temperature. Thermodynamic equilibrium conditions and Dagaut's mechanism for a kerosene surrogate were used in *Cantera* for the calculation of the operating points. The pressure loss across the burner was kept constant at $\Delta p_{a,PZ}/p_{a,PZ} \approx 4\%$ and the preheating temperature for both combustion chambers was adjusted to $T_{a,PZ} = 423\text{K}$. The adjustment of the different operating points was performed by varying the fuel mass flow $\dot{m}_{f,PZ}$ in the primary zone ($0.65\text{g/s} < \dot{m}_{f,PZ} < 1.16\text{g/s}$). The chosen operating points are similar to idle and sub-idle conditions of real aero engines. It should be mentioned that the non-premixed kerosene flame in the primary zone shows a mostly soot-free behavior in the examined operating range. However, at equivalence ratios of $\phi_{PZ} = 1.33$ and $\phi_{PZ} = 1.43$, soot pro-

duction can be seen with the naked eye.

4.3.2 Acoustic Method

For the test rig configuration in Fig. 3.15, the isolated primary zone can be treated as an acoustic two-port between two impedance measurement ducts (supply and transition duct). Acoustic two-ports can be described by transfer matrices \mathbf{TM}^{pu} , relating the acoustic variables p' and u' up- and downstream of the element according to Eq. 4.2 (cf. 2.1.4):

$$\begin{pmatrix} \frac{p'}{\rho c} \\ u' \end{pmatrix}_{\text{DS}} = \underbrace{\begin{pmatrix} TM_{11} & TM_{12} \\ TM_{21} & TM_{22} \end{pmatrix}}_{\mathbf{TM}^{\text{pu}}} \cdot \begin{pmatrix} \frac{p'}{\rho c} \\ u' \end{pmatrix}_{\text{US}}. \quad (4.2)$$

The multimicrophone method (MMM) is a common technique for characterizing acoustic two-ports by determining the four unknown elements of the transfer matrix in Eq.4.2 [53, 54, 88, 89]. The working principle for the application of the MMM is depicted for an acoustic two-port in Fig. 4.6.

Three basic steps are required for the determination of the four TM elements. First, the measurement of the dynamic pressure $p'(x_i, t)$ on several locations x_i along the impedance measurement ducts. Second, the reconstruction of the acoustic wavefield in each impedance measurement duct using the solution for the convective wave equation and the Riemann invariants (Eq. 2.25 and 2.27). Third, the calculation of the acoustic variables on a specific

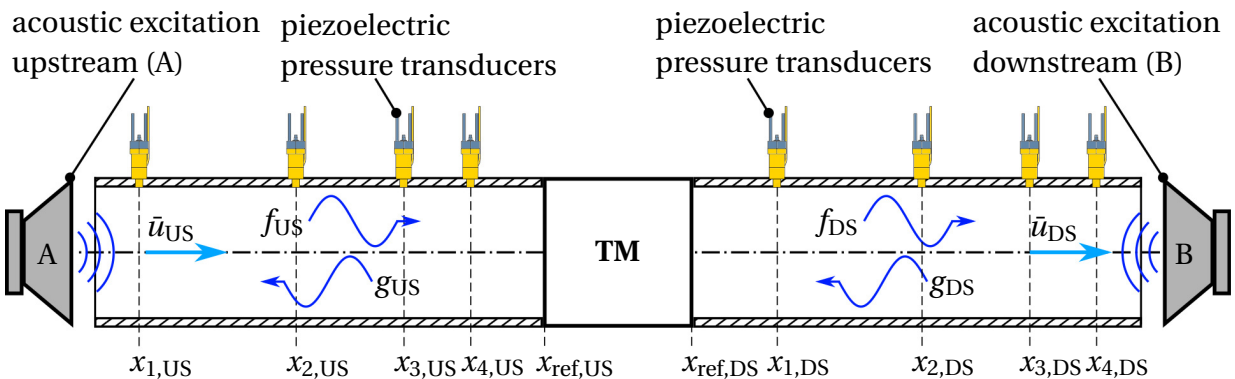


Figure 4.6: Working principle of the multimicrophone method (MMM) for the determination of acoustic transfer matrices.

reference location up- and downstream of the acoustic element, allowing to determine the transfer behavior between the chosen reference planes, e.g. $x_{\text{ref,US}}$ and $x_{\text{ref,DS}}$.

All three steps have to be performed twice for two independent test states to solve for the four unknown elements of the transfer matrix. The two-source method is one possibility and is based on the excitation from two different locations, giving two independent test states. For the primary zone setup an excitation from upstream (excitation A) and downstream (excitation B) is chosen and realized via loudspeakers. The excitation is performed in an alternating manner per excitation frequency, i.e. excitation from upstream (US) followed by excitation from downstream (DS) and subsequently proceeding to the next excitation frequency.

Dynamic Pressure Measurement: The dynamic pressure $p'(x_i, t)$ has to be measured at a minimum of three axial positions x_i along each impedance measurement duct by using piezoelectric pressure transducers *Synotech PCB 106B* mounted in *PCB 064B06* water-cooled adaptors. The sensors convert the piezoelectric high-impedance signal into a low-impedance voltage inside the sensors housing. For the primary zone setup, four PCB sensors ($N_{\text{PCB}} = 4$) are located each, up- and downstream of the combustion chamber. With this PCB setup, one backup PCB is available per impedance measurement duct. The sensors are arranged non-equidistantly to avoid half of the acoustic wavelength lying within one of the sensor distances. Details of the acoustic design can be found in section 3.1.5.

The sample frequency for the data acquisition of the dynamic pressures was adjusted to $n_s = 65536$ with a total of 524288 samples per excitation frequency ($t_s = 8$ s) and a frequency step size of $\Delta f = 10$ Hz. Subsequently, the measured time series signal of the dynamic pressure $p'(x_i, t)$ is Fast-Fourier-Transformed (FFT), resulting in the complex-valued dynamic pressure $\tilde{p}(x_i, \omega)$ at the corresponding sensor location x_i . Most commonly, the complex-valued dynamic pressure is expressed in terms of amplitude $|\tilde{p}(x_i, \omega)|$ and phase $\varphi(x_i, \omega)$ according to Eq. 4.3:

$$\tilde{p}(x_i, \omega) = |\tilde{p}(x_i, \omega)| e^{i\varphi(x_i, \omega)}. \quad (4.3)$$

In addition, the complex-valued dynamic pressure of every sensor $\tilde{p}(x_i, \omega)$ is

calibrated with the corresponding calibration curve. The calibration curves for each sensor are obtained from a measurement with a calibration unit, comparing the amplitude and phase of the sensor to be calibrated with a well-defined calibration sensor for each excitation frequency.

Acoustic Wavefield Reconstruction: The reconstruction of the acoustic wavefield in each impedance measurement duct is based on the Riemann invariants f and g , which can be interpreted as two waves traveling in up- and downstream direction (cf. 2.1). The complex-valued Riemann invariants \tilde{f} and \tilde{g} are related to the complex-valued acoustic pressure \tilde{p} according to Eq. 4.4:

$$\tilde{p}(x_i, \omega) = \bar{\rho} c \left[\tilde{f}(\omega) e^{-ik^+ x_i} + \tilde{g}(\omega) e^{ik^- x_i} \right]. \quad (4.4)$$

In Eq. 4.4 $\bar{\rho}$ is the mean density, c the speed of sound, and x_i the sensor positions along each impedance measurement duct. k is the wave number without mean flow, whereas k^+ and k^- are the convective wave numbers in positive and negative flow direction, given in Eq. 2.28. The mean density $\bar{\rho}$ and speed of sound c (characteristic impedance of the medium) can be expressed using the ideal gas law for isentropic flows with Eq. 4.5:

$$\bar{\rho} c = \bar{p} \sqrt{\frac{\gamma}{R\bar{T}}}. \quad (4.5)$$

In Eq. 4.5 \bar{p} is the static pressure, γ the isentropic exponent, R the specific gas constant and \bar{T} the static temperature of the gas.

Inside the upstream duct (supply duct) only air is present, resulting in a specific gas constant of $R = 287 \text{ J/kgK}$ and an isentropic exponent of $\gamma = 1.4$. The temperature of the preheated air in the upstream duct is measured with three thermocouples, located at the first position of a PCB ($T_{1,SD}$) and the last position of a PCB ($T_{2,SD}$) of the supply duct, as well as at the injector entrance $T_{\text{Inj,PZ}}$ (see Fig. 4.1). For each excitation frequency and excitation location, all temperatures, mass flows, and pressures are measured and stored once. Taking the mean value of all three thermocouples and the mean value of the static pressure upstream over all excitation frequencies, Eq. 4.5 can be determined. For the downstream duct the determination of density and speed of sound depends on the presence of the flame in the primary zone.

In contrary to the upstream duct, the downstream duct (transition duct) has

four thermocouples located at the same position as the four PCBs, which measure the fluid temperature. Additionally, four thermocouples are welded to the outer wall of the transition duct, again located at the same position as the PCBs (cf. Fig. 4.1). For cold measurements without flame in the primary zone, the procedure for determining density and speed of sound is analogous to that of the supply duct. During measurements with flame, the isentropic exponent γ and the specific gas constant R are calculated according to the thermodynamic equilibrium gas composition of the corresponding operating point. Furthermore, the measured hot gas temperatures are corrected, which is described in section 4.3.

With a minimum of three axial measurement positions of the dynamic pressure $\tilde{p}(x_i, \omega)$ an overdetermined equation system for the two unknowns $\tilde{f}(\omega)$ and $\tilde{g}(\omega)$ is obtained, given in Eq. 4.6:

$$\underbrace{\begin{pmatrix} \tilde{p}(x_1, \omega) \\ \cdot \\ \cdot \\ \tilde{p}(x_{N_{\text{PCB}}}, \omega) \end{pmatrix}}_{\mathbf{b}}^{\text{A/B}} = \underbrace{\begin{pmatrix} e^{-ik^+ x_1} & e^{ik^- x_1} \\ \cdot & \cdot \\ \cdot & \cdot \\ e^{-ik^+ x_{N_{\text{PCB}}}} & e^{ik^- x_{N_{\text{PCB}}}} \end{pmatrix}}_{\mathbf{H}} \cdot \underbrace{\begin{pmatrix} \tilde{f}(\omega) \\ \tilde{g}(\omega) \end{pmatrix}}_{\mathbf{x}}^{\text{A/B}}_{\text{US/DS}}. \quad (4.6)$$

The equation system must be solved for each impedance measurement duct, indicated as upstream (US) and downstream (DS), each excitation frequency ω and excitation location, indicated as A and B. A minimum-normal least-squares algorithm in *Matlab* is used for solving the overdetermined equation system of Eq. 4.6 [90].

Knowing $\tilde{f}(\omega)$ and $\tilde{g}(\omega)$ the complex-valued acoustic velocity fluctuation can be calculated at each PCB position using Eq. 4.7:

$$\tilde{u}(x_i, \omega) = \tilde{f}(\omega)e^{-ik^+ x_i} - \tilde{g}(\omega)e^{ik^- x_i}. \quad (4.7)$$

Calculation of TM-Elements: With the determination of $\tilde{p}(x_i, \omega)$ and $\tilde{u}(x_i, \omega)$ for each impedance measurement duct, the acoustic variables at every reference location up- and downstream of the acoustic element $x_{\text{ref,US/DS}}$ can be calculated. In the present work, the burner outlet plane x_{BO} was chosen as reference for the calculation of the acoustic variables for both, the upstream and downstream wavefield. With this approach of choosing the reference plane $x_{\text{ref,US/DS}}$, the transfer matrix does not contain the acoustic transfer behavior

due to straight ducts. Finally, all four complex-valued transfer matrix elements can be obtained by solving the equation system of Eq. 4.6:

$$\begin{pmatrix} \frac{\tilde{p}_A(\omega)}{\rho c} \\ \tilde{u}_A(\omega) \\ \frac{\tilde{p}_B(\omega)}{\rho c} \\ \tilde{u}_B(\omega) \end{pmatrix}_{x_{BO}} = \begin{pmatrix} \frac{\tilde{p}_A(\omega)}{\rho c} & \tilde{u}_A(\omega) & 0 & 0 \\ 0 & 0 & \frac{\tilde{p}_A(\omega)}{\rho c} & \tilde{u}_A(\omega) \\ \frac{\tilde{p}_B(\omega)}{\rho c} & \tilde{u}_B(\omega) & 0 & 0 \\ 0 & 0 & \frac{\tilde{p}_B(\omega)}{\rho c} & \tilde{u}_B(\omega) \end{pmatrix}_{x_{BO}} \cdot \begin{pmatrix} TM_{11} \\ TM_{12} \\ TM_{21} \\ TM_{22} \end{pmatrix}. \quad (4.8)$$

To obtain the transfer behavior of the flame only, the procedure of determining the transfer matrix elements described above has to be performed for each operating point with and without flame. The measurements without flame, also referred to as 'cold' conditions, are giving the burner transfer matrix (BTM), whereas the 'hot' measurements with flame are resulting in the burner and flame transfer matrix (BFTM). With the assumption that the burner transfer behavior is the same for hot and cold operating conditions [55], the flame transfer matrix (FTM) can be obtained according to Eq. 4.9:

$$\mathbf{FTM} = \mathbf{BFTM} \cdot \mathbf{BTM}^{-1}. \quad (4.9)$$

During BFTM measurements the relative velocity fluctuation at the burner outlet u'_{BO}/\bar{u} is an important parameter to ensure that the flame dynamics is linear. Due to this, the relative velocity fluctuation u'_{BO}/\bar{u} was kept at a nearly constant level of 15% for each excitation frequency during hot measurements in isolated primary zone. To prove whether the flame is in the linear regime, the electric power for the loudspeakers was reduced to 75% and 50%. This resulted in nearly identical flame transfer functions. For the cold measurements of the BTM the relative velocity fluctuation was further increased to approx. 30 % for the purpose of a higher signal-to-noise ratio, which increases the quality of the acoustic wavefield reconstruction.

Calculation of Flame Transfer Functions: The determination of the flame transfer function (FTF) is performed by using the Rankine-Hugoniot relations (RH), valid for acoustically compact flames ($He \ll 1$) (cf. 2.2.2). The RH-relations assume the flame as a compact temperature jump, as described in section 2.2. Assuming small Mach numbers ($Ma \ll 1$) the FTF is only contained in the FTM_{22} -element, according to Eq. 4.10:

$$FTF_{\text{RH}} = \frac{FTM_{22} - 1}{\frac{T_h}{T_c} - 1}. \quad (4.10)$$

T_c and T_h are the cold and hot gas temperatures before and after the temperature jump, respectively. For the present investigations T_c was assumed to be the mean preheating temperature, used for Eq. 4.5. The hot gas temperature T_h corresponds to the temperature of the flame and is usually difficult to quantify. Therefore, the temperature of the hot gas or flame temperature was assumed to be the adiabatic flame temperature T_{ad} , corresponding to the thermodynamic equilibrium conditions of each operating point. Due to this, it is assumed that the total amount of primary air is mixed with the fuel of the corresponding operating point. For operating points with the same pressure drop in the primary zone, as well as constant impingement cooling on the outer wall of the chamber, the heat loss of the combustion chamber is similar. Due to this, the adiabatic flame temperature T_{ad} and the flame temperature T_h must have roughly the same trend.

Figure 4.7 shows a comparison between the adiabatic flame temperature and the measured corrected temperature on the first PCB position downstream

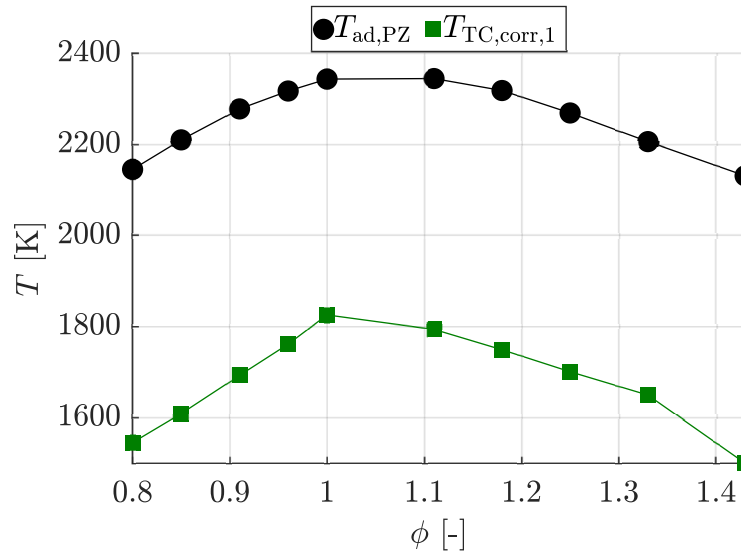


Figure 4.7: Comparison of the calculated adiabatic flame temperatures $T_{\text{ad,PZ}}$ and measured corrected hot gas temperatures $T_{\text{TC,corr,1}}$ at the first thermocouple position downstream the primary zone.

the primary zone (*Type S* thermocouple, cf. Fig. 4.1) for the operating points given in section 4.3.1. The plot confirms that the measured hot gas temperature follows the trend of the adiabatic flame temperature very well. The fuel-richest operating point ($\phi = 1.43$) behaves differently due to the higher soot production, which was observed with the naked eye. Consequently, a higher thermal loss in the combustion chamber occurs due to the high emissivity of soot leading to a larger difference between adiabatic and corrected thermocouple temperature in Fig. 4.7.

4.3.3 Optical Method

The optical method is based on the representation of heat release \bar{Q} and heat release fluctuations \dot{Q}' through the chemiluminescence of the flame [68,70,91]. The zero-dimensional measurement of the chemiluminescence from OH^* , CH^* , C_2^* , and CO_2^* and the corresponding evaluation for the steady \bar{I} and unsteady I' light intensity are described in section 4.2. Assuming that the chemiluminescences is suitable for representing heat release a hybrid flame transfer function can be formulated, given in Eq. 4.11:

$$FTF_{\text{hyb}} = \frac{I'}{\bar{I}} \frac{\bar{u}_{\text{BO}}}{u'_{\text{BO}}}. \quad (4.11)$$

The mean velocity \bar{u}_{BO} and the acoustic velocity fluctuation u'_{BO} for the hybrid FTF are calculated at the burner exit plane. The velocity fluctuation at the burner outlet u'_{BO} is obtained by using the reconstructed acoustic wavefield upstream the burner during hot measurements ($\tilde{p}'_{\text{BO,US}}$ and $\tilde{u}'_{\text{BO,US}}$) and the cold BTM, according to Eq. 4.12:

$$\tilde{u}'_{\text{BO,DS}} = BTM_{21} \cdot \frac{\tilde{p}'_{\text{BO,US}}}{\bar{\rho}c} + BTM_{22} \cdot \tilde{u}'_{\text{BO,US}}. \quad (4.12)$$

Due to the fact that the hybrid FTF uses the acoustic wavefield during hot measurements and the BTM, the optical method is not fully independent from the acoustic method. However, the hybrid FTF can be used as a cross-check whether the acoustic and optical FTFs show similar trends.

4.3.4 Optimization of Acoustic Wavefield Reconstruction

Two methods for further increasing the quality of acoustic wavefield reconstruction are explained below. First, the temperature correction method for the hot gas temperatures inside the transition duct downstream the primary zone will be explained. Second, the selection of the dynamic pressure sensor configuration used for the reconstruction procedure will be explained.

Temperature Correction: In Eqs. 4.4 and 4.5 it is shown, that the reconstruction of the acoustic wavefield depends on density and speed of sound and, hence, on the temperature along the impedance measurement ducts. Especially for the transition duct downstream the primary combustion chamber, high hot gas temperatures are present due to the near stoichiometric operating points. The high temperatures are causing a substantial heat loss of the thermocouples due to radiation to the colder duct inner wall, which further leads to too low measured gas temperatures. The presented correction method is based on a convective-radiative heat balance of a small thermocouple in a large environment. The corrected or 'true' temperature can be obtained from the convective-radiative heat balance according to Eq. 4.13:

$$T_{\text{TC,corr}} = T_{\text{TC}} + \frac{\varepsilon_{\text{TC}}\sigma}{\alpha_{\text{TC,conv}}} (T_{\text{TC}}^4 - T_{\text{w,i}}^4) \quad (4.13)$$

In Eq. 4.13 T_{TC} is the measured thermocouple temperature, ε_{TC} the emissivity of the thermocouple, $\sigma = 5.67 \times 10^{-8} \text{ W/m}^2/\text{K}^4$ the Boltzmann constant, α_{TC} the convective heat transfer coefficient of the thermocouple, and $T_{\text{w,i}}$ the inner wall temperature.

The transition duct is equipped with four thermocouples measuring the hot gas temperature T_{TC} at each location of the four PCBs (cf. 3.2). At the first position, closest to the combustion chamber, a thermocouple of *Type S* is used, while the remaining three are sheath thermocouples of *Type N*. At the same positions, four sheath thermocouples of *Type N* are welded to the outer wall of the transition duct, measuring $T_{\text{w,o}}$.

The temperature dependence of the emissivity of the different thermocouples was calculated according to different sources from the literature. *Type S* thermocouples consist of a Pt-PtRh pairing, which can withstand temperatures up to 1873 K. The temperature-dependent emissivity of the Pt-PtRh pairing

was found in [92]. The exact material specification of the *Type N* thermocouple's sheath is not disclosed by the manufacturer. However, it is known that the sheath consists of a special nickel-based alloy, resistant to oxidation up to temperatures of 1500K. To approximate the sheath material of the *Type N* thermocouples, the temperature depending emissivity of *Inconel 617* was taken [93]. Other temperature-dependent emissivities of nickel-based alloys were also tested, but mostly provided unrealistic temperature profiles along the transition duct.

The convective heat transfer coefficient $\alpha_{TC,conv}$ was calculated using a Nusselt correlation for cylinders in a cross flow [77].

The inner wall temperature can be obtained by assuming thermal equilibrium between the wall conduction and the gas convection on the inside, according to Eq. 4.14:

$$\frac{\lambda_w}{s_w} (T_{w,i} - T_{w,o}) = \alpha_i A_i (T_{TC,corr} - T_{w,i}). \quad (4.14)$$

λ_w is the thermal conductivity of the high-temperature steel 1.4841 used for the transition duct [77], $s_w = 10$ mm the wall thickness of the transition duct, α_i the heat transfer coefficient on the inner wall, and A_i the surface of the inner wall of the transition duct.

Figure 4.8 shows the measured T_{TC} (red diamonds) and corrected $T_{TC,corr}$

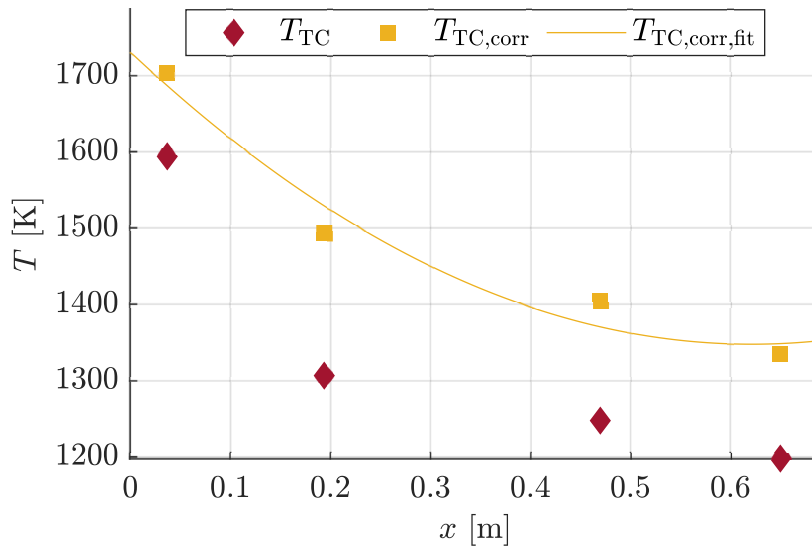


Figure 4.8: Measured T_{TC} and corrected $T_{TC,corr}$ temperatures along the transition duct.

(orange squares) temperatures along the transition duct for an operating point with an equivalence ratio of $\lambda_{PZ} = 1.25$. In addition, a polynomial fit for the corrected gas temperature $T_{TC,corr,fit}$ (solid, orange line) is provided. Due to the fact that the first thermocouple is of *Type S* and consequently has a much lower emissivity, the ratio of the corrected to the measured temperature is much smaller than for the remaining three of *Type N*.

The mean value of the four corrected thermocouple temperatures in the transition duct is inserted in Eq. 4.5 and considered during the acoustic wavefield reconstruction. To prove whether the temperature correction improves the acoustic wavefield reconstruction, the residuum in the transition duct was checked according to Eq. 4.15. Especially for higher frequencies, a slight improvement in the reconstruction error was observed, indicating that the temperature correction method was performed properly.

Selection of Dynamic Pressure Sensors and Error Criteria: The primary zone configuration uses each, four piezodynamic pressure transducers (PCB) upstream (supply duct) and downstream (transition duct) the combustion chamber (cf. 3.15). The reconstruction of the acoustic wavefield is based on a minimum of three sensors for each impedance measurement duct. Due to this, a selection of three out of four PCBs for each measurement duct can be performed. Table 4.2 gives all possible selection possibilities for an impedance measurement duct equipped with four PCBs.

Table 4.2: Selection possibilities for the acoustic wavefield reconstruction using four PCBs per impedance measurement duct.

Comb.	PCB 1	PCB 2	PCB 3	PCB 4
1	x	x	x	x
2	x	x	x	-
3	x	x	-	x
4	x	-	x	x
5	-	x	x	x

To prove which combination of PCB sensors gives the best results, an error criterion for the acoustic wavefield reconstruction has to be defined. The deviation between the dynamic pressure values of the reconstructed wavefield

and the measured values at the same position can be formulated according to Eq. 4.15 [94]:

$$\epsilon_{\text{US/DS}}^{\text{A/B}}(\omega) = \frac{\|(\mathbf{I}^n - \mathbf{H}\mathbf{H}^\dagger)\mathbf{b}\|_2}{\|\mathbf{b}\|_2}. \quad (4.15)$$

In Eq. 4.15, \mathbf{b} is the vector of the measured Fourier transformed complex dynamic pressures $\tilde{p}(x_i, \omega)$ and \mathbf{H} the coefficient matrix of \tilde{f} and \tilde{g} (cf. Eq. 4.6). The matrix \mathbf{H}^\dagger refers to the Moore-Penrose pseudoinverse of matrix \mathbf{H} . The matrix \mathbf{I}^n corresponds to the identity matrix of size $n \times n$, where n is the number of pressure sensors $n = N_{\text{PCB}}$. The l^2 -norm is denoted by $\|\dots\|_2$. Values for the error measure $\epsilon \leq 5\%$ are a good indicator for a high quality acoustic wave-field reconstruction.

The error measure ϵ is calculated for each possible combination of PCBs (Tab. 4.2), for every impedance measurement duct (e.g. supply and transition duct or up- and downstream), each excitation location (e.g. A and B), and each frequency ω .

The simplest way is to choose an individual PCB combination for each excitation location and each frequency according to the combination with the minimum error measure ϵ , given in Eq. 4.16:

$$\min [\epsilon_{\text{US/DS}}^{\text{A/B}}(\omega)] \rightarrow \text{Comb}_{\text{US/DS}}^{\text{A/B}}(\omega). \quad (4.16)$$

$\text{Comb}_{\text{US/DS}}^{\text{A/B}}(\omega)$ gives the PCB combination with the minimum error for each excitation frequency ω , each excitation location A or B, and for each impedance measurement duct, US or DS.

Another option is to select the combination with the minimum error measure ϵ for each excitation location A or B, but averaged as root-mean-square (rms) over all excitation frequencies ω , according to Eq. 4.17:

$$\min [\text{rms}_{|\forall\omega} (\epsilon_{\text{US/DS}}^{\text{A/B}}(\omega))] \rightarrow \text{Comb}_{\text{US/DS}}^{\text{A/B}}. \quad (4.17)$$

$\text{Comb}_{\text{US/DS}}^{\text{A/B}}$ gives a fixed PCB combination with the minimum error over all excitation frequencies, for each excitation location A or B and for each impedance measurement duct US or DS.

Lastly, the error measure can also be summarized for each excitation location A and B, resulting in Eq. 4.18:

$$\min [\text{rms}|_{\forall \omega} (\epsilon_{\text{US/DS}}^{\text{A+B}}(\omega))] \rightarrow \text{Comb}_{\text{US/DS}}^{\text{A+B}}. \quad (4.18)$$

$\text{Comb}_{\text{US/DS}}^{\text{A+B}}$ gives a fixed PCB combination with the minimum error over all excitation frequencies and all excitation locations A or B, for each impedance measurement duct US or DS.

Averaging the error measure for different impedance measurement ducts, e.g. US and DS, makes no sense, as the acoustic wavefield reconstruction is performed per impedance measurement duct.

The three possibilities for selecting a PCB combination for the reconstruction of the acoustic wavefield were evaluated and compared against the standard case, which is using all four PCBs (Comb. 1 in Tab. 4.2). In theory, using four PCBs should provide more accurate results regarding the acoustic wavefield reconstruction. However, in reality this is not always the case due to measurement uncertainties of the dynamic pressure transducers. In addition, the current PCB selection method automatically excludes damaged sensor from the acoustic evaluation routine in case of malfunction.

Figure 4.9 gives a comparison for the FTF-amplitude (top) and FTF-phase (bottom)

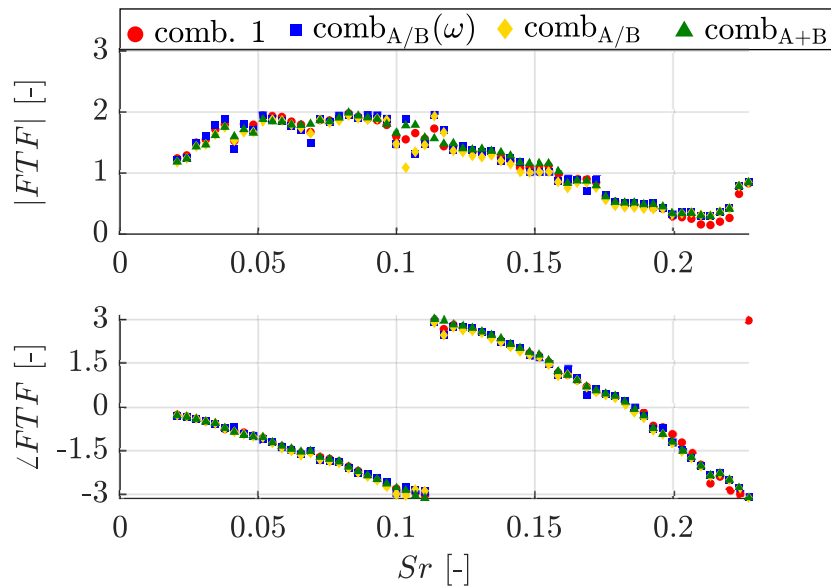


Figure 4.9: FTF amplitudes (top) and phases (bottom) for an operating point with an equivalence ratio of $\phi = 1.18$ and different approaches for the selection of the PCB combination for the acoustic wavefield reconstruction.

(bottom) for an operating point with an equivalence ratio of $\phi = 1.18$ for the different selection procedures of PCB combinations.

For the operating point shown in Fig. 4.9, comb_{A+B} shows the smoothest amplitude and phase, although the differences are very small between the different selection approaches for the PCB combinations. The selection according to Eq. 4.18 in Fig. 4.9 revealed that Comb. 4 for the upstream duct and Comb. 2 for the downstream duct (Tab. 4.2) perform best in terms of the error measure for the FTF presented. During the evaluation of the BTM and BFTM for other operating points, it was observed that the usage of the selection criteria $\text{comb}_{A/B}$ and comb_{A+B} always gave the qualitatively best results. The selection criterion presented was only applied during the measurements for the isolated primary zone. For the compact RQL setup, three PCBs per impedance measurement duct were installed due to the limited number of 12 available sensors for the experimental investigations.

5 Steady Flame Behavior Primary Zone

This chapter elucidates the flame behavior in the primary zone during steady operation. The determination of the rich blow-out (RBO), lean blow-out (LBO), and thermoacoustic stability behavior during commissioning tests is described. The approach for eliminating the self-excited dynamics of the primary zone by altering the acoustic boundary conditions is briefly discussed. The resulting operating range of the test rig is shown in terms of a stability map, and an example of a stable and unstable operating point is given. Next, global chemiluminescence investigations using photomultiplier tubes (PMT) show the dependency of OH^* , CH^* , C_2^* , and CO_2^* on the equivalence ratio and thermal power, without background correction of CO_2^* . Except for C_2^* , all radicals follow the trend of the adiabatic flame temperature. Regarding the measurement of equivalence ratio fluctuations by using the ratio of two radical pairings, CH^*/C_2^* seems to be the most appropriate choice. The last section focuses on the chemiluminescence of the primary zone's flame by comparing OH^* and CH^* images. The resulting flame parameters for both radicals are compared with each other. These serve as input for time delay calculations during thermoacoustic measurements.

5.1 Commissioning Tests and Operation Range

The commissioning tests of the isolated primary zone focus on the determination of rich blow-out (RBO), lean blow-out (LBO), and the maximization of the thermoacoustic stability behavior. The experiments were carried out by varying the thermal power \dot{Q}_{th} or fuel mass flow \dot{m}_{f} , the air mass flow $\dot{m}_{\text{a,PZ}}$, and the preheating temperature $T_{\text{a,PZ}}$. The setup of the test rig is given in Section 3.2. Table 5.1 gives an overview of the parameter range covered in the commissioning tests.

The RBO and LBO limits were detected by observing flame-out during experiments using a digital camera (*Canon EOS M50*) oriented perpendicular to the combustion chamber. For the assessment of whether an operating point is

Table 5.1: Parameter range for the commissioning tests of the isolated primary zone combustion chamber.

Parameter	Unit	Operation Range			
\dot{Q}_{th}	kW	44	\leq	\dot{Q}_{th}	\leq 62
$\dot{m}_{\text{f,PZ}}$	g/s	1	\leq	$\dot{m}_{\text{f,PZ}}$	\leq 1.4
$T_{\text{a,PZ}}$	K	423	\leq	$T_{\text{a,PZ}}$	\leq 523
ϕ_{PZ}	-	0.5	\leq	ϕ_{PZ}	\leq 1.66

stable or not, the dynamic pressure sensors were used to record the acoustic pressure fluctuations along the impedance measurement ducts. The signal of all PCBs was recorded with a sampling frequency of $f_s = 65536$ and a measurement time of $t_s = 1$ s. The raw acoustic pressure signals were fast Fourier transformed and a stability criterion was applied to the normalized acoustic pressure amplitude $|\tilde{p}'|$ according to Eq. 5.1:

$$\frac{|\tilde{p}'|}{\bar{p}} \leq 1\%. \quad (5.1)$$

An operating point was considered to be stable if none of the normalized acoustic pressure peaks were above the given limit in Eq. 5.1. For the remaining unstable operating points, the acoustic boundaries were changed using different perforated metal sheets (see Chapter 3.1.5). The maximum operation windows were finally obtained using a perforated metal sheet with a porosity of 12.4% at the entrance of the upstream and 15.7% at the exit of the downstream loudspeaker segment (cf. Fig. 3.15) resulting in minimal pressure amplitudes. Figure 5.1 illustrates typical normalized acoustic pressure spectra for a stable (top) and an unstable (bottom) operating point against the Strouhal number Sr . Both operating points have a thermal power of $\dot{Q}_{\text{th}} = 56$ kW and a preheating temperature of $T_{\text{a,PZ}} = 473$ K with an equivalence ratio for the stable point of $\phi_{\text{PZ}} = 1.33$ and for the unstable point of $\phi_{\text{PZ}} = 1.11$.

The overall low amplitudes of the stable operating point in Fig. 5.1 exhibit small peaks around a Strouhal number of $Sr \approx 0.04$, $Sr \approx 0.09$, $Sr \approx 0.18$, and $Sr \approx 0.27$, which indicate natural resonances of the test rig driven by the turbulent flame noise and/or natural coherent flow structures (cf. Section 1.3.1). On the contrary, the unstable operating point at the bottom of Fig. 5.1 shows

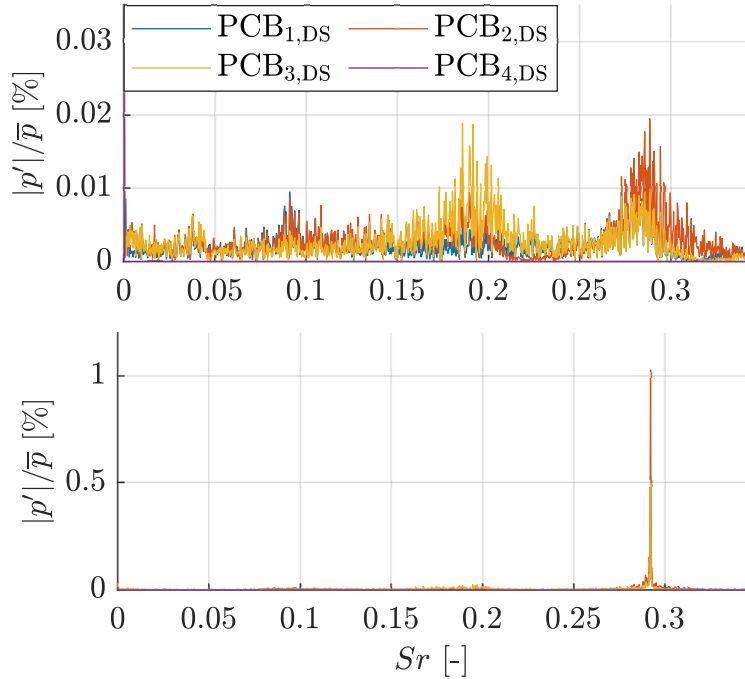


Figure 5.1: Normalized pressure spectra for a thermal power of $\dot{Q}_{th} = 56\text{kW}$ and a preheating temperature of $T_{a,PZ} = 473\text{K}$ for a stable (top) and unstable (bottom) operating point with an equivalence ratio of $\phi_{PZ} = 1.33$ and $\phi_{PZ} = 1.11$, respectively.

a distinct peak at a Strouhal number of approximately $Sr \approx 0.27$, which corresponds to the fourth maximum observed for the stable operating point. For this operating point, the Rayleigh criterion of Eq. 1.1 seems to be satisfied and the damping mechanisms of the overall thermoacoustic system are not strong enough. Other operating points during the commissioning tests showed resonance frequencies similar to those presented in Fig. 5.1.

Figure 5.2 illustrates the stability map obtained for the primary zone for all operating points with a preheating temperature of $T_{a,PZ} = 473\text{K}$. The white area in Fig. 5.2 indicates the ranges of thermal power \dot{Q}_{th} and equivalence ratios ϕ_{PZ} accessible for thermoacoustic measurements using the primary zone setup (cf. Section 3.2). Only one point in the rich combustion regime is unstable, whereas in the lean combustion regime a few unstable points are visible. Consequently, the operating points inside the gray area, color coded by the normalized acoustic pressure fluctuation $|p'|/\bar{p}$, are not usable for thermo-

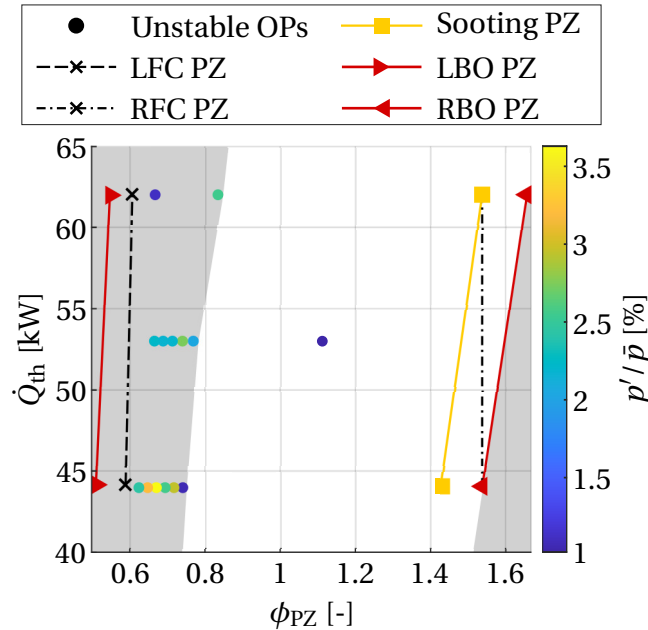


Figure 5.2: Stability map of the primary zone for an air preheating temperature of $T_{a,PZ} = 473$ K.

coustic measurements under acoustic excitation. The yellow line in Fig. 5.2 demonstrates the onset of sooting during rich combustion in the combustion chamber of the primary zone. Additionally, the RBO- and LBO-limits are indicated by the two red lines, as well as the rich-flame- (RFC) and lean-flame-constriction (LFC) limit. The latter two indicate a change in flame shape close to the RBO- and LBO-limit.

The flame shapes observed in the primary zone are illustrated in Fig. 5.3. During normal operation, the conical flame is present in the combustion chamber, which indicates proper vortex breakdown of the swirling flow from the burner. The constricted flame appears only close to the RBO- and LBO-limits and is almost independent of the thermal power due to the two vertical black lines. The lifted flame in Fig. 5.3 occurs right at the RBO and LBO limits and reflects the collapse of the flame speed. During the commissioning test it was observed that the change in flame shape depends not only on the operating points but also on the direction in which the equivalence ratio is changed (hysteresis behavior).



Figure 5.3: Flame shapes in the primary zone for an air preheating temperature of $T_{a,PZ} = 473\text{ K}$ and a thermal power of $\dot{Q}_{th} = 53.2\text{ kW}$. Conical flame (left), constricted flame (middle) and lifted flame (right).

5.2 Global Chemiluminescence

The steady global chemiluminescence study of the flame in the primary zone is carried out by investigating the behavior of different radicals for varying equivalence ratios and thermal powers. The measurements are conducted for the operating points shown in Section 4.3.1, using the setup given in Section 3.2. An additional operating point was added for steady chemiluminescence investigations at $\phi_{PZ} = 1.05$, which is very close to the maximum adiabatic flame temperature at $\phi_{PZ} = 1.07$.

Figure 5.4 shows the normalized chemiluminescence intensity of all four radi-

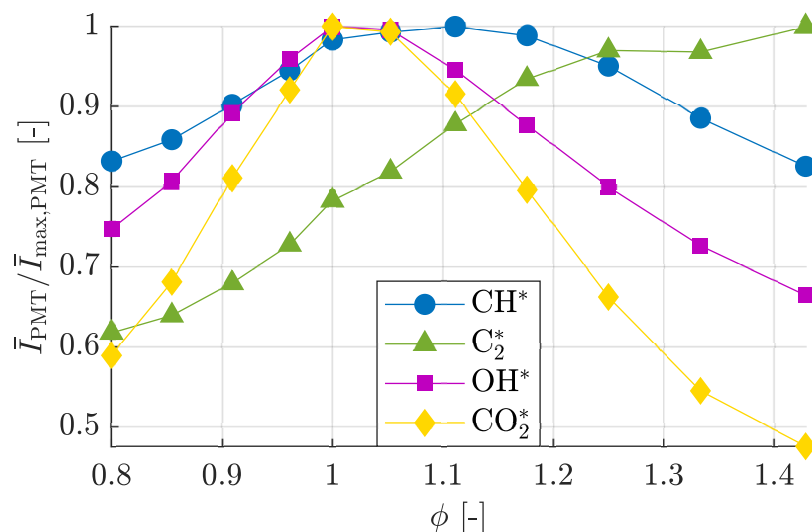


Figure 5.4: Normalized mean PMT chemiluminescence intensity for four different radicals against the equivalence ratio in the primary zone.

icals against the equivalence ratio, obtained with the photomultiplier array (cf. Section 4.2.1). The mean intensity \bar{I}_{PMT} of the different radicals was normalized with the corresponding maximum $\bar{I}_{\text{max,PMT}}$. The color coding is aligned with the respective bandpass filter wavelength except OH^* , which is in the ultraviolet. OH^* , CH^* , and CO_2^* exhibit a global maximum under slightly rich conditions ($\phi_{\text{PZ}} \approx 1.07$). Contrarily, C_2^* exhibits a completely different behavior because of an increasing intensity with increasing equivalence ratio. Due to this, C_2^* seems to be a good indicator for the effective primary zone equivalence ratio when burning hydrocarbon fuels, which was also found in other studies [95].

Under the assumption that the chemiluminescence intensity is strongly dominated by temperature, the intensity of the various radicals should follow the trend of the adiabatic flame temperature. In addition, the operating point pairs with the same adiabatic flame temperature for rich and lean conditions should be on the same intensity level (e.g. $\phi_{\text{PZ}} = 1.25$ and $\phi_{\text{PZ}} = 0.91$). In Fig. 5.4 the maximum intensities for OH^* and CO_2^* coincide very well with the maximum adiabatic flame temperature T_{ad} , while the peak of CH^* is slightly shifted to richer combustion conditions. The intensities of the operating point pairs of the CH^* -radical are on a similar level for rich and lean conditions. In contrast, the intensity of OH^* and CO_2^* is always lower for the operating point under rich conditions, regardless of the adiabatic flame temperature being nearly the same. Surprisingly, a calculation of the unexcited species for thermodynamic equilibrium conditions and a kerosene surrogate in *Cantera* showed good qualitative agreement for OH^* , C_2^* , and CO_2^* .

The optical flame transfer function FTF_{hyb} given in Section 4.3.3 linearly correlates the fluctuation of the normalized chemiluminescence intensity I'/\bar{I} with the fluctuation of the normalized velocity u'/\bar{u} . For this reason, the chemiluminescence intensity must linearly depend on thermal power \dot{Q}_{th} , otherwise optical FTF measurements are prone to errors. The dependence of the radicals' intensity on thermal power is verified by performing measurements with a variation in thermal power of +/-20%.

Figure 5.5 depicts the results for the three thermal powers versus the equivalence ratio. The same equivalence ratios as in Fig. 5.4 were chosen. The solid line corresponds to the baseline operating points, the dashed line to minus 20%, and the dashed-dotted line to plus 20% in thermal power.

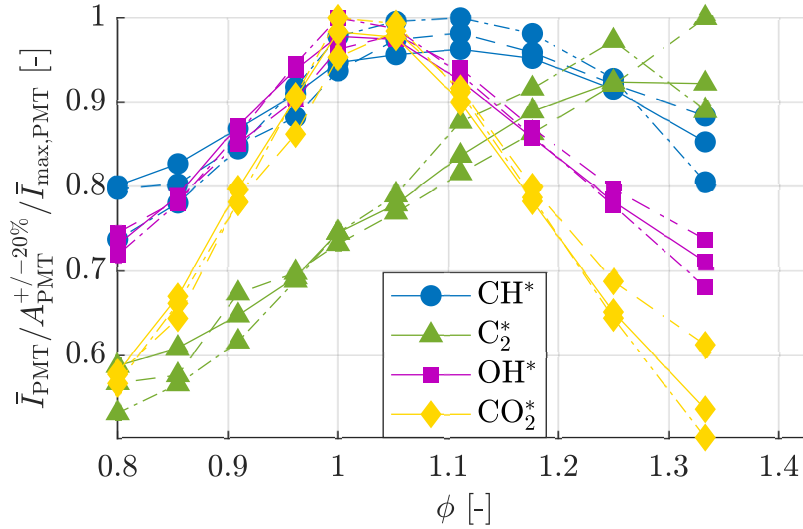


Figure 5.5: Normalized mean PMT chemiluminescence intensity for four different radicals against the equivalence ratio and a variation in thermal power of +/-20%.

A linear regression between the intensities of the baseline points and the points for varying thermal power was performed, resulting in a constant factor $A^{+/-20\%}$ according to Eq. 5.2:

$$A^{+/-20\%} = \frac{\bar{I}_{PMT}^{+/-20\%}}{\bar{I}_{PMT}^{baseline}}. \quad (5.2)$$

The factor $A^{+/-20\%}$ was used to normalize the intensity values given in Fig. 5.5. The values for the coefficient $A^{+/-20\%}$ and the corresponding coefficients of determination R^2 are given in Tab. 5.2. The results in Tab. 5.2 confirm that the chemiluminescence intensity is almost perfectly proportional to thermal power. The small deviations may be due to the varying heat losses of the combustion chamber when altering thermal power. Furthermore, maintaining the equivalence ratio while varying thermal power results in changes in pressure loss across the burner, which in turn affects the turbulence within the flame of the primary zone. For this reason, the emission of light may be suppressed in a nonlinear manner due to collisional quenching or collisions of molecules with each other (cf. Section 2.3). Comparing Fig. 5.4 to Fig. 5.5, the operating points at an equivalence ratio of $\phi_{PZ} = 1.43$ are missing. The reason for this is

Table 5.2: Coefficients of the linear regression between the chemiluminescence intensities of the baseline operating points and operating points with varying thermal power of +/-20%.

Radical	OH*		CH*		C ₂ *		CO ₂ *	
	-20%	+20%	-20%	+20%	-20%	+20%	-20%	+20%
\dot{Q}_{th}								
$A^{+/-20\%}$	0.78	1.206	0.78	1.255	0.808	1.245	0.832	1.221
R^2	0.951	0.982	0.913	0.836	0.946	0.945	0.941	0.992

the high fuel pressure required for higher thermal power, which is beyond the maximum capability of the fuel supply system.

Equivalence ratios and fluctuations are often quantified by using the chemiluminescence intensity ratio of combustion radicals. Especially CH*/OH* and CH*/CO₂* were already applied to perfectly premixed flames [68, 70, 96]. However, for non-premixed fuel-rich and near-stoichiometric kerosene combustion, no suitable radical pairs have been provided yet. To close this knowledge gap, all possible combinations of the investigated radicals were evaluated in the present work. Two essential requirements must be fulfilled by the radical pair as potential measure for equivalence ratios: an independence on thermal power and a monotonic dependence on the equivalence ratio.

In Figs. 5.4 and 5.5 it can be seen that OH*, CH*, and CO₂* show a bell-shaped curve with a maximum around stoichiometric combustion conditions. Calculating ratios using two of these three radicals again results in a bell-shaped curve, which gives two values for the equivalence ratio corresponding to only one value of the intensity ratio. Therefore, the requirement of a monotonic trend over the equivalence ratio is not fulfilled. In contrast, using the C₂* radical for the chemiluminescence ratio appears to be potentially useful. The most promising radical pair was found to be the ratio CH*/C₂*.

Figure 5.6 shows the behavior of CH*/C₂* against the equivalence ratio and a variation in thermal power. The diagram indicates that CH*/C₂* fulfills the requirement of a monotonic trend and a high level of independence on thermal power. This is why this radical pair seems to be well-suited for measuring equivalence ratios and fluctuations for rich and slightly lean combustion conditions. The ratios of OH*/C₂* and CO₂*/C₂* exhibit a distorted bell-shaped

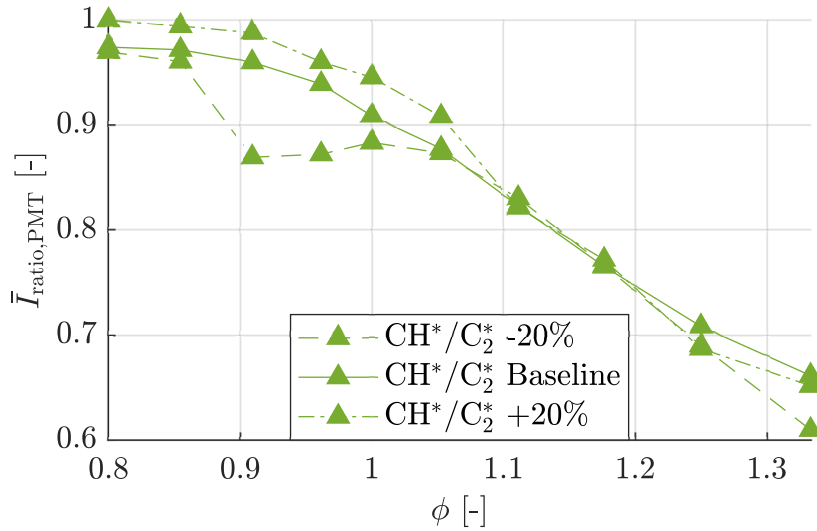


Figure 5.6: Normalized chemiluminescence intensity ratio of CH^*/C_2^* against the equivalence ratio and a variation in thermal power of $\pm 20\%$.

curve against the equivalence ratio and consequently do not show a clear monotonic trend. Therefore, it is concluded that CH^*/C_2^* seems to be an adequate radical pair for measuring equivalence ratios and fluctuations, at least in the equivalence ratio range investigated in this study.

5.3 Chemiluminescence Images

Chemiluminescence images of the steady flame were taken with the band-pass filters for OH^* and CH^* (Tab. 4.1), with the purpose of providing two-dimensional information on the shape of the primary zone's flame. Figure 5.7 depicts the OH^* -chemiluminescence in terms of time-averaged line-of-sight (upper plots) and inverse Abel-transformed (lower plots) images. On the left two lean operating points with an equivalence ratio of $\phi_{\text{PZ}} = 0.80$ and $\phi_{\text{PZ}} = 0.90$, while on the right two rich operating points with an equivalence ratio of $\phi_{\text{PZ}} = 1.11$ and $\phi_{\text{PZ}} = 1.25$ are illustrated. The same operating points are shown for the CH^* -radical in Fig. 5.8. In both figures, the center of gravity $x_{\text{CoG,fl}}$ is indicated by a white dashed line, whereas the pixel with the maximum intensity is indicated by a white cross. Additionally, the contour of the chemiluminescence intensity is given for a threshold of $Th = 0.5$. The evaluation procedure for the images is explained in Section 4.2.2.

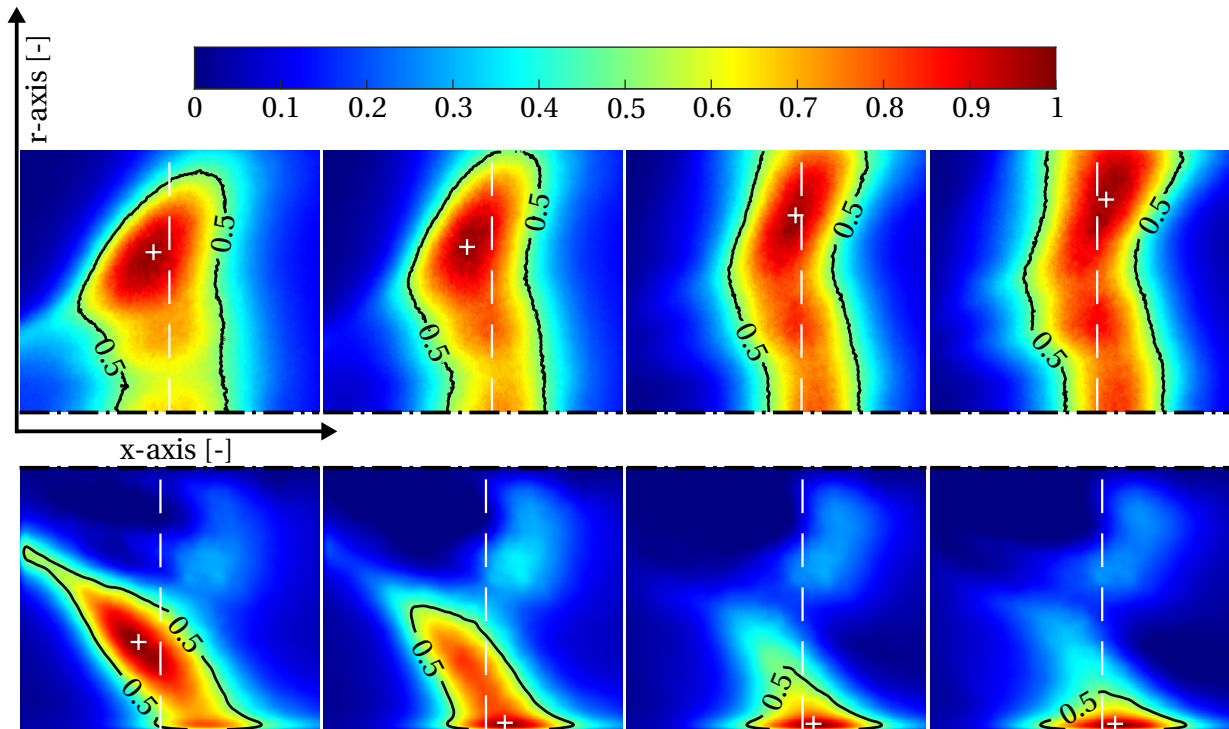


Figure 5.7: Time-averaged line-of-sight (upper plots) and inverse Abel-transformed (lower plots) OH^* -images for operating points with an equivalence ratio of $\phi_{\text{PZ}} = 0.8, 0.9, 1.11, 1.25$ (from left to right). The white dashed line indicates the axial location of the center-of-gravity $x_{\text{CoG,fl}}$ (Eq. 4.1) and the cross the pixel with the maximum intensity. The chemiluminescence intensity is normalized to the corresponding maximum of each image.

A few observations can be made by analyzing the images in Fig. 5.7 and 5.8. In general, the intensity distribution of the OH^* - and CH^* -radical is qualitatively similar for both, the LoS and Abel-transformed images. However, in axial direction the center-of-gravity $x_{\text{CoG,fl}}$ of the OH^* -images in Fig. 5.7 (white dashed line) is closer to the burner outlet than $x_{\text{CoG,fl}}$ of the CH^* -images for the same operating conditions. In radial direction the maximum intensities of the CH^* -radical are closer to the center line of the combustor.

The flame in the primary zone tends to come closer to the burner as combustion becomes leaner, clearly visible for the leanest operating point on the left in Figs. 5.7 and 5.8. This observation is most probably associated to the lower fuel mass flow $\dot{m}_{\text{f,PZ}}$. With respect to the flame shape, the flames of the

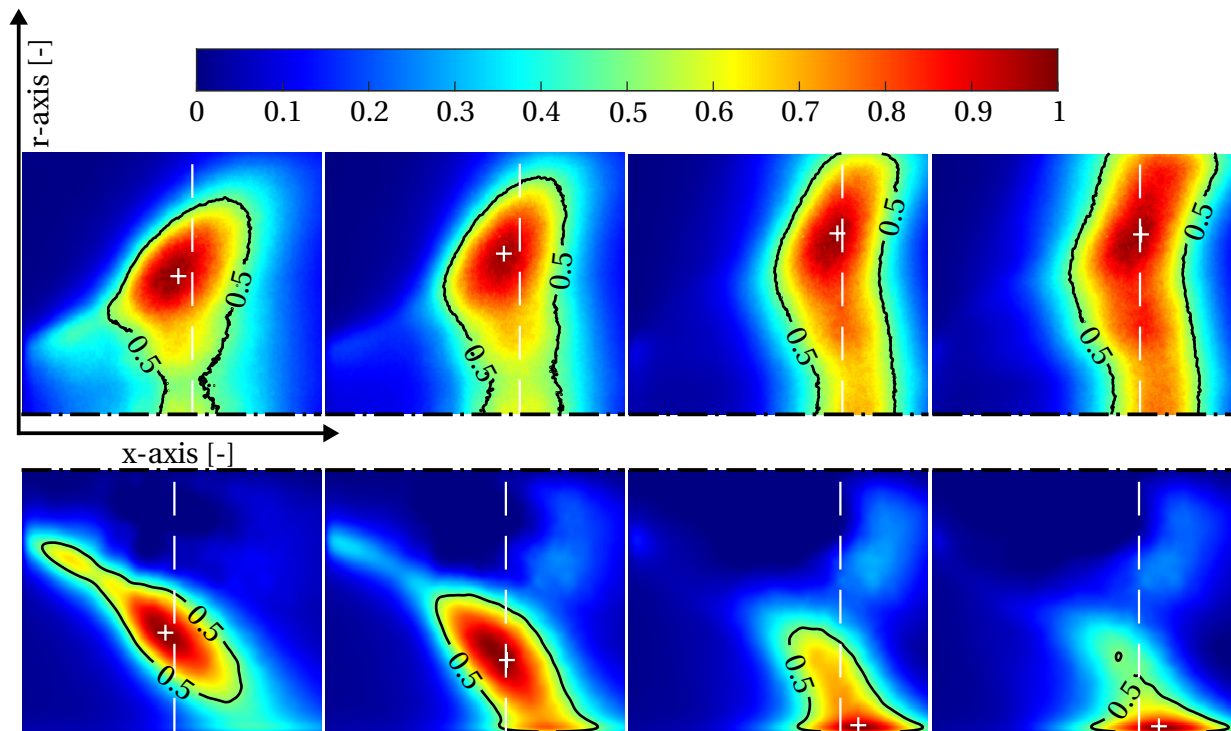


Figure 5.8: Time-averaged line-of-sight (upper plots) and inverse Abel-transformed (lower plots) CH^* -images for operating points with an equivalence ratio of $\phi_{\text{PZ}} = 0.8, 0.9, 1.11, 1.25$ (from left to right). The white dashed line indicates the axial location of the center-of-gravity $x_{\text{CoG,fl}}$ (Eq. 4.1) and the white cross the pixel with the maximum intensity. The chemiluminescence intensity is normalized with the corresponding maximum of each image.

rich and near-stoichiometric operating points seem to touch the combustion chamber's wall. The combustion chamber has a rectangular cross section and consequently the distance from the center axis to the inner corners of the chamber is higher than the normal distance to the combustor walls (cf. Section 3.1.2). In contrast to the cross section of the combustion chamber, the flow field and the flame front can be assumed to be of approx. axisymmetric type. For specific flame lengths, the flame front reaches the side walls but not the corners of the combustion chamber. At the side walls, the flame cannot move further in the radial direction but moves in the axial direction only. In addition, the reaction kinetics is influenced by the cold walls leading to a longer flame. This leads to a W-shaped flame, visible for the time-averaged

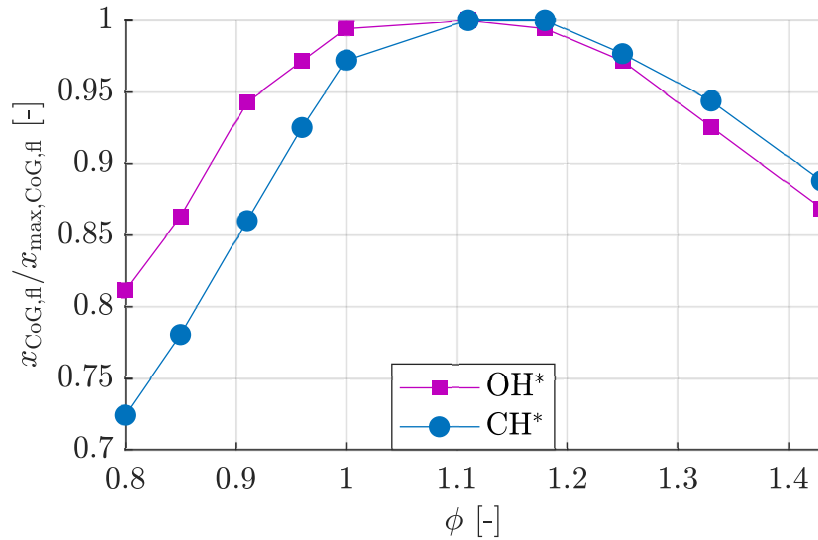


Figure 5.9: Normalized axial distance of the center-of-gravity $x_{CoG,fl}$ from the burner outlet (Eq. 4.1) of the Abel-transformed OH* - (purple) and CH* -images (blue).

LoS images in the upper plots of Figs. 5.7 and 5.8. Due to the flame being close to the wall, the inverse Abel-transformed flame of the rich operating points in the lower plots of Figs. 5.7 and 5.8 is located at the border of the image, and thus the interpretation of the images and the corresponding flame parameters must be interpreted with caution. In contrary, the W-shape is no longer visible for the leanest operating point on the left in Figs. 5.7 and 5.8 due to the shorter flame length. Consequently, the Abel-transformed images of the lean operating points are more reliable than those of the fuel-rich operating points. However, characteristic flame parameters were still calculated from the OH* - and CH* -images for each operating point given in Section 4.3.1. In particular, the determination of the center-of-gravity $x_{CoG,fl}$ was performed, which can be interpreted as the axial distance from the burner to the main heat release zone. The results for $x_{CoG,fl}$ evaluating the Abel-transformed OH* - and CH* -images are shown in Fig. 5.9. The values of $x_{CoG,fl}$ in Fig. 5.9 are normalized by the corresponding maximum of OH* and CH*. Using the LoS-images for the calculation of characteristic flame parameters (e.g. $x_{CoG,fl}$) showed similar trends, even if differing in terms of absolute values. The similar trends are confirmed by comparing the axial shift of the center-of-gravity in the LoS images in Figs. 5.7 and 5.8 (upper plots) with the shift of the Abel-transformed center-

of-gravity in the lower plots.

Fig. 5.9 reveals that the maximum center-of-gravity $x_{\text{CoG,fl}}$ corresponds to an equivalence ratio of $\phi_{\text{PZ}} \approx 1.11$. For higher and lower equivalence ratios, the flame tends to come closer to the burner outlet, which is indicated by both radicals OH^* and CH^* . Noticeable is the much stronger shift of the flame for the lean operating points compared to the rich ones, especially for CH^* . This behavior may be attributed to the flame being closer to the combustion chamber wall because of fuel-rich and near-stoichiometric equivalence ratios. As already mentioned above, the interpretation of the flame shape and parameters for fuel-rich conditions should therefore be taken with caution.

When comparing the normalized values for $x_{\text{CoG,fl}}$ of OH^* and CH^* in Fig. 5.9, it can be seen that they are nearly identical during fuel-rich combustion. In contrast, they differ for lean combustion: the center-of-gravity using the CH^* -images moves stronger to the burner outlet compared to OH^* . It should be mentioned that, in terms of absolute values, $x_{\text{CoG,fl}}$ of the OH^* -images is always located closer to the burner outlet compared to $x_{\text{CoG,fl}}$ of the CH^* images (cf. Figs. 5.7 and 5.8).

The results for $x_{\text{CoG,fl}}$ presented in the present section provide important flame characteristics, which will be used in the next Chapter 6 to evaluate and interpret the results of the thermoacoustic studies of flames in the primary zone.

6 Primary Zone Flame Dynamics

This chapter focuses on the flame in the primary zone under acoustic forcing, as well as potential root causes for the corresponding thermoacoustic behavior. In the first section, the flame transfer functions (FTF) of rich and lean operating points are investigated using the purely acoustic MMM and the Rankine-Hugoniot relations. The comparison of the fuel-rich and lean operating points shows that the amplitudes of the fuel-rich operating points exhibit a strong dependence on the equivalence ratio, resulting in a diminishing amplitude against frequency.

Understanding and physically explaining the behavior of the flame is the subject of the following section. First, the influence of atomization and evaporation is clarified by comparing the FTF amplitude of the non-premixed kerosene case with that of a non-premixed natural gas case. Second, the temperature decrease due to the high heat of vaporization of kerosene is investigated.

Afterwards, an alternative approach is presented to calculate the FTF from the FTM22-element, which takes into account the chemical conversion and temperature dependencies across the flame front.

In the last section, the optically measured FTFs using four different radicals are compared with the acoustically measured FTFs. The results indicate a qualitatively similar trend for the amplitudes and quantitatively correct results for the phases. This chapter concludes with a recommendation on the best radical choice for measuring optical FTFs.

6.1 Acoustic Flame Transfer Functions

The purely acoustic determination of the flame dynamics of the primary zone was obtained using the multimicrophone method (MMM) and the Rankine-Hugoniot relations, described in Section 4.3.2. The measurements were performed for the operating points pointed out in Section 4.3.1, resulting in five FTF_{RH} for rich and five for lean combustion conditions. The adjustment of

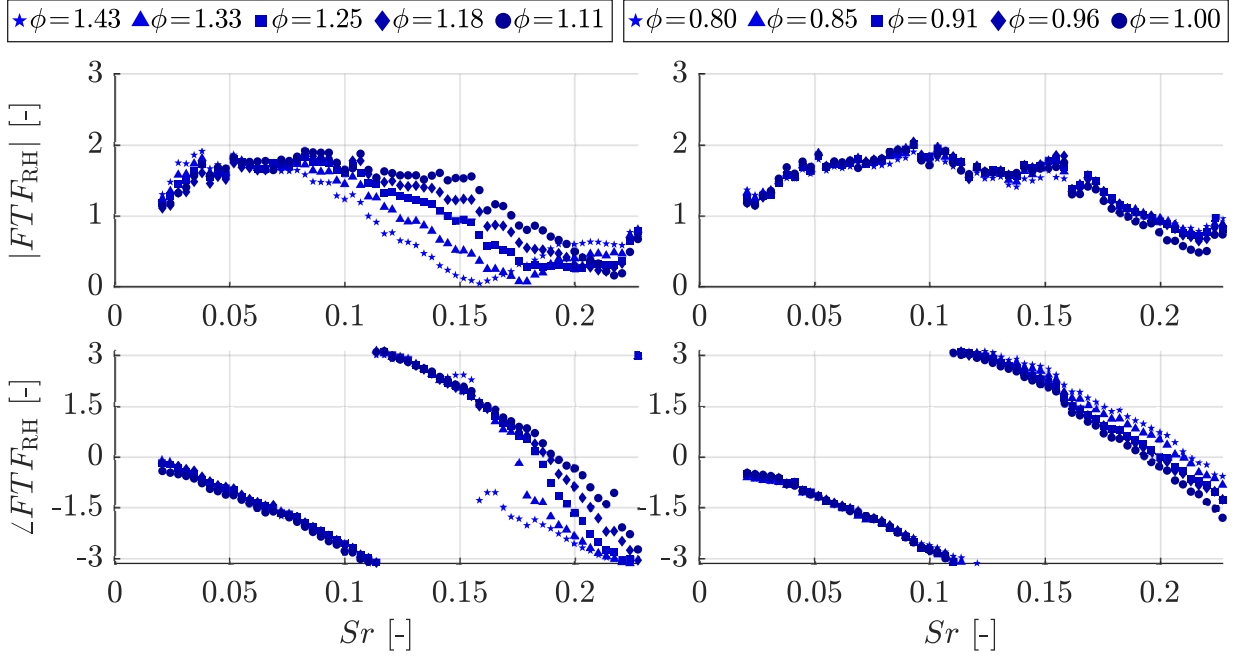


Figure 6.1: FTF amplitudes (top) and phases (bottom) for rich (left) and lean (right) equivalence ratios, an air preheating temperature of $T_{a,PZ} = 423\text{K}$ and a pressure loss of $\Delta p_{a,PZ}/p_{a,PZ} \approx 4\%$ obtained with the purely acoustic MMM and the Rankine-Hugoniot relations.

the different equivalence ratios was performed by varying the fuel mass flow $\dot{m}_{f,PZ}$ in the primary zone ($0.65\text{g/s} < \dot{m}_{f,PZ} < 1.16\text{g/s}$). The preheating temperature and pressure loss of the primary air was kept constant at $T_{a,PZ} = 423\text{K}$ and $\Delta p_{a,PZ}/p_{a,PZ} \approx 4\%$, respectively.

Figure 6.1 illustrates the measured flame transfer functions FTF_{RH} for the rich (left) and lean (right) operating points investigated. The same symbols correspond to the same adiabatic flame temperature for rich and lean combustion conditions (cf. Fig. 4.5).

The FTF amplitudes of all lean operating points (Fig. 6.1 right, top) are almost identical throughout the entire Strouhal number range. Moreover, the FTFs have high amplitude values up to high Strouhal numbers. Bobusch et al. observed a similar behavior for the FTF amplitude in their lean 'diffusion type' kerosene flame, although the absolute values of their acoustically measured FTF were an order of magnitude smaller [71]. Kaufmann et al. conducted measurements with the MMM on a dual fuel burner for lean premixed kerosene

combustion and their FTFs obtained had amplitudes of the same order of magnitude as the current study [97]. However, their amplitude trend showed a dependence on the equivalence ratio, which is not the case for the lean operating points in the present work.

The FTF amplitudes of the fuel-rich operating points (Fig. 6.1 top, left) show a clear dependence on the equivalence ratio. At low Strouhal numbers, the individual curves are similar, but from around $Str \approx 0.1$ onward a growing divergence is observed. The richer the combustion, the smaller the FTF magnitude, and the faster a minimum is attained. The observations made for the rich and lean FTF amplitudes lead to the conclusion that during rich combustion, a physical effect depending on the equivalence ratio alters the flame dynamics. For this reason, in Section 6.2 a root cause study will be performed to provide an explanation for the behavior of fuel-rich FTF amplitudes.

The phases for rich and lean combustion are almost identical up to high Strouhal numbers of approximately $Str \approx 0.15$. For the rich operating points with an equivalence ratio of $\phi_{PZ} = 1.43$ and $\phi_{PZ} = 1.33$ a phase jump of $\approx \pi$ is observable at a Strouhal number of $Str \approx 0.16$ and $Str \approx 0.17$, respectively. The phase jump indicates a sign change of the FTF_{RH} due to the corresponding amplitudes at values close to zero. Especially for the lean operating points, the divergence of the individual phases for higher Strouhal numbers is assumed to be a convective time delay effect.

The time delay model (TDM) is based on disturbances that alter the flame dynamics and are convectively transported to the main reaction zone. The time between the origin of the disturbance and the main reaction zone of the flame causes a phase shift φ_{TDM} , which can be calculated according to Eq. 6.1:

$$\varphi_{TDM} = \omega \tau_{conv} = \omega \frac{x_{TDM}}{\bar{u}_{TDM}}. \quad (6.1)$$

In Eq. 6.1 ω is the angular velocity, x_{TDM} the distance between the origin of the disturbances, and the flame and \bar{u}_{TDM} the mean convective transport velocity of the disturbances. The distance x_{TDM} can be obtained from the chemiluminescence images given in Section 5.3. A few parameters were investigated to represent x_{TDM} , e.g. lift-off height $x_{LO,fl}$, flame length $x_{len,fl}$, and center of gravity $x_{CoG,fl}$ (cf. Section 4.2.2). The center of gravity $x_{CoG,fl}$ of the inverse Abel-transformed OH^* -images in Fig. 5.9 gave the results most close to the measured FTF phases. The evaluation of the convective mean velocity \bar{u}_{TDM} was

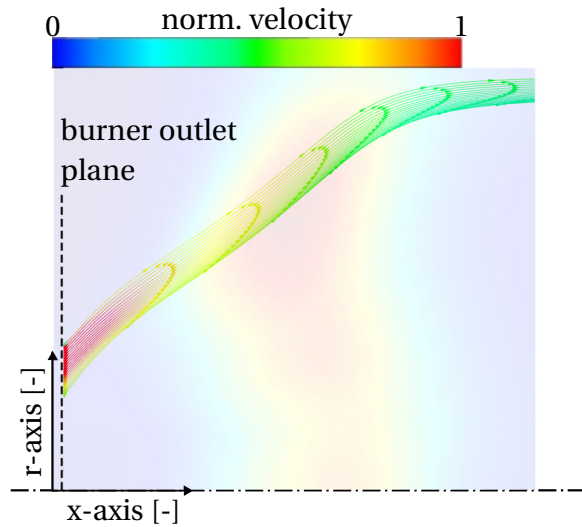


Figure 6.2: Normalized mean velocity from an isothermal CFD simulation in the mid plane of the primary zone combustion chamber. The streamlines are starting at the burner outlet and are color coded according to the normalized velocity. Additionally, an LoS OH^{*}-image is superimposed as an example.

obtained by isothermal CFD calculations for the same preheating temperature $T_{a,PZ}$ and pressure loss $\Delta p_{a,PZ}/p_{a,PZ}$ as for the FTF measurements. Assuming the temperature and consequently the mean velocity from the burner outlet to the flame zone is not highly influenced by the presence of the flame, this approach seems to be justified.

Figure 6.2 shows the normalized velocity in the mid-plane of the combustion chamber along 20 streamlines, starting from the burner outlet plane. Combining the OH^{*}-images with the CFD velocity field, the time $\tau_{conv,i}$ to reach $x_{CoG,fl}$ on each streamline i can be obtained. The different time delays $\tau_{conv,i}$ on the corresponding streamlines were subsequently averaged and evaluated for each operating point, resulting in $\tau_{conv}(\phi)$. The normalized standard deviation for the velocity of the individual streamlines was always below 11%.

The phase delay can now be calculated according to Eq. 6.1 using the time delay of each operating point $\tau_{conv}(\phi)$ and the angular velocity ω for each excitation frequency. Figure 6.3 gives the resulting calculated phase delay (top) in comparison to the acoustically measured phases (bottom) for all rich (left) and lean (right) operating points.

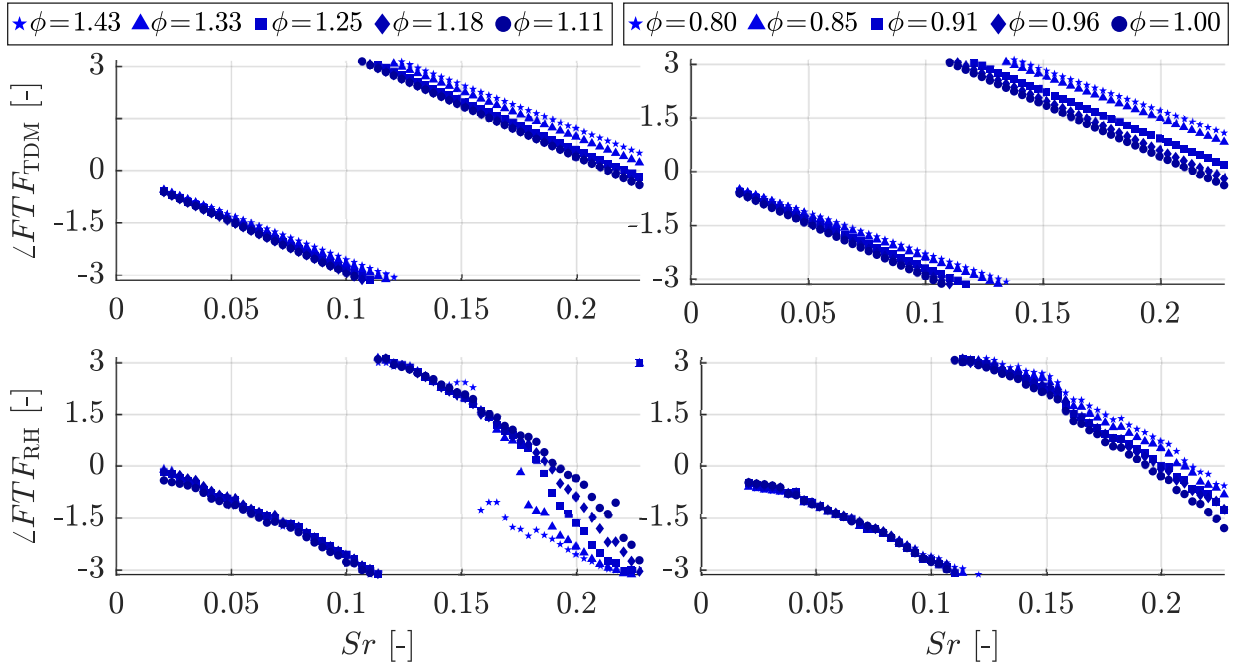


Figure 6.3: Comparison of the phase delay for all rich (left) and lean (right) operating points measured with the purely acoustic MMM (bottom) and calculated with the phase delay model (top).

The slope of the measured and calculated phase delay is in very good agreement for both rich and lean operating points. Furthermore, the change in the slope of the phase only becomes visible at higher Strouhal numbers and is clearly stronger for the lean operating points. As described in Section 5.3, the shift of the flame closer to the burner outlet with dropping fuel mass flow emerges much more for the lean operating points and leads to a rapidly decreasing $x_{\text{CoG,fl}}$. This causes a flatter phase delay as $\tau_{\text{conv}}(\phi)$ decreases. In conclusion, the time delay model combining isothermal CFD calculations and the center of gravity $x_{\text{CoG,fl}}$ of the inverse Abel-transformed OH^* -images confirms the behavior of the phases for all operating points, giving further confidence in the results. Furthermore, it can be concluded that the flame dynamics of the non-premixed kerosene flame in the primary zone is driven by convectively forced coherent flow structures and/or equivalence ratio waves (cf. Section 1.3.1).

6.2 Root Cause Study

In the previous Section 6.1 it was shown that the purely acoustically measured FTF amplitudes of the separated primary zone demonstrate a clearly different behavior when comparing rich and lean combustion (cf. Fig. 6.1). The FTF amplitudes in the rich combustion regime drop with increasing equivalence ratio beyond $\phi_{PZ} \geq 1$. In the following, a root cause study is made to provide more insight into the characteristics of the fuel-rich FTFs.

6.2.1 Atomization and Evaporation

Atomization and evaporation are often a driver of the flame dynamics in liquid fueled non-premixed flames [34, 42, 97]. Especially in the low-frequency range, droplets can potentially follow the harmonic fluctuation of the combustion air if their inertia is small enough. The effect of atomization and evaporation on the flame dynamics of the primary zone was investigated by comparison with a non-premixed natural gas combustion case. The design of the non-premixed natural gas fuel nozzle is described in Section 3.1.2. The remaining burner and combustion chamber hardware of the primary zone remained the same.

A similar flame shape is required for a correct comparison of both combustion cases. Otherwise, additional thermoacoustic differences would arise, which are not caused by atomization and evaporation. Due to this constraint, steady OH* -images of both cases were compared with each other a priori to guarantee a similar flame shape.

Figure 6.4 depicts the obtained OH* -images (time averaged, line-of-sight) of the non-premixed kerosene (upper half) and non-premixed natural gas case (lower half) for two different equivalence ratios (left $\phi_{PZ} = 0.91$ and right $\phi_{PZ} = 1.11$). Both cases in Fig. 6.4, i.e. non-premixed kerosene and natural gas combustion, exhibit a very similar flame shape for both equivalence ratios. In both cases the flame tends to come closer to the burner outlet for decreasing fuel mass flow (cf. Section 5.3). However, the non-premixed natural gas flame has a slightly larger flame volume and the axial location of the center of gravity (dashed white line) is slightly further downstream.

The qualitative similarity of the heat release zones represented by the OH* -images in Fig. 6.4 allows an isolation of effects due to atomization and evaporation when comparing both combustion cases. Differences must be expected

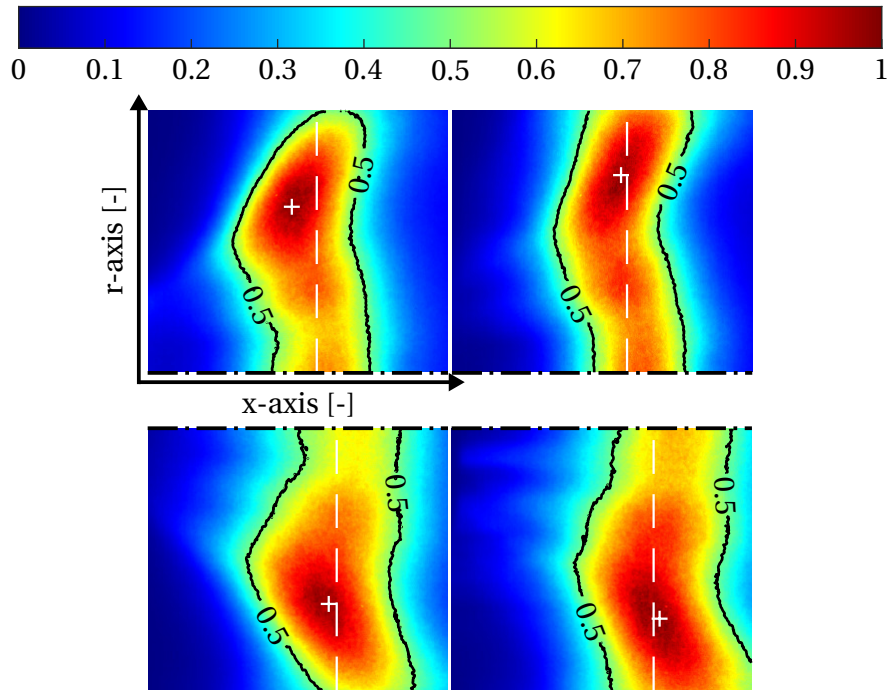


Figure 6.4: Time averaged LoS OH* -images for kerosene (top) and natural gas combustion (bottom) in the primary zone for an equivalence ratio of $\phi_{PZ} = 0.91$ (left) and $\phi_{PZ} = 1.11$ (right). The white dashed line indicates the axial location of the center of gravity $x_{CoG,fl}$ (Eq. 4.1) and the white cross the pixel with the maximum intensity.

due to the slightly different distances of the center of gravity from the burner outlet, which lead to a change in the slope of the FTF phase.

Figure 6.5 illustrates the purely acoustically obtained FTFs for the non-premixed natural gas and kerosene case for an equivalence ratio of $\phi_{PZ} = 1.11$ (left) and $\phi_{PZ} = 0.91$ (right). The phase slope of the natural gas case in Fig. 6.5 is flatter compared to the kerosene case. This can be attributed partly to a higher flow velocity due to the lower density of the air-fuel-mixture using natural gas which leads to a shorter time delay and consequently smaller phases. Furthermore, it can be concluded that the influence of the higher flow velocity due to the gaseous fuel on the FTF phase dominates the phase slope, despite the fact that the heat release zone of the natural gas case is shifted further downstream according to Fig. 6.4 (cf. Eq. 6.1).

In contrast to the phases, the FTF amplitudes for both combustion cases exhibit a nearly identical behavior, especially in the low-frequency range. Par-

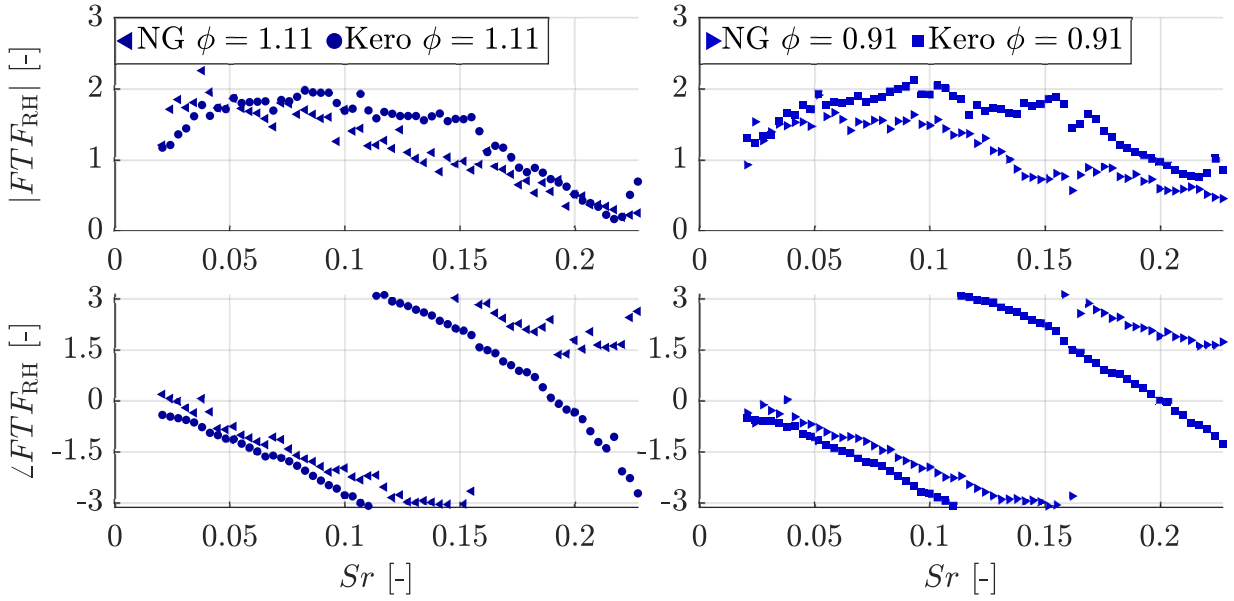


Figure 6.5: Comparison of the purely acoustically measured FTF_{RH} for kerosene and natural gas combustion for an equivalence ratio of $\phi_{PZ} = 1.11$ (left) and $\phi_{PZ} = 0.91$ (right).

ticularly, the FTF amplitudes of the fuel-rich kerosene operating point (Fig. 6.5 left) are very close to the natural gas one. Therefore, it is concluded that atomization and evaporation does not play a major role regarding the flame dynamics in the isolated primary zone. Furthermore, the assumption can be made that the fuel of the non-premixed kerosene gas case is already largely evaporated before reaching the flame front, thus showing a thermoacoustic behavior similar to that of the non-premixed natural gas combustion. The remaining differences may be attributed to the different characteristics of both hydrocarbon fuels (e.g. slightly higher reaction enthalpy of natural gas) and/or the varying mixing behavior.

6.2.2 Thermal Effects

The cold injected fuel into the primary zone in the case of the non-premixed kerosene combustion causes a temperature decrease in the mixture zone, mainly due to the heat of vaporization of the fuel droplets. The influence of the evaporating liquid fuel on the temperature of the fuel-air mixture increases as combustion becomes richer due to the higher fuel mass flow. In addition, a

smaller temperature decrease is directly related to the enthalpy of the cold liquid fuel. Lower fuel-air mixture temperatures lead to longer flames due to the reaction kinetics being strongly dependent on temperature according to the Arrhenius equation [98]. FTFs of long flames tend to exhibit lower amplitudes because of increasing destructive acoustic interferences along the flame for higher frequencies or smaller acoustic wavelengths. The FTF amplitudes in the fuel-rich regime shown in Fig. 6.1 exhibit a drop with increasing equivalence ratio ϕ_{PZ} , which may be attributed to an increasing flame length. For this reason, the temperature decrease of the fuel-air mixture was calculated for the operating point with the highest fuel mass flow ($\phi_{PZ} = 1.43$) and a preheating temperature of $T_{a,PZ} = 423$ K, using the energy equation given in Eq. 6.2:

$$T_{f-a-mix} = T^0 + \frac{\dot{H}_{a,PZ} + \dot{H}_{f,PZ} - r_{f,PZ}}{\dot{m}_{f-a-mix} c_{p,f-a-mix} \Big|_{T^0}^{T_{f-a-mix}}}. \quad (6.2)$$

In Eq. 6.2 $T^0 = 298$ K is the reference temperature, $\dot{H}_{a,PZ}$ the enthalpy flux of the preheated primary air, $\dot{H}_{f,PZ}$ the enthalpy flux of the liquid fuel, $r_{f,PZ}$ the heat of vaporization of the liquid fuel, and $c_{p,f-a-mix} \Big|_{T^0}^{T_{f-a-mix}}$ the specific heat capacity of the fuel-air mixture. During all experiments *Jet A-1* kerosene was used as liquid fuel. The data for *Jet A-1* needed as input for Eq. 6.2 were taken from the work of Rachner [99].

Assuming that all liquid fuel is vaporized within the entire preheated primary air $\dot{m}_{a,PZ}$, the resulting fuel-air mixture temperature becomes $T_{f-a-mix} = 382$ K (-41 K or -9.7%). Considering only the amount of air through the swirler being in direct contact with the fuel droplets after injection, the temperature of the fuel-air mixture drops to $T_{f-a-mix} = 361$ K (-62 K or -14.7%). In Fig. 4.7 it was shown that the hot gas temperature at the exit of the primary combustion chamber follows the trend of the adiabatic flame temperature very well, although the absolute values differ. Therefore, the influence of the fuel-air mixture temperature on the flame temperature is estimated by calculating the adiabatic flame temperature for a kerosene surrogate and equilibrium conditions in *Cantera* [76]. The resulting adiabatic flame temperature for the worst-case scenario with the highest fuel mass flow ($\phi_{PZ} = 1.43$) is reduced to $T_{ad} = 2094$ K (-2%).

The above calculation reveals little impact of the evaporating kerosene on the temperature of the fuel-air mixture and the flame. Due to this, it is not

expected that the evaporating fuel has the potential to substantially lengthen the primary zone's flame and thus modify the flame dynamics during rich combustion, as is the case in Fig. 6.1. Furthermore, the results for the FTF phases in the fuel-rich regime in Fig. 6.1 indicate that the drop of the amplitudes already occurs at low Strouhal numbers, at which the phases are still perfectly the same. If the root cause of the low-pass behavior would be a lengthening of the flame, the phases must change substantially, which is not the case. The conclusion that the flame length is not the root cause for the behavior of the fuel-rich FTF amplitudes is further supported by the small change of x_{CoG} in Fig. 5.9 for OH* - and CH* -imaging. Consequently, thermal effects that lower the flame temperature and thus increase the flame length are not expected to alter the flame dynamics of the isolated primary zone.

6.2.3 Synthesis Gas Formation

After having seen that atomization and evaporation, as well as thermal effects, do not substantially alter the flame dynamics of the primary zone, synthesis gas formation remains as a possible physical explanation. The synthesis gas formation is a chemical process only taking place during combustion under a lack of oxygen. The higher the equivalence ratio, the more of the species H₂ and CO are formed when burning hydrocarbon fuels. Assuming that during acoustic excitation the equivalence ratio is globally or locally fluctuating may lead to an interaction of the acoustics with the synthesis gas formation, which becomes stronger the higher the equivalence ratio gets. Considering that the synthesis gas formation is an endothermic process, the heat consumption due to the formation of H₂ and CO counteracts the heat release using the oxygen available during fuel-rich combustion. These opposed effects may lead to a diminishing expansion of the flame and consequently to a lower acoustic fluctuation, which in turn reduces the amplitude of the corresponding flame transfer function. Using the purely acoustic Rankine-Hugoniot relations for the determination of FTFs of fuel-rich flames results in measuring both the heat release rate of the flame and the heat consumption of the synthesis gas formation. However, assuming quasi-steady flame dynamics behavior, the temperature of the products would approach the temperature of the reactants if the heat consumption due to the formation of synthesis gas compensates

for the exothermic reactions of the flame. The adiabatic flame temperatures for the fuel-rich equivalence ratios studied in this work are still relatively high. Due to this, additional effects may contribute to the decrease of the FTF amplitude for the equivalence ratio studied in this work.

An additional effect could be the wall contact of the flame, which increases with increasing equivalence ratio (cf. Section 5.3). Because the wall temperature is much lower than the gas temperature, a partial quenching of the chemical reactions of the flame at the location of the wall can be expected. The quenching of the flame would lead to an additional decrease in the heat release fluctuation and consequently to a diminishing FTF amplitude.

6.3 Alternative Determination of Flame Transfer Functions

The classic Rankine-Hugoniot relations for the determination of the flame transfer function from the FTM22-element are assuming the flame as a compact temperature jump only (cf. Section 2.2.2). The gas properties of the reactants upstream of the flame and the combustion products downstream of the flame are considered to stay the same using the Rankine-Hugoniot relations. Changes in the gas composition and molar amount of gas, as well as the temperature dependence of gas properties are not taken into account. For very lean flames, the classic Rankine-Hugoniot relations may be a sufficient approximation due to the large excess of air. In contrast, for near-stoichiometric and fuel-rich flames, the neglect of chemical conversion processes and temperature-dependent gas properties may cause an increased error regarding the resulting FTF from the FTM22-element.

Due to the chemical reactions of the combustion process, the molar quantity and gas composition significantly change across the flame. Furthermore, the properties of an ideal gas depend on the gas temperature, e.g. the specific heat capacity. For example, an increase in the number of molecules due to the combustion process would lead to a higher volumetric expansion of the flame, which in turn results in a higher acoustic velocity fluctuation. Consequently, the classic Rankine-Hugoniot relations incorrectly interpret the increase in molecules as a higher heat release rate or higher FTF amplitude. Analogously, the temperature dependence of the specific heat capacity could be wrongly

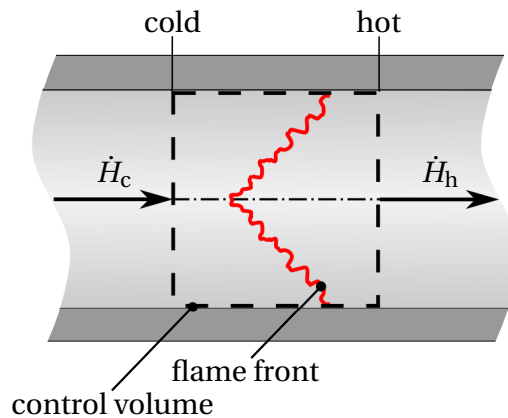


Figure 6.6: Control volume for an acoustically compact flame with the cold state upstream (c) and the hot state downstream (h) of the flame.

attributed to a change in heat release rate. For ideal gases, the specific heat capacity increases with increasing temperature, meaning that more heat can be absorbed by the gas before an increase in temperature takes place. The classic Rankine-Hugoniot relations neglect the temperature dependence of the specific heat capacity and for this reason underestimate the heat release rate of the flame or FTF amplitude, considering that the FTF is calculated from the FTM22-element only.

In the following, an alternative approach for the calculation of the FTF will be derived to fully account for the gas composition and temperature dependencies of the combustion reactants and products as a result of the combustion. Furthermore, the movement of the flame during acoustic excitation will be taken into account. Figure 6.6 illustrates the corresponding control volume and the flame front. The incoming, cold flow upstream of the flame is described by the corresponding enthalpy flux \dot{H}_c , consisting of the reactants air and fuel. Contrarily, the outgoing, hot enthalpy flux is referred to as \dot{H}_h , containing the combustion products.

The following assumptions will be made with respect to Fig. 6.6:

- 1D adiabatic system ($\dot{Q} = 0$)
- No work fluxes are present ($\dot{W} = 0$)
- Gravity forces of the gas can be neglected
- Weakly incompressible, steady mean flow

- Neglection of terms of the order $\mathcal{O}(Ma^2)$
- Steady mean flow with linearly superposed harmonic perturbations
- Acoustically compact flame
- Neglection of products of fluctuating quantities (e.g. $\rho' u'$)

The continuity equation of the unsteady system in Fig. 6.6 can be written according to Eq. 6.3:

$$\dot{m}_c - \dot{m}_h = \frac{dm_{\text{sys}}}{dt}. \quad (6.3)$$

In Eq. 6.3 m_{sys} is the amount of mass in the control volume or system of Fig. 6.6. The flame in the control volume of Fig. 6.6 is propagating with a turbulent flame speed s_t against the velocity u_c of the incoming cold flow of the reactants. For the steady case, the mass is conserved ($dm_{\text{sys}}/dt = 0$) and the flame is at rest at a fixed position in our control volume ($u_c = s_t$). However, considering flow perturbations the flame may move with a velocity u_s relative to the fixed control volume. For example, if the incoming cold flow of the reactants increases and the corresponding increase of the turbulent flame speed s_t (e.g. due to a change in the chemical kinetics and turbulent mixing) does not overcome the increased u_c , the flame tends to move in downstream direction ($u_c > s_t$). Consequently, the movement or velocity of the flame relative to the control volume can be expressed by Eq. 6.4:

$$u_s = s_t - u_c. \quad (6.4)$$

The consideration of the flame movement in the conservation equations was first shown by Chu [100] and extended by Strobio-Chen [101]. Applying the approach of Chu to the system of Fig. 6.6 yields Eq. 6.5:

$$A_{\text{CC}}\rho_c(u_c + u_s) - A_{\text{CC}}\rho_h(u_h + u_s) = 0. \quad (6.5)$$

In Eq. 6.5 A_{CC} is the constant cross section of the combustion chamber up- and downstream of the flame. Equation 6.5 can now be rearranged resulting in Eq. 6.6:

$$\rho_c u_c - \rho_h u_h = \underbrace{u_s (\rho_h - \rho_c)}_{\frac{dm_{\text{sys}}}{dt}}. \quad (6.6)$$

The RHS of Eq. 6.6 clearly shows the change of mass in the system due to the movement of the flame with the velocity u_s relative to the control volume. For

example, considering that the flame moves downstream ($u_s < 0$), the volume of the reactants in the fixed control volume increases to the same extent as the volume of the products decreases. Due to the density of the reactants being usually large than the one of the products, the mass in the system of Fig. 6.6 increases.

The mass conservation up- and downstream of the flame from Eq. 6.6 can now be linearized around a mean value according to Eq. 6.7:

$$(\bar{\rho}_c + \rho'_c)(\bar{u}_c + u'_c) - (\bar{\rho}_h + \rho'_h)(\bar{u}_h + u'_h) = (\bar{u}_s + u'_s) [(\bar{\rho}_h + \rho'_h) - (\bar{\rho}_c + \rho'_c)]. \quad (6.7)$$

The mean quantities can be subtracted from Eq. 6.7 and relative density or temperature fluctuations are assumed to be small compared to velocity fluctuations ($\rho'/\bar{\rho} \ll u'/\bar{u}$). It has to be mentioned that the assumption of small density fluctuations is permissible for small Mach numbers up- and downstream of the flame, but not across the flame ($\bar{\rho}_c u'_c \neq \bar{\rho}_h u'_h$ for $A = \text{const.}$). Furthermore, we apply the assumptions made above (e.g. neglect of products of fluctuating quantities). As a result we obtain Eq. 6.8 for the mass flow fluctuations up- and downstream of the flame under consideration of the flame movement:

$$\bar{\rho}_c u'_c - \bar{\rho}_h u'_h = u'_s (\bar{\rho}_h - \bar{\rho}_c). \quad (6.8)$$

From Eq. 6.8 it can be seen that the flame is moving if the density ratio of the reactants and products differs from the ratio of the acoustic velocity fluctuation up- and downstream of the flame ($\bar{\rho}_c / \bar{\rho}_h \neq u'_h / u'_c = FTM_{22} \Rightarrow u'_s \neq 0$). Please note that due to steady mean flow the flame on average is at rest ($\bar{u}_s = 0$).

Next, the energy balance or first law of thermodynamics using the assumptions made above is given by Eq. 6.9:

$$\frac{dE_{\text{sys}}}{dt} = \dot{m}_c \left(h + \frac{u^2}{2} \right)_c - \dot{m}_h \left(h + \frac{u^2}{2} \right)_h. \quad (6.9)$$

In Eq. 6.9 the LHS describes the time derivative of the energy contained in the system E_{sys} , which are the specific internal energy e_i and specific kinetic energy $u_{\text{sys}}^2/2$. On the RHS of Eq. 6.9 the specific enthalpies of the reactants h_c and products h_h , as well as the corresponding specific kinetic energies $u_c^2/2$ and $u_h^2/2$ are present. Due to the assumption of small terms of the order $\mathcal{O}(Ma^2)$, the kinetic energies of Eq. 6.9 can be neglected (transported and

internal kinetic energy) and we obtain Eq. 6.10:

$$\frac{dE_i}{dt} = \dot{H}_c - \dot{H}_h. \quad (6.10)$$

The classic Rankine-Hugoniot relations simulate the heat release rate of the flame as an external energy source \dot{Q} , which adds heat to the combustion system. Especially for fuel-rich flames, this approach is no longer valid and the reaction enthalpy has to be introduced, representing the heat being released due to the combustion process. Consequently, Eq. 6.9 can be rearranged leading to Eq. 6.11:

$$\frac{dE_i}{dt} = \dot{m}_c (h - h^0)_c - \Delta_R \dot{H}^0 - \dot{m}_h (h - h^0)_h. \quad (6.11)$$

On the RHS of Eq. 6.10 the sensible enthalpy fluxes of the reactants $(h_c - h_c^0)$ and products $(h_h - h_h^0)$ relative to standard state, as well as the reaction enthalpy flux $\Delta_R \dot{H}^0$ of the combustion process in the standard state are present. It should be mentioned that the reaction enthalpy flux $\Delta_R \dot{H}^0$ for complete combustion of lean flames is considered as the product of the lower heating value and fuel mass flow $(\dot{m}_f H_u)$ when simulating the heat release of the chemical process as an external heat added to the system.

The time derivative of the internal energy E_i on the LHS of Eq. 6.10 can be described analogously to the approach used for the continuity equation (Eq. 6.6) [100], [101]. In this case, the flame movement relative to the control volume causes an unsteady change of the internal energy E_i inside the control volume due to the difference in density of the combustion reactants and products, represented by Eq. 6.12:

$$\frac{dE_i}{dt} = u_s (\rho_h e_{i,h} - \rho_c e_{i,c}) A_{CC}. \quad (6.12)$$

It should be mentioned that the specific internal energy of the reactants and products using the assumptions made above is the same ($e_{i,c} = e_{i,h}$). In contrast, the densities of the reactants and products are different for most combustion processes. As a consequence and analogously to the mass conservation in Eq. 6.6: if the flame moves, the internal energy is fluctuating due to the increase/decrease of reactants/products to the same volumetric extent but with different densities and consequently a different amount of internal energy resulting in an increase/decrease of the internal energy in the fixed control volume of Fig. 6.6 ($dE_i/dt \neq 0$).

From 6.12 it can be seen that the internal energy is fluctuating due to the difference of the density of the reactants and products. For practical reasons we define a volumetric internal reaction energy $\Delta_R e_{i,v}$ in the standard state, according to Eq. 6.13:

$$\Delta_R e_{i,v}^0 = \rho_h e_{i,h}^0 - \rho_c e_{i,c}^0. \quad (6.13)$$

Equation 6.13 can now be inserted into Eq. 6.12, leading to Eq. 6.14:

$$\frac{dE_i}{dt} = u_s [\rho_h (e_i - e_i^0)_h + \Delta_R e_{i,v}^0 - \rho_c (e_i - e_i^0)_c] A_{CC}. \quad (6.14)$$

Inserting Eq. 6.14 into Eq. 6.11 gives the overall energy balance for the control volume in Fig. 6.6 under consideration of the flame movement according to Eq. 6.15:

$$u_s [\rho_h (e_i - e_i^0)_h + \Delta_R e_{i,v}^0 - \rho_c (e_i - e_i^0)_c] A_{CC} = \dot{m}_c (h - h^0)_c - \Delta_R \dot{H}^0 - \dot{m}_h (h - h^0)_h. \quad (6.15)$$

Equation 6.15 can now be linearized around a mean value and the mean quantities can be eliminated by subtracting the energy equation for the mean values only, leading to Eq. 6.16:

$$\begin{aligned} u'_s \left[\bar{\rho}_h (\overline{e_i - e_i^0})_h + \Delta_R \bar{e}_{i,v}^0 - \bar{\rho}_c (\overline{e_i - e_i^0})_c \right] A_{CC} &= -\Delta_R \dot{H}^{0'} \\ + \bar{m}'_c (h - h^0)'_c - \bar{m}'_h (h - h^0)'_h & \\ + \dot{m}'_c (\overline{h - h^0})_c - \dot{m}'_h (\overline{h - h^0})_h &. \end{aligned} \quad (6.16)$$

Equation 6.16 can be rearranged and divided by the mean reaction enthalpy flux $\Delta_R \bar{\dot{H}}^0$, resulting in Eq. 6.17:

$$\begin{aligned} \frac{\Delta_R \dot{H}^{0'}}{\Delta_R \bar{\dot{H}}^0} &= \frac{\bar{m}'_h (h - h^0)'_h - \bar{m}'_c (h - h^0)'_c}{-\Delta_R \bar{\dot{H}}^0} \\ &+ \frac{\dot{m}'_h (\overline{h - h^0})_h - \dot{m}'_c (\overline{h - h^0})_c}{-\Delta_R \bar{\dot{H}}^0} \\ &+ \frac{u'_s \left[\bar{\rho}_h (\overline{e_i - e_i^0})_h + \Delta_R \bar{e}_{i,v}^0 - \bar{\rho}_c (\overline{e_i - e_i^0})_c \right] A_{CC}}{-\Delta_R \bar{\dot{H}}^0}. \end{aligned} \quad (6.17)$$

The mean reaction enthalpy flux $\Delta_R \bar{H}^0$ can be expressed according to Eq. 6.18:

$$\Delta_R \bar{H}^0 = \bar{H}_h^0 - \bar{H}_c^0 = \bar{m} (\overline{h_h^0 - h_c^0}) = A_{CC} \bar{\rho}_c \bar{u}_c (\overline{h_h^0 - h_c^0}). \quad (6.18)$$

Using Eq. 6.18 and the relation for the mass flow fluctuations $\dot{m}' = A_{CC} \bar{\rho} u'$ (cf. Eq. 6.8), Eq. 6.17 can be further simplified, which yields Eq. 6.19:

$$\begin{aligned} \frac{\Delta_R \dot{H}^{0'}}{\Delta_R \bar{H}^0} &= \frac{(h - h^0)'_h - (h - h^0)'_c}{-(\overline{h_h^0 - h_c^0})} \\ &+ \frac{\bar{\rho}_h u'_h (\overline{h - h^0})_h - \bar{\rho}_c u'_c (\overline{h - h^0})_c}{-\bar{\rho}_c \bar{u}_c (\overline{h_h^0 - h_c^0})} \\ &+ \frac{u'_s \left[\bar{\rho}_h (\overline{e_i - e_i^0})_h + \Delta_R \bar{e}_{i,v}^0 - \bar{\rho}_c (\overline{e_i - e_i^0})_c \right]}{-\bar{\rho}_c \bar{u}_c (\overline{h_h^0 - h_c^0})}. \end{aligned} \quad (6.19)$$

The flame movement relative to the control volume, expressed by u'_s , can be substituted by using the continuity equation from Eq. 6.8, providing Eq. 6.20 :

$$\begin{aligned} \frac{\Delta_R \dot{H}^{0'}}{\Delta_R \bar{H}^0} &= \frac{(h - h^0)'_h - (h - h^0)'_c}{-(\overline{h_h^0 - h_c^0})} \\ &+ \frac{\bar{\rho}_h u'_h (\overline{h - h^0})_h - \bar{\rho}_c u'_c (\overline{h - h^0})_c}{-\bar{\rho}_c \bar{u}_c (\overline{h_h^0 - h_c^0})} \\ &+ \frac{\bar{\rho}_c u'_c - \bar{\rho}_h u'_h \left[\bar{\rho}_h (\overline{e_i - e_i^0})_h + \Delta_R \bar{e}_{i,v}^0 - \bar{\rho}_c (\overline{e_i - e_i^0})_c \right]}{\bar{\rho}_h - \bar{\rho}_c \quad -\bar{\rho}_c \bar{u}_c (\overline{h_h^0 - h_c^0})}. \end{aligned} \quad (6.20)$$

In Eq. 6.20 the first term on the RHS represents fluctuations of the specific enthalpy of the combustion products h'_h and reactants h'_c which can take place if the gas temperature and/or gas composition of an ideal gas is fluctuating, e.g. due to equivalence ratio fluctuations. In contrast, the second term on the RHS corresponds to mass flow fluctuations of the combustion products \dot{m}'_h and reactants \dot{m}'_c . The last term on the RHS represents the fluctuation of the internal energy in the control volume due to the flame movement.

Using the relation of the FTM22-element ($FTM_{22} = u'_h / u'_c$), Eq. 6.20 can be

rearranged according to Eq. 6.21:

$$\begin{aligned}
 \frac{\Delta_R \dot{H}^{0r}}{\Delta_R \dot{H}^0} &= \frac{(h-h^0)'_h - (h-h^0)'_c}{-(\overline{h_h^0} - \overline{h_c^0})} \\
 &+ \frac{u'_c \left[\bar{\rho}_h FTM_{22} (\overline{h-h^0})_h - \bar{\rho}_c (\overline{h-h^0})_c \right]}{-\bar{\rho}_c \bar{u}_c (\overline{h_h^0} - \overline{h_c^0})} \\
 &+ \frac{u'_c (\bar{\rho}_c - \bar{\rho}_h FTM_{22}) \left[\bar{\rho}_h (\overline{e_i - e_i^0})_h + \Delta_R \bar{e}_{i,v}^0 - \bar{\rho}_c (\overline{e_i - e_i^0})_c \right]}{\bar{\rho}_h - \bar{\rho}_c} \frac{1}{-\bar{\rho}_c \bar{u}_c (\overline{h_h^0} - \overline{h_c^0})}.
 \end{aligned} \tag{6.21}$$

From the third term on the RHS of Eq. 6.21 it can be seen that for a moving flame and a different density of the combustion reactants and products, the internal energy in the control volume is fluctuating resulting in a modulation of the overall heat release fluctuation.

The multimicrophone method used for the determination of flame transfer function in this work only provides the relations of the acoustic quantities up- and downstream of the flame, e.g. p' and u' . Consequently, the first term on the RHS of Eq. 6.21 can not be obtained with the purely acoustic multimicrophone method as it depends on fluctuations in gas composition and temperature. It should be mentioned that for a perfectly premixed flame, the first term on the RHS could be neglected because no equivalence ratio fluctuations are present.

The derivation of a purely acoustic formulation for the flame transfer function from Eq. 6.21 can only be made by assuming that the enthalpy fluctuations in the first term on the RHS are small compared to the second and third term containing the fluctuations of enthalpy and internal energy due to mass flow fluctuations up- and downstream of the flame, as well as the flame movement, respectively.

An estimation if this assumption is justified can be made by assuming quasi steady behavior, e.g. for frequencies close to zero, and equivalence ratio fluctuations being present. Furthermore, values for the FTM22-element have to be assumed, because the resulting velocity fluctuation downstream of the flame u'_h is not known a priori. If a flame at rest would be considered, the FTM22-element could be theoretically obtained from the mass conservation in Eq. 6.8 due to the flame movement being zero ($u'_s = 0$). The estimation on

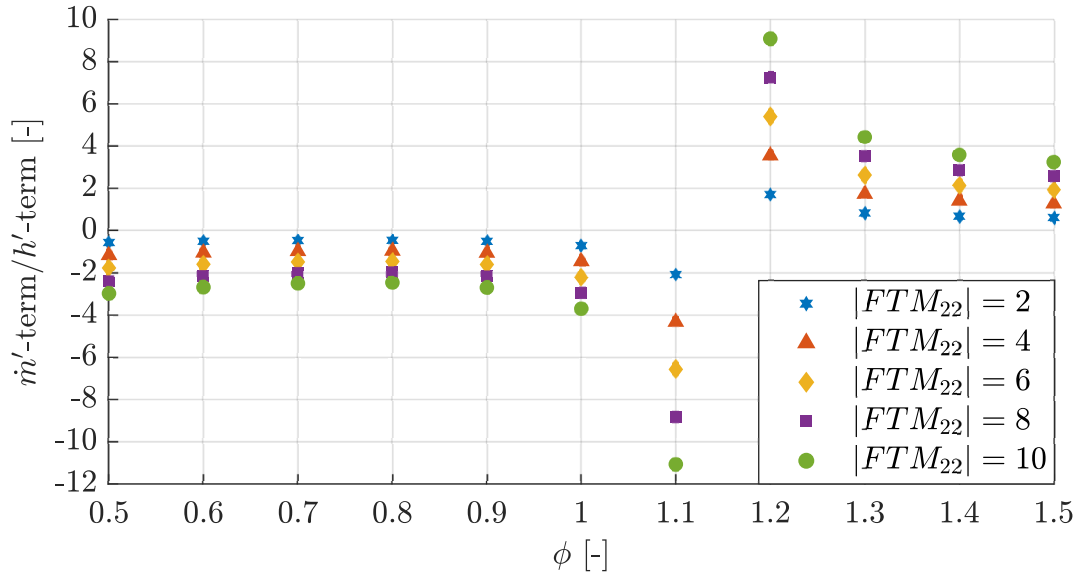


Figure 6.7: Contribution of the m' -term compared to the h' -term to the overall heat release fluctuation in Eq. 6.21 for an air preheating temperature of $T_a = 423\text{K}$ for varying equivalence ratios and FTM22-amplitudes.

the contribution of the terms on the RHS in Eq. 6.21 is based on thermodynamic equilibrium conditions in *Cantera* for a relative velocity fluctuation of the preheated air ($T_a = 423\text{K}$) of $u'_a/\bar{u}_a = 10\%$, a constant fuel mass flow of a kerosene surrogate ($\dot{m}'_f = 0$) and for varying FTM22-amplitudes and equivalence ratios.

Fig. 6.7 illustrates the obtained ratio of the second two terms (m' -term) to the first term (h' -term) on the RHS of Eq. 6.21 against the equivalence ratio for varying FTM22-amplitudes. The following conclusions can be made from Fig. 6.7. For FTM22-amplitudes of $FTM_{22} \geq 4$, the contribution of the m' -term to the heat release fluctuation in Eq. 6.21 is always equal or greater than the contribution of the h' -term. At combustion conditions near the maximum adiabatic flame temperature ($\phi(T_{ad,max}) = 1.07$), the contribution of the h' -term is much smaller than that of the m' -term. Furthermore, for fuel rich combustion conditions the ratio of the m' to the h' -term is generally higher compared to the lean combustion regime. The reason for the behavior of the h' -term in Fig. 6.7 is mainly due to the domination of the adiabatic flame temperature

fluctuation used for the calculation of the specific enthalpy of the combustion products in Eq. 6.21. Due to this, the contribution of the h' -term near the peak of the adiabatic flame temperature is very low. Additionally, the sign of the m' - and h' -term is the same for fuel rich combustion conditions meaning that both terms increase the heat release fluctuation if the air mass flow is increasing, while for lean combustion conditions the sign and correspondingly the effect on the heat release fluctuation is opposite.

The experimentally obtained FTM22-amplitudes for the primary zone investigations for low Strouhal numbers $Sr \leq 0.07$ exhibit average values between 6.8 and 7.7, depending on the equivalence ratio. Furthermore, the estimation on the contribution of the h' -term in Fig. 6.7 on the overall heat release fluctuation was based on assuming maximum equivalence ratio fluctuations for a constant fuel mass flow. Considering that non-premixed flames are locally burning predominantly near stoichiometric combustion conditions (most reactive mixture fraction), the estimation based on a maximum global equivalence ratio fluctuation made above can be considered as a worst case scenario. Due to this, the assumption of neglecting the h' -term in Eq. 6.21 seems to be justified, especially for near stoichiometric and fuel rich combustion conditions. It should be mentioned that the formulation for the FTF out of the FTM22-element using the classic Rankine-Hugoniot relations does not account for the enthalpy fluctuations or h' -term too.

Finally, the formulation for the alternative flame transfer function FTF_{AN} from the FTM22-element can be obtained from Eq. 6.21, resulting in Eq. 6.22:

$$\underbrace{\frac{\Delta_R \dot{H}^{0'} \bar{u}_c}{\Delta_R \dot{H}^0 \bar{u}'_c}}_{FTF_{AN}} = \frac{\bar{\rho}_h FTM_{22} \left(\overline{h - h^0} \right)_h - \bar{\rho}_c \left(\overline{h - h^0} \right)_c}{-\bar{\rho}_c \left(\overline{h_h^0 - h_c^0} \right)} + \frac{(\bar{\rho}_c - \bar{\rho}_h FTM_{22}) \left[\bar{\rho}_h \left(\overline{e_i - e_i^0} \right)_h + \Delta_R \bar{e}_{i,v}^0 - \bar{\rho}_c \left(\overline{e_i - e_i^0} \right)_c \right]}{\bar{\rho}_h - \bar{\rho}_c \quad -\bar{\rho}_c \left(\overline{h_h^0 - h_c^0} \right)}. \quad (6.22)$$

The sensible specific enthalpies $\overline{h - h^0}$ and sensible specific internal energies

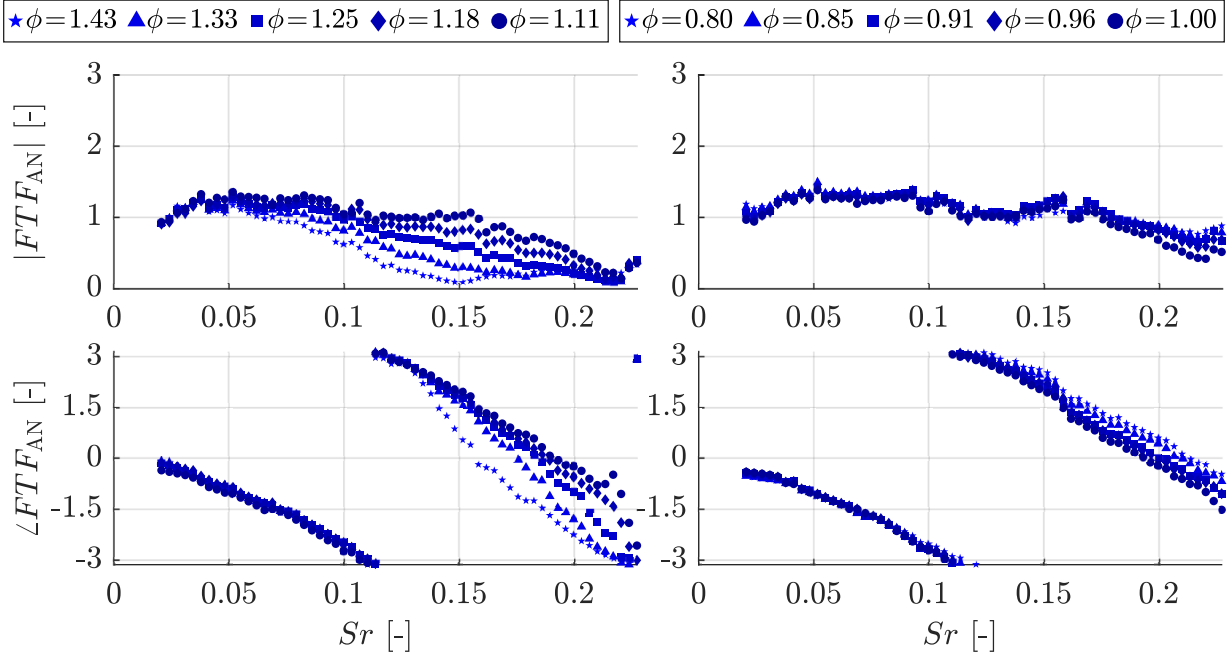


Figure 6.8: FTF amplitudes (top) and phases (bottom) for rich (left) and lean (right) equivalence ratios, an air preheating temperature of $T_{a,PZ} = 423\text{K}$ and a pressure loss of $\Delta p_{a,PZ}/p_{a,PZ} \approx 4\%$ obtained with the purely acoustic MMM and the alternative approach using Eq. 6.22 for the determination of the FTF from the FTM22-element (cf. Fig. 6.1).

$\overline{e_i - e_i^0}$ of the mean flow can be expressed by Eq. 6.23 and 6.24, respectively:

$$\overline{h - h^0} = \bar{c}_p \Big|_{T^0}^T (T - T^0), \quad (6.23)$$

$$\overline{e_i - e_i^0} = \bar{c}_v \Big|_{T^0}^T (T - T^0). \quad (6.24)$$

Equation 6.22 can be converted to the classic Rankine-Hugoniot relations of Eq. 4.10 by assuming that there is no change in gas composition, no temperature dependence of the gas properties, no flame movement and by simulating the heat release rate as external heat added to the system.

The resulting FTF_{AN} obtained from the FTM22-element using Eq. 6.22 are illustrated in Fig. 6.8 for all rich and lean operating points of the isolated primary zone (cf. Fig. 6.1). The properties of the combustion reactants and products of the mean flow in Eq. 6.22 were calculated for thermodynamic equilib-

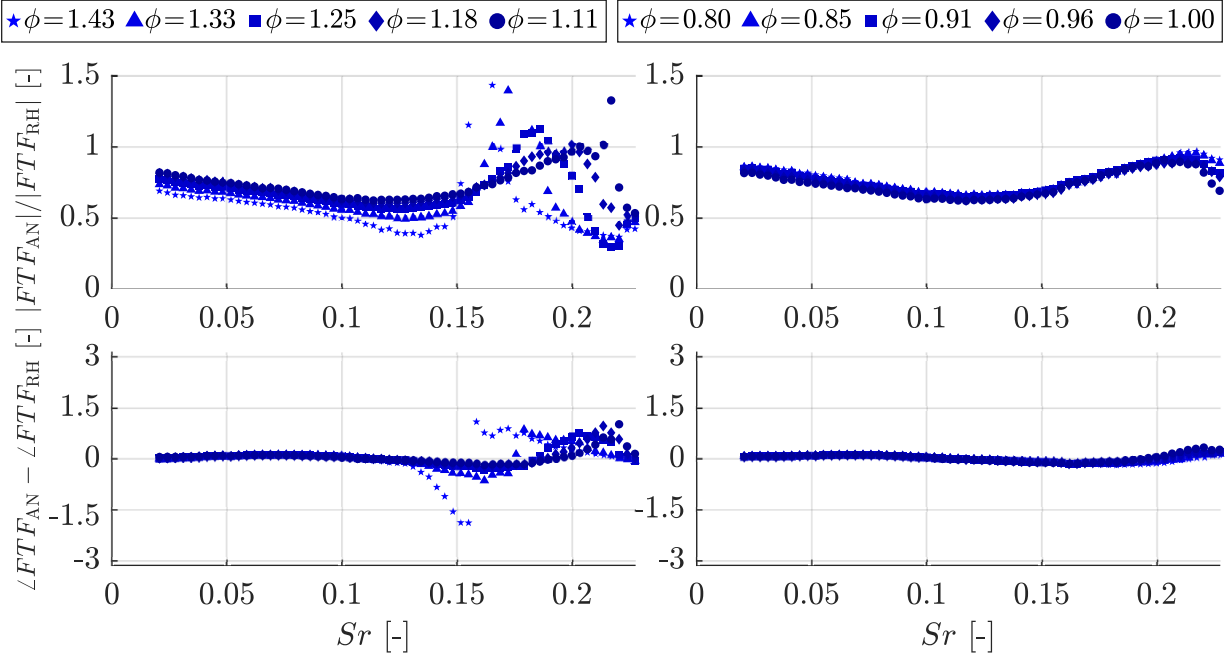


Figure 6.9: Ratio of the FTF_{AN} - and FTF_{RH} -amplitudes on top and phase difference on bottom for all rich (left) and lean (right) operating points of the isolated primary zone.

rium conditions in *Cantera*, using Dagaut’s mechanism for a kerosene surrogate [76].

Comparing Fig. 6.8 with Fig. 6.1 it can be seen that the amplitudes of the FTFs obtained with Eq. 6.22 are substantially lower, while the phases seem to agree very well. However, the diminishing FTF-amplitude with increasing equivalence ratio for the fuel rich operating points is still present for the FTFs in Fig. 6.1 calculated with the alternative FTF formulation of Eq. 6.22. A direct quantification of the differences in amplitude and phase between the FTF_{AN} , according to Eq. 6.22, and the FTF_{RH} , using the classic Rankine-Hugoniot relations according to Eq. 4.10, is shown in Fig. 6.9.

Figure 6.9 reveals that the phases of the FTFs do not change significantly, especially for low Strouhal numbers. Some higher deviations are visible at Strouhal numbers with very low FTF amplitudes and phase jumps. In contrast, the ratio of the FTF amplitudes shows a dependency on frequency, with the highest deviations being present in the mid range of the Strouhal numbers. Furthermore, the richer the operating point, the higher the deviation of the FTF_{AN}

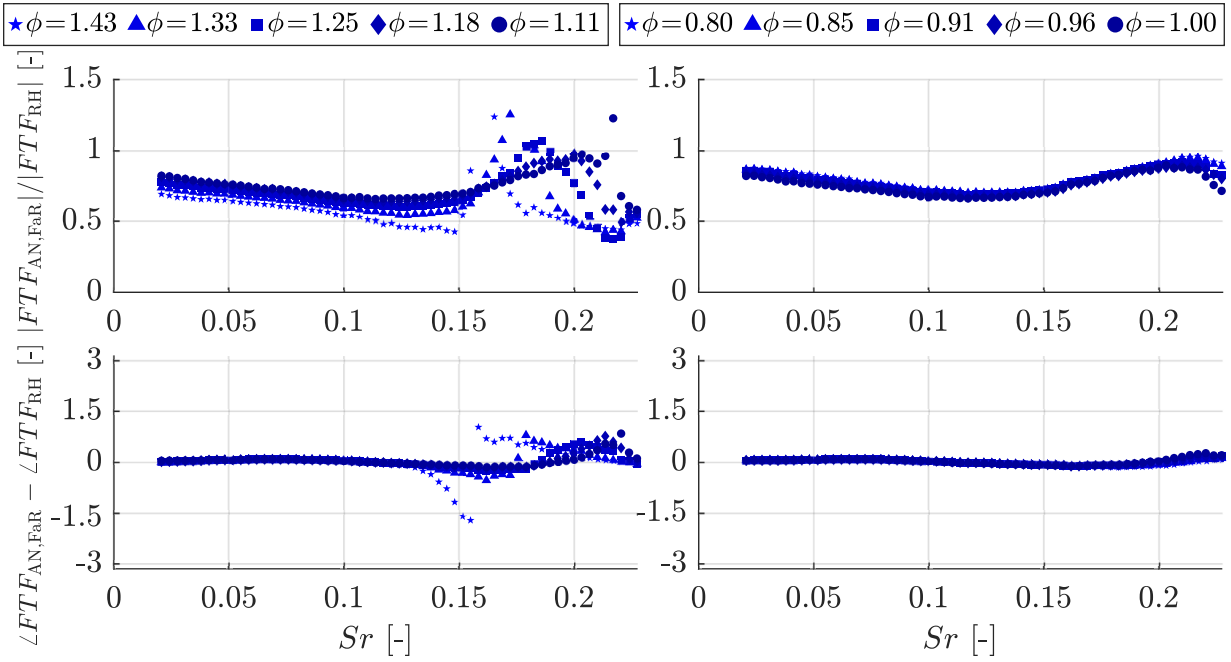


Figure 6.10: Ratio of the $FTF_{AN, FaR}$ - and FTF_{RH} -amplitudes on top and phase difference on bottom for all rich (left) and lean (right) operating points of the isolated primary zone.

compared to the FTF_{RH} obtained with the classic Rankine-Hugoniot relations (maximum deviation of approximately 50%). This seems to be justified, as the gas composition of the combustion products is increasingly different compared to the reactants as the combustion becomes richer.

The FTF using Eq. 6.22 does account for the effects due to the chemical conversion, the temperature dependencies of the gas properties, e.g. specific heat capacity, as well as the flame movement. To visualize the contribution of the flame movement to the alternative FTF formulation in Eq. 6.22, the second term on the RHS is omitted, leading to Eq. 6.25 and providing the FTF from the FTM22-element for a flame at rest (FaR) $FTF_{AN, FaR}$:

$$FTF_{AN, FaR} = \frac{\bar{\rho}_h FTM_{22} \left(\overline{h - h^0} \right)_h - \bar{\rho}_c \left(\overline{h - h^0} \right)_c}{-\bar{\rho}_c \left(\overline{h_h^0 - h_c^0} \right)}. \quad (6.25)$$

Figure 6.10 shows the ratio of the alternative FTF obtained with Eq. 6.25 under neglect of the flame movement compared to the FTF using the classic Rankine-Hugoniot relations. By comparing Fig. 6.10 with Fig. 6.9 it can be seen

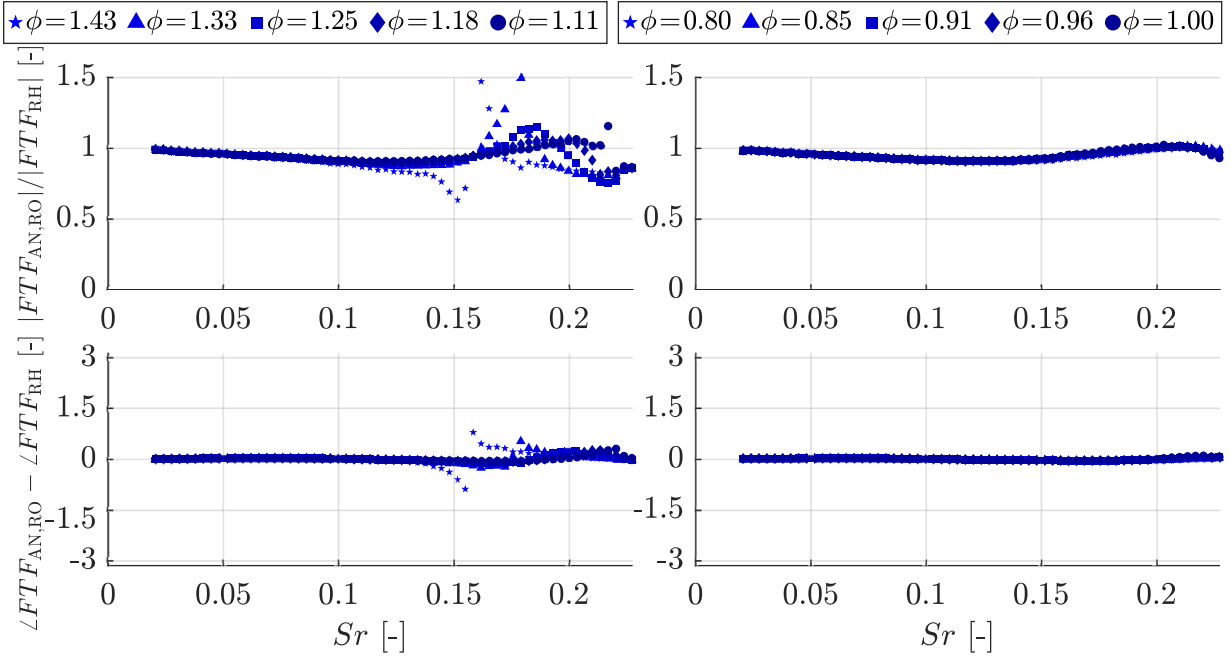


Figure 6.11: Ratio of the $FTF_{AN,RO}$ - and FTF_{RH} -amplitudes on top and phase difference on bottom for all rich (left) and lean (right) operating points of the isolated primary zone.

that the second term on the RHS of Eq. 6.22, which represents the flame movement, has minor influence on the overall FTF for the primary zone's flame investigated in this work. However, in general the influence of the flame movement on the resulting FTFs depends on the characteristics of the flame being investigated and can not be neglect in general.

The determination of the FTF using Eq. 6.25 does still consider both, the effect due to the chemical conversion, as well as the temperature dependence of the gas properties, e.g. specific heat capacity. The influence of the chemical conversion on the FTF can be obtained by considering only the temperature dependencies of the specific heat capacity, but by assuming only the reactants (air and fuel) being present up- and downstream of the flame, leading to the $FTF_{AN,RO}$ for the reactants only (RO) in Eq. 6.26:

$$FTF_{AN,RO} = \frac{FTM_{22} \bar{c}_{p,c}(T_h) - \bar{c}_{p,c}(T_c)}{\bar{c}_{p,c}(T_h) \frac{T_h}{T_c} - \bar{c}_{p,c}(T_c)}. \quad (6.26)$$

In Eq. 6.26 $FTF_{AN,RO}$ is the flame transfer function from the FTM22-element

considering only the temperature dependence of the gas properties, but assuming the same gas composition up- and downstream of the flame.

The resulting deviations using Eq. 6.26 for the determination of the FTF compared to the classic Rankine-Hugoniot FTF are illustrated in Fig. 6.11. Comparing Fig. 6.10 and 6.11 it can be seen that due to the neglect of the chemical conversion the alternative FTF (Eq. 6.26) and classic Rankine-Hugoniot FTF (Eq. 4.10) are very similar. In other words, considering only the temperature dependence of the gas properties does not alter the resulting alternative FTF substantially, neither phase nor amplitude. The consideration of the chemical conversion across the flame therefore dominates the resulting difference between the classic FTF_{RH} and the alternative FTF_{AN} in Fig. 6.9 and is due to change in gas composition, as well as change in molar quantity.

As a conclusion, the determination of the FTF from the FTM22-element for near stoichiometric and fuel-rich kerosene flames using the classic Rankine-Hugoniot relations can lead to substantial errors, especially regarding the FTF amplitude. Using the alternative approach presented in this section, more reliable results can be obtained, even if thermodynamic equilibrium conditions are assumed downstream of the flame. The assumption of thermodynamic equilibrium is still closer to the real conditions in gas turbine combustors than the neglect of chemical conversion and temperature dependence of the gas properties using the classic Rankine-Hugoniot relations. However, the alternative FTF formulation provided in this section can be seen as an extension to the classic Rankine-Hugoniot relations, incorporating more detailed physics of the flame dynamics in terms of FTFs.

6.4 Optical Flame Transfer Functions

The suitability of the different radicals mentioned in Section 5.2 (OH^* , CH^* , C_2^* , and CO_2^*) as potential measures for representing heat release fluctuations is presented in the following. The purely acoustically measured FTF_{RH} (Fig. 6.1) serves for the validation of the optically measured FTF_{hyb} (cf. Section 4.3.3). The hybrid FTF was calculated for each of the radicals using the same operating points as for the acoustic FTFs. Figure 6.12 depicts the resulting FTF_{hyb} for one rich $\phi_{PZ} = 1.25$ and one lean $\phi_{PZ} = 0.91$ operating point for each of the radicals in comparison to the acoustic FTF_{RH} . Both operating points

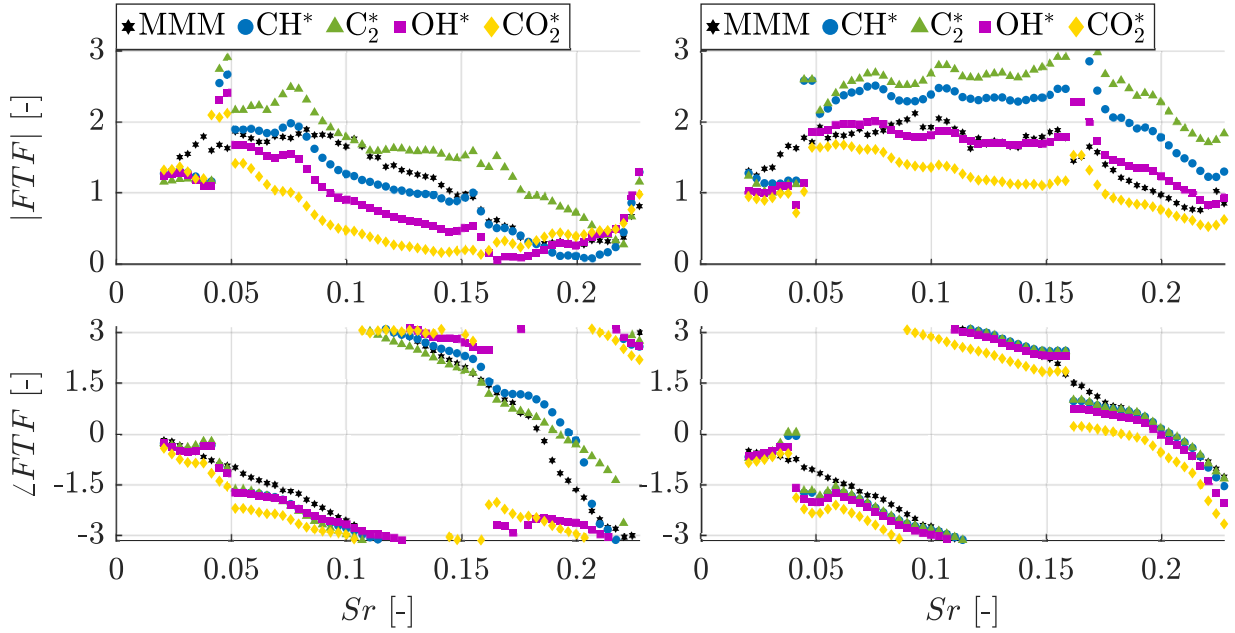


Figure 6.12: Comparison of the purely acoustically measured FTF_{RH} with the optically measured FTF_{hyb} using OH*, CH*, C₂*, and CO₂* for one rich $\phi_{PZ} = 1.25$ (left) and one lean $\phi_{PZ} = 0.91$ (right) operating point with the same adiabatic flame temperature.

have the same adiabatic flame temperature.

A qualitative agreement for the amplitudes between all four optically measured FTF_{hyb} and acoustically measured FTF_{RH} can be identified in Fig. 6.12. However, the absolute values of the FTF_{hyb} amplitudes differ from those of the FTF_{RH} . For example, the CH* FTF_{hyb} amplitudes for the rich operating point are quantitatively in line with the FTF_{RH} amplitudes (Fig. 6.12 left). In contrast, for the lean operating point this is not the case for CH* anymore, but instead the OH* FTF_{hyb} amplitudes are quantitatively in good agreement with the acoustic FTF_{RH} amplitudes (Fig. 6.12 right). For the rich and lean operating points the order from the highest to the lowest $|FTF_{RH}|$ values remains the same: 1.) C₂*, 2.) CH*, 3.) OH*, and 4.) CO₂*. The first three chemiluminescence species were not corrected for the background radiation of CO₂*. For this reason, the FTF_{hyb} amplitude of CO₂* always exhibits the smallest values, as the remaining radicals are a superposition of CO₂* and the corresponding individual intensity, e.g. OH* + CO₂*. In addition, it can be seen in 6.12 that the intensity of the amplitudes of OH* + CO₂* are lower than those of CH* + CO₂*

and $C_2^* + CO_2^*$. These findings are in line with the typical chemiluminescence spectrum of kerosene flames shown in Fig. 2.3.

Some outliers for the optically measured amplitudes can be seen for both operating points at a Strouhal number of $Sr \approx 0.04$ and $Sr \approx 0.17$. Very small velocity fluctuations at the burner outlet of $u'_{BO} / \bar{u}_{BO} \approx 5\%$ lead to rather high amplitude values for the optically FTF_{hyb} . Due to the not fully anechoic boundary conditions of the test rig there are always frequency ranges with low acoustic pressure fluctuations at the sensor locations. The low signal level leads to a poor reconstruction of the acoustic wavefield and, consequently acoustic velocity fluctuation u'_{BO} . The most crucial step during the evaluation of the optical FTF is the determination of the acoustic velocity fluctuation u'_{BO} , which needs a high quality BTM and the acoustic wavefield upstream the burner during measurements with flame as input.

In contrary to the amplitudes, the phases in Fig. 6.12 agree very well with the acoustically measured ones for both, rich and lean operating conditions. Outliers regarding the phases for the OH^* - and CO_2^* -radical can be seen for the rich operating point at a Strouhal number of $Sr \approx 0.17$ due to the low chemiluminescence intensity.

A linear regression was performed between the amplitudes of the FTF_{hyb} and

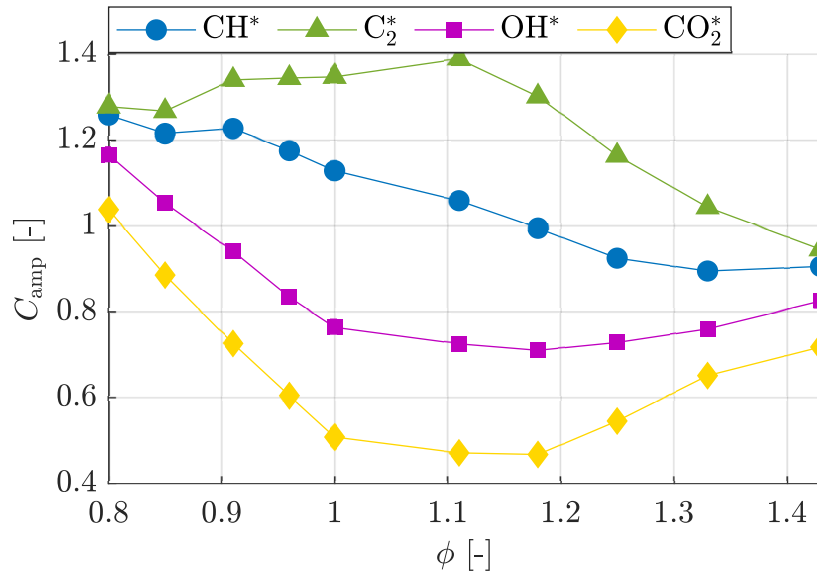


Figure 6.13: Amplitude calibration factor C_{amp} for the optically measured FTF_{hyb} related to the purely acoustically measured FTF_{RH} .

the FTF_{RH} for every operating point ϕ_{PZ} resulting in a calibration factor for each radical according to Eq. 6.27:

$$|FTF_{hyb}(\phi)| = C_{amp}(\phi) |FTF_{RH}(\phi)|. \quad (6.27)$$

The calibration factors $C_{amp}(\phi)$ were calculated up to Strouhal numbers of $Sr = 0.155$ because of the poor signal-to-noise ratio and/or scattering for higher frequencies of the optically measured FTF. However, the application of the calibration factors should give quantitative good results for all investigated radicals. Figure 6.13 illustrates the results for the amplitude calibration factor $C_{amp}(\phi)$ over the equivalence ratio ϕ_{PZ} .

Figure 6.13 shows that there is no calibration factor independent of the equivalence ratio for any of the radicals. However, quantitatively good results for the optically measured FTF can be obtained by using the chemiluminescence signal of CH^* without the need of a calibration factor for rich and near stoichiometric combustion conditions in non-premixed kerosene flames. In contrary, for lean conditions the OH^* -signal is more suitable to get quantitatively good FTF_{hyb} amplitudes. Considering the FTFs obtained with the alternative formulation in Sec. 6.3 (Fig. 6.8), the CO_2^* -signal seems to be the most suitable for representing heat release and fluctuations without the need of a calibration factor.

The presented results show that the application of the optical measurement technique has the potential to avoid the complex setup of the purely acoustic MMM for FTF measurements, assuming the velocity fluctuations at the burner outlet u'_{BO} of a given non-premixed kerosene injector is known (e.g. from CTA-measurements or burner modeling).

7 Compact RQL Combustor Flame Dynamics

In this chapter, the thermoacoustic behavior of the compact RQL combustor with both combustion zones located in one of the two combustion chambers is studied. First, an analytical approach to transfer the flame dynamics of the isolated primary and secondary zone based on the superposition of the heat release fluctuations is explained. Next, the measurement data obtained for the compact RQL combustor is evaluated. The corresponding operating points and flame images of the RQL flame are given. Subsequently, an acoustic network model and an evaluation approach to extract the primary zone flame dynamics from the compact RQL flame dynamics will be discussed. The validation of the model and evaluation technique based on one dimensional acoustic approximations is conducted in the following section by comparing the burner transfer matrix of the isolated primary zone to that in the compact RQL combustor. In the following section the purely acoustically investigated flame dynamics of the primary zone of the RQL combustor are compared to the flame dynamics of the isolated primary zone. First, operating points with a stoichiometric and fuel-rich primary zone are investigated to clarify whether the flame dynamics of the isolated primary zone can be transferred to the compact RQL combustor. Second, the primary zone under stoichiometric and fuel-lean combustion conditions will be compared to the RQL primary zone. The results of the experimental study will clarify whether the isolated flame dynamics can be transferred to the compact RQL combustor and which combustion zone dominates the overall thermoacoustics.

7.1 Transfer of the Isolated Flame Dynamics

The FTFs presented in Fig. 6.1 correspond to the isolated primary zone. The flame dynamics of the isolated secondary zone were also studied on the same test rig with respect to the velocity fluctuations of the cross-flow as well as the

dilution holes [47]. The FTFs obtained for the isolated secondary zone showed a strongly decreasing FTF amplitude against frequency with maximum values of approximately unity for both excitation modes (acoustic excitation of the cross-flow or the dilution holes).

In real aero engines the primary and secondary zone are located close to each other in one combustion chamber, referred to as a compact RQL combustor. Due to this, the relation between the primary and secondary zone flame dynamics and the compact RQL combustor is of major, practical interest. Based on the isolated measurements in the primary and secondary zone, an approach and the corresponding assumptions for estimating the contribution of the individual zones to the overall flame dynamics in a compact RQL combustor will be given in the following.

The total heat release of the compact RQL combustor \dot{Q}_{RQL} can be expressed as the heat release in the primary \dot{Q}_{PZ} plus the heat release in the secondary zone \dot{Q}_{SZ} , according to Eq. 7.1:

$$\dot{Q}_{\text{RQL}} = \dot{Q}_{\text{PZ}} + \dot{Q}_{\text{SZ}}. \quad (7.1)$$

Considering a linear behavior of heat release, the heat release fluctuations \dot{Q}' can be linearized around a mean value \bar{Q} , leading to Eq. 7.2 and 7.3:

$$\dot{Q}'_{\text{RQL}} = \dot{Q}'_{\text{PZ}} + \dot{Q}'_{\text{SZ}}, \quad (7.2)$$

$$\bar{Q}_{\text{RQL}} = \bar{Q}_{\text{PZ}} + \bar{Q}_{\text{SZ}}. \quad (7.3)$$

The mean heat release or reaction enthalpy of the individual combustion zones can be linked to the total heat release using the equivalence ratio in the primary zone for $\phi_{\text{PZ}} \geq 1$, which results in Eq. 7.4 and 7.5:

$$\bar{Q}_{\text{PZ}} = \bar{Q}_{\text{RQL}} \frac{1}{\phi_{\text{PZ}}}, \quad (7.4)$$

$$\bar{Q}_{\text{SZ}} = \bar{Q}_{\text{RQL}} \left(1 - \frac{1}{\phi_{\text{PZ}}} \right). \quad (7.5)$$

Dividing Eq. 7.2 by the total mean heat release of the compact RQL combustor \bar{Q}_{RQL} and inserting Eq. 7.4 and 7.5 leads to Eq. 7.6:

$$\frac{\dot{Q}'_{\text{RQL}}}{\bar{Q}_{\text{RQL}}} = \frac{\dot{Q}'_{\text{PZ}}}{\bar{Q}_{\text{PZ}}} \frac{1}{\phi_{\text{PZ}}} + \frac{\dot{Q}'_{\text{SZ}}}{\bar{Q}_{\text{SZ}}} \left(1 - \frac{1}{\phi_{\text{PZ}}} \right). \quad (7.6)$$

In Eq. 7.6 $\dot{Q}'_{PZ}/\bar{Q}_{PZ}$ and $\dot{Q}'_{SZ}/\bar{Q}_{SZ}$ are the relative heat release fluctuations of the isolated primary and secondary zone. It can be seen that the relative heat release fluctuations from the isolated measurements of the primary and secondary zone have to be weighed by the equivalence ratio when combining them in the compact RQL combustor.

The heat release fluctuation in the secondary zone can potentially react to velocity fluctuations from the cross-flow between the two zones (int) and the dilution holes (DH). Both heat release responses can be summed up as the total relative heat release response in the secondary zone, resulting in Eq. 7.7:

$$\frac{\dot{Q}'_{SZ}}{\bar{Q}_{SZ}} = \frac{\dot{Q}'_{DH,SZ}}{\bar{Q}_{SZ}} + \frac{\dot{Q}'_{int,SZ}}{\bar{Q}_{SZ}}. \quad (7.7)$$

Assuming that $\dot{Q}'_{DH,SZ}/\bar{Q}_{SZ}$ is coupled to velocity fluctuations from the dilution holes only and $\dot{Q}'_{int,SZ}/\bar{Q}_{SZ}$ to velocity fluctuations from the cross-flow only, results in two linearly superposed FTFs for the secondary zone, given in Eq. 7.8:

$$\frac{\dot{Q}'_{SZ}}{\bar{Q}_{SZ}} = FTF_{DH,SZ} \frac{u'_{DH}}{\bar{u}_{DH}} + FTF_{int,SZ} \frac{u'_{int}}{\bar{u}_{int}}. \quad (7.8)$$

In contrast to the secondary zone, the primary zone's FTF links the heat release fluctuation of the primary zone's flame to the relative velocity fluctuation at the burner outlet (BO), according to Eq. 7.9:

$$\frac{\dot{Q}'_{PZ}}{\bar{Q}_{PZ}} = FTF_{PZ} \frac{u'_{BO}}{\bar{u}_{BO}}. \quad (7.9)$$

Inserting Eqs. 7.9 and 7.8 in Eq. 7.6 yields Eq. 7.10:

$$\frac{\dot{Q}'_{RQL}}{\bar{Q}_{RQL}} = FTF_{PZ} \frac{u'_{BO}}{\bar{u}_{BO}} \frac{1}{\phi_{PZ}} + \left(FTF_{DH,SZ} \frac{u'_{DH}}{\bar{u}_{DH}} + FTF_{int,SZ} \frac{u'_{int}}{\bar{u}_{int}} \right) \left(1 - \frac{1}{\phi_{PZ}} \right). \quad (7.10)$$

The values for the different FTFs in Eq. 7.10 can be obtained from isolated measurements in the primary and secondary zone. For the secondary zone, isolated FTFs showed maximum amplitudes of $|FTF_{DH,SZ}| \approx 1$ and $|FTF_{int,SZ}| \approx 1$ for low frequencies and both excitation modes (cross-flow and dilution holes) [47]. Furthermore, a rapid drop in the FTF amplitude was observed with values being lower than $|FTF_{SZ}| < 0.5$ from approximately 250 Hz

onward [47]. In contrast, the amplitudes of the isolated primary zone presented in Fig. 6.1 exhibit amplitudes up to $|FTF_{PZ}| \approx 2$.

The assessment of the relative velocity fluctuations in Eq. 7.10 is based on further assumptions and measurement input. Assuming low frequencies and an air mass flow distribution of $\dot{m}_{a,PZ}/\dot{m}_{a,SZ} \approx 1$, the relative velocity fluctuations at the burner outlet and the dilution holes have similar amplitudes and are nearly in phase ($u'_{BO}/\bar{u}_{BO} \approx u'_{DH}/\bar{u}_{DH}$).

The relative velocity fluctuation from the cross flow u'_{int}/\bar{u}_{int} can be estimated with the help of the measurements in isolated primary zone. The FTM22-element of the isolated primary zone relates the velocity fluctuation at the burner outlet u'_{BO} to the velocity fluctuation downstream the flame u'_{int} and showed average amplitude values of $|FTM_{22,PZ}| \approx 7$ for the lowest acoustic excitation frequencies ($Sr \leq 0.05$). Regarding the mean flow velocity at the burner outlet and downstream of the primary flame, the density change across the flame must be considered ($\bar{\rho}_{BO}/\bar{\rho}_{int} \approx 3.73$). Consequently, the ratio of the relative velocity fluctuation between the two combustion zones u'_{int}/\bar{u}_{int} to that at the burner outlet u'_{BO}/\bar{u}_{BO} is calculated to approx. 1.6. Again it is assumed that the relative velocity fluctuations are in phase due to the long wavelengths in the low-frequency range.

Equation 7.10 can now be rearranged considering all the information and assumptions regarding the relative velocity fluctuations described above, leading to Eq. 7.11:

$$\underbrace{\frac{\dot{Q}'_{RQL} \bar{u}_{BO}}{\bar{Q}_{RQL} u'_{BO}}}_{FTF_{RQL}} = FTF_{PZ} \frac{1}{\phi_{PZ}} + \left(FTF_{DH,SZ} + FTF_{int,SZ} FTM_{22,PZ} \frac{\bar{\rho}_{int}}{\bar{\rho}_{BO}} \right) \left(1 - \frac{1}{\phi_{PZ}} \right). \quad (7.11)$$

Finally, the maximum contribution from the primary and secondary zone to the overall flame dynamics of the compact RQL combustor can be calculated by additionally assuming that all three FTFs of Eq. 7.11 are in phase. Considering an operating point with an equivalence ratio of $\phi_{PZ} = 1.25$ reveals that the contribution of the primary zone flame dynamics in a compact RQL combustor is approximately three times higher than that of the secondary zone, according to Eq. 7.11 and the assumptions described above.

Table 7.1: Equivalence ratios for the investigations of the compact RQL combustion chamber.

$\phi_{\text{PZ,RQL}} [-]$	$\phi_{\text{RQL}} [-]$
1.43	0.64
1.33	0.60
1.25	0.56
1.18	0.53
1.11	0.50
1.00	0.45

7.2 Measured Flame Dynamics

In Section 7.1 an estimation on the contribution from the primary and secondary zone to the overall flame dynamics based on the isolated measurements was given. However, the estimation was based on several assumptions without further proof. Due to this, thermoacoustic measurements of the compact RQL combustor were also performed to provide a reliable insight into the contribution of the primary and secondary zone to the overall RQL flame dynamics. Furthermore, it will be clarified whether a linear superposition of the isolated flame dynamics from the primary and secondary zone in the compact RQL arrangement is valid. The corresponding evaluation method and results are described in the following.

7.2.1 Operating Points and Flame Images

The operating conditions of the compact RQL arrangement are based on those of the isolated primary zone (cf. Section 4.3.1). A constant preheating temperature for the primary and secondary air of $T_{\text{a,PZ}} = T_{\text{a,SZ}} = 423 \text{ K}$ and a pressure loss of $\Delta p_{\text{a,PZ}}/p_{\text{a,PZ}} \approx 4\%$ across the primary burner and $\Delta p_{\text{a,SZ}}/p_{\text{a,SZ}} \approx 2.5\%$ across the dilution holes was used. The equivalence ratios for the primary zone in the compact RQL arrangement and the resulting overall equivalence ratios are given in Tab. 7.1. The same primary zone equivalence ratios were studied for the isolated primary zone setup ($\phi_{\text{PZ,RQL}} = \phi_{\text{PZ}}$, cf. Section 4.3.1). An overview of the experimental setup for the investigation of the RQL combustor on the test rig is given in Section 3.3. Figure 7.1 illustrates the cross

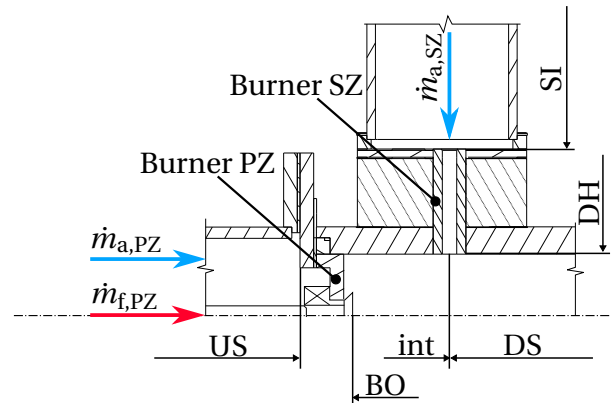


Figure 7.1: Simplified cross section of the compact RQL combustor with mass flows, as well as relevant reference positions.

section of the compact RQL burner, the corresponding mass flows, and the reference positions. As measurement technique, the purely acoustic multimicrophone method was used in combination with an acoustic excitation from upstream (US) and downstream (DS), as well as the dynamic pressure measurements and acoustic wavefield reconstruction in all impedance measurement ducts, e.g. upstream, downstream and on the side (cf. Section 4.3.2).

Figure 7.2 depicts the flame images of the isolated primary zone (bottom) and the compact RQL combustor (top) for an equivalence ratio in the primary zone of $\phi_{PZ} = \phi_{PZ,RQL} = 1.43$ and $\phi_{PZ} = \phi_{PZ,RQL} = 1.00$. The images were taken with a digital camera (*Canon EOS M50*) and averaged over time. From Fig. 7.2 it is clearly visible that the flame of the isolated primary zone exhibits a different behavior compared to the flame in the compact RQL combustor. Especially the fuel-rich operating point shows nearly no sooting behavior in the presence of the additionally injected secondary air. Furthermore, the compact RQL flame in the primary zone appears to be closer to the burner outlet, and the jets of the secondary flame are only barely visible for the fuel-rich operating point. The shift of the flame closer to the burner outlet was already observed for the lean operating points of the isolated primary zone (cf. Section 5.3). For this reason, the assumption could be made that secondary air is sucked into the primary zone via the inner recirculation zone, leading to a fuel-lean primary flame. However, the following thermoacoustic investigations will provide further insight and proof.

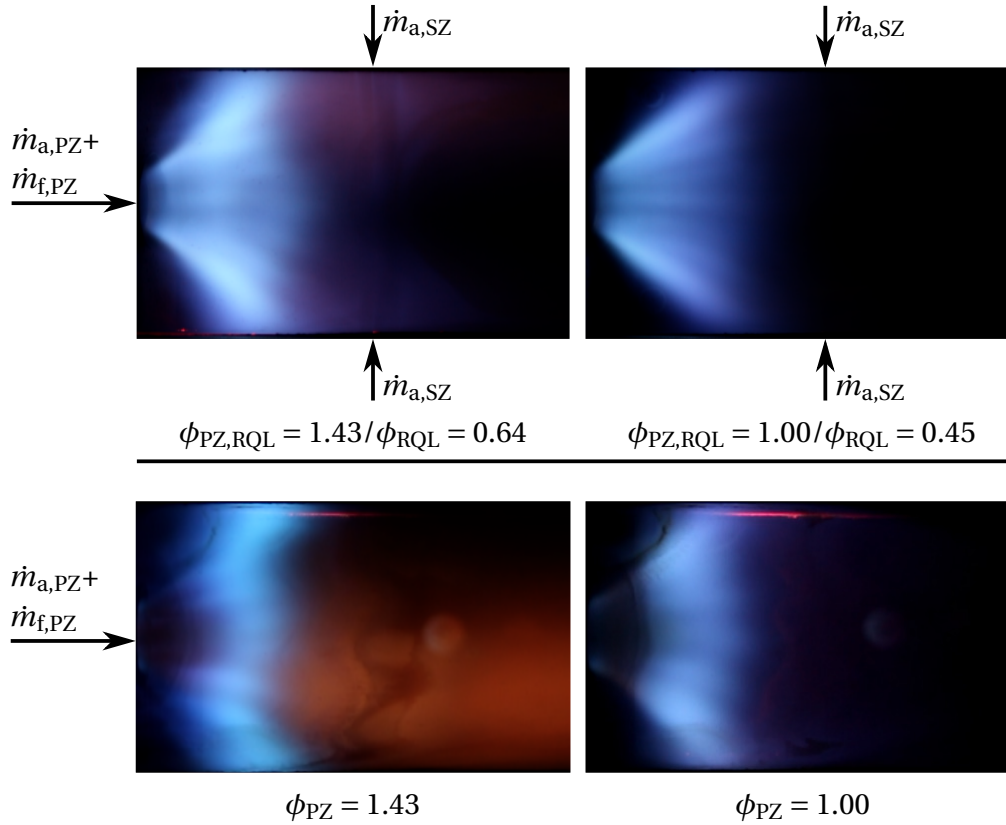


Figure 7.2: Flame images of the compact RQL flame (top) and isolated primary zone flame (bottom) for an equivalence ratio in the primary zone of $\phi_{PZ} = \phi_{PZ,RQL} = 1.43$ (left) and $\phi_{PZ} = \phi_{PZ,RQL} = 1.00$ (right).

7.2.2 Compact RQL Model and Evaluation Method

Fig. 7.3 illustrates the 1D acoustic model of the compact RQL combustion chamber as an acoustic three-port by using the burner and flame transfer matrix \mathbf{BFTM}_{RQL} (upper half of Fig. 7.3). Upstream of the primary zone burner p'_{US} and u'_{US} are considered as acoustic variables, while upstream of the dilution holes p'_{SI} and u'_{SI} describe the acoustics of the dilution air in the side ducts (cf. Figures 3.6 and 7.1). Assuming symmetric injection and acoustics of the dilution air, only one side branch of the dilution air has to be considered. Downstream of the RQL combustor, p'_{DS} and u'_{DS} are used to represent the acoustics of the hot combustion gases leaving the combustion chamber. The RQL model can be further divided when assuming that the acoustic three-port model of the RQL combustor \mathbf{BFTM}_{RQL} is a superposition of the primary

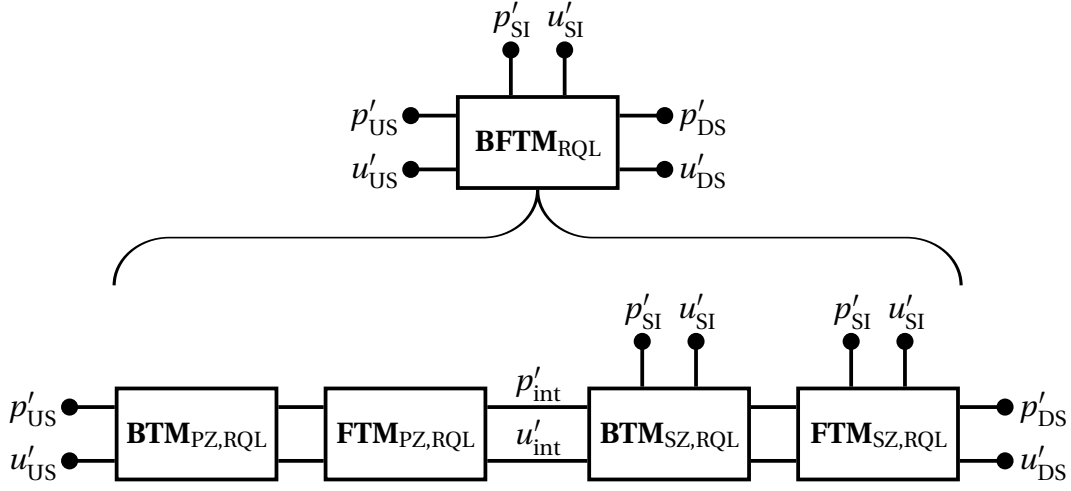


Figure 7.3: Acoustic network model of the RQL combustor ($\mathbf{BFTM}_{\text{RQL}}$) as linear combination of the burner and flame transfer matrix of the primary zone ($\mathbf{BTM}_{\text{PZ,RQL}}$ and $\mathbf{FTM}_{\text{PZ,RQL}}$), as well as the burner and flame transfer matrix of the secondary zone ($\mathbf{BTM}_{\text{SZ,RQL}}$ and $\mathbf{FTM}_{\text{SZ,RQL}}$).

and secondary zone. Consequently, the burner and flame in the primary zone can be described by the acoustic two-port elements $\mathbf{BTM}_{\text{PZ,RQL}}$ and $\mathbf{FTM}_{\text{PZ,RQL}}$, respectively. Furthermore, the burner transfer matrix $\mathbf{BTM}_{\text{SZ,RQL}}$ of the dilution holes and the secondary flame $\mathbf{FTM}_{\text{SZ,RQL}}$ are considered to be acoustic three-ports. Downstream of the primary flame, the intermediate acoustic variables p'_{int} and u'_{int} are acoustically coupling the primary and secondary zone. With the given assumptions, the compact RQL combustion chamber can be expressed by Eq. 7.12:

$$\begin{aligned} \mathbf{BFTM}_{\text{RQL}} &= \mathbf{BFTM}_{\text{SZ,RQL}} \cdot \mathbf{BFTM}_{\text{PZ,RQL}} \\ &= \mathbf{FTM}_{\text{SZ,RQL}} \cdot \mathbf{BTM}_{\text{SZ,RQL}} \cdot \mathbf{FTM}_{\text{PZ,RQL}} \cdot \mathbf{BTM}_{\text{PZ,RQL}}. \end{aligned} \quad (7.12)$$

The proof of whether the assumed superposition in Eq. 7.12 is permissible is provided by comparing the measurements of the isolated primary zone (\mathbf{BTM}_{PZ} and \mathbf{FTM}_{PZ} , cf. Section 6.1) with those of the primary zone in the compact RQL environment ($\mathbf{BTM}_{\text{PZ,RQL}}$ and $\mathbf{FTM}_{\text{PZ,RQL}}$). In addition, it will be demonstrated which combustion zone, primary or secondary zone, domi-

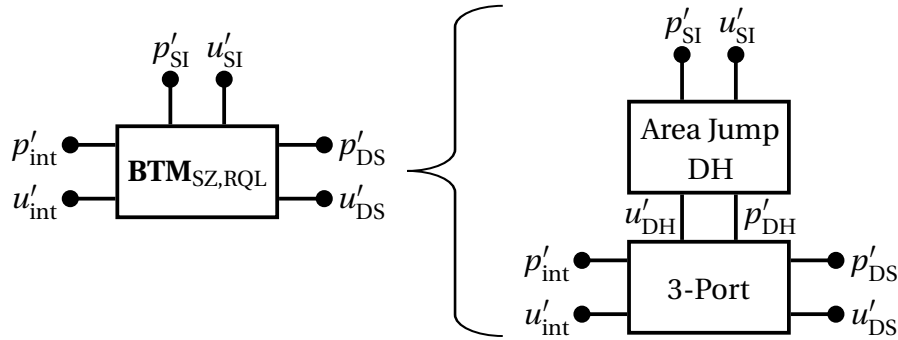


Figure 7.4: Acoustic network model of the secondary zone burner $\mathbf{BTM}_{\text{SZ,RQL}}$ with the dilution holes represented as an acoustic area jump and the acoustic three-port inside the RQL combustion chamber.

nates the overall thermoacoustic behavior of the compact RQL combustor.

For the isolation of $\mathbf{BTM}_{\text{PZ,RQL}}$ and $\mathbf{FTM}_{\text{PZ,RQL}}$ of the primary zone in the compact RQL arrangement, the intermediate acoustic variables p'_{int} and u'_{int} have to be determined analytically, as the dynamic pressure sensors can not be positioned between the two combustion zones. Due to this, the burner of the secondary zone $\mathbf{BTM}_{\text{SZ,RQL}}$ will be modeled using a 1D acoustic approach.

The secondary zone burner can be split into the transfer behavior of the dilution holes and a connected acoustic three-port, shown in Fig. 7.4 (cf. Fig. 7.1). The dilution holes are represented by an area jump, which relates the acoustic variables in the side duct at the entrance to the dilution holes (p'_{SI} and u'_{SI}) to those at the exit of the dilution holes inside the RQL combustor (p'_{DH} and u'_{DH}). In addition, the acoustic three-port describes the interaction between the downstream (p'_{DS} and u'_{DS}), the dilution (p'_{DH} and u'_{DH}) and the intermediate acoustic variables (p'_{int} and u'_{int}). The application of the multi-microphone method during the experimental investigations of the compact RQL combustor is limited to the location upstream of the primary burner (US), downstream (DS) and on the side of the RQL combustor (SI). Due to this, the intermediate acoustic variables and the acoustic variables at the exit of the dilution holes cannot be obtained experimentally. The acoustic relations describing the transfer behavior of the secondary zone burner are obtained by using the following assumptions:

- 1D acoustic waves

- Acoustic compactness
- Neglection of products of fluctuating quantities (e.g. $\rho' u'$)
- Neglection of terms of the order $\mathcal{O}(Ma^2)$
- Incompressible flow

Under the given assumptions, the mass conservation for the acoustic three-port in Fig. 7.4 can be obtained, according to Eq. 7.13:

$$A_{DS} \left(\frac{p'_{DS}}{c_{DS}} Ma_{DS} + \bar{\rho}_{DS} u'_{DS} \right) = A_{int} \left(\frac{p'_{int}}{c_{int}} Ma_{int} + \bar{\rho}_{int} u'_{int} \right) + A_{DH} \left(\frac{p'_{DH}}{c_{DH}} Ma_{DH} + \bar{\rho}_{DH} u'_{DH} \right). \quad (7.13)$$

In case of low Mach numbers ($Ma \approx 0$) Eq. 7.13 can be simplified and rearranged for u'_{int} resulting in Eq. 7.14:

$$u'_{int} = \frac{A_{DS} \bar{\rho}_{DS} u'_{DS} - A_{DH} \bar{\rho}_{DH} u'_{DH}}{A_{int} \bar{\rho}_{int}}. \quad (7.14)$$

Furthermore, the momentum equation of the acoustic three port for $Ma \approx 0$ and the isentropic exponent $\kappa \approx \text{const.}$ reveals a constant pressure in all three acoustic branches, given in Eq. 7.15:

$$p'_{DS} = p'_{int} = p'_{DH}. \quad (7.15)$$

From Eqs. 7.14 and 7.15 it can be seen that the acoustic velocity fluctuation at the exit of the dilution holes u'_{DH} is still unknown. The determination of u'_{DH} can be performed by using the mass conservation of an isothermal area jump, according to Eq. 7.16:

$$u'_{DH} = Ma_{SI} \frac{A_{SI}}{A_{DH}} \left(\frac{p'_{SI}}{\bar{\rho}_{SI} c_{SI}} - \frac{p'_{DH}}{\bar{\rho}_{DH} c_{DH}} \right) + \frac{A_{SI}}{A_{DH}} u'_{SI}. \quad (7.16)$$

Usually the first term on the RHS of Eq. 7.16 is very small compared to the second term. This assumption was validated during the evaluation process of the experimental data and confirmed. Due to this, Eq. 7.16 simplifies to Eq. 7.17:

$$u'_{DH} = \frac{A_{SI}}{A_{DH}} u'_{SI}. \quad (7.17)$$

Finally, u'_{int} can be determined by inserting Eq. 7.17 in Eq. 7.14, resulting in Eq. 7.18:

$$u'_{\text{int}} = \frac{A_{\text{DS}}\bar{\rho}_{\text{DS}}u'_{\text{DS}} - 2A_{\text{SI}}\bar{\rho}_{\text{SI}}u'_{\text{SI}}}{A_{\text{int}}\bar{\rho}_{\text{int}}}. \quad (7.18)$$

For simplicity, in Eq. 7.18 the mean density inside the dilution holes $\bar{\rho}_{\text{DH}}$ was already considered to be the same as the density at the entrance of the dilution holes $\bar{\rho}_{\text{SI}}$. The total effective cross section of the dilution holes per side is referred to as A_{DH} (two rows of dilution holes $A_{i,\text{DH}}$ per side $\Rightarrow A_{\text{DH}} = 2A_{i,\text{DH}}$). Therefore, the additional factor of 2 in Eq. 7.18 considers that in the RQL combustor setup two rows of dilution holes are located on two opposing side walls (cf. Section 3.1.3). Consequently, the mass flow fluctuations of the secondary air have to be doubled (symmetric four-port).

In the RQL combustor setup investigated in the current work, the cross section of the combustion chamber is constant ($A_{\text{DS}} = A_{\text{int}}$). In addition, the cross section of the side duct is only 0.9% larger than that of the combustion chamber ($A_{\text{SI}} \approx A_{\text{DS}}$). As a consequence, Eq. 7.18 can be further simplified to Eq. 7.19:

$$u'_{\text{int}} = \frac{\bar{\rho}_{\text{DS}}u'_{\text{DS}} - 2\bar{\rho}_{\text{SI}}u'_{\text{SI}}}{\bar{\rho}_{\text{int}}}. \quad (7.19)$$

It should be mentioned that the variables in Eqs. 7.13 - 7.19 are calculated on the corresponding reference positions according to Fig. 7.1. For comparison with the measurements of the isolated primary zone, p'_{int} and u'_{int} must be shifted from the location of the secondary zone to the burner outlet of the primary zone in the compact arrangement, using Eqs. 7.21 and 7.20:

$$\frac{p'_{\text{BO}}}{\rho_{\text{int}}c_{\text{int}}} = \frac{1}{2} \frac{p'_{\text{DS}}}{\rho_{\text{int}}c_{\text{int}}} \left(e^{-ik_{\text{int}}^+\Delta x} + e^{ik_{\text{int}}^-\Delta x} \right) + \frac{1}{2} u'_{\text{int}} \left(e^{-ik_{\text{int}}^+\Delta x} - e^{ik_{\text{int}}^-\Delta x} \right), \quad (7.20)$$

$$u'_{\text{BO}} = \frac{1}{2} \frac{p'_{\text{DS}}}{\rho_{\text{int}}c_{\text{int}}} \left(e^{-ik_{\text{int}}^+L} - e^{ik_{\text{int}}^-L} \right) + \frac{1}{2} u'_{\text{int}} \left(e^{-ik_{\text{int}}^+L} + e^{ik_{\text{int}}^-L} \right). \quad (7.21)$$

An alternative approach for the calculation of the acoustic velocity at the exit of the dilution holes u'_{DH} as input for Eq. 7.14 is the momentum or Bernoulli equation for an acoustic area jump, given in Eq. 7.22:

$$u'_{\text{DH}} = \frac{\frac{p'_{\text{SI}}}{\bar{\rho}_{\text{SI}}c_{\text{SI}}} - \frac{p'_{\text{DH}}}{\bar{\rho}_{\text{DH}}c_{\text{DH}}} + Ma_{\text{SI}}u'_{\text{SI}}}{Ma_{\text{DH}}(1 + \zeta)}. \quad (7.22)$$

From Eq. 7.15 we obtain $p'_{\text{DH}} = p'_{\text{DS}}$, while the loss coefficient can be set to $\zeta \approx 1$ if Ma_{DH} refers to the maximum mean velocity inside the dilution holes \bar{u}_{DH} . The latter can be obtained by knowing the measured pressure loss over the dilution holes and using the Bernoulli equation for mean quantities. The third term in the nominator of Eq. 7.22 is usually very small due to low Mach numbers. Consequently, Eq. 7.22 can be simplified to Eq. 7.23:

$$u'_{\text{DH}} = \frac{p'_{\text{SI}} - p'_{\text{DS}}}{2\bar{\rho}_{\text{SI}}c_{\text{SI}}Ma_{\text{DH}}}. \quad (7.23)$$

In theory, the transfer behavior of an acoustic three-port can be obtained purely experimentally by using the multimicrophone method and three independent test cases, e.g. excitation from upstream (A), downstream (B) and from the side (C). With this approach, the above modeling is not necessary and the full 3x3 transfer matrix is directly obtained from the evaluation of the measurement data. However, during the evaluation of the measurement data of the compact RQL study it was observed that the acoustic excitation level in the upstream duct is too weak when forcing the test rig with the loudspeakers in the side duct and vice versa. Consequently, the acoustic wavefield reconstruction using the multimicrophone method showed high errors (cf. Eq. 4.15) and the results were not reliable for the determination of the 3x3 transfer matrix. Only during excitation from downstream, the quality of the acoustic wavefield in all impedance measurement ducts was acceptable. The reason for this behavior is most probably associated with the pressure losses of the primary burner and the dilution holes. Considering an excitation from upstream, the acoustic waves have to travel across the primary burner and the dilution holes before reaching the dynamic pressure sensors in the side duct, leading to substantial acoustic losses along this path.

For this reason, the determination of the transfer matrices is based on the acoustic excitation from up- and downstream (similar to the isolated primary zone measurements), as well as the modeling approach described above for the inclusion of the dilution hole acoustics and the calculation of the intermediate acoustic variables.

Obviously, the acoustic wavefield has to be reconstructed in all impedance measurement ducts (upstream, downstream and side) of the compact RQL combustor setup to apply Eqs. 7.13 - 7.23. However, due to the low signal-to-noise ratio in the side duct during excitation from upstream (A), the influence

of the dilution hole acoustics is negligible ($u'_{\text{DH}}|^{\text{A}} \approx 0 \rightarrow u'_{\text{int}}|^{\text{A}} = u'_{\text{DS}}|^{\text{A}}$). Consequently, the influence of the dilution hole acoustics on the intermediate variables was only considered during excitation from downstream (B) by using the modeling approach described above.

7.2.3 Case without Combustion

The measurements of the compact RQL combustor without combustion serve for validation of the modeling approach described in Section 7.2.2. The network model of the RQL combustor in Fig. 7.3 simplifies due to the missing flame dynamics in the primary and secondary zone ($\text{FTM}_{\text{PZ,RQL}} = 1$ and $\text{FTM}_{\text{SZ,RQL}} = 1$). As a consequence, the validation of the modeling approach is performed by comparing the burner transfer matrix of the isolated primary zone (BTM_{PZ}) to that of the primary zone in the compact arrangement ($\text{BTM}_{\text{PZ,RQL}}$). If both burner transfer matrices are the same, the modeling approach of Section 7.2.2 is appropriate as it is not expected that the transfer behavior of the primary burner changes between the isolated and compact RQL setup.

For the present case without combustion, the continuity equation of the acoustic three-port in Eq. 7.14 simplifies due to isothermal conditions in the compact RQL combustor, leading to Eq. 7.24:

$$u'_{\text{int}} = u'_{\text{DS}} - 2u'_{\text{DH}} \frac{A_{\text{DH}}}{A_{\text{DS}}}. \quad (7.24)$$

According to Section 7.2.2, two options are present for the calculation of the acoustic velocity fluctuation at the exit of the dilution holes u'_{DH} : the modeling of the dilution holes by using the mass conservation in Eq. 7.17 or the Bernoulli method in Eq. 7.23. The former approach further simplifies Eq. 7.24 to Eq. 7.25 (cf. Eq. 7.19):

$$u'_{\text{int}} = u'_{\text{DS}} - 2u'_{\text{SI}}. \quad (7.25)$$

In contrast to the intermediate velocity fluctuation u'_{int} , the pressure fluctuations remain the same due to the approximation of Eq. 7.15 ($p'_{\text{int}} = p'_{\text{DS}}$). The acoustic quantities upstream (p'_{US} and u'_{US}), downstream (p'_{DS} and u'_{DS}) and on the side (p'_{SI} and u'_{SI}) are obtained from the reconstruction of the acoustic wave field in combination with an excitation from up- and downstream.

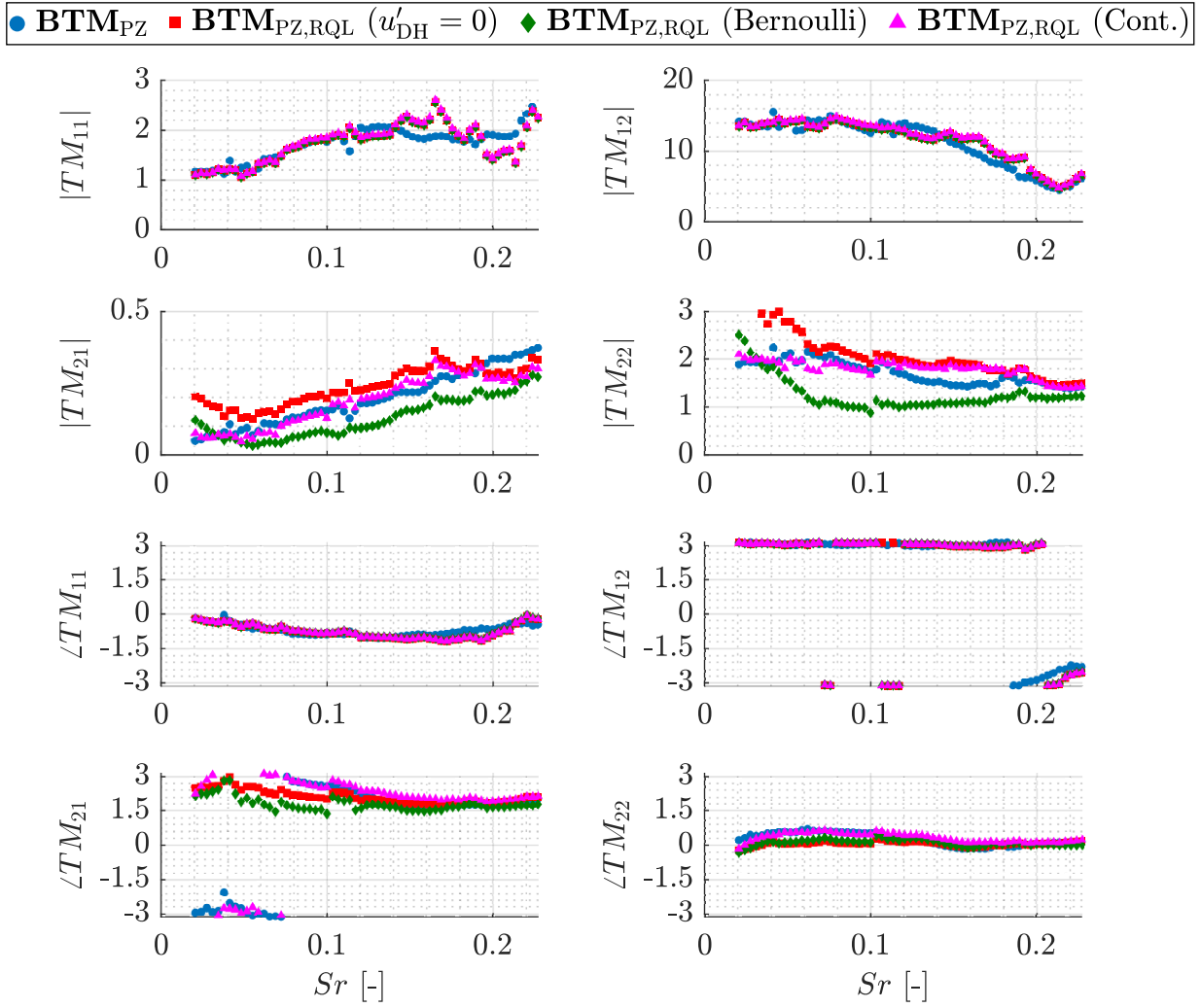


Figure 7.5: Burner transfer matrices of the isolated primary zone \mathbf{BTM}_{PZ} (blue dots), the primary zone in the compact RQL combustor without consideration of the dilution hole acoustics $\mathbf{BTM}_{\text{PZ,RQL}} (u'_{\text{DH}} = 0)$ (red squares), with consideration of the dilution holes acoustics using the Bernoulli approach $\mathbf{BTM}_{\text{PZ,RQL}} (\text{Bernoulli})$ (green diamonds) and with consideration of the dilution holes acoustics using the continuity approach $\mathbf{BTM}_{\text{PZ,RQL}} (\text{Cont.})$ (purple triangles).

Figure 7.5 illustrates the resulting elements of the burner transfer matrices of the isolated primary zone \mathbf{BTM}_{PZ} (blue dots) and the primary zone in the compact arrangement $\mathbf{BTM}_{\text{PZ,RQL}}$ without considering the acoustics of the dilution

hole (red squares, $u'_{\text{DH}} = 0, u'_{\text{int}} = u'_{\text{DS}}$). Additionally, the burner transfer matrices of the primary zone in the compact RQL combustor with consideration of the secondary burner acoustics by using the continuity approach (purple triangles $\mathbf{BTM}_{\text{PZ,RQL}} \text{ Cont.}$, Eq. 7.17) or Bernoulli approach (green diamonds $\mathbf{BTM}_{\text{PZ,RQL}} \text{ Bernoulli}$, Eq. 7.23), both together with Eq. 7.24 are shown (cf. Section 7.2.2).

The TM_{11} - and TM_{12} -element of the BTM indicate the coupling of the upstream pressure p'_{US} and velocity fluctuation u'_{US} to the pressure fluctuation downstream of the primary zone burner p'_{BO} , respectively. Analogously, the TM_{21} - and TM_{22} -element relate the upstream pressure p'_{US} and velocity fluctuation u'_{US} to the velocity fluctuation downstream of the primary burner u'_{BO} , respectively.

Several observations can be made from Fig. 7.5. Looking at the amplitude and phase of the TM_{11} - and TM_{12} -element, almost perfect agreement can be seen between the isolated and the primary zone in the compact arrangement. For this reason, the approximation of the acoustic pressure fluctuations across the acoustic three-port being constant in the axial direction is justified ($p'_{\text{int}} = p'_{\text{DS}}$ according to Eq. 7.15). The fact that all curves of the TM_{11} - and TM_{12} -element for $\mathbf{BTM}_{\text{PZ,RQL}}$ lie on top each other is related to the same approximation, which is used for all three evaluation methods with respect to the acoustic pressure. Only for higher Strouhal numbers deviations are visible due to a low acoustic signal-to-noise ratio and consequently to a low quality of the acoustic wavefield reconstruction, which was indicated by the residual error of Eq. 4.15.

Next, the TM_{21} - and TM_{22} -element of Fig. 7.5 will be investigated, which represent the acoustic velocity fluctuation at the burner outlet u'_{BO} as a function of the pressure and velocity fluctuation upstream of the burner (p'_{US} and u'_{US}). Especially the TM_{22} -element is mainly influencing the transfer behavior of the acoustic velocity fluctuation across the primary burner ($u'_{\text{BO}} = TM_{22} u'_{\text{US}}$). From the TM_{22} -element in Fig. 7.5 it can be seen that the influence of the dilution hole acoustics in the RQL combustor is only present for very low Strouhal numbers and vanishes at approx. $St \approx 0.06$. This observation can be identified by comparing the curves of the TM_{22} -element of the isolated primary zone (blue dots in Fig. 7.5) with the primary zone in the compact arrangement without considering the acoustics of the dilution holes (red squares in Fig. 7.5).

The green diamonds and purple triangles in Fig. 7.5 show the resulting burner transfer matrix of the primary zone in the RQL combustor taking into account the acoustics of the dilution holes ($\mathbf{BTM}_{\text{PZ,RQL}}$ Bernoulli and $\mathbf{BTM}_{\text{PZ,RQL}}$ Cont.). The former uses the Bernoulli method (Eq. 7.23) and the latter uses the continuity approach (Eq. 7.17) to determine the acoustic velocity fluctuation at the exit of the dilution holes u'_{DH} needed as input for Eq. 7.24. The results for the TM_{21} - and TM_{22} -element of $\mathbf{BTM}_{\text{PZ,RQL}}$ in Fig. 7.5 using the continuity method (purple triangles) are almost in perfect agreement with the curves of the isolated primary zone \mathbf{BTM}_{PZ} (blue dots). In contrast, the results for the TM_{21} - and TM_{22} -element using the Bernoulli approach (green diamonds) clearly reveal that this method provides poor results. Furthermore, the Bernoulli results are even worse than the TM_{21} - and TM_{22} -curves without consideration of the dilution hole acoustics (red squares in Fig. 7.5).

Several investigations were conducted to identify the root cause of the bad results using the Bernoulli approach (e.g. inclusion of effective and reduced length, verification of symmetric acoustic excitation in the side ducts). Finally, the acoustic pressure fluctuation at the exit of the dilution holes p'_{DH} was identified to be not the same as the pressure fluctuation p'_{DS} at the axial location of the dilution holes ($p'_{\text{DH}} \neq p'_{\text{DS}}$, cf. Eq. 7.15). The theoretical correct p'_{DH} can be calculated by using u'_{DH} from the continuity method (Eq. 7.17) and inserted in Eq. 7.23, leading to Eq. 7.26:

$$p'_{\text{DH}} = p'_{\text{SI}} - 2\bar{\rho}_{\text{SI}}c_{\text{SI}}Ma_{\text{DH}}u'_{\text{DH}}. \quad (7.26)$$

The comparison between p'_{DH} from Eq. 7.26 and p'_{DS} from the acoustic wave-field reconstruction is illustrated in Fig. 7.6. Figure 7.6 confirms that the calculated pressure fluctuation at the exit of the dilution holes p'_{DH} using Eq. 7.26 is different in amplitude and phase compared to the downstream pressure fluctuation at the axial location of the dilution holes p'_{DS} . Therefore, the assumption of Eq. 7.15 that $p'_{\text{DH}} = p'_{\text{DS}}$ does not hold for the current RQL combustor setup. This is probably due to two orthogonal plane acoustic waves hitting each other in the exit plane of the dilution holes (cf. 7.1) leading to a more complex two-dimensional acoustic field. Contrarily, the approximation of $p'_{\text{DS}} = p'_{\text{int}}$ is valid, according to the TM_{11} - and TM_{12} -element in Fig. 7.5. It should be mentioned that the influence of the wrongly approximated $p'_{\text{DH}} = p'_{\text{DS}}$ has nearly no influence on the continuity equations due to the low Mach number term in Eq. 7.13 and Eq. 7.16. As a consequence, the approach using the continuity

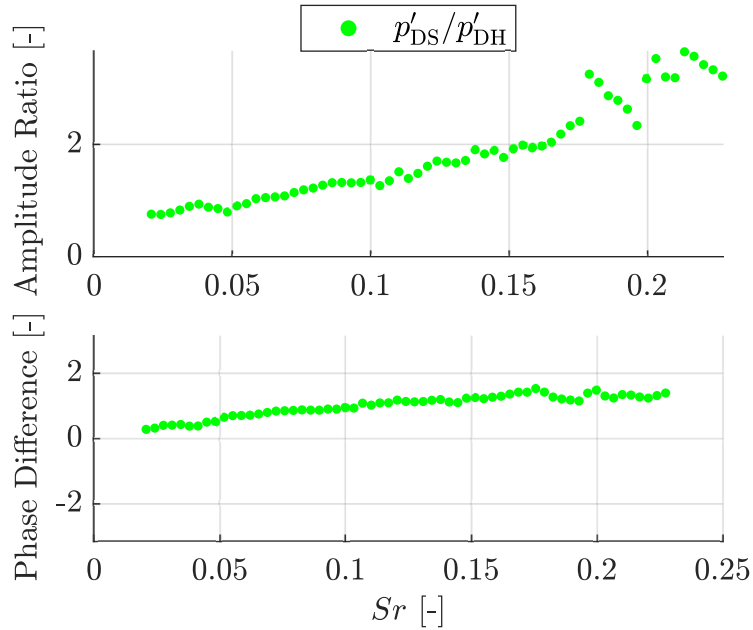


Figure 7.6: Comparison of the calculated pressure fluctuation at the exit of the dilution holes using the continuity approach p'_{DH} with the pressure fluctuation downstream at the location of the dilution holes p'_{DS} .

equations provides an accurate modeling method to assess the influence of the acoustics of the dilution holes $\mathbf{BTM}_{SZ,RQL}$ on the RQL combustor studied in this work. The investigation of the flame dynamics in the RQL combustor in the next section is therefore only considering the modeling approach using the continuity equation (Eq. 7.17).

7.2.4 Case with Combustion

In this section, the thermoacoustic behavior of the primary zone in the compact RQL combustor will be investigated. To proof whether the superposition of the primary and secondary zone flame dynamics is permissible (cf. Section 7.3 and Eq. 7.12), the measurement results of the isolated primary zone (cf. Chapter 6) will be compared to those of the primary zone in the compact RQL arrangement. If the thermoacoustic behavior of the primary zone in the isolated and the compact arrangement stays the same, the approach of linearly combining the individual flame dynamics of the primary and secondary zone is valid.

The extraction of the primary zone flame dynamics in terms of the flame transfer matrix $\mathbf{FTM}_{\text{PZ,RQL}}$ is based on the RQL model described in Section 7.2.2. According to the linear model in Fig. 7.3, the flame dynamics of the primary $\mathbf{FTM}_{\text{PZ,RQL}}$ and secondary zone $\mathbf{FTM}_{\text{SZ,RQL}}$ can be obtained by knowing the burner transfer matrices of the primary $\mathbf{BTM}_{\text{PZ,RQL}}$ and secondary zone $\mathbf{BTM}_{\text{SZ,RQL}}$. The $\mathbf{BTM}_{\text{PZ,RQL}}$ is obtained from the measurements in the isolated primary zone and is not expected to change in the compact RQL combustor ($\mathbf{BTM}_{\text{PZ,RQL}} = \mathbf{BTM}_{\text{PZ}}$). In addition, the intermediate acoustic variables p'_{int} and u'_{int} in Fig. 7.3 must be known to isolate the flame dynamics of the primary zone. Due to this, the influence of the secondary burner and dilution holes $\mathbf{BTM}_{\text{SZ,RQL}}$ on the overall RQL acoustics has to be quantified by applying the evaluation approach described in Section 7.2.2. This approach was already applied to the RQL combustor for isothermal conditions in the last Section 7.2.3 and provided good results in quantifying the influence of the secondary zone burner on the overall acoustics of the RQL combustor. However, for the current case with combustion the isothermal approximation in Eq. 7.24 is not valid anymore. Due to this, the densities in the side duct, downstream of the combustor and between the two combustion zones (intermediate) have to be considered according to Eq. 7.19. The density in the side and downstream ducts is obtained with the help of the corresponding thermocouples and the ideal gas law. In contrast, between the two combustion zones no thermocouples are present. For consistency reasons, the density downstream of the primary flame in the compact arrangement should be the same as the density downstream of the isolated primary flame, if the assumption of superposition is valid. As a consequence, $\bar{\rho}_{\text{int}}$ is assumed to be the same as the density downstream of the isolated primary combustion chamber $\bar{\rho}_{\text{DS}}$. Finally, knowing the influence of $\mathbf{BTM}_{\text{PZ,RQL}}$ and $\mathbf{BTM}_{\text{SZ,RQL}}$ on the overall acoustics of the compact RQL combustor, the flame dynamics of the primary $\mathbf{FTM}_{\text{PZ,RQL}}$ and secondary zone $\mathbf{FTM}_{\text{SZ,RQL}}$ can be extracted according to Eq. 7.12. However, both flame dynamics are still present ($\mathbf{FTM}_{\text{PZ,RQL}}$ and $\mathbf{FTM}_{\text{SZ,RQL}}$).

The following two hypotheses will be verified by comparing the measurement results of the compact RQL combustor to that of the isolated primary zone.

1. The flow field and the flame dynamics in the primary zone are not modified in the compact RQL arrangement compared to the isolated primary zone, despite the injection of secondary air ($\mathbf{FTM}_{\text{PZ,RQL}} \stackrel{?}{=} \mathbf{FTM}_{\text{PZ}}$).
2. The influence of the secondary flame on the overall RQL flame dynamics is assumed to be low ($\mathbf{FTM}_{\text{SZ,RQL}} \ll \mathbf{FTM}_{\text{PZ,RQL}} \Rightarrow \mathbf{FTM}_{\text{RQL}} \stackrel{?}{\approx} \mathbf{FTM}_{\text{PZ,RQL}}$). As a consequence, p'_{int} and u'_{int} are unaffected by the secondary zone flame dynamics, but affected by the dilution holes acoustics only ($\mathbf{BTM}_{\text{SZ,RQL}}$).

The hypotheses can be verified by comparing the flame dynamics of the primary zone in the RQL combustor with that of the isolated primary zone for the same operating conditions in the primary zone, especially the equivalence ratio ($\phi_{\text{PZ,RQL}} = \phi_{\text{PZ}}$).

The resulting FTM_{22} -elements of all operating points with a fuel-rich and stoichiometric primary zone (cf. 7.1) are presented in Fig. 7.7.

Regarding the phases of the FTM_{22} -elements in the lower half of Fig. 7.7, a similar behavior is observable between the primary zone in the compact and the isolated arrangement. The phases agree very well for Strouhal numbers up to 0.1, while above $Sr = 0.1$ an increasing deviation is observable. The higher the equivalence ratio, the more the phases between the isolated and the primary zone in the compact RQL combustor differ from each other. However, for an equivalence ratio of $\phi_{\text{PZ}} = \phi_{\text{PZ,RQL}} = 1$ the phase is almost in perfect agreement, even for $Sr > 0.1$ (green and blue triangles in Fig. 7.7).

In contrast to the phases, the amplitudes of the isolated primary zone and the compact RQL primary zone differ strongly from each other. Again, the deviation is higher, the higher the equivalence ratio in the primary zone. The increasing decay of the amplitude in the isolated primary zone with an increasing equivalence ratio is not observable for the primary zone in the compact arrangement. In the latter case, the amplitudes show the same qualitative trend for all operating points, similar to the amplitudes of the fuel-lean isolated primary zone ($\phi_{\text{PZ}} \leq 1$ in Fig. 6.1). This observation is confirmed by comparing the amplitudes of the isolated and the RQL primary zone for an equivalence ratio of $\phi_{\text{PZ}} = \phi_{\text{PZ,RQL}} = 1$ in Fig. 7.7, which show a similar amplitude trend. For the special case of a stoichiometrically operated primary zone in

7.2 Measured Flame Dynamics

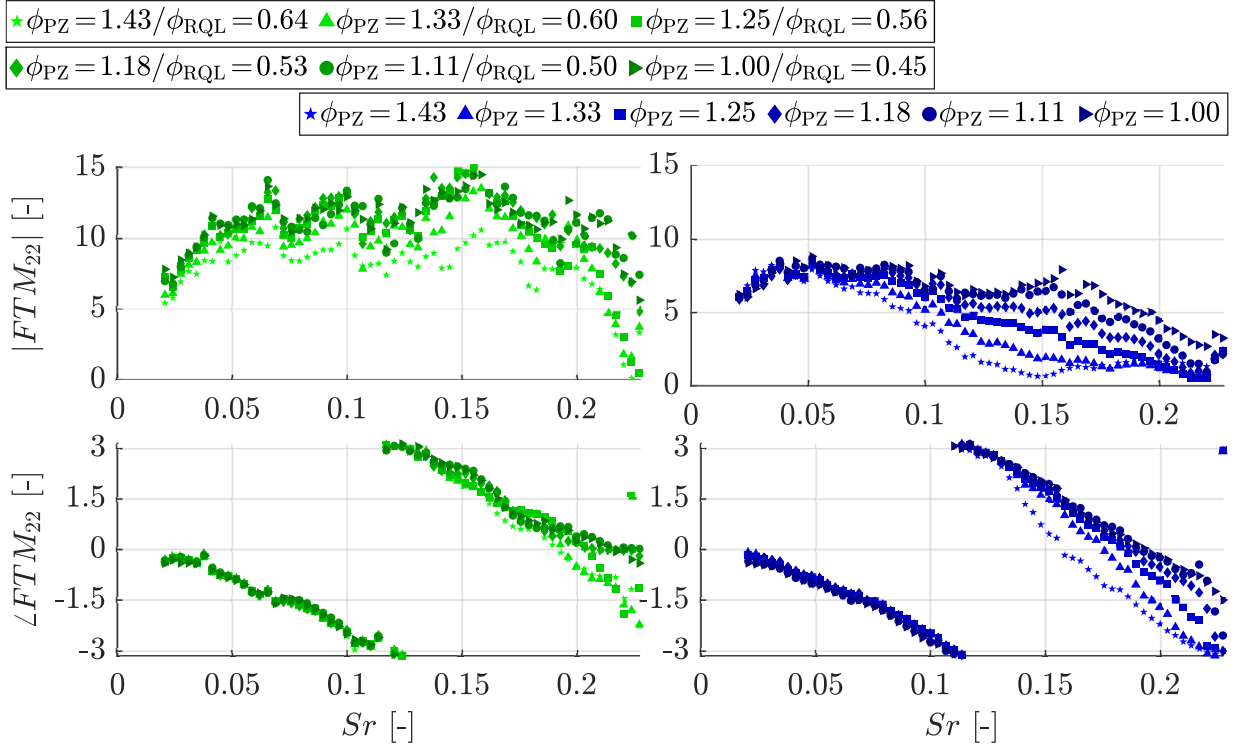


Figure 7.7: FTM_{22} amplitudes (top) and phases (bottom) of the fuel-rich and stoichiometric primary zone in the compact RQL (green symbols on the left) and the isolated primary zone arrangement (blue symbols on the right) for varying equivalence ratios in the primary zone ϕ_{PZ} .

the compact arrangement, it can be assumed that the flame dynamics in the secondary zone does not influence the flame dynamics of the primary zone. This is because there is little or no fuel transported from the primary zone to the dilution air jets in the secondary zone for $\phi_{PZ,RQL} = 1$. However, the amplitudes of the primary zone in the compact RQL combustor seem to be shifted to approximately 1.5 times higher values than in the isolated primary zone under stoichiometric combustion conditions. Due to the qualitative similarity of the amplitudes of the fuel-lean isolated primary zone and the primary zone in the compact arrangement, as well as the exclusion of the secondary zone flame dynamics for $\phi_{PZ,RQL} = 1$, it can be concluded that secondary air is sucked into the primary zone through the inner recirculation zone, resulting in a decrease in the effective equivalence ratio $\phi_{PZ,RQL}$. Consequently, the additional sec-

ondary air mixed into the primary zone leads to a lower intermediate temperature \bar{T}_{int} and increases the density $\bar{\rho}_{\text{int}}$ between the two combustion zones. The first hypothesis stated above is therefore not fulfilled and the superposition of the primary and secondary zone flame dynamics to obtain the overall flame dynamics of the RQL combustor is not permissible for a theoretically fuel-rich operated primary zone ($\mathbf{FTM}_{\text{PZ,RQL}} \neq \mathbf{FTM}_{\text{PZ}}$ for $\phi_{\text{PZ,RQL}} = \phi_{\text{PZ}} > 1$). The estimation of the secondary air being sucked into the primary zone via the inner recirculation zone can be performed by comparing the Rankine-Hugoniot relations for the FTM22-element of the primary zone in the compact RQL arrangement to that of the isolated primary zone in Eq. 7.27 (cf. Section 2.2.2):

$$\frac{FTM_{22,\text{PZ}} - 1}{FTM_{22,\text{PZ,RQL}} - 1} = \frac{\left(\frac{T_{\text{h}}}{T_{\text{c}}} - 1\right) FTF_{\text{PZ}}}{\left(\frac{T_{\text{h}}}{T_{\text{c}}} - 1\right) FTF_{\text{PZ,RQL}}}. \quad (7.27)$$

For the operating point with stoichiometric combustion conditions in Fig. 7.7 ($\phi_{\text{PZ,RQL}} = \phi_{\text{PZ}} = 1$), the FTM22-element was calculated with the assumption that no secondary air is entrained into the primary zone. Due to this, the intermediate density $\bar{\rho}_{\text{int}}$ and the flame temperature \bar{T}_{h} of the primary zone in the compact RQL arrangement were considered to be the same as for the isolated primary zone measurements ($\bar{\rho}_{\text{int}} = \bar{\rho}_{\text{DS,PZ}}$ and $T_{\text{h,PZ,RQL}} = T_{\text{h,PZ}} = T_{\text{ad}}(\phi = 1)$). Therefore, Eq. 7.27 simplifies to Eq. 7.28:

$$\frac{FTM_{22,\text{PZ}} - 1}{FTM_{22,\text{PZ,RQL}} - 1} = \frac{FTF_{\text{PZ}}}{FTF_{\text{PZ,RQL}}}. \quad (7.28)$$

Despite assuming the same combustion conditions in the isolated primary zone and the primary zone in the compact RQL combustor for $\phi_{\text{PZ,RQL}} = \phi_{\text{PZ}} = 1$, a substantial shift of the FTM22-amplitudes was observed in Fig. 7.7.

The flame transfer function of the primary zone relates the relative heat release fluctuation \dot{Q}'/\bar{Q} to the relative velocity fluctuation at the burner outlet $u'_{\text{BO}}/\bar{u}_{\text{BO}}$ (Eq. 2.39). The location at the burner outlet corresponds to the location upstream of the primary flame. The observation that secondary air is entrained into the primary zone must therefore be considered for the determination of the FTF out of the FTM22-element. Due to the additional secondary air in the primary zone, the enthalpy being transported into the flame region is higher, and consequently the heat release rate is lower according to

the energy balance across the flame (cf. Eq. 2.49). Because of the higher enthalpy flux, the corresponding mean velocity $\bar{u}_{\text{BO,PZ,RQL}}$ in the compact RQL combustor is different from that of the isolated primary zone $\bar{u}_{\text{BO,PZ}}$. A detailed derivation of the Rankine-Hugoniot relations for the consideration of additional air upstream of the flame front can be found in [102]. According to Eq. 7.28 and the made assumptions for the flame temperature and intermediate density, the ratio of the FTM22-amplitude levels on the LHS must directly correspond to the ratio of the mean velocity at the burner outlet of the primary zone when considering the classical FTF formulation of Eq. 2.39. The amount of secondary air being entrained into the primary zone in the compact RQL combustor can therefore be estimated using Eq. 7.29:

$$\frac{FTM_{22,\text{PZ}} - 1}{FTM_{22,\text{PZ,RQL}} - 1} = \frac{\bar{u}_{\text{BO,PZ}}}{\bar{u}_{\text{BO,PZ,RQL}}} = \frac{\bar{\dot{m}}_{\text{BO,PZ}}}{\bar{\dot{m}}_{\text{BO,PZ,RQL}}} = \frac{\bar{\dot{m}}_{\text{BO,PZ}}}{\bar{\dot{m}}_{\text{BO,PZ}} + \bar{\dot{m}}_{\text{BO,SZ,RQL}}}. \quad (7.29)$$

In Eq. 7.29 $\bar{\dot{m}}_{\text{BO,PZ}}$ is the mass flow across the burner of the primary zone ($\bar{\dot{m}}_{\text{BO,PZ}} = \bar{\dot{m}}_{\text{a,PZ}} + \bar{\dot{m}}_{\text{f,PZ}}$) and $\bar{\dot{m}}_{\text{BO,SZ,RQL}}$ the air mass flow from the secondary zone being entrained into the primary zone. For the present case of stoichiometric combustion conditions in the primary zone, the ratio on the LHS in Eq. 7.29 calculates to approximately 0.66. Consequently, approximately 50% of the secondary air is entrained into the primary zone of the compact RQL combustor, due to the ratio of 1:1 for the air mass flows of both combustion zones ($\bar{\dot{m}}_{\text{a,PZ}} \approx \bar{\dot{m}}_{\text{a,SZ}}$).

The correct flame dynamics of the primary zone in the compact RQL combustor have now to be recalculated by considering the amount of additional secondary air in the primary flame $\bar{\dot{m}}_{\text{BO,SZ,RQL}}$. The FTM22-element of the primary zone in the compact RQL combustor relates the acoustic velocity fluctuation at the burner outlet $u'_{\text{BO,PZ,RQL}}$ to that downstream of the primary flame u'_{int} . The intermediate velocity fluctuation u'_{int} in the compact RQL combustor depends on $\bar{\rho}_{\text{int}}$ according to Eq. 7.19. The intermediate density can be estimated by using the energy equation and considering the additional secondary air for the intermediate state temperature \bar{T}_{int} , given in Eq. 7.30:

$$\bar{T}_{\text{int}} \approx \frac{\bar{H}_{\text{DS}} - 0.5\bar{H}_{\text{SI}}}{1.5c_{\text{p,int}}\bar{\dot{m}}_{\text{a,PZ}}} + 298 \quad (7.30)$$

In Eq. 7.30, \bar{H}_{DS} is the mean enthalpy flux downstream the compact RQL combustor and \bar{H}_{SI} the enthalpy flux of the secondary air. The gas composition

needed to obtain the intermediate specific heat capacity is obtained from thermodynamic equilibrium conditions in *Cantera*. The additional factors of 0.5 and 1.5 consider that 50% of the secondary air is entrained into the primary zone and consequently alters the intermediate quantities and effective equivalence ratio. The intermediate density $\bar{\rho}_{\text{int}}$ can now be obtained by applying the ideal gas law using \bar{T}_{int} . Finally, u'_{int} is calculated according to the evaluation procedure in Section 7.2.2, which results in the FTM22-element of the primary zone in the compact RQL arrangement. The evaluation procedure shown above for a stoichiometric operating point was also applied to the remaining operating points of the RQL combustor by assuming that the entrained secondary air will remain approximately constant ($\bar{m}_{\text{BO,SZ,RQL}}(\phi) \approx \text{const.}$). Due to the additional secondary air, the fuel-rich operating point of the compact RQL combustor with a theoretical equivalence ratio of $\phi_{\text{PZ}} = 1.43$ is shifted to fuel-lean combustion conditions with an effective equivalence ratio of $\phi_{\text{PZ,RQL}} = 0.95$. More certainty on the amount of secondary air being entrainment into the primary zone of the compact RQL combustor could be obtained from an isothermal CFD calculation and analysis of the interdependent flow fields.

The FTM22-elements of the primary zone in the compact RQL combustor under consideration of the entrained secondary air are illustrated in Fig. 7.8 on the left, whereas the FTM22-elements of the lean and stoichiometric primary zone are depicted on the right.

Looking at the phases in Fig. 7.8 bottom, an almost perfect agreement is visible between the primary zone in the compact RQL combustor and the isolated primary zone. For this reason, it can be concluded that the main heat release zone remains in the primary zone and is not affected by the flame dynamics of the secondary zone, which are consequently very low ($\mathbf{FTM}_{\text{SZ,RQL}} \ll \mathbf{FTM}_{\text{PZ,RQL}}$). The FTM22-amplitudes on top of Fig. 7.8 confirm the domination of the primary zone flame dynamics in the RQL combustor (left) due to the qualitatively similar behavior to the lean and stoichiometric operated isolated primary zone (right). The second hypothesis stated above regarding the major contribution to the overall flame dynamics of the compact RQL combustor is therefore true ($\mathbf{FTM}_{\text{RQL}} \approx \mathbf{FTM}_{\text{PZ,RQL}}$). In addition, the qualitative flame dynamics of the compact RQL combustor for the equivalence ratio range investigated in this work can be obtained by measuring the iso-

7.2 Measured Flame Dynamics

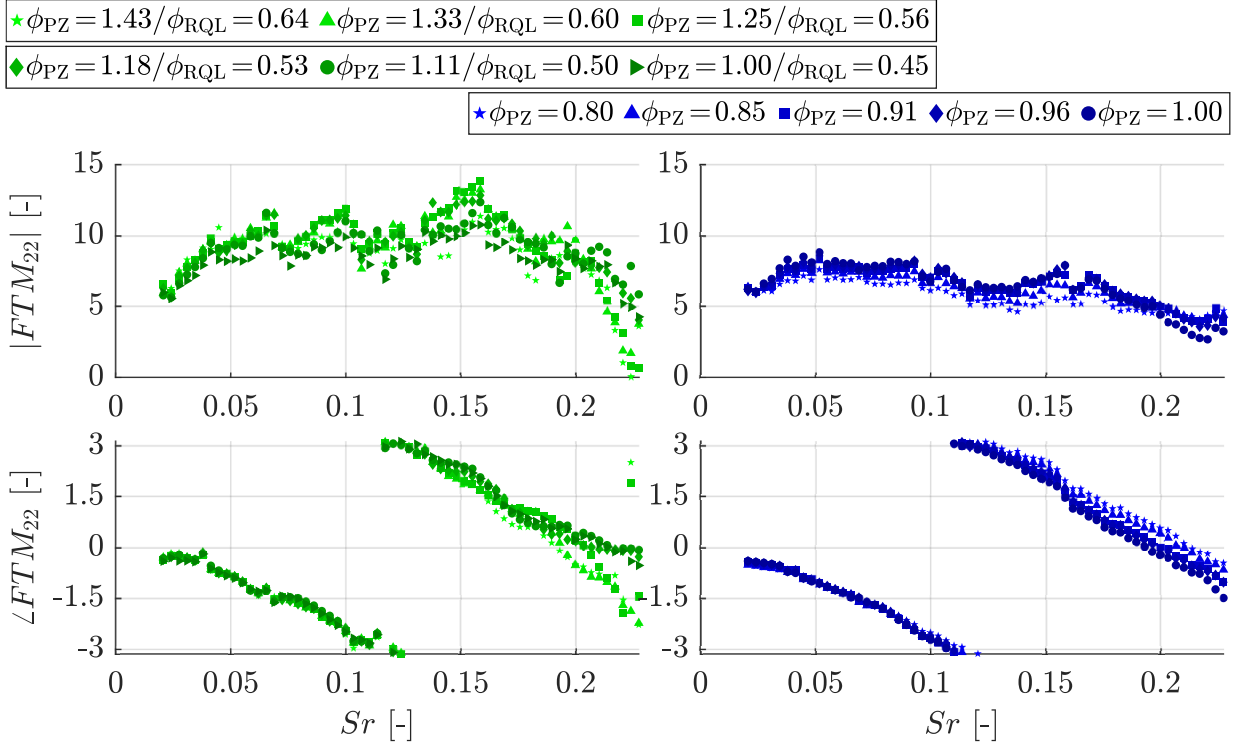


Figure 7.8: FTM_{22} -amplitudes (top) and -phases (bottom) of the primary zone in the compact RQL arrangement for varying equivalence ratios in the primary zone $\phi_{PZ,RQL}$ (green symbols on the left) and the stoichiometric and lean operated, isolated primary zone (blue symbols on the right). The FTM_{22} -amplitudes of the compact RQL combustor were calculated by considering the additional secondary air being entrained into the primary zone.

lated flame dynamics of a stoichiometric or fuel-lean operated primary zone ($\mathbf{FTM}_{RQL} \approx \mathbf{FTM}_{PZ,RQL} \propto \mathbf{FTM}_{PZ}$ for $\phi_{PZ} \leq 1$). When additionally considering the secondary air being entrained into the primary zone in the compact RQL combustor (e.g. using Eq. 7.29), the quantitative flame dynamics of the primary zone in the compact RQL arrangement can be obtained. It should be mentioned that during the evaluation of the compact RQL combustor it was observed that the consideration of the velocity fluctuation at the exit of the dilution holes u'_{DH} on the resulting FTMs is very low. Due to this, neither the secondary burner nor flame have to be considered when estimating the flame dynamics of the compact RQL combustor.

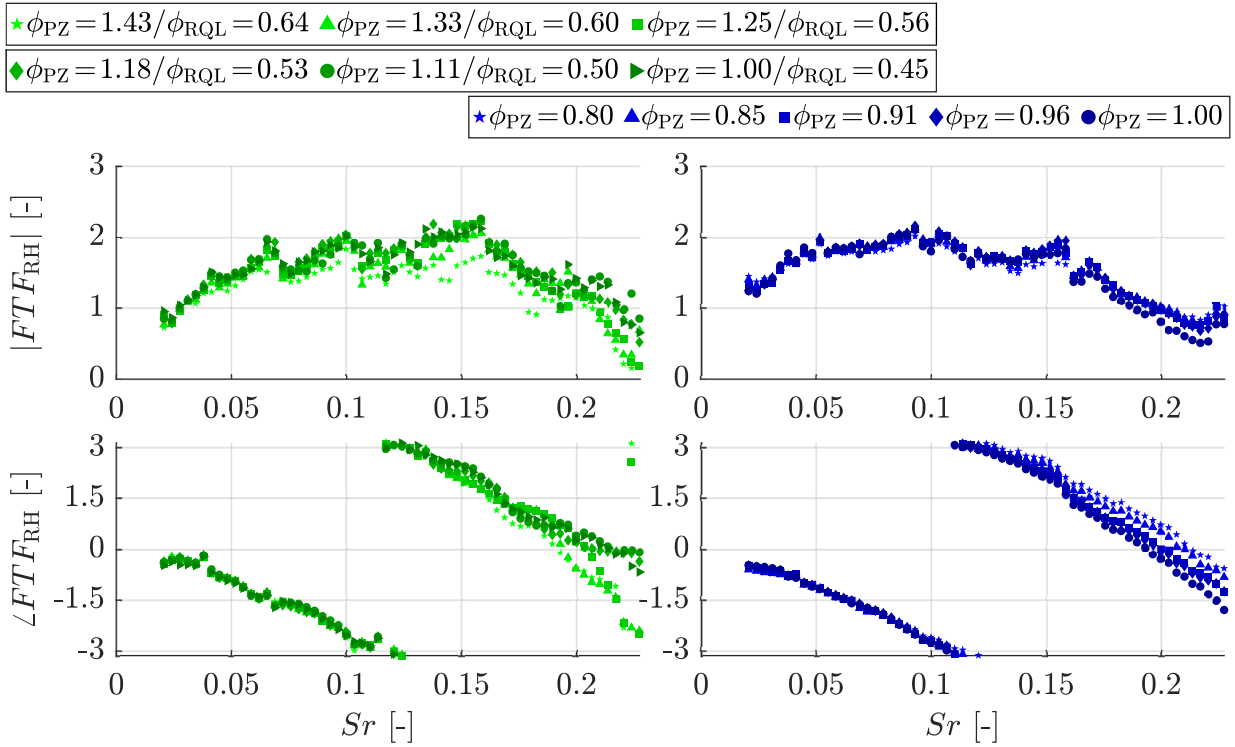


Figure 7.9: FTF_{RH} -amplitudes (top) and -phases (bottom) of the primary zone in the compact RQL arrangement for varying equivalence ratios in the primary zone $\phi_{PZ,RQL}$ (green symbols on the left) and the stoichiometric and lean operated, isolated primary zone (blue symbols on the right). The FTF amplitudes of the compact RQL combustor were calculated by considering the additional secondary air being entrained into the primary zone.

The resulting flame transfer functions of the FTM22-elements in Fig. 7.8 using the adiabatic flame temperature of the corresponding equivalence ratio in the primary zone as T_h are illustrated in Fig. 7.9 (cf. Eq. 4.10). Due to the additional secondary air in the primary zone of the compact RQL combustor, the effective equivalence ratio and consequently the adiabatic flame temperature is shifted to leaner combustion conditions.

The same findings can be drawn from Fig. 7.9 as from the FTM22-elements in Fig. 7.8. Again the phases are in almost perfect agreement between the RQL and the isolated primary zone (green symbols bottom left and blue symbols bottom right in Fig. 7.9, respectively). The amplitudes of the isolated lean and

stoichiometric primary zone and the primary zone of the compact RQL combustor on top of Fig. 7.9 exhibit a very similar trend, with some smaller discrepancies at certain Strouhal numbers (e.g. $Sr \approx 0.05$ or $Sr \approx 0.15$). However, the conclusions will be summarized again for the flame transfer functions of Fig. 7.9.

First, due to secondary air being entrained into the primary zone, the flame dynamics of the isolated primary zone under fuel-rich conditions cannot be transferred to the primary zone in the compact RQL combustor ($FTF_{PZ,RQL} \neq FTF_{PZ}$ for $\phi_{PZ,RQL} = \phi_{PZ} > 1$). Second, the main heat release zone is located in the primary zone due to the very good agreement of the phases between the RQL and the isolated primary zone under stoichiometric or lean combustion conditions ($\phi_{PZ} \leq 1$). This observation is confirmed by the amplitudes of the FTMs and FTFs leading to a diminishing influence of the secondary flame in the RQL combustor ($FTF_{SZ,RQL} \ll FTF_{PZ,RQL}$). Due to the diminishing influence of the secondary flame as well as the dilution hole acoustics, neither the secondary burner nor flame has to be considered for the estimation of the overall flame dynamics of the RQL combustor. Third, the flame dynamics in terms of FTMs and FTFs of the isolated, stoichiometric or fuel-lean operated primary zone shows qualitatively the same trend as the compact RQL combustor for the equivalence ratio range studied in this work ($FTF_{RQL} \approx FTF_{PZ,RQL} \propto FTF_{PZ}$ for $\phi_{PZ} \leq 1$). Quantitative good results can be obtained if the additional secondary air sucked into the primary zone is considered. An estimation on the amount of secondary air being entrained into the primary zone can be obtained by applying Eq. 7.29. As a result, the measurement of the flame dynamics of the isolated primary zone for stoichiometric or fuel lean combustion conditions reveals the flame dynamics of the compact RQL combustor under consideration of the entrained secondary air ($FTF_{RQL} \approx FTF_{PZ,RQL} \approx FTF_{PZ}$ for $\phi_{PZ} \leq 1$).

8 Summary and Conclusions

The aim of the present work is the investigation and clarification of the driving mechanisms on the flame dynamics of the primary zone in air-staged aero engine combustion chambers (RQL). In addition, the transfer of the flame dynamics of the isolated primary zone to the compact RQL combustor is demonstrated. A new scientific approach realized in a specially designed thermoacoustic test rig allowed the identification of the isolated thermoacoustic behavior of the primary and secondary zone, as well as their combination in the compact RQL combustion chamber.

The main objectives of the test rig concept were a high modularity and the thermodynamic design to ensure auto-ignition in the separated secondary zone. The heat losses between the two separated combustion chambers were estimated using simple 1D flow calculations, as well as CFD calculations for the primary zone and the adjacent transition duct. The results showed that auto-ignition should take place in the lean burn-out zone, despite the heat losses along the path from the primary to the secondary combustion chamber. The acoustic design focused on the realization of high-quality FTF measurements by using piezodynamic pressure transducers and loudspeakers. The length of the impedance measurement ducts and the distancing of the PCBs were determined by considering high quality acoustic wavefield reconstruction down to low excitation frequencies. As acoustic excitation, a 12 inch loudspeaker model was chosen according to an acoustic 1D network model of the test rig, indicating the loudspeaker model providing the best acoustic signal-to-noise ratio.

In the primary zone a prototype aero engine injector consisting of a double radial swirler with a pressure atomizer nozzle was integrated into the combustion chamber. Additionally, a natural gas nozzle was designed to compare the dynamic flame behavior between non-premixed kerosene (Jet-A1) and natural gas combustion.

The operating points investigated in the primary zone were based on pairs of equivalence ratios with similar adiabatic flame temperature for rich and lean

combustion conditions. Consequently, each operating point pair largely excludes flame temperature effects on the thermoacoustic behavior.

The assessment of the flame dynamics was carried out by using the purely acoustic multimicrophone method, as well as the optical method based on the flame's chemiluminescence and the acoustic velocity fluctuation. Latter flame transfer functions were quantified by using an array of photomultiplier tubes equipped with bandpass filters and without correction of the CO_2^* background radiation. OH^* , CH^* , C_2^* , and CO_2^* were chosen as potential measures for representing heat release and heat release fluctuations. Spatial information of the qualitative heat release zone was obtained by means of a high-speed camera equipped with OH^* - and CH^* -bandpass filters. The quality of the acoustic wavefield reconstruction needed for both FTF measurement methods was improved by implementing a thermocouple correction method based on the radiation error in the hot gas environment along the impedance measurement duct downstream the primary zone. In addition, a selection criterion for the dynamic pressure sensors in each impedance measurement duct based on an error measure was implemented but showed less influence on the final flame transfer function results.

Before experimentally quantifying the flame transfer functions of the primary zone, the commissioning of the new thermoacoustic test rig had to be performed. The commissioning tests focused on identifying rich- and lean-blow-out (LBO and RBO), as well as the thermoacoustic stability behavior of the combustion chambers. The arising self-excited combustion instabilities could be largely mitigated by optimizing the acoustic boundary conditions resulting in a wide operating range of the test rig.

The steady global chemiluminescence measurements of the non-premixed kerosene combustion for the rich and lean operating points using photomultiplier tubes indicate a bell-shaped intensity distribution for OH^* , CH^* , and CO_2^* with a maximum at slightly rich combustion conditions. Only the intensity of C_2^* is monotonously increasing with equivalence ratio and found to be a good indicator for the effective equivalence ratio in the primary zone. All four radicals showed a linear dependence on thermal power indicating a potential usability of chemiluminescence intensity for measuring heat release fluctuations. For purpose of equivalence ratio fluctuation measurements, the ratios of all radicals were evaluated. Only the ratio of CH^*/C_2^* gave a clear

monotonous trend over the equivalence ratio and is consequently found to be potentially suitable for measuring equivalence ratio and its fluctuations. Apart from the zero-dimensional photomultiplier measurements, chemiluminescence imaging of the primary zone's flame was performed. The qualitative heat release zone, as well as relevant flame parameters, e.g. center of gravity, could be quantified by using a high-speed camera equipped with bandpass filters for either OH^* or CH^* . The inverse Abel-transformed images for near stoichiometric and rich operating points of both radicals showed that the fuel-rich flame approaches the combustor's wall. Due to this, interpretation of the flame images should be taken with caution. However, the center of gravity for fuel-rich combustion conditions gave similar values for OH^* and CH^* . In contrast, during lean combustion the center of gravity of OH^* was located closer to the burner outlet as OH^* .

The purely acoustically measured flame transfer functions of the isolated primary zone were evaluated for five rich and five lean equivalence ratios according to the operating points with similar adiabatic flame temperature using the Rankine-Hugoniot relations. The lean flame transfer functions showed high amplitudes and a nearly identical behavior up to high Strouhal numbers, whereas the phases at higher Strouhal numbers become flatter the leaner the combustion gets. Contrarily, the amplitudes of the fuel-rich flame transfer functions demonstrate a clearly different behavior. An increasing deviation above low Strouhal numbers is observable indicating a distinct influence of the primary zone equivalence ratio: the richer the combustion the lower the amplitude and the sooner a minimum is reached. In contrast, the phases of the fuel-rich FTFs coincide up to high Strouhal numbers. To verify the phases in the rich and lean combustion regimes, the isothermal CFD flow field was combined with the calculated center of gravity from the OH^* -images. Using the time delay model the measured and calculated phase delays were compared and showed good agreement.

A more detailed investigation was conducted to clarify the root cause of the dependency of the flame transfer function amplitudes in the fuel-rich regime on the primary zone equivalence ratio. For this purpose, the flame dynamics using non-premixed natural gas nozzle were measured. Except the fuel nozzle the same burner hardware as in the non-premixed kerosene case was used allowing to isolate effects on the flame dynamics due to atomization and

evaporation. The resulting flame transfer function amplitudes of both combustion modes exhibited a very similar behavior, especially for low Strouhal numbers. These similarities led to the conclusion that atomization and evaporation does not have a major influence on the flame dynamics of the burner studied. The reduction of the fuel-air mixture temperature due to the increase in fuel mass flow with increasing equivalence ratio was estimated in a separate investigation. A maximum decrease of -14.7% of the fuel-air mixture temperature led to a reduction in the adiabatic flame temperature of -2%. This was found to be not sufficient to have a large impact on the flame dynamics. Furthermore, the purely acoustically measured flame transfer function phases and the OH^{*}-images do not indicate a substantial lengthening of the flame during rich combustion. Consequently, the synthesis gas formation is expected to potentially alter the flame dynamics in the fuel-rich primary zone, but this hypothesis was not verified. Apart the synthesis gas formation, the wall contact of the flame during fuel-rich combustion is expected to further lower the heat release of the flame due to local quenching of the chemical reactions on the cold combustor wall.

The determination of the flame transfer function from the flame transfer matrix using the classic Rankine-Hugoniot relations is based on assuming the flame as a temperature jump only. For this reason, an alternative approach for the determination of the flame transfer function was derived, which considers the change in gas composition, the temperature dependencies of the gas properties up- and downstream of the flame, as well as the flame movement. The resulting alternative flame transfer functions showed substantially lower amplitudes compared to the results using the classic Rankine-Hugoniot relations. The consideration of the chemical conversion was identified to dominate the deviation between the alternative and the classic Rankine-Hugoniot approach, while the temperature dependence of the gas properties and the flame movement showed minor influence. In conclusion, the alternative approach for the determination of flame transfer functions for near stoichiometric and fuel-rich flames provides more reliable results than using the classic Rankine-Hugoniot relations.

The determination of flame transfer functions in the isolated primary zone using the chemiluminescence of the flame was investigated by comparing the flame transfer functions based on chemiluminescence with the purely

acoustically measured flame transfer functions. All four investigated radicals (OH^* , CH^* , C_2^* , and CO_2^*) were found to be suitable representations of heat release and fluctuations. The amplitudes of the optical flame transfer functions were in qualitative agreement for all radicals, whereas the phases additionally showed good quantitative agreement with the acoustically measured flame transfer functions. A linear regression was performed resulting in a calibration factor for each of the investigated radicals to obtain quantitative correct amplitudes. All calibration factors were dependent on the equivalence ratio and did not show universal applicability. The best results could be obtained by using the chemiluminescence intensity of the CH^* molecule for rich and near stoichiometric combustion conditions, whereas for lean combustion conditions OH^* seems to be more suitable.

In practical aero engine combustion chambers the overall flame dynamics of both combustion zones is of interest. Due to this, an analytical approach for the flame transfer function of the compact RQL combustor based on a linear combination of the individual heat release fluctuations in the primary and secondary zone was derived. The resulting model was evaluated with data from the experimentally obtained flame transfer functions of the isolated primary and secondary zone. It was demonstrated that the flame dynamics of the primary zone dominates the overall thermoacoustic behavior of practical or compact RQL combustion chambers, assuming that the individual flame dynamics in both stages can be linearly combined.

The experimental investigation of the compact RQL combustor is based on a comparison of the flame dynamics in the isolated primary zone to that of the primary zone in the compact RQL combustor. A one-dimensional acoustic modeling approach was derived, based on the analytical formulations for an acoustic three-port and the mass conservation of the dilution holes to represent the secondary stage. The modeling approach was verified by comparing the burner transfer matrix of the isolated primary zone measurements with that of the primary zone in the compact RQL combustor and showed almost perfect agreement. The influence of the acoustics of the dilution holes on the overall RQL combustor was only visible for low Strouhal numbers. Using the obtained model, the elements of the flame transfer matrix coupling the up- and downstream acoustic velocity fluctuation of the primary flame in the RQL combustor were evaluated and compared to the isolated primary

zone results for the same primary zone equivalence ratios. For stoichiometric (no secondary flame) and fuel-rich combustion conditions in the primary zone, the phases showed good agreement, whereas the amplitudes of the fuel-rich isolated primary zone were not in line with those of the primary zone in the compact RQL combustor, which all showed the same qualitative behavior. In contrary, the amplitudes of the lean and stoichiometric operated isolated primary zone showed qualitative good agreement with the amplitudes of the flame transfer matrix of the compact RQL combustor. However, the amplitudes of the flame transfer matrix of the compact RQL combustor were shifted to higher values compared to those of the isolated primary zone for stoichiometric and lean combustion conditions. The amplitudes of the relevant element of the flame transfer matrix are influenced by the hot gas temperature between the two combustion zones, which was assumed to be the same as in the isolated primary zone measurements. As a conclusion, secondary air must be sucked into the primary zone via the inner recirculation zone, lowering the temperature downstream the primary flame and leading to lower amplitudes. This conclusion is supported by images of the compact RQL combustor flame being similar to that of the isolated primary zone for lean combustion conditions. An estimate of the amount of secondary air being entrained into the primary zone could be obtained by the comparison of the flame transfer functions of the isolated primary zone and the primary zone in the compact RQL combustor for stoichiometric conditions. Finally, the correct consideration of the additional secondary air results in similar flame transfer functions of the isolated, fuel-lean operated primary zone and the theoretically fuel-rich operated primary zone in the compact RQL arrangement. However, the interaction of the flow fields of the primary and secondary zone leads to an altered flame dynamics in the primary zone of the compact RQL combustor compared to that of the isolated primary zone for the same theoretical equivalence ratio. For this reason, the superposition of the individually measured flame dynamics of the primary and secondary zone does not result in the flame dynamics of the compact RQL combustor due to the interaction of the flow fields of both combustion zones.

Previous Publications

Significant parts of this Ph.D. thesis have been published by the author beforehand in conference proceedings and journal papers. All of these relevant prior printed publications are registered according to the valid doctoral regulations and are listed below. However, not all of them are quoted explicitly everywhere as they are part of this present work being official documents. Whether these personal prior printed publications were referenced, depended on maintaining comprehensibility and providing all necessary context.

1. March, M., Renner, J., and Sattelmayer, T., 2023. "Acoustic and Optical Investigations of the Flame Dynamics of Rich and Lean Kerosene Flames in the Primary Zone of an Air-Staged Combustion Test-Rig". *Journal of Engineering for Gas Turbines and Power*, **146**(1), p. 011004.
2. Renner, J., March, M., Do, T.-A., Merk, M., Hirsch, C., and Sattelmayer, T., 2023. "Flame Transfer Functions of the Lean Burnout Zone of an RQL Combustion Chamber - Dynamic Response to Primary Zone and Mixing Port Velocity Fluctuations". *International Journal of Spray and Combustion Dynamics*, **15**(2), pp. 105-116.
3. Renner, J., March, M., Hirsch, C., Sattelmayer, T., 2022. "Flame Dynamics in the Lean Burnout Zone of an RQL Combustion Chamber - Response to Primary Zone Velocity Fluctuations". *International Journal of Spray and Combustion Dynamics*. **14**(3-4), pp. 238-250.
4. March, M., Renner, J., Hirsch, C., and Sattelmayer, T., 2021. "Design and Validation of a Novel Test-Rig for RQL Flame Dynamics Studies". In *Proceedings of the ASME Turbo Expo*, Volume 3A: Combustion, Fuels, and Emissions, p. V03AT04A007. GT2021-58602.

Supervised Student Thesis

The author of this Ph.D. thesis supervised several student theses which were carried out at the Lehrstuhl für Thermodynamik, Technische Universität München in the years 2018 to 2022. Sections of these student theses are integrated into the current thesis.

The author would like to express his heartfelt thanks to all the students they have previously supervised for their dedication and assistance in this research endeavor.

Name	Thesis title, type, submission date
Korbinian Götz	Konstruktion und Auslegung der Kerosinversorgung für einen Fluggasturbineninjektor, Bachelor's Thesis, April 8th, 2019
Claude Kremer	CFD-Simulation of the Combustion Chamber of a Test Rig for Combustion Instabilities in Aero-Engines with Air Staging (RQL), Master's Thesis, August 26th, 2019
Florian Winter	Characterization of a Kerosene-Injektor for Aero-Gasturbines Regarding Spray Quality, Semester Thesis, February 1st, 2020
Victor Martius	Design of the Cooling System for the Aero-Engine Combustion Test-Rig, Semester Thesis, May 31st, 2020
Dominik König	Characterization of Fuel Rich Combustion for Different Fuel Types in a RQL Combustion Test Rig for Aero Engines, Semester Thesis, January 28th, 2021
Joao Antonio A. G. Avelino	On the Effect of Spray Atomization on Thermoacoustic Instabilities in the Primary Zone of an RQL Combustion Test-Rig, Semester Thesis, April 30th, 2022
Martin Maierhofer	Analytische und messtechnische Erfassung des Temperaturfeldes nach der Primärzone eines RQL-Verbrennungsprüfstandes, Bachelor's Thesis, June 30th, 2022
Justus Benteler	Experimentelle, optische Untersuchung von Verbrennungsinstabilitäten in der Primärzone eines RQL Verbrennungsprüfstandes, Semester Thesis, December 6th, 2022

Bibliography

- [1] ACI World, 2023. "Global Passenger Traffic Expected to Recover by 2024 and Reach 9.4 Billion Passengers". <https://aci.aero>. Accessed: 2024-01-14.
- [2] European Union Aviation Safety Agency, 2022. "European Aviation Environmental Report 2022". Tech. rep., Publications Office of the European Union, Luxembourg.
- [3] International Civil Aviation Organization, 2022. "2022 Environmental Report". Tech. rep., International Civil Aviation Organization, Montreal, Canada.
- [4] Lee, D., Fahey, D., Skowron, A., Allen, M., Burkhardt, U., Chen, Q., Doherty, S., Freeman, S., Forster, P., Fuglestvedt, J., Gettelman, A., Leon, R. D., Lim, L., Lund, M., Millar, R., Owen, B., Penner, J., Pitari, G., Prather, M., Sausen, R., and Wilcox, L., 2021. "The Contribution of Global Aviation to Anthropogenic Climate Forcing for 2000 to 2018". *Atmospheric Environment*, **244**, p. 117834.
- [5] European Commission and Directorate-General for Mobility and Transport and Directorate-General for Research and Innovation, 2011. "Flightpath 2050 - Europe's Vision for Aviation - Maintaining Global Leadership and Serving Society's Needs". Tech. rep., Publications Office of the European Union, Luxembourg.
- [6] Chang, C., and Holdeman, J., 2001. "Low Emissions RQL Flametube Combustor Test Results". Tech. Rep. TM-2001-210678, NASA, Cleveland, US.
- [7] Rosfjord, T. J., Padget, F. C., and Tacina, R., 2001. "Experimental Assessment of the Emissions Control Potential of a Rich/Quench/Lean Com-

- bustor for High Speed Civil Transport Aircraft Engines". Tech. Rep. CR-2001-210613, NASA, East Hartford, US.
- [8] Samuelsen, G. S., Brouwer, J., Vardakas, M. A., and Holdeman, J. D., 2012. "Experimental and Modeling Investigation of the Effect of Air Preheat on the Formation of NO_x in an RQL Combustor". *Heat and Mass Transfer*, **49**, pp. 219–231.
- [9] Makida, M., Yamada, H., and Shimodaira, K., 2012. "Detailed Research on Rich-Lean Type Single Sector Combustor for Small Aircraft Engine Tested Under Practical Conditions up to 3MPa". In *Proceedings of the ASME Turbo Expo*, Vol. 2: Combustion, Fuels and Emissions, Parts A and B, pp. 341–349. GT2012-68468.
- [10] Palies, P., Acharya, R., and Hoffie, A., 2019. "Design and Challenges of Lean Fully Premixed Injectors for Gas Turbine Engines". In *AIAA Propulsion and Energy 2019 Forum*. AIAA 2019-4257.
- [11] Correa, S., 1993. "A Review of NO_x Formation Under Gas-Turbine Combustion Conditions". *Combustion Science and Technology*, **87**(1-6), pp. 329–362.
- [12] Samuelsen, G. S., Brouwer, J., Vardakas, M. A., and Holdeman, J. D., 2013. "Experimental and Modeling Investigation of the Effect of Air Preheat on the Formation of NO_x in an RQL Combustor". *Heat and Mass Transfer*, **49**(2), pp. 219–231.
- [13] Lefebvre, A. H., and Ballal, D. R., 2010. *Gas Turbine Combustion: Alternative Fuels and Emissions*. Taylor & Francis, Boca Raton, US.
- [14] Lechner, C., and Seume, J., 2010. *Stationäre Gasturbinen*. Springer Berlin Heidelberg, Heidelberg, Germany.
- [15] Lieuwen, T. C., 2012. *Unsteady Combustor Physics*. Cambridge University Press, Cambridge, UK.
- [16] Keller, J. J., 1995. "Thermoacoustic Oscillations in Combustion Chambers of Gas Turbines". *AIAA Journal*, **33**(12), pp. 2280–2287.

- [17] Dowling, A. P., 1995. "The Calculation of Thermoacoustic Oscillations". *Journal of Sound and Vibration*, **180**(4), pp. 557–581.
- [18] Rayleigh, 1878. "The Explanation of Certain Acoustical Phenomena". *Nature*, **18**(455), pp. 319–321.
- [19] Sattelmayer, T., 2003. "Influence of the Combustor Aerodynamics on Combustion Instabilities from Equivalence Ratio Fluctuations". *Journal of Engineering for Gas Turbines and Power*, **125**(1), pp. 11–19.
- [20] Clavin, P., and Siggia, E. D., 1991. "Turbulent Premixed Flames and Sound Generation". *Combustion Science and Technology*, **78**(1-3), pp. 147–155.
- [21] Cumpsty, N. A., and Marble, F. E., 1977. "Core Noise from Gas Turbine Exhausts". *Journal of Sound and Vibration*, **54**(2), pp. 297–309.
- [22] Strahle, W. C., 1971. "On Combustion Generated Noise". *Journal of Fluid Mechanics*, **49**(2), pp. 399–414.
- [23] Komarek, T., and Polifke, W., 2010. "Impact of Swirl Fluctuations on the Flame Response of a Perfectly Premixed Swirl Burner". *Journal of Engineering for Gas Turbines and Power*, **132**(6), p. 061503.
- [24] Syred, N., 2006. "A Review of Oscillation Mechanisms and the Role of the Precessing Vortex Core (PVC) in Swirl Combustion Systems". *Progress in Energy and Combustion Science*, **32**(2), pp. 93–161.
- [25] Hirsch, C., Fanaca, D., Reddy, P., Polifke, W., and Sattelmayer, T., 2005. "Influence of the Swirler Design on the Flame Transfer Function of Premixed Flames". In *Proceedings of the ASME Turbo Expo*, Vol. 2: Combustion, Fuels and Emissions, pp. 151–160. GT2005-68195.
- [26] Paschereit, C. O., Gutmark, E., and Weisenstein, W., 1998. "Structure and Control of Thermoacoustic Instabilities in a Gas-Turbine Combustor". *Combustion Science and Technology*, **138**(1-6), pp. 213–232.
- [27] Schadow, K. C., and Gutmark, E., 1992. "Combustion Instability Related to Vortex Shedding in Dump Combustors and their Passive Control". *Progress in Energy and Combustion Science*, **18**(2), pp. 117–132.

- [28] Poinso, T. J., Trouve, A. C., Veynante, D. P., Candel, S. M., and Esposito, E. J., 1987. “Vortex-Driven Acoustically Coupled Combustion Instabilities”. *Journal of Fluid Mechanics*, **177**, pp. 265–292.
- [29] Cho, J. H., and Lieuwen, T. C., 2003. “Modeling the Response of Premixed Flames to Mixture Ratio Perturbations”. In *Proceedings of the ASME Turbo Expo*, Vol. 2: Combustion, Fuels and Emissions, pp. 67–76. GT2003-38089.
- [30] Lieuwen, T., and Zinn, B. T., 1998. “The Role of Equivalence Ratio Oscillations in Driving Combustion Instabilities in Low NO_x Gas Turbines”. *Symposium (International) on Combustion*, **27**(2), pp. 1809–1816.
- [31] Richards, G. A., and Janus, M. C., 1998. “Characterization of Oscillations During Premix Gas Turbine Combustion”. *Journal of Engineering for Gas Turbines and Power*, **120**(2), pp. 294–302.
- [32] Eckstein, J., Freitag, E., Hirsch, C., Sattelmayer, T., von der Bank, R., and Schilling, T., 2005. “Forced Low-Frequency Spray Characteristics of a Generic Airblast Swirl Diffusion Burner”. *Journal of Engineering for Gas Turbines and Power*, **127**(2), pp. 301–306.
- [33] Christou, T., Stelzner, B., and Zarzalis, N., 2021. “Influence of an Oscillating Airflow on the Prefilming Airblast Atomization Process”. *Atomization and Sprays*, **31**(3), pp. 1–14.
- [34] Kulkarni, S., Silva, C. F., and Polifke, W., 2022. “Response of Spray Number Density and Evaporation Rate to Velocity Oscillations”. *International Journal of Spray and Combustion Dynamics*, **14**(1-2), pp. 107–117.
- [35] Eckstein, J., Freitag, E., Hirsch, C., and Sattelmayer, T., 2006. “Experimental Study on the Role of Entropy Waves in Low-Frequency Oscillations in a RQL Combustor”. *Journal of Engineering for Gas Turbines and Power*, **128**(2), pp. 264–270.
- [36] Polifke, W., Paschereit, C., and Döbbeling, K., 2001. “Constructive and Destructive Interference of Acoustic and Entropy Waves in a Premixed Combustor with a Choked Exit”. *International Journal of Acoustics and Vibration*, **6**(3), pp. 135–146.

- [37] Keller, J. J., Egli, W., and Hellat, J., 1985. “Thermally Induced Low-Frequency Oscillations”. *Zeitschrift für angewandte Mathematik und Physik ZAMP*, **36**(2), pp. 250–274.
- [38] Marble, F. E., and Candel, S. M., 1977. “Acoustic Disturbance from Gas Non-Uniformities Convected Through a Nozzle”. *Journal of Sound and Vibration*, **55**(2), pp. 225–243.
- [39] Dowling, A., and Williams, J., 1983. *Sound and Sources of Sound*. E. Horwood, Michigan, US.
- [40] Culick, F. E. C., 1994. “Some Recent Results for Nonlinear Acoustics in Combustion Chambers”. *AIAA Journal*, **32**(1), pp. 146–169.
- [41] Zahn, M., 2018. “Vorhersage und Optimierung des Thermoakustischen Stabilitätsverhaltens von Ringbrennkammern unter Einsatz Passiver Dämpfer”. PhD Thesis, Technical University of Munich, Munich, Germany.
- [42] Eckstein, J., 2004. “On the Mechanisms of Combustion Driven Low-Frequency Oscillations in Aero-Engines”. PhD Thesis, Technical University of Munich, Munich, Germany.
- [43] Cai, J., Ichihashi, E., Mohammad, B., Tambe, S., Kao, J.-H., and Jeng, S.-M., 2010. “Gas Turbine Single Annular Combustor Sector: Combustion Dynamics”. In *48th AIAA Aerospace Sciences Meeting Including the New Horizons Forum and Aerospace Exposition*. AIAA 2010-21.
- [44] Abdelnabi, B., Cai, J., Tambe, S., Kao, J.-H., and Jeng, S.-M., 2011. “Combustion Dynamics and Emissions Characterization for a Gas Turbine Combustor Burning Methane and Propane”. In *47th AIAA/ASME/SAE/ASEE Joint Propulsion Conference & Exhibit*. AIAA 2011-5704.
- [45] Weber, M., Song, J., and Lee, J. G., 2021. “Characterization of Dynamics of Unstable Fuel-Rich Flame”. In *Proceedings of the ASME Turbo Expo*, Vol. 3B: Combustion, Fuels, and Emissions, p. V03BT04A034. GT2021-60121.

- [46] Venkatesan, K., Cross, A., and Han, F., 2022. "Acoustic Flame Transfer Function Measurements in a Liquid Fueled High Pressure Aero-Engine Combustor". In *Proceedings of the ASME Turbo Expo*, Vol. 3A: Combustion, Fuels, and Emissions, p. V03AT04A049. GT2022-81769.
- [47] Renner, J., 2023. "Flame Dynamics Investigation of the Lean Burnout Zone of an RQL Combustion Chamber". PhD Thesis, Technical University of Munich, Munich, Germany.
- [48] Spurk, J., and Aksel, N., 2019. *Strömungslehre: Einführung in die Theorie der Strömungen*. Springer Berlin Heidelberg, Heidelberg, Germany.
- [49] Morse, P. M. C., and Ingard, K. U., 1986. *Theoretical Acoustics*. Princeton University Press, Princeton, US.
- [50] Poinso, T., and Veynante, D., 2011. *Theoretical and Numerical Combustion*. CNRS, Toulouse, France.
- [51] Polifke, W., van der Hoek, J., and Verhaar, B., 1997. "Everything You Always Wanted to Know About f and g". Tech. rep., Technical Report of ABB Research, Baden, Switzerland.
- [52] Munjal, M. L., 2014. *Acoustics of Ducts and Mufflers*. Wiley, New York, US.
- [53] Munjal, M. L., and Doige, A. G., 1990. "Theory of a Two Source-Location Method for Direct Experimental Evaluation of the Four-Pole Parameters of an Aeroacoustic Element". *Journal of Sound and Vibration*, **141**(2), pp. 323–333.
- [54] Fischer, A., 2003. "Hybride, thermoakustische Charakterisierung von Drallbrennern". PhD Thesis, Technical University of Munich, Munich, Germany.
- [55] Alemela, P. R., 2009. "Measurement and Scaling of Acoustic Transfer Matrices of Premixed Swirl Flames". PhD Thesis, Technical University of Munich, Munich, Germany.
- [56] Åbom, M., 1991. "Measurement of the Scattering-Matrix of Acoustical Twoports". *Mechanical Systems and Signal Processing*, **5**(2), pp. 89–104.

- [57] Bade, S., 2014. “Messung und Modellierung der thermoakustischen Eigenschaften eines modularen Brennersystems für vorgemischte Drallflammen”. PhD Thesis, Technical University of Munich, Munich, Germany.
- [58] Freitag, E., 2009. “On the Measurement and Modelling of Flame Transfer Functions at Elevated Pressure”. PhD Thesis, Technical University of Munich, Munich, Germany.
- [59] Balachandran, R., Ayoola, B. O., Kaminski, C. F., Dowling, A. P., and Mastorakos, E., 2005. “Experimental Investigation of the Nonlinear Response of Turbulent Premixed Flames to Imposed Inlet Velocity Oscillations”. *Combustion and Flame*, **143**(1), pp. 37–55.
- [60] Armitage, C. A., Balachandran, R., E., M., and Cant, R. S., 2006. “Investigation of the Nonlinear Response of Turbulent Premixed Flames to Imposed Inlet Velocity Oscillations”. *Combustion and Flame*, **146**(3), pp. 419–436.
- [61] Palies, P., Durox, D., Schuller, T., and Candel, S., 2011. “Nonlinear Combustion Instability Analysis Based on the Flame Describing Function Applied to Turbulent Premixed Swirling Flames”. *Combustion and Flame*, **158**(10), pp. 1980–1991.
- [62] Noiray, N., Durox, D., Schuller, T., and Candel, S., 2008. “A Unified Framework for Nonlinear Combustion Instability Analysis Based on the Flame Describing Function”. *Journal of Fluid Mechanics*, **615**, pp. 139–167.
- [63] Chu, B. T., 1953. “On the Generation of Pressure Waves at a Plane Flame Front”. *Symposium (International) on Combustion*, **4**(1), pp. 603–612.
- [64] Gaydon, A., and Wolfhard, H., 1953. *Flames: Their Structure, Radiation, and Temperature*. Chapman & Hall, London, UK.
- [65] Nori, V., and Seitzman, J., 2007. “Chemiluminescence Measurements and Modeling in Syngas, Methane and Jet-A Fueled Combustors”. In *45th AIAA Aerospace Sciences Meeting and Exhibit*. AIAA 2007-466.

- [66] Gaydon, A. G., 1974. *The Spectroscopy of Flames*. Chapman and Hall Ltd, London, UK.
- [67] Lakowicz, J. R., 2007. *Principles of Fluorescence Spectroscopy*. Springer Verlag US, Springer New York, US.
- [68] Vogel, M., 2023. "Determination of Equivalence Ratio Fluctuations in a Lean Premixed Dual Fuel Gas Turbine Combustor". PhD Thesis, Technical University of Munich, Munich, Germany.
- [69] Woisetschläger, J., 2017. "Laser in der Schwingungs- und Strömungsmesstechnik". Tech. rep., Technical University of Graz, Graz, Austria.
- [70] Lauer, M., 2011. "Determination of the Heat Release Distribution in Turbulent Flames by Chemiluminescence Imaging". PhD Thesis, Technical University of Munich, Munich, Germany.
- [71] Bobusch, B. C., Moeck, J. P., Paschereit, C. O., and Sadig, S., 2012. "Thermoacoustic Stability Analysis of a Kerosene-Fueled Lean Direct Injection Combustor Employing Acoustically and Optically Measured Transfer Matrices". In *Proceedings of the ASME Turbo Expo*, Vol. 2: Combustion, Fuels and Emissions, Parts A and B, pp. 781–794. GT2012-69034.
- [72] Lefebvre, A. H., and McDonell, V. G., 2017. *Atomization and Sprays*. CRC press, Boca Raton, US.
- [73] Ashgriz, N., 2011. *Handbook of Atomization and Sprays: Theory and Applications*. Springer New York, New York, UK.
- [74] Ricou, F. P., and Spalding, D. B., 1960. "Measurements of Entrainment by Axisymmetrical Turbulent Jets". *Journal of Fluid Mechanics*, **11**(1), pp. 21–32.
- [75] Goodwin, D. G., Moffat, H. K., Schoegl, I., Speth, R. L., and Weber, B. W., 2023. "Cantera: An Object-oriented Software Toolkit for Chemical Kinetics, Thermodynamics, and Transport Processes". <https://www.cantera.org>. Version 3.0.0.

- [76] Dagaut, P., and Cathonnet, M., 2006. "The Ignition, Oxidation, and Combustion of Kerosene: A Review of Experimental and Kinetic Modeling". *Progress in Energy and Combustion Science*, **32**(1), pp. 48–92.
- [77] Verein Deutscher Ingenieure, 2013. *VDI-Wärmeatlas*. Springer Berlin Heidelberg, Heidelberg, Germany.
- [78] Smith, T. F., Shen, Z. F., and Friedman, J. N., 1982. "Evaluation of Coefficients for the Weighted Sum of Gray Gases Model". *Journal of Heat Transfer*, **104**(4), pp. 602–608.
- [79] Zalosh, R. G., 2003. *Industrial Fire Protection Engineering*. John Wiley & Sons, Ltd, Massachusetts, US.
- [80] Petrov, V., and Reznik, V., 1972. "Measurement of the Emissivity of Quartz Glass". *High Temperatures-High Pressures*, **4**, pp. 687–693.
- [81] Kremer, C., 2019. "CFD-Simulation of the Combustion Chamber of a Test Rig for Combustion Instabilities in Aero-Engines with Air Staging". Master Thesis, Technical University of Munich, Munich, Germany.
- [82] Thiele, N., 1971. "Loudspeakers in Vented Boxes: Part 1". *Journal of the Audio Engineering Society*, **19**(5), pp. 382–392.
- [83] Small, R. H., 1972. "Direct Radiator Loudspeaker System Analysis". *Journal of the Audio Engineering Society*, **20**(5), pp. 383–395.
- [84] Small, R. H., 1973. "Vented-Box Loudspeaker Systems Part 1: Small Signal Analysis". *Journal of the Audio Engineering Society*, **21**(5), pp. 363–372.
- [85] Hamamatsu Photonics, 2024. "About PMTs | Photomultiplier tubes (PMTs)". https://www.hamamatsu.com/us/en/product/optical-sensors/pmt/about_pmts.html. Accessed: 2024-01-10.
- [86] Dribinski, V., Ossadtchi, A., Mandelshtam, V. A., and Reisler, H., 2002. "Reconstruction of Abel-Transformable Images: The Gaussian Basis-Set Expansion Abel Transform Method". *Review of Scientific Instruments*, **73**(7), pp. 2634–2642.

- [87] Hickstein, D. D., Gibson, S. T., Yurchak, R., Das, D. D., and Ryazanov, M., 2019. "A Direct Comparison of High-Speed Methods for the Numerical Abel Transform". *Review of Scientific Instruments*, **90**(6), p. 065115.
- [88] Schuermans, B., 2003. "Modeling and Control of Thermoacoustic Instabilities". PhD Thesis, École Polytechnique Fédérale de Lausanne, Lausanne, Switzerland.
- [89] Paschereit, C., Schuermans, B., Polifke, W., and Mattson, O., 2002. "Measurement of Transfer Matrices and Source Terms of Premixed Flames". *Journal of Engineering for Gas Turbines and Power*, **124**(2), pp. 239–247.
- [90] The MathWorks Inc., 2022. "MATLAB". <https://www.mathworks.com>. Version R2022b.
- [91] Yi, T., and Santavicca, D. A., 2009. "Flame Spectra of a Turbulent Liquid-Fueled Swirl-Stabilized Lean-Direct Injection Combustor". *Journal of Propulsion and Power*, **25**(5), pp. 1058–1067.
- [92] Bradley, D., and Entwistle, A. G., 1961. "Determination of the Emissivity, for Total Radiation, of Small Diameter Platinum-10% Rhodium Wires in the Temperature Range 600–1450°C". *British Journal of Applied Physics*, **12**, pp. 708–711.
- [93] Balat-Pichelin, M., Sans, J.-L., Bêche, E., Charpentier, L., Ferrière, A., and Chomette, S., 2021. "Emissivity at High Temperature of Ni-Based Superalloys for the Design of Solar Receivers for Future Tower Power Plants". *Solar Energy Materials and Solar Cells*, **227**, p. 111066.
- [94] Stadlmair, N., 2018. "Influence of Water Injection on the Thermoacoustic Stability of a Lean-Premixed Combustor". PhD Thesis, Technical University of Munich, Munich, Germany.
- [95] Lee, H., and Seo, S., 2015. "Experimental Study on Spectral Characteristics of Kerosene Swirl Combustion". *Procedia Engineering*, **99**, pp. 304–312.
- [96] Clark, P., 1954. "A Study of the Radiation from Laminar and Turbulent Open Propane Air Flames as a Function of Flame Area, Equivalence Ratio and Fuel Flow Rate". Tech. Rep. RM E54F29, NASA, Cleveland, US.

-
- [97] Kaufmann, J., Vogel, M., Papenbrock, J., and Sattelmayer, T., 2022. "Comparison of the Flame Dynamics of a Premixed Dual Fuel Burner for Kerosene and Natural Gas". *International Journal of Spray and Combustion Dynamics*, **14**(1-2), pp. 131–142.
- [98] Arrhenius, S., 1889. "Über die Reaktionsgeschwindigkeit bei der Inversion von Rohrzucker durch Säuren". *Zeitschrift für Physikalische Chemie*, **4U**(1), pp. 226–248.
- [99] Rachner, M., 1998. "Die Stoffeigenschaften von Kerosin Jet A-1". *DLR-Mitteilungen*, **98-01**(1).
- [100] Chu, B. T., 1956. "Stability of Systems Containing a Heat Source - The Rayleigh Criterion". Tech. Rep. RM 56D27, National Advisory Committee for Aeronautics, Washington, US.
- [101] Strobio Chen, L., Bomberg, S., and Polifke, W., 2016. "Propagation and Generation of Acoustic and Entropy Waves Across a Moving Flame Front". *Combustion and Flame*, **166**(1), pp. 170–180.
- [102] Beaulieu, A. F., Dharmaputra, B., Schuermans, B., Wang, G., Caruso, S., Zahn, M., and Noiray, N., 2024. "Measuring Acoustic Transfer Matrices of High-Pressure Hydrogen/Air Flames for Aircraft Propulsion". *Combustion and Flame*, **270**, p. 113776.